Micro-structural and functional properties of TiAlCN/VCN coating produced by High Power Impulse Magnetron Sputtering Technology.

KAMATH, Ganesh K.

Available from Sheffield Hallam University Research Archive (SHURA) at:

http://shura.shu.ac.uk/20171/

This document is the author deposited version. You are advised to consult the publisher's version if you wish to cite from it.

Published version

KAMATH, Ganesh K. (2011). Micro-structural and functional properties of TiAlCN/VCN coating produced by High Power Impulse Magnetron Sputtering Technology. Doctoral, Sheffield Hallam University (United Kingdom)..

Copyright and re-use policy

See http://shura.shu.ac.uk/information.html

Sheffield Hallam University Research Archive
http://shura.shu.ac.uk

Acisetis Centre, City Campus
Sheffield S1 1WD

102 006 846 9

Sheffield Haliam University
I Learning and information Services
| Adsetts Centre, City Campus
Sheffield S1 1WD

I

REFERENCE

ProQuest Number: 10700006

All rights reserved

INFORMATION TO ALL USERS
The quality of this reproduction is dependent upon the quality of the copy submitted.

In the unlikely event that the author did not send a complete manuscript
and there are missing pages, these will be noted. Also, if material had to be removed,
a note will indicate the deletion.

uest

ProQuest 10700006

Published by ProQuest LLC(2017). Copyright of the Dissertation is held by the Author.

All rights reserved.
This work is protected against unauthorized copying under Title 17, United States Code
Microform Edition © ProQuest LLC.

ProQuest LLC.
789 East Eisenhower Parkway
P.O. Box 1346
Ann Arbor, MI 48106- 1346

Micro-structural and functional properties of TiAlCN/VCN coating produced by High Power Impulse Magnetron Sputtering Technology

Ganesh Kamath K

(Dedicated to my dear parents and brothers Jayesh and Radhesh)

A thesis submitted for the degree of

Doctor of Philosophy

in Materials Engineering and Research Institute,

Sheffield
Hallam University

November 2011

Declaration

The work reported in this thesis is original and was carried out by me under the supervision my Ph.D director Prof. Papken Eh Hovsepian and supervisor Prof. Arutiun P Ehiasarian, during my tenure as a Ph.D student at Nanotechnology Centre for PVD research lab, Materials Engineering and Research Institute, Sheffield Hallam University, UK. Thus the work carried out and explained in this particular thesis will not form basis for any other degree, diploma, associateship, membership or similar title of any university or institution.

(Ganesh Kamath)
November 2011

NanoTechnology Centre
for PVD Research

Materials Engineering and Research Institute
Sheffield Hallam University
UK-S1 1WB

ABSTRACT

Nanoscale TiAlCN/VCN multilayer coating was deposited in an industrial size 1000x4 Hauzer Techno Coating machine capable to operate with both unbalanced magnetron sputtering (UBMS) and high power impulse magnetron sputtering (HIPIMS) mode. The work was directed to study the impact of HIPIMS on the microstructure of the nanoscale TiAlCN/VCN coating, in relation to its properties at both room and elevated temperatures.

TiAlCN/VCN coatings were deposited by three different ways in combination of reactive UBM and HIPIMS technique. These are (i) reactive pure UBMS, (ii) reactive combined UBMS and HIPIMS, (iii) reactive pure HIPIMS. The microstructure and mechanical properties of the nanoscale TiAlCN/VCN coatings deposited in all the above combination of deposition have been studied. In all three cases, coatings were deposited in three major steps: (a) HIPIMS etching by $Ar^+ + V^+$ ions (b) a 300 nm thick TiAlN base layer deposition in Ar + N_2 atmosphere followed by 2.5 μm thick TiAlCN/VCN coating deposition in mixed $Ar+N_2+CH_4$ reactive atmosphere. PVD chamber furnished with two pairs of opposing magnetrons with TiAl and V targets were utilised deposit this coating. During the second case of combined deposition, two opposing magnetrons were enabled to operate in HIPIMS mode and other two magnetrons were operated in UBMS mode, where as in third case only two opposing targets with HIPIMS power supply were utilised to deposit the TiAlCN/VCN coating respectively. In all the three cases, deposition parameters such as bias voltage ($U_b = -75V$), deposition temperature ($T_s = 450$ °C) and total pressure of reactive gas mixture ($Ar+N_2+CH_4; P \cong 4\,X\,10^{-3}$ mbar) were maintained at similar conditions.

The V+ HIPIMS etching used in all three processes has shown excellent adhesion (Lc>50) of the coating to the substrate. The plasma compositional analysis of V+ HIPIMS etching has shown high metal-to-gas ion ratio with ionization states of V up to 5+. The ionic composition of the HIPIMS plasma as a function of discharge current was analysed by plasma sampling using energy-resolved mass spectrometery. During the coating of TiAlCN/VCN, the plasma analysis has confirmed the higher production rate of metal ions and free carbon in case of HIPIMS-UBM in contrast to pure UBM. This has resulted to a denser closed columnar microstructure of the coating during the HIPIMS-UBM technique than UBM. Whereas in case of reactive pure

HIPIMS case, production rate of metal ions were appeared to gradually reduce at the expense of more free carbon production. XTEM analysis of pure HIPIMS deposited coating revealed the formation of three zones with different nanostructures across the film thickness. In the initial stages of deposition a TiAlCN/VCN nanoscale multilayer structure was formed (first zone) followed by a nanocomposite structure comprising TiAlCN/VCN crystalline grains surrounded by a carbon rich tissue phase (second zone). The grain size of the crystalline phase gradually decreased with thickness from diameter of 10-15 nm to complete dissolution in the third zone where Me- carbon with XRD amorphous structure was formed. In dynamic oxidation conditions, thermogravimetric analysis determined the temperature of the onset of rapid oxidation to be 800 °C for pure HIPIMS deposited coating. Compared to UBM and HIPIMS-UBM deposited TiAlCN/VCN coating, the oxide mass gain of the HIPIMS coatings was less than 30-50%. A dry sliding wear tests were conducted at room temperature and different elevated temperatures of 200°C, 450°C, and 650°C on coatings deposited by all three cases. The friction coefficient was found to be $\mu = 0.45$ at room temperature, where the coefficient steadily decreased from 0.7 at 200°C, to 0.5 at 450°C and 0.4 at 650°C respectively. The scanning electron microscope and X-ray diffraction studies of the oxidised surface of the UBM and HIPIMS-UB deposited coating has revealed the formation of lubricant Magneli phase oxides of V_2O_5 and TiO_2 at elevated temperature. The wear coefficient of the coating deposited by (HIPIMS-UBM) has shown two orders of magnitude lower value than that for the UBM deposited coatings, which represents significant advantage for coatings deposited by UBM. The wear coefficient in case of HIPIMS deposited coating reduces by one order of magnitude with the wear depth, with initial value of $K_c = 3.8 \times 10^{-15}\ m^3N^{-1}m^{-1}$after 500 laps to $K_c = 4.4 \times 10^{-16}\ m^3N^{-1}m^{-1}$after 10000 laps. In comparison, UBM deposited TiAlCN/VCN coatings tested under similar conditions show an order of magnitude higher wear coefficient of $4.1 \times 10^{-15}\ m^3N^{-1}m^{-1}$ thus demonstrating the beneficial effect of the HIPIMS process. This peculiar wear behaviour is believed to result from the graded coating phase and micro structures of TiAlCN/VCN coating deposited by this pure HIPIMS technique. The overall enhanced performance in oxidation resistance, dry sliding wear conditions at room and elevated temperatures can be attributed to the extremely dense structure resulted by high energy bombardment achieved due to more metal ion production during HIPIMS. The formation of graded like microstructure achieved during reactive pure HIPIMS case, further plants the importance of HIPIMS in producing advanced nanostructured coatings for high technology applications.

ACKNOWLEDGEMENTS

My sincere thanks to Prof. Papken Eh. Hovsepian for his valuable directions and guidance given during my stay at nanotechnology centre for PVD research (NTCPVD) lab. He is an inspiring guide and counsel. I admire his craving perfection and unquestionable ability of logical thinking. I truly enjoyed every bit of interaction I had with him, during my stay at NTCPVD research lab. Dear Professor, thank you very much for all the support and help I received.

I shall also very grateful to Prof. Arutiun P Ehiasarian for his constant support and guidance; supervision and encouragement; which helped me in giving a shape to this work. The credit for my early journal publications in IEEE transaction on plasma science and SVC 2010 Techkon proceedings; a full part of which is a content of my initial thesis, should go to him for his persistent push and guidance. I truly thank him for being very kind and supportive throughout my stay at NTCPVD.

I am indebted to Dr. Yashodhan Purandare, senior research fellow at NTCPVD, for his useful discussion during my early tenure of Ph.D work. His constant assistance during the deposition of multilayer thin films in industrial sized coating machine and handling of other laboratory scale instruments, were much valuable. I am very much thankful to Mr. Garry Robinson, principal technician at NTCPVD, whose quick help in terms of solutions to the technical problems faced during the Ph.D work made me to finish my Ph.D experimental work on time.

I deeply thank our collaborator Prof. Ivan Petrov and his colleagues at Fedric sietze materials research lab, University of Chicago, USA, for their outstanding help in high resolution Transmission Electron Microscopic and related work, which contributed a high quality result to my thesis. The endeavour of Mr. Stuart Creasy and Mr. Vinay Patel, Scanning Electron Microscope (SEM) experts at Materials Engineering and Research Institute, Sheffield Hallam University are gratefully acknowledged as well, for their true support for my SEM related work of present thesis.

I acknowledge Dr. Heath and Dr. Peter Korgul for their assistance during my TEM microscope work at Sorby nano centre, University of Sheffield. I owe them a lot for their help came at a crucial stage of my research work.

Materials Engineering and Research Institute (MERI) at Sheffield Hallam University is greatly acknowledged for providing the financial support by way of fellowships to carry out this work. The director of MERI, both the present and past, are acknowledged for providing required facility. Office staffs at MERI, especially, Mrs. Indira, Mrs Gelian, Mrs Rachael, Mrs Jane, Miss Corrie, were also very helpful at times of need. They deserve to be thanked for their co-operation. Prior to my Ph.D work, I was doing my research at Crystal growth lab, Department of Physics, Indian Institute of Science, Bangalore India, where I had got the opportunity to start my research career in materials physics. I am very happy and would like to grately acknowledge Prof. H.L.Bhat and Dr. J.N.Babu Reddy (then Ph.D student of the department) for their supportive guidance. If not for this opportunity, I would not have got in to the field of research. I learnt many basics about research in that short period, while working on the non linear single crystal growth and their physical and optical properties. Interacting with the then Crystal growth lab members, viz. Dr. Vinayak (prl), Dr. Vanishri, Ganesan, Hari, and Naveen was illuminating. I am thankful to GOD for giving me an opportunity to get associated with my best friends Dr. Vinayak, Mohan, Prathap, Dr. Nonappa, Dr. Venkatesh, Dr. Anantheshwara, the Ph.D students from IISc, who encouraged me to continue research career.

I am fortunate to have met many nice people in MERI, who made my research life rich with pleasant memories. I shared many exciting moments with MERI research students Dr. Ante Hecimovic, Prakash muthudoss, Khairudhin, Dr. Mousa, Dr. Salaha, Daniel, Arun, Steve Dodds, Sampan, Itai Vutabwarova, Vikas. I certainly miss the light moments in beautiful Sheffield pubs, where I used to go out on some weekends with Harry (my supervisor), Yash, Daniel, Arun. I should not forget my B.Sc mentor Prof. K.G.Rathnakar and Prof. M.S.Adiga who taught me Physics and Maths respectively. I shall thankful to them.

I spent most of my evening in swimming and exercise and sort of got addicted to the these activities. Also, I should not forget to pay my grate thanks to Mr. Santhosh and Mrs Rekha Santhosh (Rekha babhi), and darling Malavika Santhosh (Malu), with whom I regularly used to spend my most of the night times and engaged to have dinner. Their moral support was very crucial for me to the successful concentration in my Ph.D work.

Also, Prakash, Padmashree (sister) and Rajesh are my best friends with whom I spent my almost three years in UK. I miss them a lot in coming days.

Top of all, Blessings from my parents, without which I wouldn't have completed my Ph.D. The care which they took from my childhood is very important for my success today. I bow to them throughout my life. Also, I owe a lot to my brothers Jayesh and Radhesh and all my family members who supported me morally and strengthened me mentally to leave my country and stay abroad. Here, I should not forget to mention the name of one non family member, Mrs Usha Rai, to whom I consider as my sister. She also stayed as my strong supporter and encouraged me throughout my research career and still continuing her care for me. Every year, she used to conduct prayers for me in temple for my success, which I cann't forget. I do not have words to express my feelings (which is true with most) for her persistent guidance, support, unceasing my difficult situations. Without all these encouragement, I wouldn't have reached the goal.

Certification and conference attended during PhD

- **Transmission electron microscopy for nanostructured materials**, theory and practical training inTEM imaging; at Sorby nanocenter, University of Sheffield

- **Sputter Deposition for industries** advanced course given by Prof. Joe Greene, D.B.Willett professor from University of Illinois, Chicago,USA,

- **Micro-structural Evolution during Thin Film growth**, course by Prof. Joe Greene
  D.B.Willett professor of materials Science, From University of Illinois, USA.

- **Fundamentals of HIPIMS**, course given by Prof. Arutiun Ehiasarian, NTCPVD, Sheffield Hallam Unviersity, UK, and Prof. Andre Anders, Lawrence berkeley.

- **1st International HIPIMS conference**, Sheffield Hallam University, Sheffield, United Kingdom, (2009) **: Presented Poster** "Structural and High temperature tribological studies on HIPIMS/UBM deposited TiAlCN/VCN nanoscale multilayer coating", G.Kamath, A.P.Ehisarian, P.Eh.Hovsepian

- **Electron microscopy and Analysis group conference**, University of Sheffield, Sheffield, United Kingdom. **Presented Poster**: "Microstructural and Raman spectroscopy of worn surface generated on TiAlCN/VCN at room and elevated temperature", G.Kamath, A.P.Ehiasarian, P.Eh.Hovsepian

- **2nd International HIPIMS conference**, Sheffield Hallam University, Sheffield, United Kingdom, (2010) : Presented Oral "Micro-Structural and Oxidative Mechanical Wear studies of TiAlCN/VCN Nanostructured Multilayer Coating Deposited by HIPIMS/HIPIMS-UBM Technique, G.Kamath, A.P.Ehiasarian, P.Eh.Hovsepian.

- **53rd Annual Technical Conference of Society of Vacuum Coaters**, Orlando, April 17- 22 Florida, (FL), United States (2010).

- **12th International Conference on Plasma Surface Engineering,** "Structure evolution in TiAlCN/VCN nanoscale multilayer coatings deposited by reactive High Power Impulse Magnetron Sputtering technology", Papken Hovsepian, A. Ehiasarian, G. Kamath, Rick Haasch, Ivan Petrov.

- **54th Annual Technical Conference of Society of Vacuum Coaters,** Chicago, April 17- 22 Illinois, United States (2011). Presented Oral "Micro-structural, Oxidation and Tribological Properties of TiAlCN/VCN coatings deposited by Reactive HIPIMS, G. Kamath, P. Eh. Hovsepian, A. P. Ehiasarian and I. Petrov.

List publications

Journal publications

- Tribological and Oxidation Behavior of TiAlCN/VCN Nanoscale Multilayer Coating Deposited by the Combined HIPIMS/(HIPIMS-UBM) technique, G. Kamath, A. P. Ehiasarian, Y. Purandare, P. Eh. Hovsepian, Surface Coatings and Technology, 205, (2011), 2823-2829.

- Microstructure, Oxidation and Tribological Properties of TiAlCN/VCN Coatings Deposited by Reactive HIPIMS, Submitted for publication in J.Vac.Sci.Tech.A, P. Eh. Hovsepian, A. P. Ehiasarian, G. Kamath, R.Haasch, I. Petrov, 2011.

- Properties of TiAlCN/VCN Nanoscale Multilayer Coatings Deposited by Mixed High Power Impulse Magnetron Sputtering and Unbalanced Magnetron UBM) Processes-Impact of HIPIMS during coating, G. Kamath, A. P. Ehiasarian, P. Eh. Hovsepian, IEEE transaction on plasma science (special issue), 38, No.11, 2010, 3062.

Conference papers

- Micro-structural, Oxidation and Tribological Properties of TiAlCN/VCN coatings deposited by Reactive HIPIMS, G. Kamath, P. Eh. Hovsepian, A. Ph. Ehiasarian and I. Petrov, 54th Annual Technical Conference of Society of Vacuum Coaters, Chicago, April 16-22, Chicago, United States (2011).

- Micro-Structural and Oxidative Mechanical Wear Study on TiAlCN/VCN Nanostructured Multilayer Coating Deposited by HIPIMS/HIPIMS Technique - Impression of High Density Metal-Ion Irradiation in Reactive Atmosphere, G. Kamath, Y. Purandare, A. P. Ehiasarian, P. Eh. Hovsepian, 53rd Annual Technical Conference of Society of Vacuum Coaters, Orlando, April 17- 22 Florida, (FL), United States (2010).

Table of Contents

Abstract .... **III**

Acknowledgments .... **V**

Certification and conference attended during PhD .... **VIII**

List publications .... **IX**

Journal publications .... **IX**

Table of Contents .... **X**

CHAPTER 1 .... **1**

Introduction **1**

1.1. Motivation 1

1.2 Purpose of present research work 3

1.3 Methods of approach 6

1.4 Structure of thesis 8

CHAPTER 2 .... **9**

Literature Review **9**

2.1 Physical Vapour Deposition Coating Technology (PVD) 9

2.1.1 Fundamentals of Plasma 10

2.1.2 Plasma Discharge 16

2.1.3 Sputtering 20

2.1.4 DC Magnetron Sputter deposition technique 23

2.1.5 Cathodic Arc deposition 25

2.1.6 Unbalanced Magnetron Sputtering 27

2.1.7 High Power Impulse Magnetron Sputtering (HIPIMS) 29

2.2 Thin film microstructural evolution 34

2.3 Nanostructured coatings 40

2.4 Nanostructured and composite coatings- for advanced Tribological applications 44

2.4.1 Nanostructured carbon films 45

2.4.2 Advanced deposition systems for nanostructured and carbon based films 48

CHAPTER 3 .... **52**

Experimental Methodology **52**

3.1 Substrate material, specimen preparation and deposition method 52

3.1.1 Substrate material and specimen preparation techniques followed prior to nanoscale TiAlCN/VCN deposition 52
3.2 Deposition Process and system geometry 54
3.2.1 Reactive pure UBM and HIPIMS-UBM technology 54
3.3 Coating characterising techniques 59
3.3.1 Adhesion test 59
3.3.2 Rockwell C (HRc) Indentation method 60
3.3.3 Pin-on-disc test 61
3.3.4 Nano-hardness test 63
3.4 Plasma characterisation 64
3.4.1 Energy resolved mass spectrometry 64
3.4.2 Time averaged mode 66
3.5 X-ray diffraction (XRD) 68
3.5.1 Glancing angle geometry (GAXRD) 69
3.5.2 Bragg-Brentano (θ/2θ) geometry 70
3.6 Raman spectroscopic analysis 71
3.7 Thermo gravimetric Analysis 73
3.7.1 Operating Principle 74
3.8 Scanning electron microscope (SEM) 75
3.8.1 Secondary electron and back scattered electron image 76
3.9 Transmission Electron Microscopy (TEM) 79
3.9.1 TEM Sample preparation 82
3.10 Dry high-speed milling test 82
CHAPTER 4 84
Results 84
4.1 Plasma compositional analysis during TiAlCN/VCN deposition 84
4.1.1. Metal ion-to-gas ion ratio during HIPIMS etching 85
4.1.2 Metal ion-to-gas ion ratio during deposition of TiAlCN and VCN by UBM 88
4.2 Mechanical and tribological properties 93
4.2.1 Adhesion scratch and Rockwell-C indentation test 94
4.2.2 Tribological test 97
4.2.3 Nanohardness measurements 103
4.3 Structure and microstructure analysis 104
4.3.1 X-ray diffraction studies 104

4.3.2 Raman Spectroscopy analysis 107

4.4 Microstructural analysis 110

4.4.1 Scanning electron microscope analysis 110

4.4.2 Transmission electron microscope analysis 113

4.4.3 Electron diffraction X-ray Analysis (SAED) 117

4.5 Oxidation analysis 119

4.5.1 Thermo gravimetric analysis 120

4.5.2 Phase composition and microstructure of the oxide scale on TiAlCN/VCN films deposited by mixed HIPIMS-UBM techniques 120

4.5.3 Morphology of worn surface after sliding friction 127

4.5.4 Raman analysis of worn surface 130

4.6 Machining performance of TiAlCN/VCN coating deposited by combined HIPIMS-UBM technique 131

4.6.1.... Raman spectroscopy investigation of the worn tool-work piece material surface 133

(A) Analysis of tool cutter coated with TiAlCN/VCN by UBM and HIPIMS-UBM technique 133

CHAPTER 5 136

DISCUSSION 136

5.1 HIPIMS and UBM plasma-a comparison in terms of ionic composition 136

5.1.1 $V^+ + Ar^+$ ion etching by HIPIMS 136

5.1.2 Plasma composition during the deposition of TiAlCN/VCN coating 138

5.2 Mechanical and Tribological Properties of nanoscale TiAlCN/VCN coating 141

5.2.1 Mechanical properties determined for UBM and HIPIMS-UBM deposited coating 141

5.2.2. Room temperature friction and wear behaviour for UBM and HIPIMS- 143

UBM deposition case 143

5.2.3 Room temperature friction and wear behaviour for pure HIPIMS deposited case 146

5.2.4 Friction and wear behaviour at elevated temperature 149

5.3 Microstructural analysis of TiAlCN/VCN coating – Impact of HIPIMS 151

5.3.1 X-ray diffraction and SEM cross sectional analysis of nanoscale TiAlCN/VCN deposited by UBM and HIPIMS-UBM technique 151

5.3.2 Raman Spectroscopy 153

5.3.3 SEM cross sectional analysis of nanoscale TiAlCN/VCN deposited by pure UBM and HIPIMS-UBM technique 154

5.3.4 Glancing angle X-ray diffraction analysis of reactive pure HIPIMS deposited TiAlCN/VCN coating 156

5.3.5 Microstructural evolution of nanostructured TiAlCN/VCN coating – TEM study 157

A. Reactive pure UBM and mixed HIPIMS-UBM deposited case 157

B. Reactive pure HIPIMS deposited case 161

5.4 Oxidation behaviour 163

5.5 Wear mechanism and cutting performance of TiAlCN/VCN coated cutter in machining Al-alloy 168

Chapter 6 172

Conclusions 172

Further research 176

CHAPTER 1

Introduction

1.1. Motivation

Advanced fast growing industries like automotive and aerospace are facing the challenging problems of high speed cutting (HSC) and forming of soft and metallurgical aggressive materials such as Ti-, Al-, and Ni- based alloys [1]. During HSC machining operations, huge amount of heat is generated (with temperatures exceeding 700°C), which accumulates at the cutting edge. Since the above mentioned soft alloys have poor thermal conductivity and poor transfer of heat to the outgoing chip (especially Ti and Ti- based alloys), the counterpart should possess good thermal conductivity to dissipate heat away from the contact area of the cutting edge. One solution to this problem is the use of advanced tool protective coatings deposited by PVD methods. The overarching challenges in the current PVD technology is also to provide nanostructured multilayer coatings suitable for machining of above mentioned "sticky" alloys [1]. Essential requirements for successful tool coatings are high density, smooth surface morphology, high adhesion, and high wear resistance at cutting temperatures, low friction, good oxidation resistance, chemical stability and inertness relative to the work piece [2].

The early generation transition metal containing Nitrides, Carbides and Carbo-Nitride based monolayer coatings (TiN, CrN, TiCN,) were used substantially in machining carbon and alloy steels [3]. These coatings have been successfully developed by both CVD and PVD technology. But in the later stages of the research studies reveals that PVD technology was preferred over CVD technique to deposit coatings protecting the tools. The reasons are as follows [4]:

(i) Relative ease of deposition at lower temperature which preserves hard metal edge toughness, (ii) less compressive stress which helps to inhibits cracks on the surface, (iii) easy to deposit on sharp cutting edges without changing the interfacial reaction by product, (iv) fine grain structures can be achieved with higher microhardness, (v) less hazardous to environment compared to CVD process. However, the poor temperature stability of these monolayer coatings lead to a higher wear rate of the coated tool (due to tribo-oxidation) which in turn shortened its life time and restricted its use at elevated temperature range [5]. Although, TiAlN coatings provide efficient protection against tribo-oxidation and wear at 700°C -850°C range when machining various steels, the higher friction coefficient value ($\mu \approx 0.85$) has paved the way to explore more suitable coatings especially when machining of softer alloys is concerned. The reasons are the formation of huge build-up-edge (BUE) due to diffusion reaction with the work piece material, rough surface and high coefficient of friction against the ceramic nitride coatings [6]. Confronting these situations, compositionally modified Ti-Al-C-N based coatings, metal-carbon containing nanocomposite coating and DLC (Cr/WC/a-CH) coatings have been introduced which have shown a considerable success in the market for the machining of these "sticky" alloys. Particularly the highly inert DLC coating have shown reduced BUE formation, however, due to adhesion problems, their life time is still insufficient [1]. Over-stoichiometric carbon based nanocrystalline/amorphous structured coatings (TiC/a-C) have also found their importance in low friction and wear resistance applications [7], but their poor thermal and oxidation resistance restricts wider applicability in cutting tools/machining industries [8].

Low friction in dry sliding conditions has been achieved by incorporating V in the coating constitution. It has been shown that an increasing content of V incorporated in monolithically grown Ti-Al-N coating leads to decreased friction coefficient value at elevated temperature [9]. This has been attributed to the formation of several V-O phases (Magneli oxide phases), which provide easily shearable crystallographic planes along with the formation of low melting point (650°C) oxides such as V_2O_5, which act as a solid lubricant in the tribocontact [10, 11].

Recently, new class V- based nanoscale multilayer $Ti_{1-x}Al_xN$/VN coatings deposited by the latest PVD techniques such as unbalanced magnetron sputtering (UBM), high power impulse magnetron sputtering (HIPIMS) and mixed HIPIMS-UBM have been very successful in machining of "sticky" alloys [1]. The nanolaminate structure provides a new tool for enhancement of the solid lubrication mechanisms at elevated temperature but requires further understanding of the thermal stability of the coating materials in order to retain the integrity of the coating and avoid intermixing of the multilayers which often leads to degradation in performance. Although the TiAlN/VN multilayer coating has proved to be a very good alternative to machining Al-, Ti-, and Ni-based soft alloys, the tribofilm which forms during the machining process was found to bond to the worn surface, so complete avoidance of the BUE was not achieved [1]. Another type of carbon based multilayer coating combining the abrasive material TiAlN and friction reducing WC/C was developed, i.e, TiAlN/WC/C coating designed for protecting drill for dry machining applications. But the top layer WC/C is easily abraded away during the machining process [4].

After the deep retrospection on earlier efforts and pros and cons in field of cutting tool application, P.Eh.Hovsepian et.al., developed a carbon based nanostructured coating for the wear applications at elevated temperature. This involves TiAlCN/VCN and CrAlCN/CrCN. These coatings have shown considerable assurance to protect tools at elevated temperature applications [12, 13]. These coatings have revealed the ability to adapt self lubrication during sliding at elevated temperatures, (700 °C) by forming variety of Magnèli phase oxides such as $AlVO_4$, Ti_nO_{2n}, V_nO_{2n} ,V_nO_{2n+1} and achieved low friction force against the work piece material [14]. In case of TiAlCN/VCN nanoscale coating, it was shown that besides the formation of magneli phases, carbon atoms segregated at the interfaces between the individual nanolayers change the wear mechanism of the coating by providing low shear strength interfaces as well as reduce friction due to a graphitization mechanism taking place during sliding at elevated temperatures 300 ˉ 700 °C [14]. Thus during the dry sliding, weak atomic bonding , low decohesion energy of magneli oxide phases [15] and graphitic nature of carbon along with special nanolaminate layered structure of the TiAlCN/VCN coating was realized as a unique combination in stabilizing the friction and wear behavior of the coating. The relatively low friction coefficient values of μ=0.45 at room temperature which reduces to μ=0.38-0.4 at elevated temperatures, 300 ˉ 700 °C and wear rate of the order10^{-17} $m^3/N/m$ at room and10^{-15} $m^3/N/m$ at elevated temperatures have made TiAlCN/VCN coating [14] a potential candidate for application such as protective tool coating.

1.2 Purpose of present research work

In the present market, number of tool protective coatings and suitable technologies are available. It is well understood that a competitive coating performance requires proper material, microstructure and deposition technology selection. Deposition techniques influence strongly the coatings microstructure, and, therefore, their performance, due to differences in the plasma conditions intrinsic to the method. High Power Impulse Magnetron Sputtering (HIPIMS) is an emerging technology which provides new alternative in the fabrication of nano-scale multilayer structures [16]. The unique aspect of the HIPIMS discharge is the production of highly ionised plasma containing almost equal concentration of gas and metal ions with higher energy states [17].

The important purpose of this research work was to depict the difference between HIPIMS and UBM technologies in the production of nano-structured TiAlCN/VCN coating, and thereby to enhance its functional properties. Further, it was also our purpose to investigate the HIPIMS and UBM plasma properties during the deposition of nanostructured TiAlCN/VCN coating to further correlate the impact of plasma chemistry on the microstructure of as deposited coating which inturn impact on the functional properties. Previous research has confirmed unambiguously that when HIPIMS plasma is used for surface pre-treatment enhanced adhesion is achieved due to the production of atomically clean interface, preserved crystallinity of the substrate material and the promotion of local epitaxial growth of the coating over large areas [18]. It has also been shown that during the deposition, higher metal-to-gas ion ratio, higher dissociation rate of reactive gas, higher metal ionisation degree and higher energy of the condensing species attained in HIPIMS produces denser coatings by eliminating columnar voids formed due to atomic shadowing effect often observed in lower ion bombardment energy processes such as UBM for example [16, 19].

The past ten years of research on HIPIMS technology has clearly shown its importance in several aspects when compared to UBM technology. The following table compares briefly the differentiate between these above technologies, which helps the reader to understand the purpose of author in utilising HIPIMS technology.

HIPIMS	UBMS
High power density pulses applied on target with controlled duty cycle, which leads to achieve high plasma density near target vicinity	Constant DC power applied on target with relatively less plasma density near the target vicinity
High metal ion (>1) -to-neutral ratio	Metal ions (<1) are significantly less when compared to neutrals
Effective technology for surface pretreatment where etching mechanism is predominantly by metal ions; lead to highly crystalline coating-substrate interface and good adhesion	Comparatively inferior technology for surface pretreatment where gas ion bombardment is predominant which could lead to amorphous interface and subsequently results in defective coating growth and poor adhesion
Highly stable transition zone for reactive sputter deposition	Transition zone during reactive deposition is not stable and frequent plasma monitoring is necessary
Denser coating with smooth coating surface morphology without following conventional columnar coating growth	Under dense columnar coating growth is often observed with relatively rough surface morphology
Enable very successful uniform coating deposition on variety of complex shaped substrates	Line of sight deposition method where atomic shadowing effect leads to poor coating coverage on complex shaped substrates
Enable to deposit coating with strong desired texture and efficient control over phase composition	Very difficult to achieve desired texture and phase composition control is poor

After revealing the importance HIPIMS over the conventional UBM technique, it was the major purpose of the authors to inculcate HIPIMS for the deposition of TiAlCN/VCN coating to enhance its functional properties for both at room and elevated temperature application.

In order to full fill the purpose a systematic approach was undertaken. The nanostructured TiAlCN/VCN coating was deposited by three different methods, these are (i) HIPIMS/UBM (ii) HIPIMS/(HIPIMS-UBM) and (iii) HIPIMS/HIPIMS. In the first case, HIPIMS was utilized for only surface pretreatment of substrates and UBM was used to deposit the coating part. In the second case, the HIPIMS has been utilized for both surface pretreatment and coating was deposited by mixed HIPIMS/UBMtechnique. In the final case, reactive deposition was carried out by only HIPIMS tehchnology. The aim of this work is to show the effect of HIPIMS, when employed in both surface pretreatment and coating deposition steps, on the microstructure, oxidation resistance and thermal stability at elevated temperature of TiAlCN/VCN nanostructured multilayer coatings. Hence a comparative study has been carried out of the microstructure and isothermal oxidation of TiAlCN/VCN nanostructured multilayer coating deposited by pure UBM and mixed HIPIMS-UBM techniques. Further, in order to understand the impact of HIPIMS alone, the TiAlCN/VCN coating was deposited by reactive pure HIPIMS alone. Subsequent investigation involves the micro-structural and functional properties of the TiAlCN/VCN nano-scale coating, deposited by higher fraction of metal (Ti, Al and V) and carbon ions identified [20] in pure reactive HIPIMS plasma.

1.3 Methods of approach

According the aim of this particular research work, the approach was set in three different parts by depositing the TiAlCN/VCN nanostructured coating by three different ways in combination of UBM (Unbalanced magnetron sputtering) and HIPIMS (High Power Impulse Magnetron sputtering) technique. The process was carried out in an industrial size Hauzer HTC 1000/4 PVD coater, furnished with four rectangular targets of size 400x600 mm. Prior to deposition of the coating, substrate pretreatment (etching) was carried out by HIPIMS in all the three cases. During the deposition of the coating, deposition parameters were kept similar in all the three techniques. In the first part of the work, coating was deposited by UBM technique, where coating was deposited by reactive pure UBM technique. In the next part of the work, coating was deposited by mixed (HIPIMS-UBM) technique and in final part of the work coating was deposited by reactive pure HIPIMS technique.

The aim of the research work was to understand the impact of HIPIMS on the microstructure of TiAlCN/VCN coating and investigating the functional coating properties (oxidation, tribological) at both ambient and non ambient atmospheres. Hence, in all the three different cases of deposition, the deposition parameters such as gas pressure, average target power, bias voltage, and coil current were not altered in each case. The bias voltage during etching and coating deposition step was U_b = -1000 V and -75 V respectively. Hence, the plasma diagnostic has to be carried out in a laboratory scale ultra high vacuum chamber to further understand the importance of HIPIMS plasma over conventional UBM during the deposition of TiAlCN/VCN coating. In this direction, the energy resolved mass spectrometer was used to identify the ionic composition of the UBM and HIPIMS plasma separately. During the plasma analysis, the deposition parameters were kept similar to that of actual deposition of the coating in industrial sized machine.

After the deposition of TiAlCN/VCN coating by three different processes, a comparative analysis of the coating microstructure and performance was carried out. The micro-structural analysis was carried out by cross sectional SEM and TEM analysis. This was very important to correlate between the microstructure and the functional property of the coating. Thermogravimetric analysis was carried out in order to understand the thermal stability of TiAlCN/VCN coating, which is very essential if the coating performance has to be known at elevated temperature. The tribological performance of the coating was also carried out which was very important aim of the research work. The tribological tests were carried out at both room and elevated temperatures of 200 °C, 450 °C and 650 °C respectively. These tests were conducted at laboratory scale. Also, the coating was deposited on complex shaped machining tool substrate by HIPIMS/UBM and further importance of the HIPIMS and coating has been realised after carrying high speed machining operation of aerospace grade AlSi alloy. As obtained results for high speed machining operation was compared with previously reported high speed machining results for the same coating when deposited by UBM technique, under similar deposition conditions.

1.4 Structure of thesis

A brief review has been done in the chapter 2, which explains the important aspects related to Physical Vapour deposition (PVD) and its successful research and development toward advanced device fabrication industry. Further, important discussion proceeds on thin film microstructure evolution, which was assumed to be a fundamental base for understanding kinetics of thin film growth. Also, advanced nanostructured coating such as multilayer coatings, carbon based nanocomposite coatings, DLC etc. and its application and deposition methods have been reviewed, which also gives a motivation for further research and development work.

Chapter 3 describes the experimental details of this research work. Section 3.1 and 3.2 explains about the deposition related aspects in which substrate material preparation prior to the coating deposition, methods carried out during the deposition and process parameters used for the deposition of TiAlCN/VCN nanoscale coating by UBM, HIPIMS-UBM and pure HIPIMS have been discussed. Section 3.3 explains about the fundamental mechanical and tribological characterization techniques utilized in this work. Section 3.4 explains the plasma characterization technique used to investigate the plasma chemistry of UBM and HIPIMS plasma generated during the deposition of TiAlCN/VCN coating. The section 3.5 to 3.9 explains the phase, oxidation and microstructure analysis techniques carried out in this research work, such as XRD, Raman, TGA and SEM, TEM.

Final two chapters 4 and 5 illustrate the important results obtained and relevant discussion pertaining to the results.

CHAPTER 2

Literature Review

The objective of this chapter is to give the reader a perspective on latest advancement in sputtering based plasma processing techniques which are utilized in high technology applications. The discussion will begin with fundamentals of plasmas followed by most fundamental plasma generation method which is well known DC discharge. Further, review has been done on magnetically enhanced DC discharge. Based on this discharge principle, literature review was also carried out on most advanced ionised physical vapour deposition (IPVD) coating technologies; this includes Cathodic Arc, Unbalanced Magnetron Sputtering (UBMS) and High Power Impulse Magnetron Sputtering (HIPIMS) technique. The basic principle behind these two technologies has been reviewed in order to understand the importance of deposition parameters such as metal-to-gas ion ratio and its impact on the film microstructure during coating growth, which further helps to understand coating performance and its functional properties in real world applications. The fundamental mechanism of microstructural evolution and coating growth was also reviewed to gain more knowledge on the importance of ion bombardment during PVD coating growth. The basic microstructural discussion has been done on Nanoscale multilayer structure, Nanocrystalline and Nanocomposite and graded like microstructures. At the end of this chapter reader can see the bonding configurations, structure and properties of traditional carbon based coatings to recently developed carbon based multilayer structures.

2.1 Physical Vapour Deposition Coating Technology (PVD)

Physical vapour deposition is a atomic deposition technique, in which material is vaporized from a solid or liquid source and transported in a vacuum or low pressure plasmas to the substrates where it condensates. This technique can be used to deposit thin films of elements and molecules and also of compound materials by the reaction of depositing material with the ambient gas environments (e.g. TiN) or with a co-depositing material (e.g., TiC). Examples to PVD processes are vacuum evaporation, ion plating, and sputter deposition. All the three techniques can be used to deposit films with thickness in the range of few nanometers to thousands of nanometers. The majority of thin films are deposited nowadays by sputter deposition techniques where material atoms are sputtered and ionised during the process and finally bombarded on to the substrate at low temperature to form the film. Figure 1 shows the two major types of PVD process.

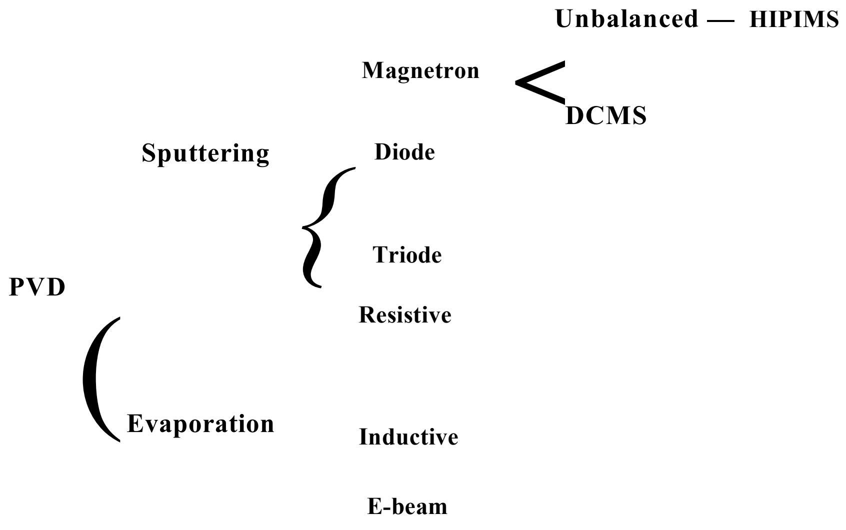

Figure 1 Hierarchy of PVD system

2.1.1 Fundamentals of Plasma

Over the last two-three decades, plasmas have been extensively studied and utilized in various fields of surface engineering processes with desired functional properties. Basically "Plasma" is *quasi-neutral ionised* gas containing a mixture of positive, negatively charged particles and few numbers of un-ionised neutral atoms or molecules. The fundamental mechanisms which sustain and stabilize the plasma are *ionisation and recombination, excitation and relaxation.* The detailed explanation of these processes can be seen in [21, 22]. All these mechanisms will be initiated as a consequence of inelastic collision between electron and neutral atom. The primary electron knocks out the outer most electron from the neutral atom and produces a positive ion along with two electrons. This process For example in Ar atmosphere can be equated as,

$$e + Ar \longrightarrow Ar^{+} + 2e \qquad — \ (1)$$

In order to sustain the plasma, it is very essential to maintain the balance between electrons and ions, as continuous recombination process (by 3-body collision) might reduce the number of electrons.

Hence to sustain the plasma, requires an additional external energy source which is electric field ($\vec{E}$) in this case, can act on these charged particles and maintain the balance between electrons and ions produced by ionisation process. Effectively, the electric field can energise and accelerate the electrons produced during primary ionisation process, which results in to more ionisation due to further ionising collision process (avalanche) between these accelerated energetic electrons and neutral atoms. Besides electron impact ionisation, there are several other ionising collisions which takes place inside the plasma which sustains its glow, For example dissociative collision, ion-neutral atom collision, metastable-neutral atom collision, metastable-metastable atomic collision etc. But the ionising probability by these collision processes is very less compared to electron impact ionisation as electric field interact less with heavy ions and neutral atoms. Figure 2 shows the energy transfer mechanism from electric field to the electron [21].

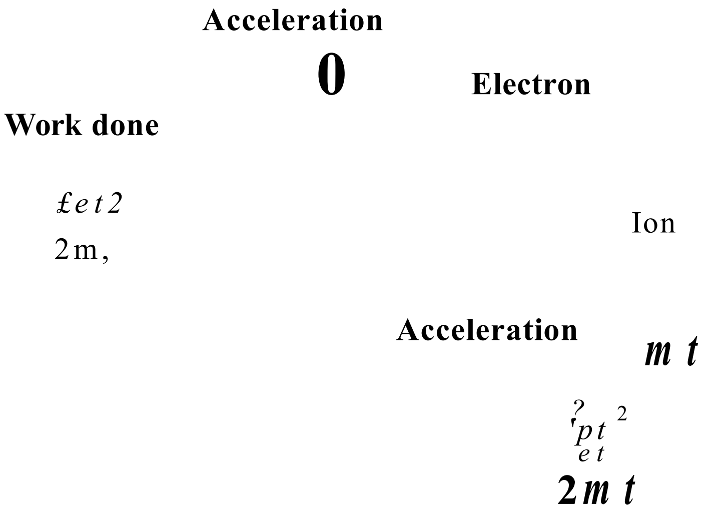

Figure 2 Conceptual explanation of energy transfer from the field to the electrons and ions [Ref: 21].

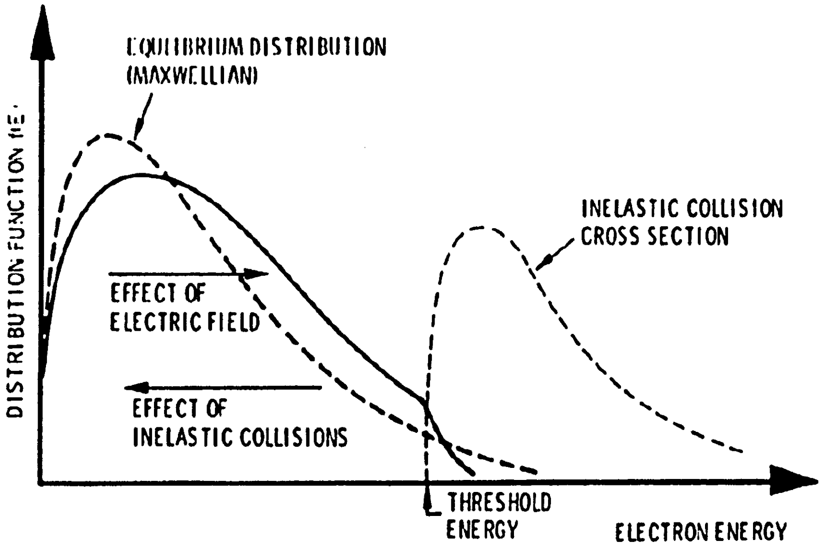

Figure 3 The electron energy distribution function; when electric field is applied and inelastic collision cross section [Ref: 22].

The average electron energy was reported to be about 2-8 eV. Whereas the average energy of ions and neutral atoms are much less (0.03 eV at 300 K) as compared to electrons due to their limited interaction with the electric field [21]. But in practice, the plasma processes will takes place in low pressure atmospheres. At these conditions electron energies are characterised by a term kT_e, where T_e is the electron temperature. The electron temperature ($\approx$ 23000 K) is always yield higher value than ion temperature ($\approx$ 500 K) and neutral gas atom temperature at low pressure plasmas. Thus, highly energetic electrons participate very effectively in high temperature plasma chemistry, although the actual temperature in the gas is low [23]. Following paragraph (A) briefly summarises about electron energy distribution function in glow discharge plasma with their energy state in terms of electron temperature T_e.

A. Electron energy distribution [Fe(E)]

Figure 3 illustrates the electron energy distribution function in comparison with equilibrium Maxwellian distribution. In presence of electric field ($\vec{E}$), the electrons will gain higher energy. Moreover, low pressure plasma conditions were expected to limit the electron energy loss due to lower chance of inelastic collisions of electrons with neutral gas atoms.

Hence, the presence of electric field will over populates these electrons towards higher energy regions of Maxwellian distribution. Electron energy distribution functions are measured by electrostatic probe analyzer and its energy state is always characterised in terms of electron temperature T_e.

B. *Sheath, plasma potential (V_p) and floating potential (V_f)*

Bulk plasma can be explained as a quasi-neutral region, where charge densities nearly cancel each other. The charge density neutrality was realised to disturb the bulk plasma at the plasma-solid interfaces. Here, the solid surface refers to surfaces of cathode and substrate walls. As a consequence there will be a potential drop across the solid surface. The potential drop across this region depends upon the charge separation between the bulk plasma and solid surface [24]. A schematic diagram of this plasma-surface interface is shown in Figure 4. This interface region is called "*Sheath*". Inside the plasma, high temperature electrons (dominant negative charge careers) masses are less (1/1823 amu) than ionic mass. Their response to the applied electric field is quite random and faster than ions [21]. This electronic response inside the plasma and across the sheath varies with respect to whether electrode surface is non-conducting (also called Floating electrode) or conducting. If the solid surface is electrically neutral, the charge imbalance would slowly develop space charge (ρ) across the sheath by repelling electron and attracting ions towards it continuously. This space charge can be given as [24]:

$$\varepsilon_0[\nabla * \overrightarrow{E}] = \rho \qquad (2)$$

Where, ε_0 = permittivity of free space ≈ 8.854×10^{-12} F/m,

$\nabla * \overrightarrow{E}$ = variation of potential across the sheath, $\rho = n_i - n_e$ Space charge.

The charge flow across the sheath will be controlled by the electric field caused due to space charge ρ. At this situation, the potential formed inside the plasma is called *"plasma potential (V_p)"*. The voltage associated with the isolated electrode wall is called *"floating potential* V_f*"*. The plasma potential is always positive with respect to the floating potential, i.e. $V_f < V_p$. The voltage $V_P - V_f$ will always repel the electrons and attract ions. In this way, sheath can be thought of as a region surrounded by positively charged plasma [21]. When the electrode is biased, i.e. if electrode is conducting, the electric field changes and it allows net current to flow across the sheath due to the modified space charge distribution and electric field $\vec{E}$[24]. The amplitude of this current is limited by the current source. The charge distribution and voltage drop in this case is different than those in the case of the isolated (unbiased) electrode.

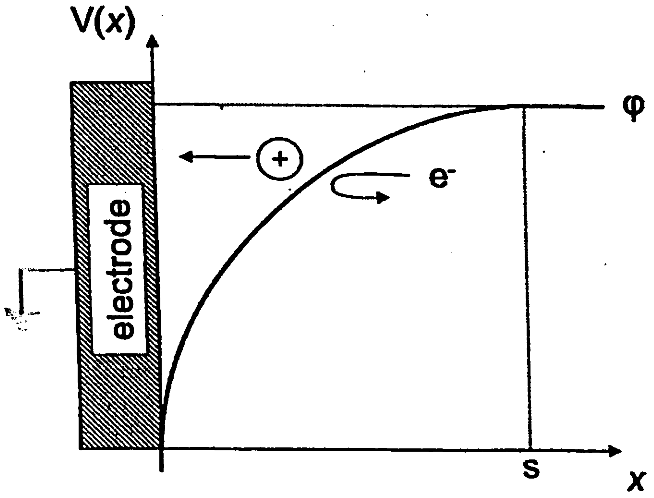

Figure 3 Schematic of plasma-surface interface region showing the potential drop from φ to zero, where X is distance from grounded electrode surface [Ref: 26].

Assuming "n_{es}" as number of electrons with average velocity $\overline{u}_{es}$ (averaged over Maxwellian form), moving randomly across the sheath edge at potential difference of $V_P - V_f$; the expression for electron current can be given as [24]:

$$j_e = \frac{1}{4}\, e\, n_{es}\, \overline{u}_{es} \exp\left[\frac{eV_o}{kT_e}\right] \tag{3}$$

Where, $$\overline{u}_{es} = \left[\frac{8kT_e}{\pi m_e}\right]^{\frac{1}{2}}$$

Similarly expression for ion current is given as [25],

$$j_i = \overline{Q}\, e\, n_{is} \overline{u}_{is} \tag{4}$$

Where, $\overline{Q} =$ average ion charge state

$$\overline{u}_{is} = \left[\frac{kT_e}{m_i}\right]^{\frac{1}{2}}$$ is Bhom velocity

When electrode surface is floating, both electron current and ion currents flowing across the sheath edge are equal. In this situation the floating potential V_f can be given as

$$V_f = -\frac{kT_e}{2e}\ln[\frac{m_i}{2\pi m_e}] \qquad (5)$$

Based on above these equations, values of j_e, j_i *and* V_f were calculated respectively for argon plasma which can be seen in [24]. When electrode surface is conducting or biased (second case), the charge separation becomes complex, so as Eq. (2). More elaborate explanation for Eq. (2) and solution for this equation finding the space charge that limits the current at biased condition have been explained by Child [26] and Langmuir [27].

C. Debye Length (λ_D)

If the bulk plasma is not disturbed, then the net coulomb interaction with a particular charge "q" (electron or ion) sums to zero. If suppose the plasma is perturbed, then the spatial variation in the potential V(x), with respect to this charge "q" always tries to oppose this perturbation. Conversely, this perturbation can be realised within certain distance from this charge "q" [21]. This length is termed as "Debye length". The expression for this length can be given as:

$$\lambda_D = (\frac{kT_e\varepsilon_0}{n_e e^2})^{\frac{1}{2}} \qquad (6)$$

This length describes the effective perturbation attenuation length inside the plasma [21]. The sheath thickness is always greater than the Debye length with respect to the voltage across the sheath. Hence Debye length can be used to calculate Sheath thickness when the electrode is biased, and expression can be given as [24]:

$$S = \frac{\sqrt{2}}{3}\lambda_D(\frac{2eV_0}{kT_e})^{\frac{3}{4}} \qquad (7)$$

D. Plasma Frequency (f)

When plasma in equilibrium is perturbed by ($\vec{E}$), there exist always a restoring force which attempts to re-establish the charge neutrality mechanism between ions and electrons. Electrons being less massive than ions, show fast response to these restoring forces. This restoring force is in turn directly proportional to the displacement of electrons from its equilibrium position. The equation for this restoring force exerted by ($\vec{E}$), can be given as:

$$m_e \frac{d\Delta}{dt} = -e(\vec{E}), \qquad (8)$$

$$m_e \frac{d\Delta}{dt} = \frac{-ne^2}{\varepsilon_0} \Delta \qquad (9)$$

Here, Δ is the displacement of electrons by electric field perturbation, which in turn is a function of time. The equation (9) is an equation for simple harmonic oscillator with angular frequency "ω_e", which can also be called in this case as "Plasma frequency", with the value of about 8.98 x 10^3 $n_e^{\frac{1}{2}}$ Hz, where n_e is the density per cm^3. Since, the interaction between ions and the electrons determine the plasma frequency; this can also be correlated to the Debye length. Time required for an electron to travel one Debye length is the time required for the electrons to shield the plasma from applied field ($\vec{E}$), Hence the plasma frequency is equal to the inverse time required for an electron to travel a Debye length [21]. Approximately this frequency can be given as [26]:

$$\omega_e = 9000\sqrt{n_e} \qquad (10)$$

So, plasma frequency "ω_e" is the minimum frequency for propagation of longitudinal waves in the plasma.

2.1.2 Plasma Discharge

The Plasma discharge or glow discharge plasma generation is based on ionising the gas in a closed chamber by applying sufficient energy to it. This energy can be supplied either by DC or RF electric field. This electric field initiate the gas ionisation mechanism by energising stray electrons that can gradually ionise the background gas by inelastic collision (explained in previous section). Further through basic avalanche process, the plasma density increases and reaches steady state where ionisation rate equals the electron and ion loss rate. Most of the materials processing utilize nowadays this glow discharge plasmas to enhance their functional properties. The configuration or geometry and orientation of electric field used for this glow discharge plasma might differ with respect to individual materials processing. The following section discuss only about DC discharge as authors Ph.D thesis work is based on this principle. More detailed explanation on RF discharge mechanism and RF generated plasma can be read in [21].

A. The DC discharge

The most simple configuration and geometry utilized from history to produce glow discharge plasma is DC discharge configuration. Figure 4 shows simple DC discharge configuration where potential difference of (V) is created between two opposing electrodes (Cathode and Anode). In general a DC power supply will be used to create this potential difference. Though glow discharge plasma appears very simple, the bulk regions and boundaries inside the chamber containing plasma are complex in nature.

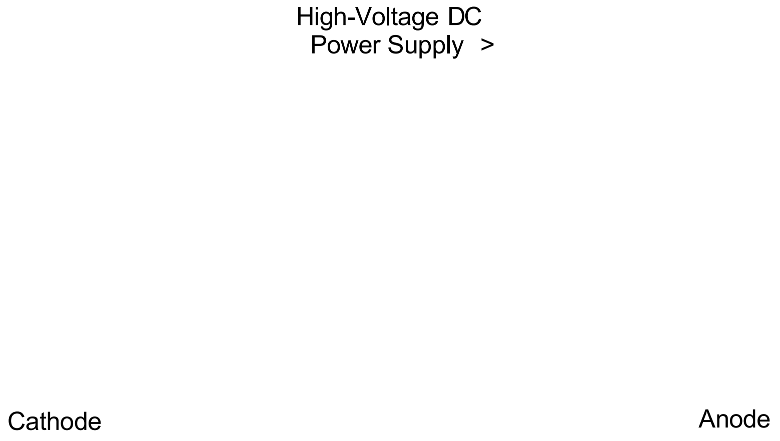

Figure 4 Simple DC discharge. DC power supply is connected across cathode and anode [Ref: 28].

The DC discharge can be operated in different modes, such as by controlling the voltage, pressure and distance between the electrodes [22]. In a given chamber, all these conditions have to be considered properly for the plasma discharge glow. The Figure 5 depicts normal glow discharge of neon gas in a chamber maintained at pressure of 1 torr. Each region inside the glow discharge is explained below [22].

Cathode dark space:

The region corresponding to sheath, where secondary electrons are accelerated and enter negative glow region assisting ionisation by excitation.

Negative glow:

Very bright glow region where predominant excitation-recombination mechanism takes place. In this region primary electrons were expected to consume fully their energy and it continues to extend until their travel distance from cathode.

Positive column:

Largely occupied discharge region between the cathode and anode. Most likely resembles plasma and hence predominantly used region for measurements carried out by classic probes. The electric field in this region assist in transporting the discharge current from negative glow to anode.

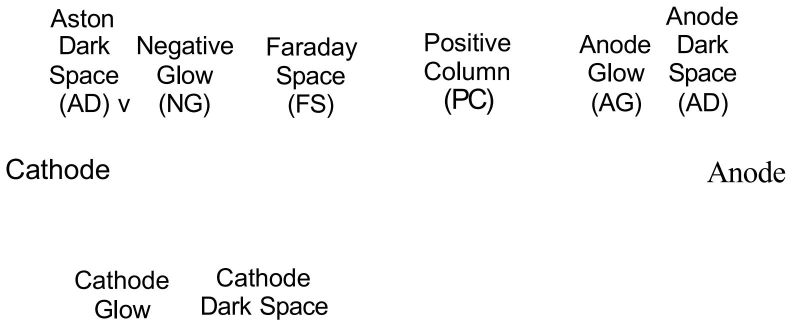

Figure 5 A typical DC glow discharge regions (neon gas) in at p= 1 torr [21].

It was found that, when two electrodes were brought near to each other, the positive column was appeared to shrink without disturbing the negative glow and cathode dark space regions. It is very essential to keep minimum distance between the cathode and anode to sustain the glow discharge plasma. Sustaining the plasma continuously inside the chamber depends upon ionisation rate, which should be compensated with loss rate of ions and electrons by volume recombination process or due to bombarding with walls of the chamber. The rate of ionisation in turn depends upon the type of gas through its ionisation cross section, the gas pressure, and electric field which drives the electrons.

These are the factors which decide the break down voltage of a gas which results in the sustained plasma discharge. The curves meeting the conditions for gas breakdown with respect to back ground pressure (for air and Ar) and inter electrode distance were obtained drawn by Paschen. Figure 6 shows the Paschen curves for gas breakdown between two electrodes in air and Ar atmosphere. These curves can be used to decide the exact operating conditions for steady plasma discharge.

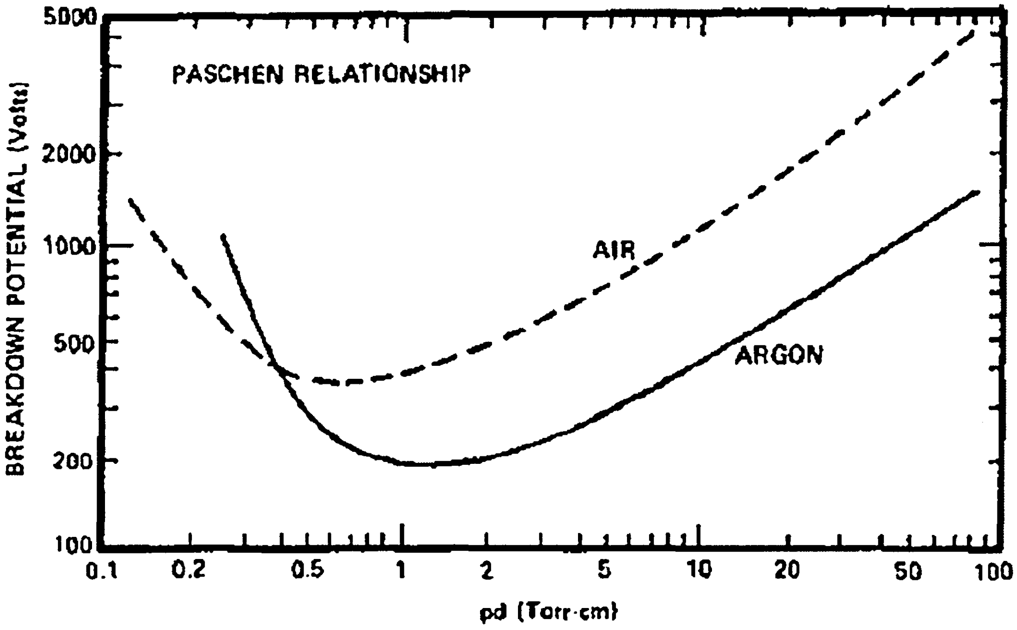

Figure 6 Paschen curve showing the possible gas (in air & Ar) breakdown conditions between electrodes at 20 °C [Ref: 22].

B. *Secondary Electron Emission*

Despite the energetic primary electrons, secondary electrons emitted from the cathode and chamber walls when particles strikes its surface, will also play a major role in sustaining the plasma. These surfaces will emit secondary electrons when bombardment occurs due to primary electrons, ions, neutrals. Individual bombardment types will lead to unique secondary electron yield. These secondary electrons are highly energetic, due to the energy they gain in the sheath region and accelerated towards the bulk region. Hence these secondary emissions are very important in sustaining DC discharge plasma as this will compensate electron loss process by increasing electron density in the bulk region and helping in higher ionisation rate. Further, these secondary electrons will also play a very significant role in the growth of sputtered film which will be discussed later.

2.1.3 Sputtering

Sputtering is a Non-thermal physical process where atoms are ejected from the solid surface when ions or neutral atoms with energy of few keV, are impinged on it. The kinetics of bombardment which leads to ejection of atoms from the surface is a function of series of binary collisions which can be characterised by energy transfer function given by [21]:

$$\epsilon = \frac{4m_i m_t}{(m_i + m_t)^2} \tag{11}$$

Where, m_i *and* m_t are the masses of colliding species. From above equation, it is clear that sputtering of atoms also depends upon the mass of incident ions. Overall energy transfer is not restricted to single atomic layer, rather to several atomic layers beneath the surface through the collision cascade mechanism. During this collision cascade, momentum exchange is the dominant mechanism which sputters the atoms bound beneath the two or three atomic layers from the top surface. Sputtering can be measured by a quantity called "sputtering yield (S)". Sputtering yield can be defined as the number of target atoms ejected per incident particle. This depends upon the type, energy and angle of incidence of the particle [22]. Figure 7 shows the experimentally determined sputtering yield for various metal targets as Ar^+ ion energy under normal angle of incidence. Initially up to 20-40 eV sputtering yield low and gradually increases linearly until about 100 eV. At higher energies, the yield increases sub-linearly with ion energy. Detailed analysis of dependence of the yield on the angle of incidence can be seen in [27].

The sputtering mechanism discussed above is from targets composed of single chemical elements. But the sputtering process mechanism is equally valid for alloys or compound targets. In the former case, it is very essential to maintain the cooling of the target to avoid bulk diffusion of constituent species, homogeneity of target without its decomposition, and its cleanness.

A. Sputter Deposition

Sputter deposition is the deposition of vaporised atoms ejected from a target surface, by physical sputtering process as explained in the above paragraph. The deposition processes are generally carried out in low pressure vacuum environment at working pressure of about than 5 mTorr to avoid gas phase collisions with the energetic sputtered particles. As sputter deposition technique nowadays are widely used in depositing thin films of hard coatings, coatings of architectural glass, magnetic films, semiconductor materials etc; in the coming sections of discussions reader can overview selective advanced sputter deposition techniques such as simple DC sputter deposition, Magnetically enhanced DC sputter deposition (DCMS), Cathodic arc deposition technique and High Power Impulse Magnetron Sputtering (HIPIMS) technique.

B. DC sputter deposition technique

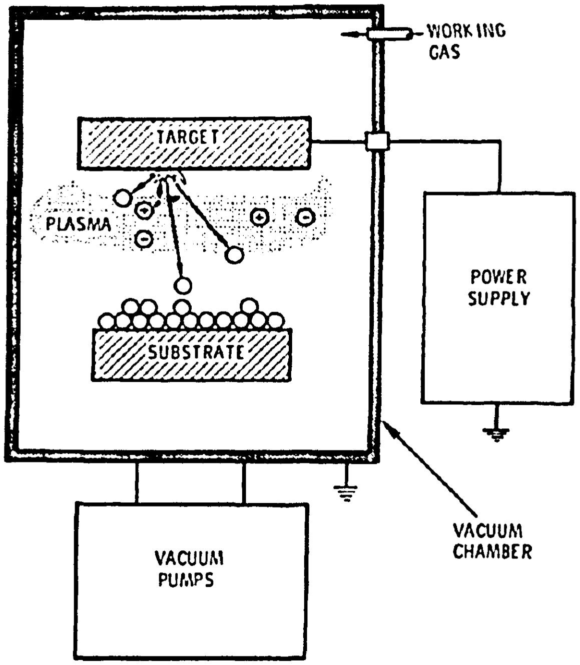

Figure 7 A simple parallel plate DC sputter deposition system. [Ref: 22].

DC sputter deposition is based on DC discharge mechanism discussed in the previous paragraph. Figure 7 can be informative to understand the DC sputter deposition technique in detail. The material intended to be sputtered, which was called "Cathode" (DC discharge circuit), is now named as "Sputtering Target". Generally, a high negative voltage (V) is applied to this target. The substrates are placed at a distance of few cm away from the cathode which are electrically grounded or conducting (biased) “Anode”. The whole system will be furnished in a vacuum chamber. Ar gas is introduced inside the chamber to some predetermined pressure value. The electric field will energise and accelerate electrons which in turn engage with collision with Ar atoms and result to ignite glow discharge plasma. Brief explanation on DC discharge plasma was discussed initially in this chapter. During this process, electrons will be attracted towards anode causing more ionisation; Ar^+ ions will be attracted towards cathode, finally leading to sputtering. Due to this motion of charged particle discharge current “I” flows. The voltage “V” applied to the sputtering target, which drives the current “I”, depends upon the gas pressure “P” in the vacuum chamber [21]. The deposition rate in this case relies on the amount of atoms sputtered from the target, which in turn rely on the “plasma density” near the target. This plasma density is drives the current “I” linearly on the target. But as sputtering yield also decides the amount of sputtering atoms, voltage “V” also plays a very important role in the DC sputtering system. For most of the industrial purposes, planar target DC sputtering systems are used. The film properties directly proportional to the amount of metal ions sputtered from the target (necessarily high) and the amount of metal ions can be achieved by increasing the sputtering yield. Normal attempt to increase the deposition rate is by increasing the sputtering yield, i.e by increasing the target voltage “V”. Optimum operating conditions for DC sputtering system was given in [22]. Those are listed below:

Cathode current density – 1 mA/cm^2

Discharge voltage-3 kV

Ar Pressure – 75 mTorr (10 Pa)

Deposition rate – 40 nm/min

Disadvantage of DC sputtering system:

High plasma impedance was observed which lead to very low discharge current of few mA/cm^2 at higher target voltage of several kV.

Higher thermal load imposed on the target when operated at higher voltage, which could damage the target.

Non-uniform sputtering of atoms leads to poor carriage of metal atoms to the substrate surface leading to poor quality films.

2.1.4 DC Magnetron Sputter deposition technique

In mid 1970's the invention of magnetically enhanced DC sputtering technique by Chapin was considered to be a major breakthrough in thin film technology [29]. The aim of his work was to completely come up with the solution for the disadvantages found with conventional DC magnetron sputtering.

The process of ejecting atoms or molecules from magnetically confined solid surface, in a low pressure, non-reactive/reactive ambient atmospheric conditions (of the order 0.2- 2 millitorr) can be termed as "Magnetron Sputtering". The application of magnetic field by connecting the magnets to cathode was realized after the necessity of high purity film, high deposition rate, low working pressure, ease of sputtering any metal, alloy or compound, with high adhesion to the substrate, ability to coat heat-sensitive substrates, uniform deposition, etc. These were often difficult to achieve in traditional vacuum coating techniques such as thermal evaporation and electron-beam evaporation. The principle of magnetron operation can be known by understanding the direction of magnetic and electric field confinement inside the vacuum chamber and electron drift motion, which in turn depends upon the configuration of magnetron. Basically, the magnetic and electric fields were configured on the cathode surface in such a way that electrons drift current $\vec{E} \times \vec{B}$ would flow along its own closed loop [30, 31]. The detailed explanation of electron motion under the influence of magnetic and electric field was explained in [32]. The trapped electron drift motion will be controlled only near the orbit of cathode sheath region as both fields are stronger near at this region and relatively week at larger distance. Thus, both magnetic and electric fields assist electrons to participate in the forced collisions with gaseous atoms and subsequent effective sputtering discharge to be sustained inside the vacuum cavity. In this manner the ionisation efficiency with the gas atoms was increased. As a result the impedance of plasma to electron motion reduces to voltages (500-600 V compared with several kV) less than that of traditional diode systems.

The history of research and development in the PVD field has introduced variety of magnetrons configurations. For example, S-gun type magnetron, planar magnetron, cylindrical magnetron [33]. Figure 8 shows the more detailed design of planar magnetron system.

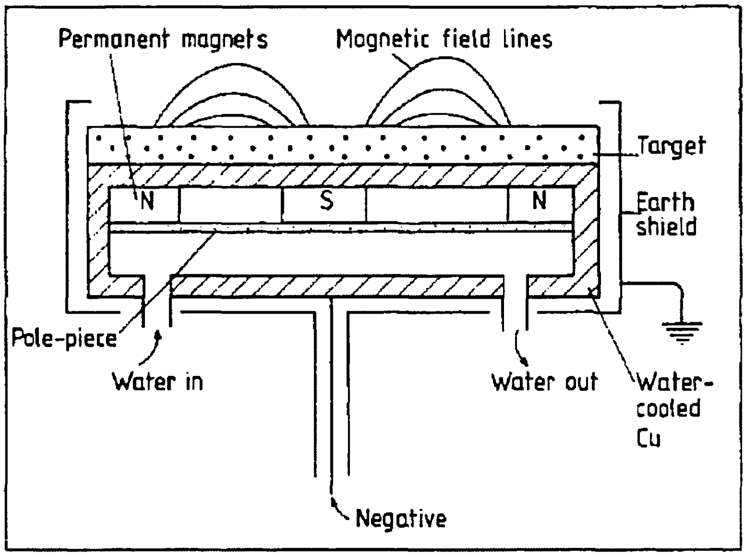

Figure 8 Schematic of Magnetron Source [Ref: 34]

The simplicity in physical construction of planar magnetron and its ability to shape in any form/size, enable this system to utilize in most of the coating industries. Normally, the permanent magnets connected to target surface were used to produce tunnel shaped magnetic fields in front of the target surface as shown in the Figure 9. The research and development in the reconstruction of magnetron source, in order to achieve higher efficiency in its overall performance is active since 1980. The moving magnetic array beneath target was new attempt in this direction. By this modification the efficiency of target utilization was reported to be increased up to 80% [34, 36].

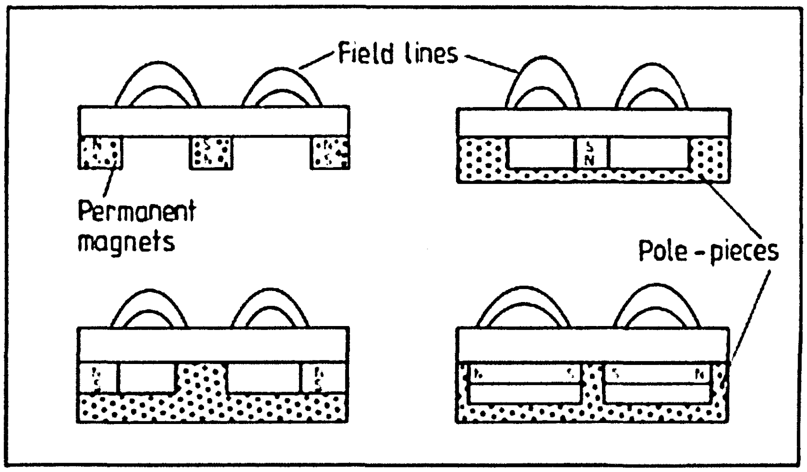

Figure 9 Possible geometries of magnetrons with tunnel shaped magnetic fields

[Ref: 34].

A. *Advantages of DC magnetron sputtering*

The primary advantage of DC magnetron sputtering over DC sputtering can be seen in terms of (1) high deposition rate in the rage from 1 nm/s to 10 nm/s. (2) Very efficient in sputtering of metal, alloy or compounds with high purity films. (3) Good adhesion of coatings can be achieved with the substrates. (4) Ability to coat heat-sensitive substrates (5) comparatively good uniformity over the substrates with broadly tunable properties (6) High discharge currents of about 1 A to 100 A at typical voltage of 500 V can be achieved due to low impedance observed in the plasma.

2.1.5 Cathodic Arc deposition

Arc deposition techniques were utilized since 1970's [37, 38] and still active in industrial applications for depositing metals and refractory compounds. This technique has demonstrated its efficiency in producing high density coatings with small grain size and higher adhesion to the substrates [39].

Arc discharge can be defined as the electrical discharges with high current of more than 1 A with low voltages of less than 50 V. The large discharge current is due to the collective electron emission mechanism from the cathode [40]. This collective emission can be (i) Thermionic or (ii) explosive. The detailed difference between these emissions can be read in [41]. Cathodic arcs can operate with cathodes at room temperature. In this case, electrons will be emitted at hot spots, non-stationary, micron size cathode spots [42]. Previous research articles have reported that these cathodes spots possess average current density of 10^{-12} Am^{-2}. Some literature have articulated the cathodic arc as local "explosive" event where phase transformation of spot area leading to achieve fully ionised plasma densities in the cathode region up to 10^{20} m^{-3} [43]. The generation of spots, its ignition and the life time on the cathode depend upon how thermal runway condition is achieved on the cathode surface [43]. Collective electron emission is a localised phenomenon, which is a result of high local electric field strength achieved on the cathode surface due to the voltage drop at sheath. This localised emission of electrons creates a spot which causes further localised ohmic heating of the emission sight. This process leads to higher electron emission with very high localized temperature reaching near the melting point of material (4000 to 7000 ^{0}C). All these events occur in a less than 10 ns [40]. The plasma emitted from the spot expands at the rate of 10^4 m/s which contract the sheath thickness [40]. This contraction of sheath thickness leads to accommodate electric field within a very small volume near the target spot. This causes further increase in the electric field strength and initial new cathode spots within an area of 10 μm. These evaporated species are highly ionised and accelerated away from the sheath and deposited on the substrate. High content of multiply charged metal ion states, e.g., Me^{3+}, Me^{4+} were reported to reach the substrate after getting ejected from the spot. Figure 10 explains the phenomenon occurring at cathode spots. Despite all the above advantages, the main disadvantage of this method is sputtering of droplets of target materials with sizes of 100-1000 nm [44, 45, 46]. These droplets are known to deteriorate the quality of deposited coatings. Also, it has been shown in some literatures that formation of these droplets initiate corrosion [47].

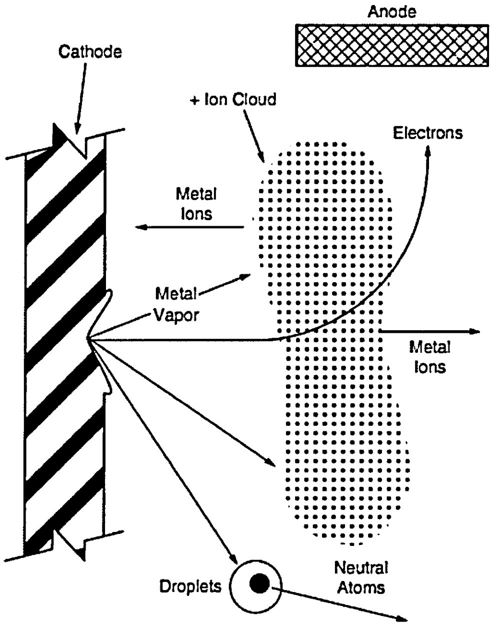

Figure 10 illustrates the possible mechanism of plasma interaction during the cathodic arc deposition technique [Ref: 42].

2.1.6 Unbalanced Magnetron Sputtering

Usage of DC magnetron configuration for sputter deposition has marked some major drawbacks during the process; For example poor plasma density between the cathode and substrate. This was attributed to the escape of electrons to the surrounding chamber walls. This has imposed a major setback to achieve good quality films especially during reactive sputter deposition conditions where plasma activation of reactive species is important. An effective method was suggested by Window et al. [48] to unbalance the magnetic field and effectively breaking the plasma confinement near target and directing it towards the substrate. This has been a very successful design for magnetron sputter deposition till today especially in case of reactive sputter deposition. The major difference between "balanced" and "unbalanced magnetron" techniques is the trap of magnetic field lines surrounding the cathode. Figure 11 shows the magnetic field shape in both cases [49]. From the figure the advantage of unbalancing the magnetic field can be clearly understood. The electron motion in this case is normal to the target surface and reaches very easily toward the near substrate region. Whereas in balanced magnetic field geometry, the electron has to break several magnetic field lines to reach the substrate.

T.E.Sheridan [50] has showed long range electron and ion transport in the unbalanced magnetron plasma which was attributed to an ambipolar diffusion process can be considered as further advantage in this geometry. S. Kadlec et al. has further proved the importance of unbalanced magnetron geometry during the deposition of tin, where ion to neutral flux can be increased by a factor of 6 [51].

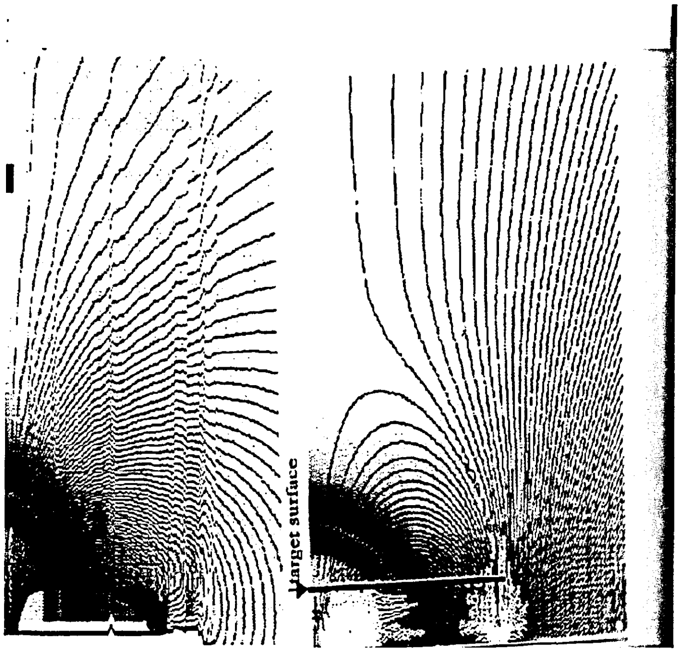

Figure 11 Magnetic field lines on the cathode surface; (a) balanced and (b) unbalanced magnetron case respectively. [Ref: 49].

A. *Closed field Unbalanced Magnetron Sputtering (CFUBM)*

Closed magnetic field geometry was successfully implemented to array of four unbalanced magnetrons in later 1990's [52, 53]. The intention was to increase the ionisation near the substrate during the coating deposition. The magnets of alternating magnetrons are arranged in the form where magnetic field shield the plasma is chamber volume without losing to chamber walls. Based on this concept W.D.Munz et al [54] introduced ABS machine to deposit hard coatings at industrial scale. Major advantage of this geometry is that plasma density can be accumulated in the centre of the chamber, which increases the ionisation efficiency and enhance ion flux to the substrates placed at the centre of the chamber. This sputter deposition technique enhanced the film properties in a large scale industrial application. The internal architecture of this geometry will be shown later as all the experiments of this work were carried out in this configuration.

2.1.7 High Power Impulse Magnetron Sputtering (HIPIMS)

In the early 1990's, "impulse" induced ionised PVD (IPVD) technology, named HIPIMS was introduced. By definition of impulse means, atoms sputter from the target when peak power of individual pulse exceeds the time-averaged power by typically two orders of magnitude with long holds between individual pulses [55]. The technology has taken a new turn in the field of thin film coating and nanofabrication industries to deposit high quality films of metals, alloys, and ceramics, beside all these, very importantly in depositing insulating oxides and nitrides, such as Al_2O_3, ZnO and SnO_2. This was mainly attributed to the higher fraction of ionised sputtered material found in the HIPIMS plasma which significantly optimises the film growth and enhances the quality of deposited film.

The Initial stages of research on HIPIMS was started by Kouznetsov et al [56], where significant increase of sputtered metal ionisation during the deposition was achieved due to the utilization of pulsed power supply on Cu target. In this case, the peak target power density attained on Cu target was reported up to 2.8 kW cm^{-2}, which has resulted the peak ion current density value to reach up to 3.4 A cm^{-2} at the substrate. Similarly, in many other examples of HIPIMS research, the target power values of >1 kW cm^{-2} was reported [57, 58-60]. These extremely high target power densities dissipated during HIPIMS have produced highly dense metals and gaseous ions in the condensing flux of the plasma (order 10^{19} m^{-3}) [57, 60-63] with more fraction of highly ionised metal ions compared to gas ions [61, 64]. Thus results obtained during HIPIMS deposition, such as dissipation of high target power density with high density metal ion plasmas condensing on to the substrates have enhanced ion bombardment on substrates. As a result the adatom mobility during the coating growth is accelerated on substrates. This has been a very essential impact of HIPIMS in producing defect free and more dense coatings when compared to conventional magnetron sputtering technique [65, 66]. Besides densification of coating films, HIPIMS has also shown advantages in uniform deposition of coating with high-aspect ratio filling for complex shaped substrates [56] and enhanced adhesion of the coating to the substrate by surface pretreatement [67, 68].

A. Electrical Parameter of HIPIMS technique

The electrical parameters of the HIPIMS power supply provides necessary information on the nature of the pulses generated. During coating deposition, the applied individual pulses of HIPIMS known to deliver average energy of 2 to 8 MW, with typical peak voltages and current of up to 1 -2 kV and 1- 4 kA respectively. Although it is very important to retain the maximum power on the target which helps to produce high metal ion-to-neutral ratio, the target heating effect which could lead to target melting also needs to be considered. Hence, In HIPIMS the pulses were applied on the magnetrons with very low duty cycle (ratio of on-time to period of cycle), where power will be dissipated at each very short on-time intervals of the pulse generated by the power supply. Due to this unique pulsing behaviour of HIPIMS, the maximum power can be achieved on the target and uniform discharge can be maintained over the cathode area. Typical operating range of pulse width reported to be 50-500 μs, between frequencies of 15-500 Hz. The regulation of pulse width/shape is very important to decide the power required dissipating on the target. Hence, with respect to the design of power supply, pulses with varying width can be generated in above mentioned ranges. U. Helmersson et al. [69] suggested that the pulse width changes with different magnetron configuration, target material, magnetic field structure, gas pressure utilized during the deposition. For example in one of the reported article, the pulse width applied for the sputtering of tantalum target started to decrease when discharge pressure increased [70]. This can be seen in Figure 12 where the voltage and current waveforms have varied with respect to the changing HIPIMS discharge gas pressure.

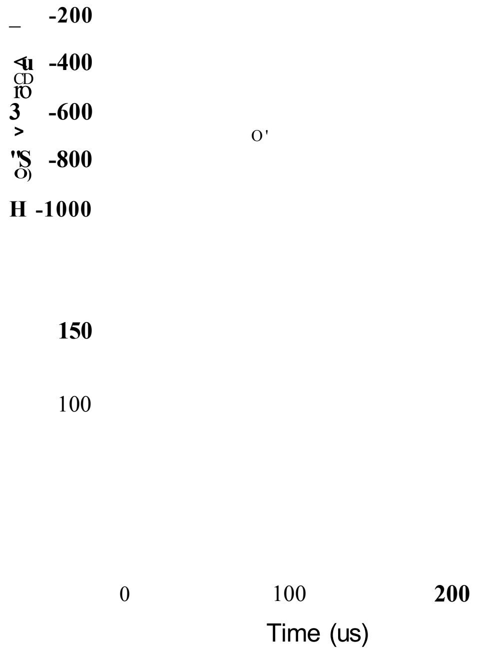

Figure 12. Temporal variation of cathode voltage and discharge current with respect to gas pressure [Ref: 69].

It has also been shown that due the decrease of discharge pressure, the plasma ignition was delayed by several ps. This has lead to design the HIPIMS power supply with pre-ionising pulse generator [71, 72, 73-76] where plasma can be pre-ionised. The Figure 13 illustrates an electric circuit diagram of HIPIMS pulse generator with pre-ioniser [75]. So far, different HIPIMS power supplies were designed which can be operated in different frequency range with different pulse widths to achieve respective target powers. For example, the pulse duration of 2-10 ms between the frequencies of 5-20 Hz has delivered peak power of 400 kW [59]. Kouznetsov et al. utilized the power supply generating the pulses with maximum power of 2.4 MW at repetition frequency 50 Hz and pulse widths of 50-100 ps. Likewise, Christie et al. reported on a power supply capable of producing peak power of 3 MW operating at single shot to 500 Hz and pulse widths of 100-500 ps.

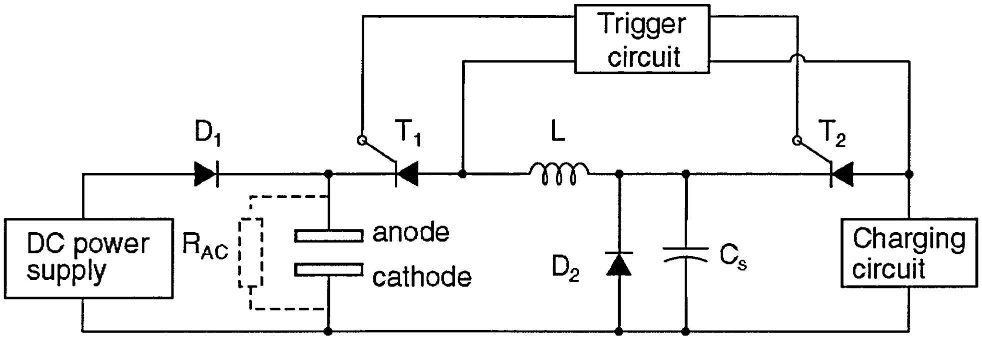

Figure 13 Circuit diagram explaining HIPIMS pulse generator with a pre-ioniser circuit [Ref: 69].

Ehiasarian et al. [76] demonstrated a HMP 6/16 pulse generator capable to supply 6 MW power in 0-200 µs pulses at 0-100 Hz frequency. Besides maintaining the pulse width, HIPIMS power supplies have also designed to detect arcs and suppress it during the deposition. More arcing during the deposition process could be detrimental to the target and generate macroparticles. Christie et al. [77] and Sproul et al. [78] suggested two methods for detecting the arcs. One way is by noticing high threshold value of current and another way is by detecting the sudden decrease of voltage value. When this arc is detected the capacitor and inductor will be disconnected without any current flown through it. Further this inductor will be disconnected from the load, and thus produces few µs order delays in the discharge pulse [79]. Helmerson U. et al. [69] suggested that this delay in pulse length can be generated only if sufficient delay in discharge breakdown time is achieved. This can be accomplished by connecting low current dc pre-ioniser in the HIPIMS circuit (Figure B) [69].

B. Industrial scale up of HIPIMS

Everlasting requirement for PVD coating industires are the production of defect free, highly dense microstructure with smooth surface morphology which enhances its functional properties in real world applications. Most of the ionised PVD techniques have shown their importance at laboratory scale to meet these requirements. But when considering the mass production on industrial scale, these plasma processing equipments technically failed in their efficient performance. For the first time HIPIMS power supply was connected to one of cathode in an industrial size PVD coating machine Hauzer HTC 1000/4, as shown in figure C. HIPIMS discharge was studies on

Ti target in Ar atmosphere at a pressure of $1\text{x}10^{-3}$ mbarr. Highly ionised plasma containing doubly charged Ti^{2+} with extremely high metal ion-to-neutral ration was achieved for high power pulses applied at power densities of up to 3 kW/cm^{-2} generated at discharge voltage of up to 2 kV. The metal ion-to-neutral ion ratio was reported to be increased due to the rapid increase in Ti^{2+}, Ti^{1+} metal ion intensity at the expense of Ti0 emission. This was attributed to the increase in the discharge current achieved during high power impulse applied on the target. Time evolution of HIPIMS discharge measured in this industrial scale experiment has shown the transition from gas to metal plasma within the pulse [80].

C. *Substrate pretreatment by HIPIMS*

Performance of the coating in most of the real world applications depends upon its adhesive bonding with the substrate on which it has been deposited. Substrate pretreatment prior to the deposition of coating deposition is very essential for this purpose and is a part of plasma processing. Pretreatment for substrate surface aims to remove contaminants existing on the surface, which might act as detrimental nucleation sights during the initial stages of coating growth and defies defect free coating. Although, several chemical sputtering processes are utilized for this purpose, the traces of oxygen contaminants still observed on the surface which paves the way to grow weak microstructure. Physical sputtering technique has shown significant advantage for pretreating the surface when compared to chemical sputtering technique. This technique implants the metal ions below the substrate surface to about 5-10 nm. This changes the gradient stress at smaller scale and improves the adhesion of the coating to the substrate. The depth of implantation range r_i is directly proportional to the bombarding ion energy, can expression can be given as:

$$r_i \sim E_i^{2m} \tag{13}$$

Where, m = 1 at high energies and 0 at low energies [81]. The depth of implantation exclusively depends upon the nature of the ion, technology used to produce these ions. These factors influence the interface region in terms of diffusion bonding between the implanted ions and substrate lattice. Traditional surface pretreatment method by gas ion (Ar^+, He^+) flux have imposed major setbacks which can be read in [82, 83]. Alternatively, metal ion implantation was considered to be very consistent for this purpose, where Cr, Ti, Nb and other transition metals tend to form unbroken bonds with the substrate lattice. Work by Hovsepian et al. has showed a incorporation of Ti ions when arc technology was used for pretreatment by Ti ion. Majority of Ti atoms sputtered during arc pretreatment were found to be doubly and triply ionised with only 20% of gas is ionised [84]. HIPIMS of Nb, V, and Cr was successfully used for surface pretreatment of High speed steel substrates prior to the deposition of CrN/NbN, TiAlN, and CrAlN coatings respectively [85]. Ehiasarian et al. showed that, HIPIMS pretreated interfaces in all the above three cases were atomically very clean without any oxide contamination. Moreover the crystallinity of the interface was not deteriorated. When compared with gas ion, and Arc etched coating-substrate interfaces, HIPIMS of metal ion etching has shown superior adhesion of the coating to the substrate.

2.2 Thin film microstructural evolution

The diverse application of polycrystalline films in the field of optics, electric, magnetic, mechanics and tribology, was realised in the mid 19th century when Sir William R. Grove discovered the mechanism of sputtering to deposit thin films [86]. The increasing demand of real world applications in above mentioned fields have also driven equal interest in understanding the mechanism behind the microstructural growth of thin films and procedures for its effective control. Thin films exhibit different microstructures, characterised by its grain size, crystallographic texture, phase and chemical composition. These individual characteristics can be varied by various atomistic deposition processes which follow its own parameters to control the microstructure. Extensive literatures are available, which describe the basic relationship between the film microstructure and plasma processing parameters influencing this microstructure. Understanding this relationship is very crucial since microstructural properties impact directly on the functional properties of thin films which decide its quality. Universally accepted model is Structure Zone Model (SZM) proposed by Movchan and Demchishin in 1969 [87] for the growth of Ti, Ni, W, ZrO_2, and Al_2O_3 coating. The atomic odyssey explained in this model was based on shadowing, surface diffusion, bulk diffusion and desorption process. The sequence of these processes and as resulted microstructure of the film was modelled on the basis of melting temperature of condensates and substrate temperature. Detailed review of this model can be seen in [88]. Thus the importance of microstructure on the coating performance has led to further development of advanced models. Plasma enhanced PVD (PAPVD) processes allows tailoring of these microstructural properties by controlling the energy of bombarding ions during the deposition process. This energy of bombarding ions depends upon several factors such as ion-to-neutral ratio, substrate bias voltage etc. In following paragraphs, brief overview has been done on SZM for sputtered films.

A. Basic SZM for sputtered film

In early1977, J. A. Thornton [89] proposed a basic SZM for metal coatings of Ti, Cr, Fe, Cu, Mo and Al. This model was based on 20 to 250 μm thick coating deposited by magnetron sputtering. Figure 14 shows SZM explaining the evolution of morphology for above mentioned coatings based on substrate temperature and inert sputtering gas pressure (P). According to this model, at low temperature, i.e. lower T_s/T_m zone 1 structure which appear in amorphous as well as crystalline deposits were reported to be the result of shadowing effects which leads to increase in adatom surface diffusion and subsequent thickening of film density [87]. As a result zone 2 evolves which can be attributed to the surface diffusion controlled growth. Grain coarsening process i.e., recrystallization through lattice and grain boundary (GB) migration was reported to be a dominant process at high temperatures [88], resulting into equixed recrystallized grains of zone 3. At the same conditions, dense array of poorly defined fibrous grains called zone T, a transition region between zone 1 and 2 occurs during coalescence of small islands with large surface to volume ratio. Mean while the GB migration reduces and crystallites become weekly textured leading to wide distribution of grain sizes. Thus during the subsequent growth process, individual crystallite size and orientation determines the intensity of activity among nearby grains. The competitive grain growth process during zone T evolution has been explained by Gilmer et al [90]. As a consequence of this growth, continuous change is morphology, texture and surface topography and film properties are expected to occur as a function of film thickness.

A systematic study further revealed the SZM at higher temperatures i.e. higher T_s/T_m bulk diffusion processes were reported to be the most significant, where the GB migration occurs not only during coalescence, but throughout the film densification process. During the coalescence stage, the growth orientation is pronounced with decrease in the GB area as well as minimization of interface and surface energy [91]. This growth was continued at the expense of smaller or unfavourably oriented grains. After this stage, there is also a possibility of abnormal grain growth, where the grain size distribution is transformed in to monomodal, through bimodal, to a new monomodal distribution with larger in-plane grain size. During this stage, enhancement in the degree of texture takes place, with homogeneous film structure along the growth direction featuring columnar crystals with flat surfaces decorated by GB grooves.

B. SZM incorporating the effects of Ion bombardment

An additional contribution to the film growth model was introduced by Messier et.al. [92], where replaced the pressure axis with bias voltage (V_s) as shown in figure 10b. In this particular case, the zone T was observed to be widened relative to zone 1 because of increase in the ion bombardment (due to bias voltage) which promotes adatom motion and therefore has the same effect as raising substrate temperature. In the mean time, the columnar grain diameter near the film surface typically observed as increasing to several hundred nanometres from 1 to 3 nm from the substrate interface. During ion bombardment, rapid transfer of kinetic energy of the bombarding ions to a very small area of atomic dimensions and subsequent rapid cooling at the rate of about 10^{14} K/s expected to takes place, which replaces the conventional heating [93]. Due to the energetic bombardment of ions (approximately with energy $E_i \approx -V_s$) [94], the surface and bulk diffusion process are believed to influence the film structure and evolution during the film deposition. For example, it has been shown earlier in case of TiN film deposition at 300 °C, the film microstructure changed from a columnar structure with open column boundaries at $-V_s \leq 80$ eV, to a void-free columnar structure at $-V_s \leq 120$ eV, and finally to a fully dense structure at $-V_s \leq 160$ eV. This was attributed to the high mobility of adatoms on the condensing surface caused due to high energy bombardment. Additional impact of energetic bombardment can also be seen in modifying the substrate surface during cleaning and etching, momentum transfer processes in the surface region, such as sputtering, desorption, recoil implantation, stress development on the growing film, defect formation, addition of het to the surface region and formation of secondary electrons which changes the plasma chemistry [95]. Despite controlling the thin film microstructure, the proper application of bias voltage have shown increased nucleation rates and film density, decrease of average grain size, prohibited columnar growth associated with high surface roughness and decreased defect density [88].

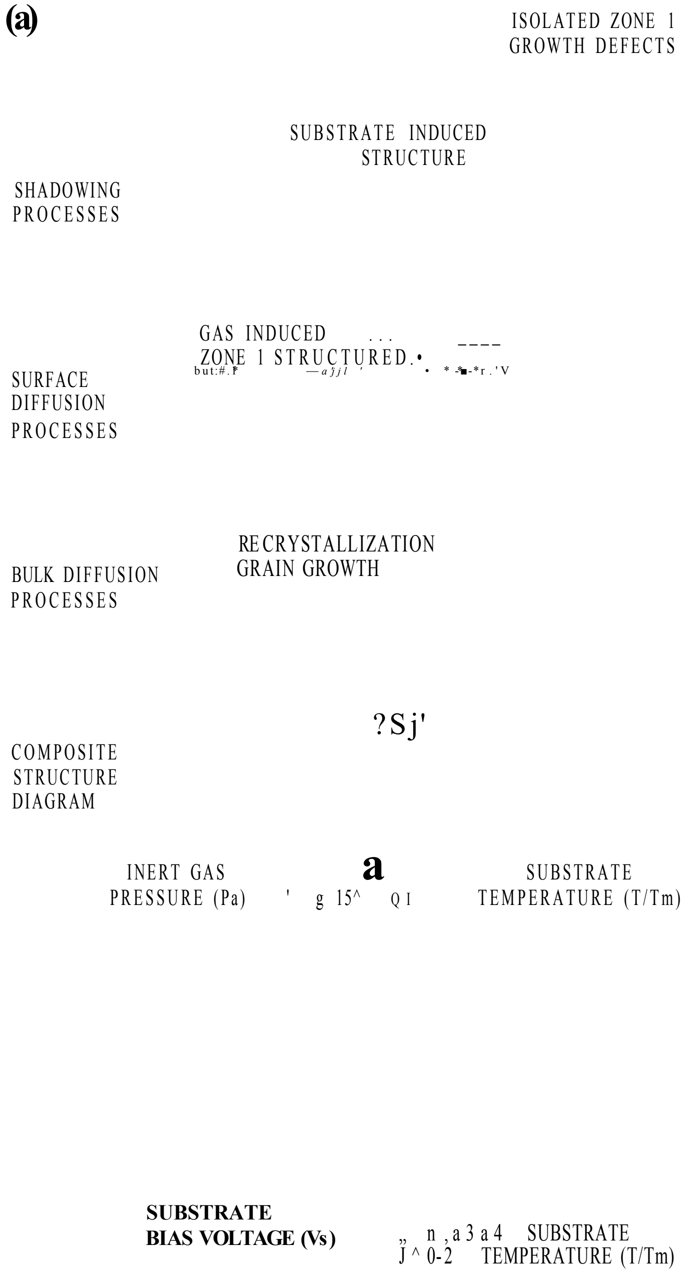

Figure 14 Schematic representation of SZM for sputtered film, showing the superposition of shadowing, surface-diffusion, and bulk-diffusion processes (b) structural evolution in case of RF sputtered film w.r.to ion bombardment and thermal induced mobility [Ref: 89, 92].

C. Effect of ion-to-neutral ratio (Ji/Jn)

The average energy carried by ions per condensing atom is determined by the ion-to-neutral ratio. Several experiments in the past have shown advantages of ion assisted film growth where high ion-to-neutral ratio has been achieved and subsequently high quality films were produced. The effect of Ar^+ ion bombardment on the growing film morphology has also been studied by theoretical modelling and simulations [96]. Figure 15 shows the computer simulation showing the influence of ion bombardment. The model shows the porous microstructure in the absence of ion bombardment, figure 13a. Whereas in figure 13b and 13c, we can clearly see the denser structure resulted due to high adatom mobility and surface diffusion caused by increased ion bombardment. Experimental evidence can be seen in [97, 98], where higher ion-to-neutral ratio at the substrate has been shown to produce refined grains and denser microstructure. The closed-field unbalanced magnetron sputtering (CFUBMS) has been proved to produce higher number of ions compared to neutrals [99]. Kelly and Arnel [99] have proposed new structure zone model relating to CFUBMS technique. In this model, major parameters such as homologous temperature (T_s/T_m) and the substrate bias voltage were taken into consideration to describe the coating microstructure. Figure 16 shows the SZM for coating deposited by CFUBMS which compares with zonal boundaries for SZM proposed for other sputtering systems in earlier papers by J. Thornton [89] and Messier [99]. According to this model, at constant bias voltage, by varying J_i/J_n ratio at particular homologous substrate temperature, one can achieve zone 2 and zone 3, as explained by Messier.

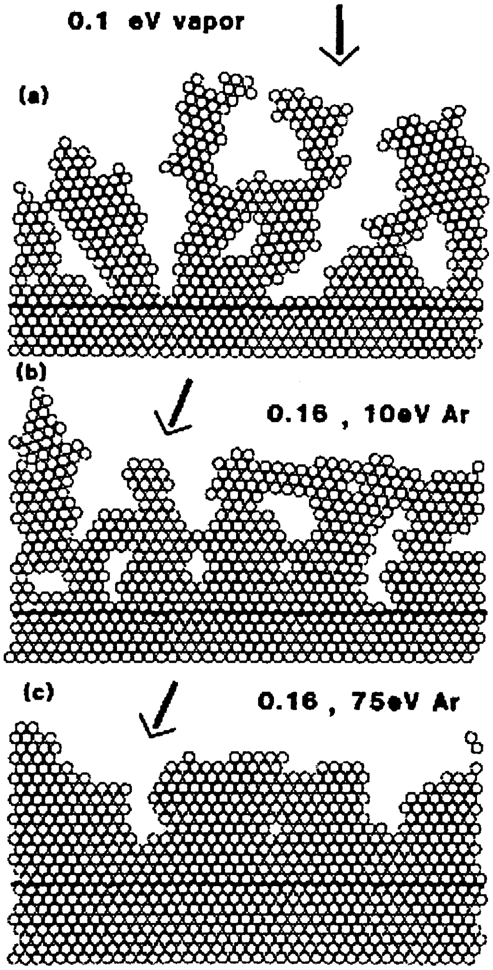

Figure 15 The microstructure obtained by computer simulation of Ar ion bombardment, (a) without ion bombardment (b) with Ar bombardment of 10 eV energy and $J_i/J_v = 0.16$ (c) Ar ion bombardment with 75 eV energy and $J_i/J_v = 0.16$ [Ref: 96].

Figure 16 Positions of zonal boundaries of SZM, (in terms of homologous temperature T/Tm) for CFUBM in comparison to other sputtering system [99].

2.3 Nanostructured coatings

Increasing overwhelming demand in multidisciplinary hi-tech applications have increased the production and widespread utilization of multifunctional nanostructured coatings in various industries, due to their outstanding mechanical (adhesion, super hardness and super toughness), chemical (erosion, corrosion etc), physical and tribological (friction and wear) properties. Moreover, recently, ceramic-based nanostructured materials have shown their importance in the application of microelectronics and transportation [100, 101]. Most of the properties are unique in case of nanostructured coatings when compared to conventional coatings with the coarse-grained polycrystalline and microscale composite structures. The outstanding properties of these nanostructured coatings can be attributed to the interface [102-104] and nanoscale effects associated with these nanostructures, with high interfacial volume fraction and lower crystallite size d which will not exceed 100 nm [105]. The conventional lattice dislocation slip is hampered by these interface and nanoscale effect in nanostructured coatings. Meanwhile the interfaces of nanostructured coatings play a very important role in deformation mechanism which differs from those conventional coatings. These are the factors which enhances the properties of nanostructured coatings in terms of its hardness (H), Young's modulus (E), plastic deformation, elastic recovery, toughness, resistance to cracking, thermal stability, oxidation resistance, etc. The manufacturing of these nanostructured coatings (metallic, ceramic, or polymeric based) and their superior performance was demonstrated in wide range of applications [103, 100, 101, 106, 107].

Basically, innovative designs in nanostructured coatings can be classified in three categories. These classifications depend upon their different nano-structured phases and constituting material composition inside the individual phase; these are (A) self organized nano structures (B) nanocrystalline nanocomposite structures.

(A) Self organised nano-structures

Self organised structures are self arranged structures of atoms during the evolution of thin films. The process is natural way of arranging atoms that crystallizes from the nucleation centres. Evolution of self organised structure is basically controlled by kinetics of condensation and inter-diffusion of depositing atoms on the substrate [91]. The most basic concern of these processes is to control the grain size, morphology and growth orientation of the atoms that crystallizes on the substrate. Final structure will evolve in multicomponent, multiphase thin films or films with desired structures of multilayer or nanocomposite phase structure. Compositionally modulated multilayered structure is usually grown by PVD methods, where inter-diffusion and roughening is hindered due to kinetic constraint. This can be overcome by controlling the ionised flux to be deposited on the substrate [108]. Research articles have revealed that the sequential magnetrons have been successfully utilized to achieve compositionally modified layered microstructure with abrupt interfaces. Also, rotating substrate holders between the fixed sources have been utilised to achieve multilayered and graded composite nanostructures [103, 108, 109].

(B) Nanocrystalline nanocomposite coating structure

Nanocrystalline nanocomposite coating structures are recent breakthrough in the field of nanostructured coatings. These structures are designed in such a way that the overall performance of the films differs very much from that of conventional coatings.

The coating material structure composed of mixed phase with two or more different nanocrystalline grains of size $d < 100$ nm is termed as "nanocrystalline nanocomposite coatings". Decreasing the grain size (d) has advantages in terms of decreasing dislocation activity. This particular process is known to replace by other intergranular deformation processes such as grain boundary enhancement, grain boundary sliding and electronic bonding between atoms in neighbouring grains and atoms in boundary regions [110]. Hence, besides increase in surface-to-volume (S/V) ratio of grains, the ratio of number of atoms in the boundary region to surrounding the grain (N_b/N_g) also expected to increase with decreasing the grain size [110]; and this factor plays a major role in determining physical and functional properties of these coatings. Depending upon the grain size (d) and distance between the grains (W) these structures are classified in to two different types: (i) nanocomposites containing nanocrystalline grains embedded in amorphous matrix, e.g. TiN embedded in DLC or a-Si_3N_4. (ii) nanocomposites containing nanograins surrounded by tissue phase, e.g. Si-DLC, TiC-Cu etc. Further, these nanocomposite structures have been differentiated with respect to its hardness H, and dimensions. Details of these can be seen in [110].

The fundamental physical quantity, i.e. energy delivered during the formation of thin films, controls its structure, elemental and phase composition which plays a crucial role in its physical properties [111-113]. J. Musil proposed that the total energy delivered to the film during the growth is the summation of other energies of deposition parameters, such as, energy delivered by substrate heating (E_s), kinetic enery of the bombarding ions (E_i) and fast neutrals (E_f), energy released during the exothermic chemical reaction (E_{ch}), energy delivered by hot magnetrons (E_{mt}), the final one is the energy due to heat radiation (E_{rad}), this can be given as:

$$E_T = E_T(T_s, t_d) + E_p(U_s, i_s, a_D, P_T, t_d) + E_{ch}(t_d) + E_{mt}(W_d, t_d, D_{s-t}) + E_{rad}(t_d) \text{ -- -- } (14)$$

Where,

t_d is the duration of film deposition, P_T is the total pressure, W_d is the magnetron voltage which is a function of magnetron voltage (U_d) and current (I_d), S is the total area of the magnetron target, d_{s-t} is the substrate to target distance. a_D is the film deposition rate, The complex interplay between all the above terms plays a very important role in the overall film formation process. For example the first two terms contribute significantly to the films growth, whereas the energy delivered by exothermic chemical reaction (third term) play a role in the growth of advanced materials, and final two terms are very important for the growth of films on sensitive substrates [110]. Further proposed theory by J. Musil et. al., about the conditions at which important structural transitions occurring between individual phases of nanocomposites such as crystalline to amorphous, crystalline phase of one material to another crystalline phase and transition between different crystallographic orientation of same material takes place; can be seen in [114, 115]. Figure 17 [110] shows the schematic diagram illustrating the structural evolution of two-phase A-B-N nanocomposite film. This figure shed light on the transition from preferred crystallographic columnar structure of AN grains separated by a-BN phase (oriented perpendicularly to substrate) in $A_{1-x}B_xN$ film to nanocomposite structure in which every AN nanograins is surrounded by a thin tissue phase of a-BN. This transition is expected when the atomic content of B is increased gradually to certain amount, For example in figure it is given as B1 to B2. Figure 17a and 17b shows the schematic of these two structures. Further increase in the quantity of B in the $A_{1-x}B_xN$ film (> B2) leads to a nanocomposite structure where nanograins are embedded in a a-BN matrix which is X-ray amorphous structure (Figure 17c). If the content of B increases further, the film structure is expected to change completely with the formation of pure a-BN phase without any AN nanograins. These type of nanostructured transition was reported in case of magnetron sputtered films of $Zr(Ni)N_x$, $Ti_{1-x}Al_xN$, Al(Si)N, nc-Ti(C, $N_{x<1}$)/a-C, etc [116-119].

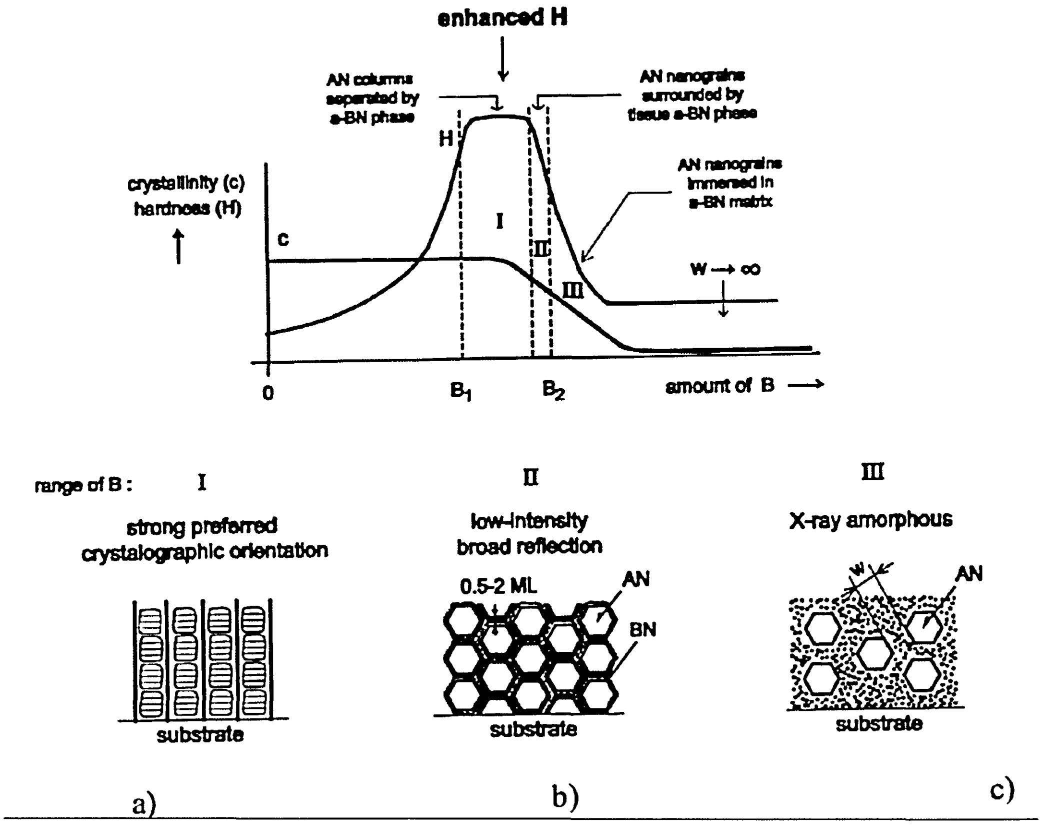

Figure 17 Schematic of nanostructured phase evolution in two phase A-B-N nanocomposite film as a function of B. (a) Nanocrystalline to X-ray amorphous transition.

2.4 Nanostructured and composite coatings- for advanced Tribological applications

Enhanced functional properties shown by advanced nanostructured and composite coatings have promised to demonstrate their greater performance, longer durability and higher efficiency in the field of advanced tribological applications [120-123]. Besides being shown their importance in tribological applications, ceramic based nanostructured coatings have also promised their necessity in the field of microelectronics, automotive, textile, biomedical and machining applications in aerospace industries [100, 109, 124]. The design and development of these innovative coatings are aimed to meet the most severe applications of advanced tribosystems [109, 124-126].

For example earlier research work have clearly revealed the multilayer and nanocomposite coating designs which can initiate self lubrication during sliding by providing lower friction force against counterpart and self-adapting properties for changing environmental conditions [128, 129]. Amongst all well developed tribological coatings, the most popular nanostructured and nanocomposite coatings are carbon based films, such as nanocrystalline diamond [130], Diamond like carbon (DLC) [131], carbide derived carbon, nitride, carbides [123] and carbon nitride [132].

2.4.1 Nanostructured carbon films

Carbon has been considered to be a very precious ingredient in most of the nanomaterial because of its well known property of being very hard (diamond, transition metal carbides, etc) [133], high lubricity or low friction [134, 135], good wear resistance, chemical inertness (Graphite, DLC, Me-DLC, Me-graphite) [128, 136-138].

The physical properties of carbon based films strictly depend upon the structure of carbon bonding with another carbon (graphite or DLC) or metal (Me-DLC). In case of DLC material, it is the ratio of sp^2 (graphitic) vs. sp^3 (diamond like) content which decides its property [139]. Usually, diamond like carbons (DLC) with amorphous nature contains mixture of hydrogen and sp^3, sp^2 and sp^1 sites [139]. The range of graphitic ordering in DLC (sp^2 site) can extend from microcrystalline to glassy carbon [140]. DLC with more hydrogen and less sp^3 content is called hydrogenated DLC (C: H) and if it contains more sp^3 content, then it is called tetragonal DLC (ta:DLC) [140]. J. Robertson [139] has showed content of DLC in ternary phase diagram, Figure 18. In summary, the property of DLC depends upon the carbon-carbon sp^3 configuration and its fraction inside the film.

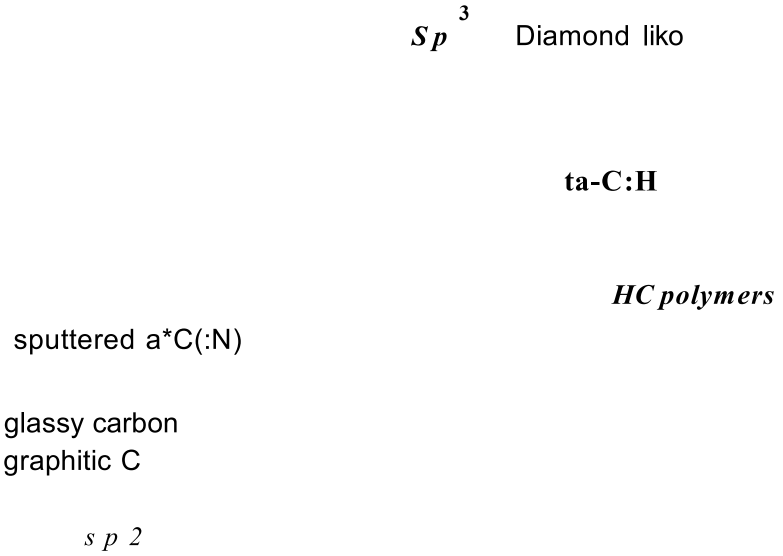

Figure 18 The diagram of sp3, sp_2 and H content in DLC films [139, 140].

Another category of carbon based coating is pure graphite. Graphite is a shiny and soft form of crystalline carbon, normally exist in layered-lattice structure [141], of either hexagonal (thermodynamically stable) or rhombohedral (thermodynamically unstable) geometry. The inter-atomic layer distance in hexagonal structure is very large (~ 3.34 A0) with high c/ao ratio [142], which allows graphite to get cleaved very easily by some external force [141]. Figure 19 shows the graphite crystal structure. Besides acting as a solid lubricant, graphite is also an excellent corrosion resistant material (e.g. composites of graphite/Cu, etc), good electrical and thermal conductor with high radiation capacity, very inert to chemical species except for group VI of periodic table [143] and good mechanical properties [144].

Figure 19 showing the hexagonal layered lattice structure of graphite [Ref: 144].

Recently, most of the research interest is concentrated on the hybrid structures of carbon materials such as Me-DLC and Me-Graphite. Me-DLC possesses nanocomposite multilayer structure with nanocrystalline metal grains surrounded by DLC. This structure favoured by both solid lubricant graphite structure as well as hard diamond crystal structure; whereas Me-Graphite exhibits only graphitic nature with properties of all the three DLC, Me-DLC and pure graphite. Examples for Me-DLC are Ti/DLC, TiC/DLC, TiAlCN/VCN, WC/DLC etc [145-147] and for Me-Graphite structure can be seen in C/Cr [123].

The self-adapting nature of carbon based films to change their structural properties such as graphitic to diamond like and amorphous to crystalline [137], further increased their interest in advanced tribological applications both at ambient room and elevated temperature (upto ~ 250 °C) tribological applications [148]. Nowadays we can see the utilisation of carbon based films in hi-tech tribology applications of cutting tools, automotive components, precision parts, bearings [149,150], etc. For example DLC coatings are well known for their tribological characteristics, such as high hardness (5- 70 GPa), good wear resistance ($10_{\sim 15}$ nr'N 'W) and low friction (<0.1) [151]. In the recent days low friction carbon based films have also shown their promise in micromechanical (MEMS) systems [152], electrical contacts, biomedical implants and mechanical seals [143]. However, the property of carbon films significantly depends upon the deposition conditions and as resulted film structure [151]. Although we have seen the potential industrial applications of these DLC films to be very impressive, the major drawback has been seen with their high internal stress and adhesion limits its application in various tribological applications. Higher the thickness, more compressive stress it develops and wear rate is faster [153].

2.4.2 Advanced deposition systems for nanostructured and carbon based films

Over the last two decades the research and development of advanced deposition technology with Physical and chemical vapour deposition techniques (PVD and CVD) are really been revolutionised. In order to achieve desired complex microstructural architecture for specified multi functional application, it is very necessary to use suitable deposition technique. The increased versatility of the deposition techniques such as, sputtering, ion plating, cathodic-arc PVD, pulsed laser deposition (PLD), ion-beam assisted deposition (IBAD), plasma enhanced CVD (PECVD), plasma enhanced PVD (PAPVD) have increased the production capability of novel coatings at large scale industrial sectors. Many research articles and textbooks which reveal these deposition techniques and their adaptability in producing nanostructured coatings can be seen in [109, 154-159]. Most of the deposition technologies utilised for the deposition of nanostructured and composite coatings have been referred to as "hybrid deposition processes" [160-162]. In contrast to conventional deposition systems, these hybrid deposition systems are not greatly changed with respect to a physical shape or architecture but involve more than one deposition techniques. These additional provisions implemented in the deposition systems have successfully produced complex microstructures with the aid of extra process control parameters required during the growth of nanostructured and composite films [147-FP162]. Moreover, the usage of two or more stages of deposition has been reduced to a single process to produce functionally graded coatings. As an example, in the case of Ti, W, Cr based carbon multilayer and nanocomposite coatings were deposited by single process, which are described seen in [147, 162, 163].

Most of the engineering materials with protective coating require chemical, structural and mechanical integrity with the substrate, which is very difficult to achieve with CVD deposition systems [164]. In this context, PAPVD deposition processes are really emerging at the behest of its control over the process parameters such as target current density. By applying high target current densities on the sputtering targets, high plasma density near the substrate with greater ionisation of depositing atoms can be achieved. This alters predominantly the growth dynamics of the film and its functional property. This particular system has enabled the deposition of nitride and carbon based coating on all substrates with complex geometry at low temperature and successfully proved to result in highly adherent, smooth, dense with chemically stoichiometric microstructure. For example cathodic arc PVD, Arc–bond sputtering, closed field unbalanced magnetron sputtering (CFUBM), and high power impulse magnetron sputtering system (HIPIMS) [109, 162, 165]. Tribological applications in the real world harsh environments necessitate the coatings to protect the substrate from peel off during the operation conditions. Hence, adhesion of the coating determines the endurance life and load bearing capacity of the component used in such operations. Above mentioned advanced deposition technologies such as Arc PVD and HIPIMS known to provide atomically clear interface of the coating-substrate interface thus by providing high level of interdiffusion and intermixing of coating atoms with substrate atoms there by creating strong bond at the interface [166, 167]. Recently, A.P. Ehiasarian and his research group have successfully implemented the HIPIMS system on industrial scale to deposit good quality nitrides, carbides thin films dedicated to the above mentioned wide range of applications [169].

In summary, plasma deposition techniques such as PAPVD, PECVD, Ion beam deposition, Pulsed laser deposition (PLD), etc are commercially utilised in the industries for the deposition of coatings ranging from magnetic hard disc, micro electronics, tribological and decorative coatings [151, 160-165, 170, 171]. These techniques have also been used to deposit carbon based films (DLC, Me-DLC, Me-Graphite, B-C-N, Ti-Si-C-N, TiAlCN/VCN etc). However, the versatility of PAPVD over PECVD technique is increased recently in many industries. PAPVD based planar magnetron sputtering techniques such as Arc-PVD, HIPIMS provide following advantages [160-162, 167, 147]:

(i) High ionisation efficiency with energetic bombardment ensures the film-substrate adhesion, denser morphology and near stoichiometric chemical integrity.

(ii) Energetic particle bombardment increases the adatom mobility, surface and bulk diffusivity which can influence the nucleation, growth and texture of the coating.

(iii) Multistage, multi rotational substrate holding capacity and provision was reported to increase the coating uniformity on complex geometry.

(iv) Low deposition temperatures (≈ 100 ^{0}C – 450 ^{0}C) compared to PECVD (≈ 600 ^{0}C).

(V) During the deposition of carbon based films, these techniques have enabled the deposition of carbon during the concurrent ion bombardment.

The following paragraphs briefly explain the deposition techniques used to deposit Me-Graphite (C/Cr) and TiAlCN/VCN coating at industrial scale in Sheffield Hallam University.

2.4.3 Arc-Bond Sputtering (ABS)

Arc-Bond sputtering is a industrial implemented deposition system comprising four target PVD coater HTC-1000, manufactured by Hauzer techno coating Europe [172]. The cathodes furnished in this particular system were enabled to operate in both the steered cathodic arc-evaporation and unbalanced magnetron sputtering techniques [172] for surface pretreatement (etching) and coating deposition, respectively. Here, one of the cathodes was operated in steered cathodic arc mode, for the pretreatment of surface prior to the deposition. Both the surface pretreatment and deposition steps in this particular system were carried out in Ar plasma. In this particular step the highly ionised metal plasma in glow discharge mode was generated and subsequently implanted inside the surface to enhance the adhesion of the coating to the substrate [173, 174]. According to the reports, metal ions generated for surface pretreatment step in this steered cathodic arc discharge were Nb^+, Nb^{+2}, Nb^{+3}, Cr^+, Ti^+ [173]. During this stage the substrates were biased negatively up to -1200 V. The samples were mounted on three-fold rotational substrate holding table, intention of which was to improve the coating thickness and uniformity [172]. The ionisation studies during the steered arc and magnetron process revealed that the ionisation capacity of the former when compared to the latter was calculated to about three factors more [175]. Examples of few popular coatings dedicated for tribological purpose deposited by this particular technique are TiAlN/TiNbN (Nb^+ ion etching) [176], CrN/NbN (with Cr^+ and Nb^+ ion etching) [109], TiAlN/ZrN (Ti^+ ion etching), C/Cr (Cr^+ etching) [162]. Furthermore detailed explanation of Arc-bond sputtering and the properties of tribological coatings deposited by this technique can be seen in [177].

2.4.4 High power impulse magnetron sputtering (HIPIMS)/Unbalance magnetron sputtering (UBM)

Steered cathodic arc processes were reported to generate charge carrier density up to 10^{18} cm^{-3} producing highly ionised flux [173]. However, the formation of droplets during the etching and coating deposition [178] step of this particular process produces very poor quality film [166]. Thus, recently the advanced PVPVD technique, HIPIMS was sought to be appropriate for adhesion enhancement. When compared to ABS system, the internal architecture of the HIPIMS/UBM deposition system was not greatly changed. But the power sources for two cathodes were replaced with HIPIMS power supply; whereas other two cathodes were operated in UBM mode. In 2004, HIPIMS was enabled to operate at industrial scale using large rectangular cathodes ($\approx$ 440 cm^2). Furthermore detailed explanation of operational control parameters of HIPIMS system can be seen [170]. Nowadays most of the research groups involved in the development of HIPIMS research are utilising HIPIMS for adhesion enhancement and coating deposition process because of its capability to produce highly ionised fraction of metal ions. This has been successfully proved to produce high quality films with enhanced desired physical properties in real world applications [170].

Recently, P.Eh.Hovespian et al. developed TiAlCN/VCN multilayer coating as a new coating for wear application, especially at elevated temperature [179]. This particular coating was deposited by mixed HIPIMS/UBM technique, where cathodes and power supplies were installed in an industrial size Hauzer techno. Coating machine HTC 1000/4 (chamber volume 1 m^3). Here, HIPIMS was utilized for surface pretreatment by V^++Ar^+ ion glow discharge plasma [180], and for TiAlCN/VCN coating was deposited by operating all the targets in UBM mode. In 2009, this nanoscale multilayer TiAlCN/VCN coating, developed by P.Eh.Hovsepian, was granted by UK patent [181].

CHAPTER 3

Experimental Methodology

In this chapter the reader will find the details on the samples used for the deposition of TiAlCN/VCN coating and explanation on deposition procedures and parameters of reactive UBM and HIPIMS-UBM and pure UBM. Subsequently, the description of characterising methods used to understand the functional properties of nanoscale TiAlCN/VCN coatings at room and elevated temperature conditions is also been discussed.

3.1 Substrate material, specimen preparation and deposition method

3.1.1 Substrate material and specimen preparation techniques followed prior to nanoscale TiAlCN/VCN deposition

Since the properties of plasma enhanced PVD (PAPVD) deposited films depends strongly on the substrate surface conditions, the type of deposition process and system geometry. It is very important to discuss these details before revealing the results of this particular work. In order to achieve desired properties on the substrate surface, it is very essential to carry out two types of cleaning process. One is initial cleaning of the substrate surface to remove oils, oxides, hydrocarbons etc. Second cleaning process is atomic cleaning, which will be carried out prior to the deposition. It is also called “Etching”. Both steps are equally important since both will decide finally the film adhesion to the substrate surface and the performance of the coated material as a whole.

In this work we have used as a substrate M2 high speed steel (HSS) with chemical composition of 0.68% of Carbon, 4% of Cr, 14% of W, 0.25% of Vanadium as substrate. This sample is coated and used to investigate the mechanical and tribological properties in hard experimental conditions. The 316 stainless steel (SS) with composition (0.08% of C, 16-18% of Cr, 10-14% of Ni, 2.0% of Manganese (Mn), 1% of Si was used for XRD measurements in order to find out the phase structure of the as-deposited coatings. For microstructural characterisation Si wafers and stainless steel coups were used. Table 3.1 informs the dimensions of substrate materials used for various characterisations. All samples were mirror polished using 1 μm diamond paste. Prior to the coating deposition the samples were cleaned in an automated cleaning line comprising a series of alkali solutions, deionised water baths and a vacuum drying furnace. Table 3.2 shows the sequence of cleaning steps carried out after polishing the surfaces.

Test	Dimensions
Rockwell C indentation, scratch, pin-on-disc, nanohardness, Raman, SEM of worn surface	30 mm x 6mm HSS coupon **(1)**
SEM, TEM	25 x 25 x 0.8 mm^3 SS square plate, **(2)** 20 X 10 mm Si wafer, **(3)**
Thermogravimetric (TG), XRD of oxidised surface and Raman	15 x 50 x 0.8 mm^3 SS (1 x 1.5 mm hole) **(3)**
XRD,	30 mm x 6 mm SS coupon **(4)**
High speed machining, Raman of tool edge	25 mm diameter, 25 mm radius two flute high speed machining end mills, made from S290 HSS material **(5)**

Table 3.1 Substrate materials and their dimensions used for various tests and analytical methods.

Step	Ultra sonic cleaning & solution used	Temperature, ^{o}C	Time, s
1	De-Ionised (DI) water +	60	20
2	DI water	30	5
3	DI water+	60	20
4	DI water	30	5
5	DI water	30	20
6	Vacuum drying	100	40

Table 3.2 Substrate cleaning procedure prior to coating deposition

3.2 Deposition Process and system geometry

3.2.1 Reactive pure UBM and HIPIMS-UBM technology

TiAlCN/VCN nanoscale multilayer coatings were deposited in an industrial sized physical vapour deposition coating machine (HTC 1000-4 ABS manufactured by Hauzer Techno Coating, The Netherlands) enabled with HIPIMS technology at Sheffield Hallam University in UK (Figure 20). This industrially developed deposition process has been known as economical process, because of the easy installation of target and substrate provision, relatively increased deposition rate in reactive deposition mode, when compared to other deposition systems due to control system for reactive gas [177]. The coating machine with the chamber volume of 1 m^3 comprises four rectangular cathodes furnished with 2-TiAl (50:50 at% pure) and 2-V (99.8% pure) targets as shown in the Figure 21. Two opposing magnetrons, furnished with TiAl and V targets respectively were operated in High Power Impulse Magnetron Sputtering (HIPIMS) mode whereas the other two magnetrons were operated in Unbalanced Magnetron Sputtering (UBM) mode. The distance between opposing target was 1 m.

In the first process, HIPIMS was used in the etching step whereas the coating was deposited by UBM (HIPIMS/UBM, etching/deposition). In the second process, HIPIMS was used for etching as well as in the coating deposition step. As only two magnetrons were connected to HIPIMS power supplies, the deposition was carried out in a mixed (HIPIMS-UBM) mode. We refer second process as HIPIMS/(HIPIMS-UBM). Utilisation of mixed deposition mode, using simultaneously HIPIMS and standard UBM sources allows significant compensation for the lower deposition rates available from pure HIPIMS sources without losing the effects of the ion assisted coating growth. In the final process, two opposing magnetrons targets, were operated in pure HIPIMS mode where as the other two magnetrons were shielded. A schematic cross section of the system in this particular process is depicted in the Figure 22. The substrates were mounted on a 3-fold rotatable planetary turnable substrate holder, which provides homogeneity in coating in the growth direction. Figure 23 shows the sequence of steps that usually carried during all the deposition process.

Figure 20 HTC1000-4 ABS manufactured by Hauzer Techno Coating, The Netherlands

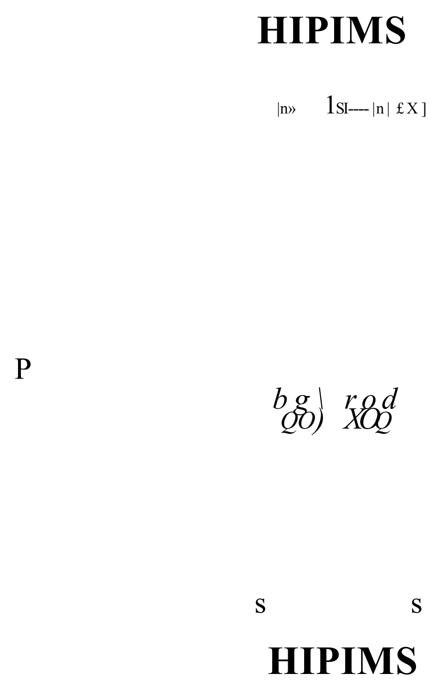

Figure 21 Schematic of HTC 1000-4 PVD coater and internal cross section of the four cathodes and three-fold substrate rotation table used for UBM and HIPIMS-UBM process.

Figure 22 Schematic cross-sections of the four cathodes of the HTC 1000-4 PVD coating system used for pure HIPIMS process.

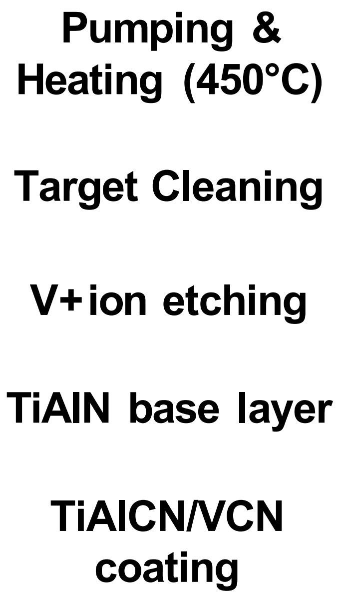

Figure 23 The sequence of steps carried out during the deposition of TiAlCN/VCN in all the three cases of deposition.

The initial pumping down process is essential to minimize the contamination level during the deposition. The base pressure of about 5 x 10^{-5} mbar will be reached before starting the next step. This pressure was attained in two stages; (i) Rough pumping via 250 m^3/h roots pump and 500 m^3/h rotary vane pumps to a pressure of $8x10^{-2}$ mbar, (ii) Fine pumping via two turbo molecular pumps with a total pumping speed of 4400 l/s to the lower pressure of 5 x 10^{-5} mbar. Hot water flows around the chamber walls were set in order to prevent condensation of moisture on the chamber walls when the machine is vented. Once sufficient base pressure suitable for the deposition is achieved, the heating step will be started which will heat the substrates at temperature equal to deposition temperature. Also, because of a heating step, the moisture desorption process from the chamber wall will be enhanced. The moment the desired temperature is reached, the target cleaning step will be initiated. The purpose of target cleaning is to remove the impurities left over on the target surface. In this particular step the shutters will cover the target surface in order to ensure that the substrate surface will not be deposited with those impurities.

Subsequently after this stage, three major steps of metal ion etching, base layer deposition and nanoscale TiAlCN/VCN deposition are being carried out. In the first step, the substrate surface was bombarded with highly ionised V^+ + Ar^+ plasma generated from a HIPIMS discharge sustained on the V target in Ar atmosphere. This resulted in the formation of clean coating-substrate interface [167] and tailoring to strong adhesion (Lc > 50 N) of the coating. To maintain constant voltage during the ion bombardment a HIPIMS dedicated power supply manufactured by Huttinger Electronic Sp. Z o.o. was used [168]. In the second step, a TiAlN base layer was deposited, which further enhances coating adhesion. The coating deposition was carried out in mixed $Ar+N_2+CH_4$ reactive atmosphere at 450°C. Throughout the process, the substrates were subjected to three- fold rotation. The three fold rotation represented as τ_1, τ_2 and τ_3 in the figure 22. The bias voltage during the coating deposition step was maintained at U_b= -75 V. Figure 3.5 highlights the deposition parameters set during each of the sequence of the deposition of nanoscale TiAlCN/VCN coating by UBM, HIPIMS-UBM and pure HIPIMS technique.

Pumping and heating

T = 450 °C

P < 7.9 x 10 mbar

Rs = 45 %

Target cleaning

(2 opposing targets were in HIPIMS & UBM mode respectively)

T = 450 °C , Q_{Ar}=200 seem, P = 1.99 x 10'3 ; Rs=45 %

Step (1): t = 3 min, C1=C2=C3=C4= 1 kW (power);

Step (2): t = 5 min, C1=C2=C3=C4= 3 kW (power);

Metal ion etching (HIPIMS discharge of V++Ar+)

T = 450 °C, Q_{AT}= 100 seem, P = 1.1 x 10'3; Rs=45 %

t = 40 min; C3 = 4 kW; Vb = - 1000 V; It = 1.5 kA

TiAIN base layer

(HIPIMS or UBM mode of target w.r.to deposition technique)

t = 40 min; C1=C3=8 kW; P = 3.48 x 10'"; Rs=35 %;

Vb = -75 V; Ar = 181-194; N_2 = 156-158

TiAlCN/VCN coating deposition

t = 180 min; C 1=C2=C3=C4=8 kW; P = 3.48 x 10'3; Rs=35 %;

Vb = -75 V; Ar = 181-194; N_2 = 156-158; CH_4=100

t = duration, Qa,- = Ar flow rate, Q_{N2} = Nitrogen flow rate, Qch_4= Methane flow rate,
P = gas pressure, C1=C3= TiAl target, C2=C4=V target, Rs = rotation speed, Vb= Bias voltage on substrate.

Figure 24 Deposition parameters used during the deposition of TiAlCN/VCN coating in all three techniques.

3.3 Coating characterising techniques

3.3.1 Adhesion test

The “Adhesion test “is the most fundamental characterization technique, which determines the mechanical strength joining the deposited coating with the substrate. A “scratch test” was used to evaluate the adhesion of the coatings with the substrate. A CSM REVETEST scratch tester was used to find out the adhesion of the coating. Initially a maximum normal load of few mili Newton was fixed and a Rockwell C diamond indenter with the diameter 0.2 mm was sliding against the coating. During sliding the load was gradually increased from minimum to a load of maximum set value. The initial coating fracture was determined by the acoustic emission sensor coupled with the scratch tester. The critical load “Lc” at which the coating spall out from the substrate was observed by optical microscope connected to the scratch tester. Figure 3.6 (a) & (b) shows the CSM REVETEST scratch tester and schematic of scratch pattern.

normal load

stylus

scrati

direction of sample

Figure 25 CSM scratch test analyser (a), schematic of scratch test (b), [Ref: 182]

3.3.2 Rockwell C(HRc) Indentation method

The hardness of as-deposited coating was determined by conventional Rockwell hardness test method. A conical shaped diamond indenter with minor load of 10 kgf was applied initially to the coating and then slowly the force was increased to 140 kgf to increase the penetration depth. Figure 26a shows the schematic of Rockwell C indentation. After releasing the indenter, the impression from the indentation was observed with optical microscope and was categorised on the basis of six grades of indentations outlined by Verein Diutscher Ingenieure (VDI) criteria as shown in the Figure 26b. In this figure, each circle like image is the depth of impression created by the indentation and hair like structures surrounding this impression typify the microcrack and subsequent spallation of the coating from the substrate. Higher the amount of crack and spallation, more poor the coating quality is. According to this criteria grading between HF1- HF4 (HF- adhesion strength) was acceptable and HF5 - HF$_6$ was considered to be poor. These gradings are given on the crack pattern and spallation of the coating around the indentation. This particular test was performed only on those coatings deposited on High speed steel substrate (HRc = 54).

1. Diamond Indenter
2. Depth to whkh the diamond indenter is forced under light load
3. Depth to which the diamond Indenter Is forced under heavy load
4. Increment in depth forms the basis for Rockwell C hardness measurement

SHH

Figure 26 (a) Schematic of Rockwell C indentation and possible area of its impression [Ref 183] (b) Verein Diutscher Ingenieure (VDI) criteria showing 6 grades for Rockwell C adhesion test

3.3.3 Pin-on-disc test

A CSM pin-on-disc contact geometry room- and high temperature tribometers have been used to conduct measurements of the friction coefficient of the coated sample in dry sliding conditions. A 6 mm diameter AFO$_3$ balls were used as counterparts under constant normal load of 5 N (Figure 27). Tests were carried out at circular speed of 10 ms’1, with wear track diameter of 7 mm at constant acquisition frequency of 1 Hz. The tests were conducted for 10000 laps at room temperature and for 5000 laps at three different elevated temperatures, (200°C, 450°C, and 650°C) in ambient atmospheric condition.

The friction curves showing COF (coefficient of friction) were displayed against the number of laps past on the coated disc for applied normal load, in real time on a PC screen. These curves can be recalled for further analysis.

Figure 27 CSM pin-on-disc tribometer.

In dry sliding conditions, frictional forces acting tangentially on the stationary disc was reported to be combined effect of adhesion force (Fade) developed at the asperity contacts and a deformation force (Fdef) needed to plough the asperities of the harder surface through the softer [184]. Basic equation for friction coefficient can be given as:

$$F$$

Where F = tangential force ~ Fade + Fdef, W is normal load, ji = friction coefficient

Fade Fdef*

Wear coefficient (Kc) calculation

A precise wear track depth profiling was carried out using a Veeco Dektak 150 instrument to generate data such as area (A) of the wear track for the calculation of coating sliding wear coefficient. The wear rate coefficient (kc) was calculated using the formula;

$$\frac{A * 2\pi R}{F_n * l} \qquad (16)$$

Where "A" is the cross section area of the wear track, "R" is the radius of the entire wear track, "Fn" is normal load and "1" is total sliding distance covered [185].

3.3.4 Nano-hardness test

The elastic modulus (E) and nano-hardenss of the as-deposited thin coating was measured by CSM nano indentation tester. A hard indenter, in our case, Berkovich diamond is gradually pressed into the film from minimum load of few mN up to the preset value of max 20 mN. During the indentation, the tip is continuously pressed against the film surface for about two seconds at various loads in the preset load range. Usually the scanning covers larger area than the indent area, in order to get the clear image of indentation marks. In order to avoid the substrate contribution, the indentation depth is always assured to be below < 10% of the total coating thickness. Nanohardness is calculated by dividing the indentation load by the projected residual area of indents [186]. The typical nano indentation curve and Young’s modulus is calculated by the Force-displacement curve obtained by the software, and relevant equations are shown in figure 28.

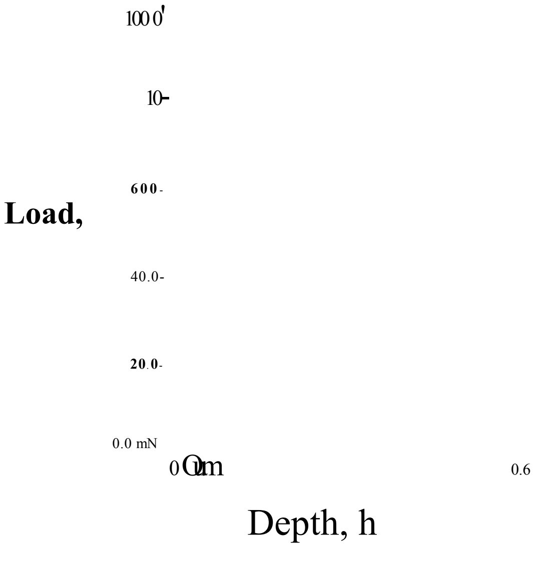

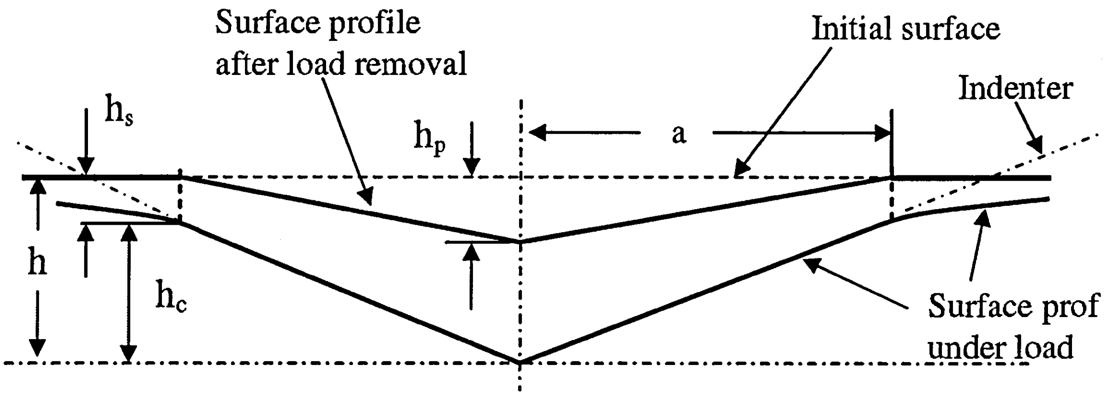

$$\text{Hardness}, = \frac{F_m}{A_p};$$

$$\text{Reduced modulus} = E^* = \frac{\sqrt{\pi}}{2}\frac{S}{\sqrt{A_p}}$$

E can be calculated by $\frac{1}{E^*} = \frac{(1-\nu^2)}{E} + \frac{(1-\nu_i{}^2)}{E_i}$ (17)

Where, F_m = maximum applied load
H_t = depth from the original surface
A_p = projected contact area which is determined from the contact depth, hc
E = strain obtained from stress-strain curve
S = contact stiffness (tangent to the unloading curve)
v = Poisson ratio of measured material (0.3 was used in this experiment)

Figure 28 Nano-indentation curve and formulas used to calculate nanohardness and Young's modulus [Ref: 185]

3.4 Plasma characterisation

3.4.1 Energy resolved mass spectrometry

The plasma analysis has been carried out in a laboratory scale ultra- high vacuum chamber model CMS-18 (Kurt J. Lesker) equipped with 3-inch diameter targets of TiAl and V operated in HIPIMS and UBM discharge mode. The discharge conditions such as average and peak power density and gas pressure were similar to those of the deposition experiments conducted in the industrial sized Hauzer HTC-1000-4 machine.

An energy-resolved mass spectrometer PSM003 (Hiden Analytical Ltd.) was utilised to quantify the time-averaged ion composition in the plasma. Schematic figure 29 shows the plasma sampling spectrometer.

The ions from the plasma are extracted by the extraction chamber. A DC voltage of about -10 V and -80 V respectively, is applied on to the electrodes inside the extractor to attract these ions from the plasma. The negative voltage is applied usually to repel electrons and attract positive ions from the plasma. The ions are filtered by Bessel box installed in the systems. Further, filter process will continue by the quadruple mass analyser (QMA). Ions with specified mass-to-charge ratio would detected by secondary electron multiplier (SEM). These SEM detectors are maintained at increasing higher positive voltage at the output signal, in order to amplify the signal output. Hence, the selectivity of the charged species with large differences in number density is possible with signal to background ratio of 10^6 [187, 188].

The basic principle of mass analyser is explained briefly. The mass analyser differentiates the ions with respect to their mass-to-charge ratio. This differentiation is based on the principles of electro magnetism in vacuum for charged species stated by Lorentz law:

$$\vec{\mathrm{F}} = \mathrm{q}\vec{\mathrm{E}} + \mathrm{q}\vec{\mathrm{v}}\,\mathrm{X}\,\vec{\mathrm{B}} \qquad (18)$$

and Newton second law:

$$\vec{F} = m\vec{a}$$

Where, $\vec{F}$ is the force applied on the ions, $\vec{E}$ is the electric field, $\vec{v}X\vec{B}$ is vector cross product of ion velocity and magnetic field, m is the mass of ion, and $\vec{a}$ is the acceleration. When both equations are equated, the expression for the force applied on the ions inside the chamber can be obtained; i.e.,

$$\frac{m}{q}\vec{a} = \vec{E} + \vec{v}X\vec{B} \qquad (19)$$

Where, $\frac{m}{q}$ is the mass-to-charge ratio. Based on this equation for the motion of the charged species, the ions can be identified. Charged species with equal mass-to-charge ratio will be influenced in similar fashion.

The fragments of energy filtered ions from the Bessel box are guided into the system of 4 rods of hyperbolic surface, called quadrupole mass analyser (Figure 30). A DC field is applied to two rods and RF field is applied to other two rods. These rods generate electric field through which ions are allowed to move. Only few ions of specific mass-to-charge ratio determined by the applied voltage are finally detected by the detector. This mechanism allows the identification of a particular ion by varying voltage.

In summary, the mass spectrum is usually measured by setting a fixed voltage on the Bessel box to define the ion energy and changing the voltage on the QMA, thus data obtained in terms of mass-to-charge ratio. The energy resolved mass spectrum collected in this work for V^+ ion etching and TiAlCN and VCN deposition is discussed in next chapter.

3.4.2 Time averaged mode

The relative content of each ion during the deposition was determined by integrating its corresponding ion energy distribution function. The mass spectrometer acquires data at certain energy for specified duration. In this particular mode the detector was assigned to collect the data for every 300 ms which is equal to around 30 pulses. By changing this acquisition time, it is possible to determine the ion energy distribution function (IEDF) for arriving charged species throughout the pulse. The IEDF measured in the average time of acquisition gives the information about ionic composition of the plasma reaching the substrate.

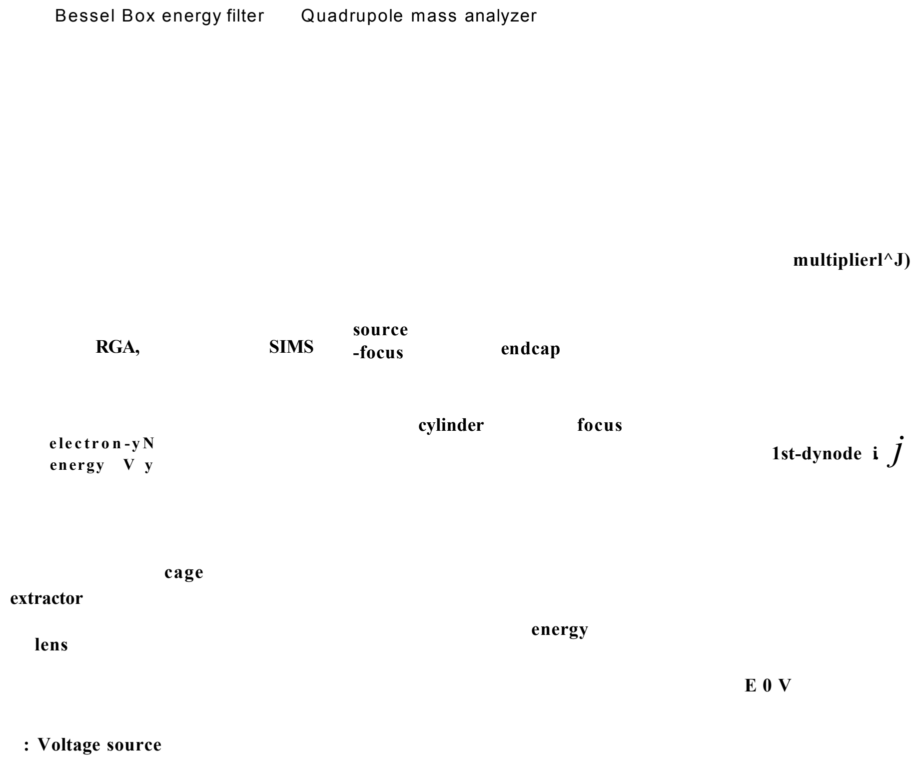

Figure 29 Schematic internal features of energy resolved mass spectrometer [Ref: 189]

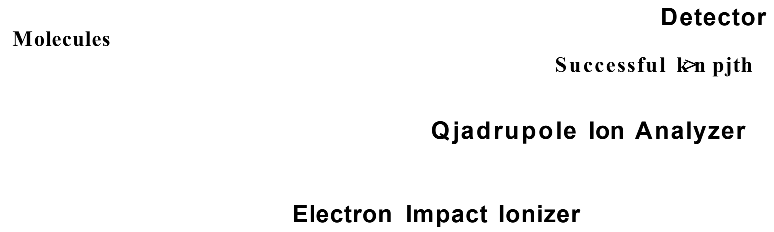

Figure 30 The schematic of quadrupole mass analyser showing the ions reaching the Detector [187].

3.5 X-ray diffraction (XRD)

The X-ray diffraction study was carried out using a Philips PW 1710 automated diffractometer. The study was carried out for two purposes. Initial purpose was to understand the microstructure of the as-deposited TiAlCN/VCN coatings by Low angle XRD and Glancing angle XRD (fixed at 1° incidence angle) technique. Another purpose was to identify the chemical phases of as-deposited and oxidised surface of TiAlCN/VCN coating by $\theta/2\theta$ measurement in Bragg-Brentano geometry. In this geometry the scanning was done from $2\theta = 10^\circ$ to 100° with a step size of 0.04°. X-ray radiation with CuK_α with 1.5405 nm wavelength is used for all the methods.

In general the diffraction of waves are more pronounced when the wavelength of an incident electromagnetic wave is in the same order of magnitude as the dimension of the diffracting objects. Because the dimensions of the atoms are equal to that of the wavelength of X-rays, which are in the range of few angstroms, Xrays are widely used to probe the atomic structure an element. If the atoms are arranged in a periodic fashion, the constructive interference maximum of the diffracted waves provides the information about the symmetry of the atomic arrangement. Hence the Xray diffreaction peaks are directly related to the atomic distrances. The periodicity, also called the distance between the successive two atomic planes is given by d_{hkl}. Where, hkl are Miller indices given for corresponding lattice planes. For simple cubic structure the maximum intensity for diffraction can be obtained only when Brag's equation is obeyed. This equation is given as [190]:

$$2\, d_{hkl} \,\mathrm{Sin}\theta = n\lambda \qquad ; \quad n = \text{reflection order}, \lambda = \text{wavelength of radiation.}$$

Where, $d_{hkl} = \frac{a}{\sqrt{h^2+k^2+l^2}}$; a = lattice parameter.

Geometrically the Brag's equation can be visualised by the figure 31 given below.

$$A, + A_2 = \boldsymbol{2d} \cos(90^\circ — \boldsymbol{6)} = \boldsymbol{2d} \sin \boldsymbol{6}$$

Figure 31 Geometrical visualization of Brag's equation [Ref: 191]

The constructive interference of the reflected waves will happen only when 2 d_{hki} Sin0 is equal to integer multiple of wavelength impinging on the crystal planes.

3.5.1 Glancing angle geometry (GAXRD)

In XRD analysis of thin films, contribution from the substrate to the diffraction can sometimes overshadow the contributions from thin film. In such conditions GAXRD is useful non-destructive technique to collect the information from actual film with minimum contribution from the substrate. Figure 32 shows the GAXRD geometry. In this geometry parallel, monochromatic X-ray beam incident on a sample surface at a fixed angle of incidence a and diffraction profile is recorded by moving the detector alone.

Detectoi

Substrate

Figure 32 Schematic of Bragg-Brentano geometry [Ref: 192]

The basic principle in this technique is that when angle of incidence is decreased from critical angle “ai”, the X-ray reflection occurs only below this critical angle because of refractive index value which is less than unity. Due to this fact the diffracted and scattered signals at 20 collected only from within the minimum depth available from the surface. In glancing angle geometry the penetration depth is defined as the distance, xe from the surface that the diffracting planes in the specimen contribute to the whole diffracted intensity by the ratio *Me:*

$$\frac{\sin v \sin(20-v)}{l4 \sin y+\sin(20-y)]} \tag{20}$$

Where p is the linear absorption coefficient for TiAlCN/VCN and y is angle of incidence [190]. By using above formula, the structural information from the film can be probed through its thickness by varying the angle of incidence.

3.5.2 Bragg-Brentano (0/20) geometry

In this case, the X-ray beam incident at an angle 0 on the film surface and the diffracted beam intensity was detected using a counter at an angle 20 relative to the incident beam. The beam obeying the Bragg’s law and planes parallel to the film surface only contribute to the diffraction intensity. Figure 33 shows the θ/2θ geometry of this technique.

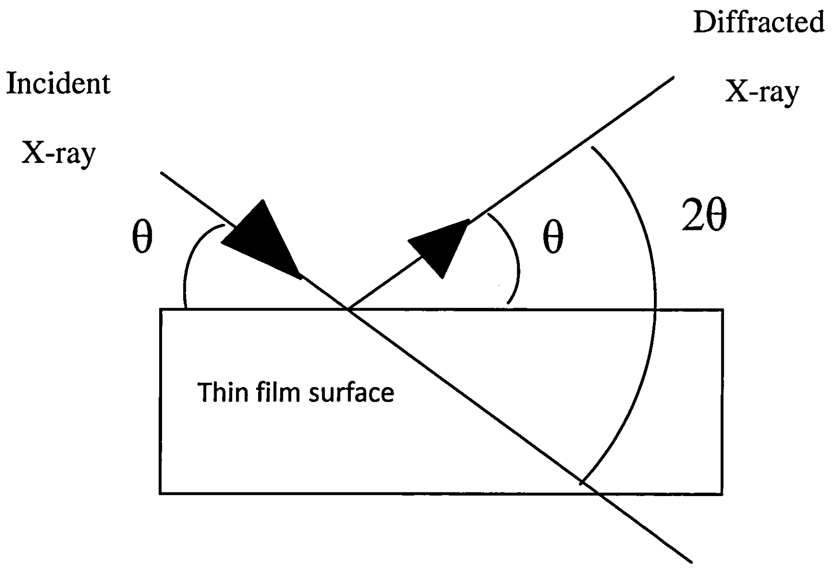

Figure 33 Schematic of θ/2θ geometry in Bragg's-Brentano XRD technique.

3.6 Raman spectroscopic analysis

Raman spectroscopy is an effective, non-destructive, non-contract, thin film characterising technique which requires no sample preparation. Especially, when characterisation is carried out in confocal mode, it offers the measurement at sub-micron special resolution. Thus, specific particle and grain regions of the as-deposited thin films can be analysed. Additionally, the confocal Raman spectroscopy provides 3D spetial resolution, allowing the analysis of discrete volume in a transparent sample also. This property is particularly suitable for the analysis of the multilayer thin films with nanolaminate structures.

Raman scattering is the phenomenon of scattering of discrete energy when monochromatic radiation of certain wavelength passed through a transparent and reflective substances. This scattered discrete energy consists frequencies above and below that of incident beam. When this monochromatic radiation with energy $E = h\nu$, interacts with the molecules of the substance, they can undergo elastic or inelastic collisions. If the scattered energy equal to that of incident energy of the radiation, then it is referred to as elastic scattering. In this scattering, only electron cloud distortion is expected. For molecules it is names "Rayleigh scattering". In the case of Raman spectroscopy the scattered radiation is different than that of incident beam energy, in which the nuclear distortion is expected. The energy change in this case may be less $hv - \Delta E$ (stokes shift) or more $hv + \Delta E$ (anti stokes shift) than the incident energy E. This is the case of inelastic scattering; also called Raman scattering. It is a very week process where only 10^6 to 10^8 photons are expected to scatter, but the modern instruments use lasers with high power density to get higher counts. The change in energy (ΔE) is either vibrational energy or rotational energy of the molecule. Figure 34(a) shows the basic process of energy change in single vibrational mode, when radiation interacts with the substance molecule. In the Raman scattering process, if molecules absorb energy from its present ground state (m) and if attains higher excited state (n) then it is called stokes line. If any transition from excited state to ground state occurs then it is called anti stokes lines. Usually Raman scattering is recorded only on the lower energy side of stokes line [193].

In this work, the Raman spectrum was measured at room temperature using HORIBAJOBIN YVON HR800 integrated Raman spectrometer fitted with UV (λ = 325 nm) and Green laser (λ = 532 nm). Figure 34 (b) shows the picture of the HR800 integrated Raman spectrometer. The microscope was coupled confocally to a 800 mm focal length spectrograph equipped with switchable two gratings (600 g/mm and 2400 g/mm). The 2400 g/mm grating was used for collecting the spectrum with a spectral resolution of 2-3 cm^{-1}. Usually, higher the groove density of the grating, higher is the spectral resolution. For example with 532 nm laser, a 100x objective and 1800g/mm and 2400 g/mm grating, the special resolution of 200-400 nm can be achieved [194]. Utilisation of UV laser excitation allowed analysing from very thin layer (nm in thickness) from the top of film. Another advantage of utilisation of UV laser is the increased sensitivity (as compared to that using excitation in visible range). Reports revealed that sensitivity of UV laser is 14 times higher than that when using 532 nm and 633 nm wavelength laser [195]. A 50 % transmission filter was used to reduce the intensity of incident beam. A silicon based multichannel array detector (CCD) was used to collect the output signal scattered from the samples.

Virtual
states

n

Vibrational
states

m

Stokes Rayleigh anti-Stokes

Figure 34 (a) The basic scattering lines when monochromatic radiation is passed through a substance [193] (b) HORIBAJOBIN YVON HR800 integrated Raman spectrometer.

3.7 Thermo gravimetric Analysis

Thermogravimetry is a technique that measures the variation of mass of a sample when it is subjected to a temperature program in a controlled atmosphere. This variation of mass can be a loss (vapour emission) or a gain (fixing of gases). As materials are heated, they can lose weight onto a simple process such as drying, or due to chemical reactions that liberate gasses. Some materials can gain weight by reacting with the atmosphere in the testing environment. Since the weight loss and gain are disruptive processes to the sample material or batch, knowledge of the magnitude and temperature range of those reactions are necessary in order to design adequate thermal ramps and holds during those critical reaction periods.

3.7.1 Operating Principle

The standard High performance modular Thermo gravimetric Analyser TGA (ambient /2400 °C) from SETARAM instrumentation was used to measure oxidation studies of coated samples. The experiments have been carried out either in an ambient air or in the inert atmosphere of Argon. The coated samples of stainless steel were suspended on a micro-balance with very high stability and fidelity; capable to measure approximately about 35 g load. The system has been provided with high-performance, optical and electronic detection system. The balance is zeroed, and the sample is heated according to a predetermined thermal cycle. The balance sends the weight signal to the computer for storage, along with the sample temperature and the elapsed time. The TGA curve plots the TGA signal, converted to percent weight change on the Y-axis against reference material temperature on the X-axis. The schematic internal electronic and mechanical circuitry of the TG analyser is given in Figure 35.

The coated samples were normally heated from ambient to the maximum temperature of 1000°C at 1° C per minute. Slow heating rates are preferred so that the weight change can occur over a narrower time span and temperature range. The resulting curves are steeper and the onset of oxidation temperature is closer to the actual coating. The SETSYS has provided the ability to set various heat up rates according to the user's requirements. The data acquisition and analysis software from the SETSYS displays the test progress on the monitor, stores the data and enables the user to perform analysis on the data.

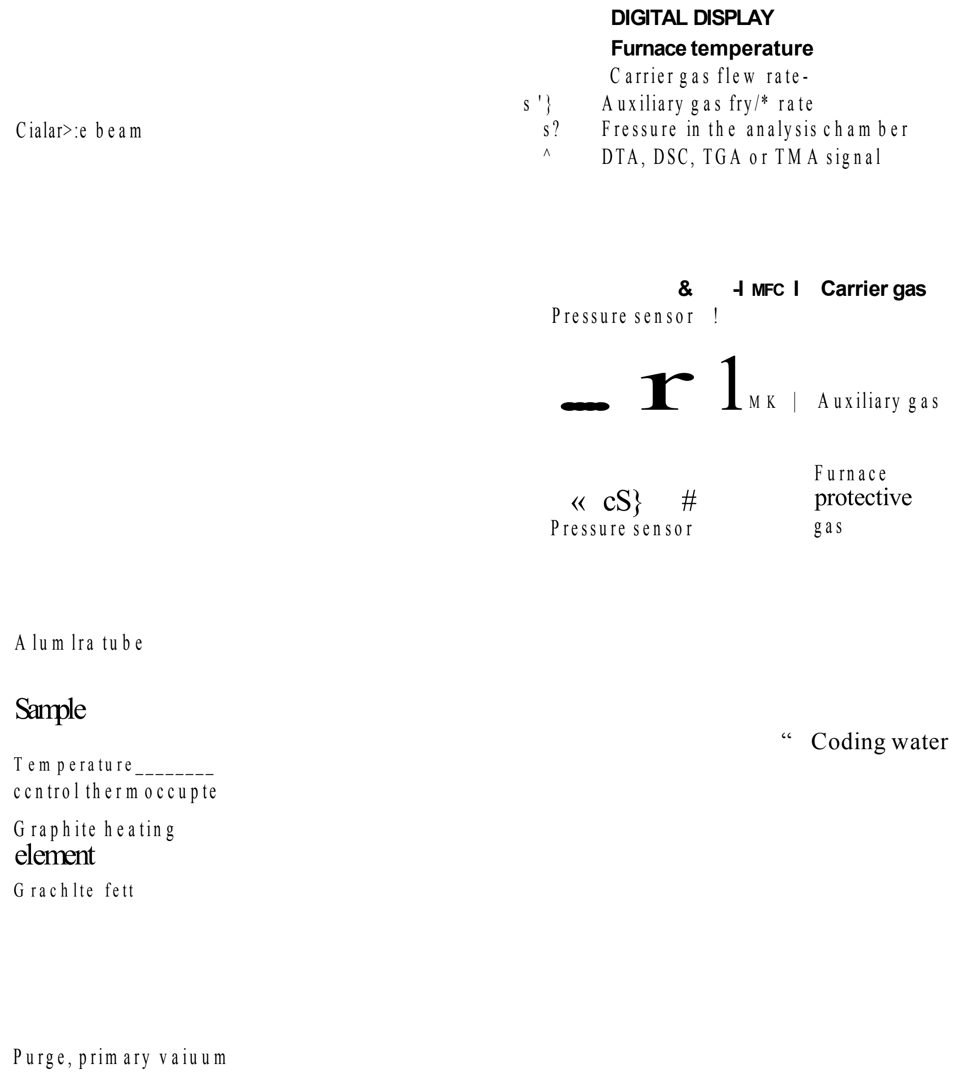

Figure 35 The internal electronic and mechanical circuitry of SETARAM TGA analyser [195].

3.8 Scanning electron microscope (SEM)

Scanning electron microscope is a vacuum technique in which highly focused beam of energetic electrons are guided on to the surface of a material to generate signals (secondary electrons or back scattered electrons) which provide information such as surface morphology, chemical compositions, crystalline structure, etc. These signals are collected from selected area of the surface and create 2-D image on the computer screen which is interfaced with the spectrometer. Besides getting the images, it is also perform analysis of the samples under investigation. For example, the qualitative analysis includes identifying chemical composition (Energy dispersive X-ray analysis), crystal structure or orientation (Electron Back scattered diffraction). Figure 37 shows the schematic internal view of the SEM.

Basically, the electrons are generated from the heated filament (tungsten or LaB6) and accelerated down a column through few voltages potential (1-50 kV). During this process the column is normally under vacuum of about 1 x 10^{-6} Torr. These energetic electrons interact with the atoms, i.e. inner shells electrons of the sample surface. This interaction is so powerful that it produces secondary electrons (helpful for surface morphology and topography), back scattered electrons (used for determining crystallinity), photons and X-rays (for chemical analysis). Figure 36 shows the schematic of possible signal which might emerge out when electron interacts with the surface atoms. Generally, SEM coupled with following necessary components which are depicted in figure 37 (a), and briefly explains the important parts of the SEM and its functions.

3.8.1 Secondary electron and back scattered electron image

Secondary electrons excited secondarily by electrons guided on the specimen. Usually, they are generated in a region of about 10 nm. This technique has very little imaging provision since the electron diffusion length has less influence on imaging. In contrast if the electrons are scattered back in to the sample and emitted again from the sample, then the contrast of the image is good. This is called back scattered imaging. This back scattered imaging depending upon the mean atomic number of the substance which constitute the specimen.

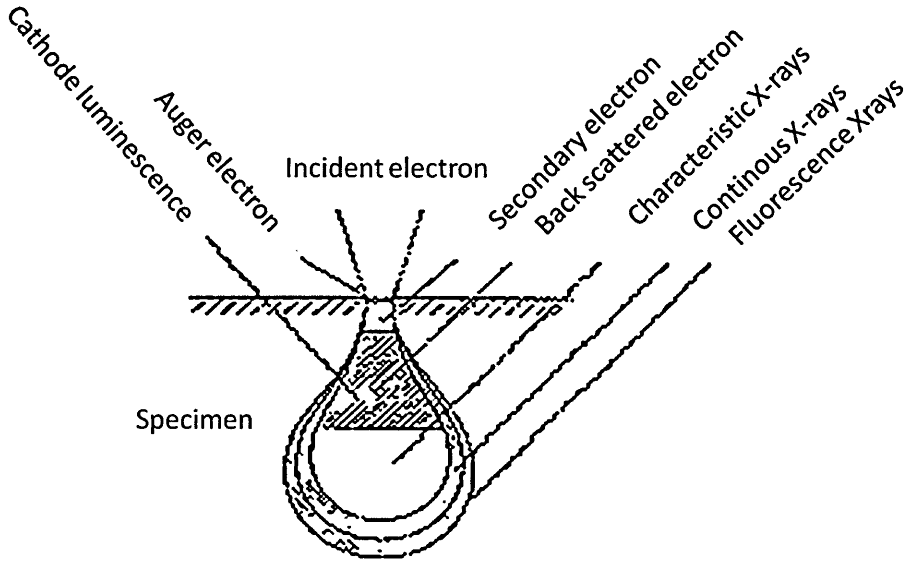

Figure 36 Shows the possible signal which can emerge out from the sample when electron interacts with the specimen surface atoms [idea taken from: 196]

In this work, relevant cross-sections from as-deposited coatings were prepared for scanning electron microscopy using FEI NOVA-NANOSEM 200 (Figure 37). This is equipped with high resolution field emission SEM column with high stability Schotky gun with two mode (field free and immersion) final lens. Prior to the imaging, the chamber was evacuated to about 10^{-6} order in order to avoid contamination during the imaging or analysis. The high imaging of the sample cross section was carried out with working distance of about 1 nm at 15 kV by using TLD or SE detector. High vacuum analysis (EDX) was carried out at working distance of about 3 nm at 15 kV, using TLD or SE detector.

Electron Source	Comprise tungsten or LaB6 filaments which are heated to produce electrons.
Electron lens	Consists condenser (CL) and objective lenses (OL); CL controls the probe current and spot size, and OL helps to focus the electron on the sample.
Sample stage	Hold the sample and helps to adjust working distance (WD); WD is the distance between the objective lens and sample surface.
Detectors for all types of signals	Various types of detectors are installed depending upon type of signal. Back scattered electron — Solid state detectors Secondary electrons — Everhart-Thornley detector X-ray — Energy dispersive spectrometer
Display	Computer monitors are interfaced to observe the test surfaces.

Electron gun ——

Gun alignment control -

'neumatic air lock valve

'-Condenser lens —

< z iL m » **Objective aperture**

Scanning coil

Objective lens

. Motorized

~ji

Sample Chamber

Figure 37(a) Brief introduction to major internal parts of SEM and its function (b) Schematic internal view of SEM [197].

3.9 Transmission Electron Microscopy (TEM)

Unlike scanning of surface of materials by electron, Transmission electron microscope (TEM) also uses energetic electrons which are allowed to pass through the material object in order to reveal the surface morphology, the crystallinity of the material, and its chemical composition. Conventionally, in TEM also, energetic electrons are generated by thermionic emission by heating the tungsten or LaB6 filaments. But all modern TEM's uses low work function LaB6 filament as their electron source. Additionally, LaB6 sources have low operating temperature, which helps to increase the brightness by reduced electron energy spread [198]. Figure 38 explains the general purpose of the TEM in materials analysis.

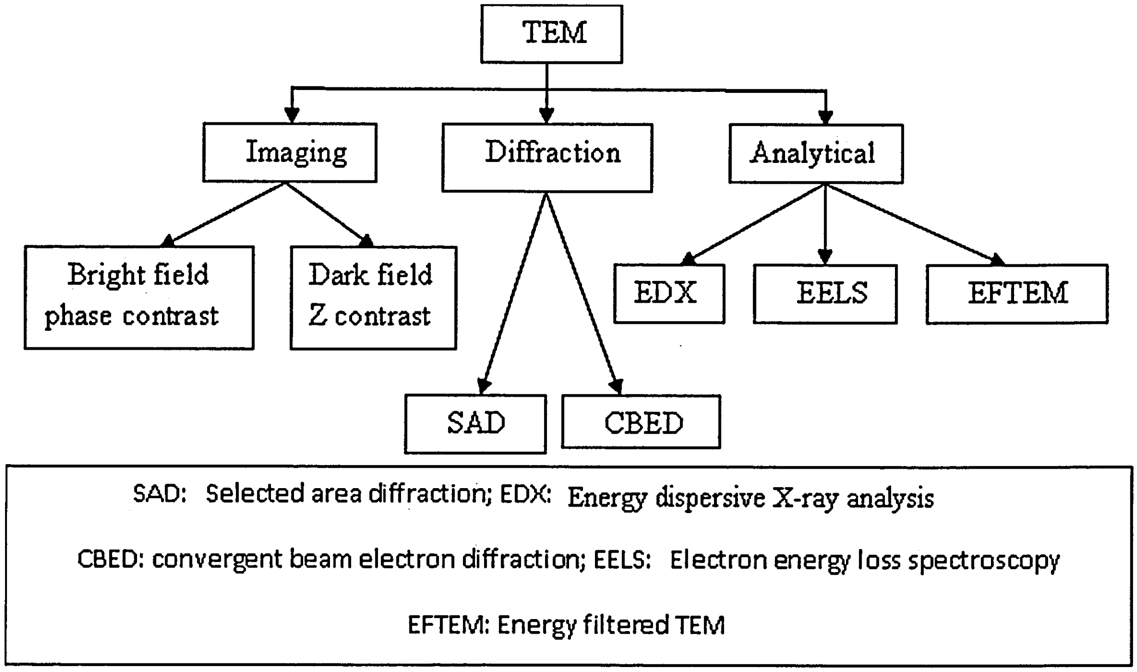

Figure 38 Basic purpose of TEM in materials science and technology.

Figure 39 shows the internal optical arrangement of TEM. The electrons generated are guided to the columns which are positively biased to about 200 kV to 400 kV (in SEM 10-20 kV). Then the condenser lens systems are used to focus the electron beam on the sample. In this way, the parallel beam spreads over the sample surface, where electrons are scattered by elastic or inelastic mechanism with nuclei of the atoms and electrons of the sample respectively.

It is important to notice here that, the samples are inserted in mid way of the TEM apparatus, where as in SEM the samples are at the bottom side of the chamber. Apparently, the electrons passing the nuclei may gain and extra velocity and thus reduce their wavelength which leads to the change in their phase. At this stage, the structural information of the specimen will be transferred to the phase of the electrons. Only those electrons which are scattered by nuclei of the atoms of the surface (elastically scattered) will contribute to the high resolution images of the specimen, whereas those scattered from the electron shells of the atoms (inelastic electrons) contribute mostly to the background of the image. The energy filters are used to remove these inelastic electrons, whose energy loss spectrum contains the information about the chemical nature of the substance. In the next stage, the phase information of the electron is converted into intensity information when electrons passed through substance reaches the objective lens. Objective lens changes the phase by few factors and converts the electron beam in to image on the screen. There are many factors which pose hurdle to the high resolution image, when electron beam passes through the objective lens. For example chromatic aberration of the objective lens, electrical instabilities of the microscope, mechanical instability and inelastic electron loss, etc, cause defocusing of the electron beam spread on the screen. More detailed information about these facts can be seen in [199]. The objective aperture are usually block the high angle scattered electrons and provide better contrast to specimen image on the screen, where as selected area aperture enables the user to examine the periodic diffraction of electrons by ordered arrangement of atoms in the sample. Figure 40 shows the diffraction and imaging modes of TEM. The final images are seen on the fluorescence screen. The darker images on the screen represent the areas through which fewer electrons are transmitted, where as brighter images signify the area through which more electrons are transmitted. The advanced TEM instruments can give a resolution of about 0.2 nm with very high magnification of 500,000X.

In this work, the microstructure of as deposited TiAlCN/VCN coating was analysed by transmission electron microscopy (TEM) observation using a Philips EM430 instruments. This microscope was Equipped with a LaB6 electron gun, the EM430 TEM provides a point resolution of 0.2 nm and has a double tilt sample holder and low-temperature sample holders. This microscope was useful throughout the analysis of nanoscale TiAlCN/VCN coating, by which the atomic arrangement of as deposited coating and microstructure was revealed.

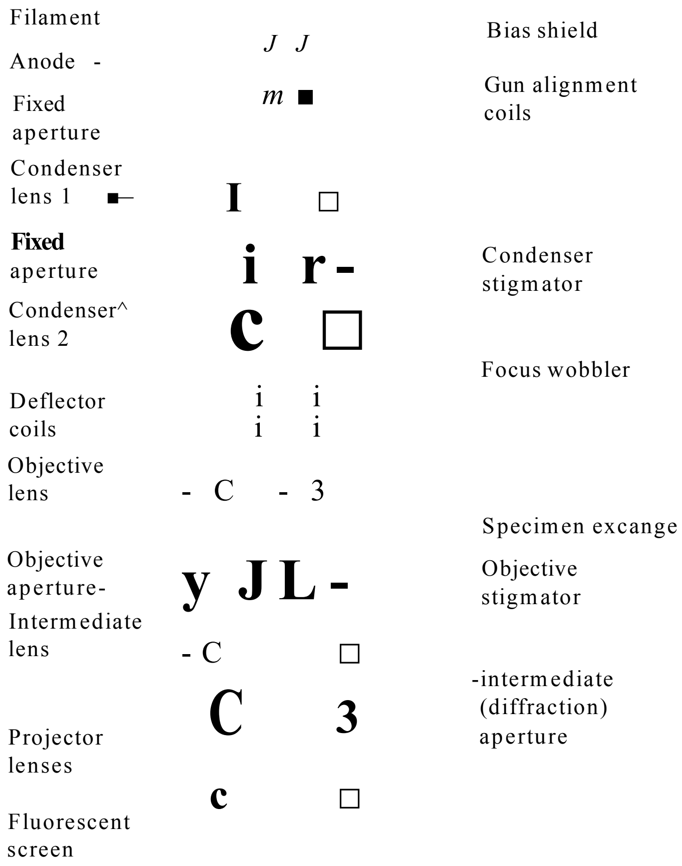

Figure 39 Schematic of internal optical architecture of TEM [200]

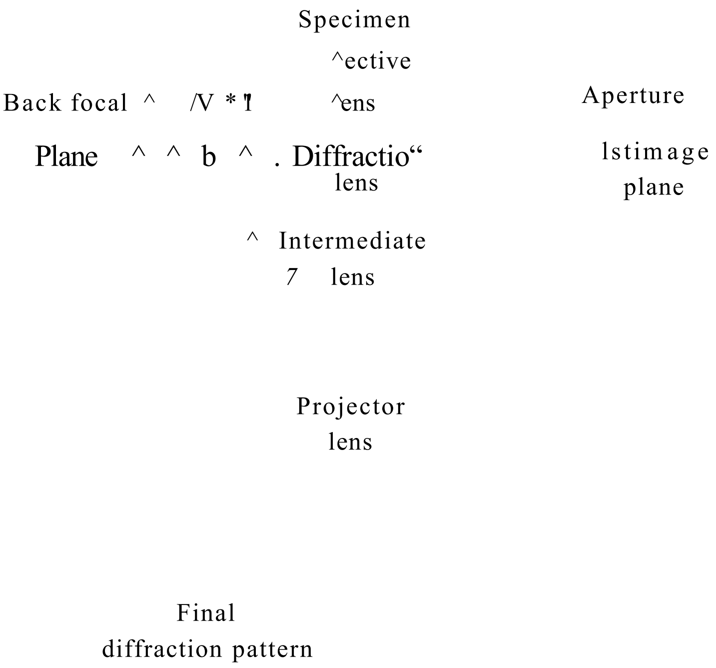

Figure 40 Optical set up during the Diffraction and Imaging mode of TEM [200]

3.9.1 TEM Sample preparation

The following points briefly explain the procedures for preparing electron transparent (~ 100 nm) cross-sections samples:

1. Cutting:
   a) The coated sample (coating face up) was cut to a dimension ~ 2.5 X 2.0 mm^2 with a high speed SiC cutting wheel.

Two cut samples with the coatings facing each other (to protect the coating surface) were glued with wax on a glass plate.

2. Grinding and Polishing
   a) The samples were ground evenly by 240,320,400, and 600 grit papers, to half the sample thickness on one side and then polished with 5 μm diamond paper.
   b) The samples were turned over to the other side and were ground to ~ 30-60 μm following step (a).
   c) Finally, the sample was glued with epoxy resin on a copper grid with a slot hole and ready for ion beam thinning to electron transparent thickness.
3. PIPS (Precision Ion Polishing System-Ion beam milling)

   A GATAN PIPS 691 system was used to thin the sample to the electron transparent thickness of 50-100 nm by Ar ion beam milling. The parameters used were:

   a) Ion gun accelerating voltage: 5.5 KeV
   b) Rotation speed : 1.5 rpm
   c) Incident angles: ± 8°

The sample was thinned until a small hole appeared on the coating region of the sample. The sample was then ready for investigation under TEM.

3.10 Dry high-speed milling test

The purpose of the development of nanoscale TiAlCN/VCN was to protect the tool edge from being damaged or getting worn out when utilised during the machining of sticky alloys (Ti, Al, and Ni based alloys). Dry high-speed machining performance of the HIPIMS-UBM deposited TiAlCN/VCN coating is revealed in this work. Two-flute

25 mm diameter, 2.5 mm radius high-speed machining end mills from S290 HSS material are coated with TiAlCN/VCN nanoscale multilayer coating by HIPIMS-UBM

technique. The end mills were used for dry machining of wrought A17010-T7651 alloy (figure 3.22), most frequently nowadays used in aerospace applications. Dry high-speed machining process is shown in figure 41. A MAZAK FJV-25 high speed milling machine is used to carry out this test. The spindle speed of about 24000 rpm, cutting speed Vc of 1850 m/min was set as milling test parameter. The feed rate Vf = 0.33 mm/rev with cutting depth Ap and cutting width Ae of 4 mm and 2 mm respectively was achieved during the machining. The flank wear was calculated by optical microscope analyser. The test was interrupted every 5 min and flank wear was calculated. Additionally, Raman spectra were collected from tool edge after certain interruptions in order to understand the chemical integrity with the microstructure of the coating. The performance of the TiAlCN/VCN coating deposited by HIPIMS-UBM technique was compared with UBM deposited TiAlCN/VCN coating under similar machining conditions. The chemical compositions of work piece (Al-alloy) are wt% Cu 1.68, Mg 2.11, Mn 0.01, Zn 5.92, Fe 0.08, Si 0.04 and rest of the composition was Al.

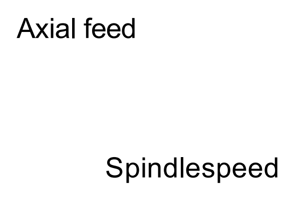

Figure 41 Schematic picture of machining by coated two-flute milling cutter.

CHAPTER 4

Results

In this chapter the results of various characterisation performed on nanoscale TiAlCN/VCN coating has been presented. The characterisation technique involves plasma compositional analysis carried out during the surface pre-treatment and deposition of nanoscale coating, followed by analysis of coating microstructure and functional properties at both room and elevated temperatures (200 ^oC, 450 ^oC, 650 ^oC). The nanoscale TiAlCN/VCN coatings were deposited by three different ways in combination of reactive pure UBM and HIPIMS, these are:

(i) Reactive pure UBM,

(ii) Combined HIPIMS and UBM (will be written later as HIPIMS-UBM),

(iii) Reactive pure HIPIMS.

Prior to actual deposition of the coating, initial surface pretreatment step was carried out by HIPIMS technique in all three cases. During this step, the Ar^++V^+ ions were attracted towards the substrate at a voltage of about U_b = - 1000 V. Hence, the effective energy of the bombarding ions were maintained in the range between 900 - 1000 eV. In the later steps of the processes, deposition of TiAlN base layer and nanoscale TiAlCN/VCN coating was carried out at bias voltage of U_b = - 75 V, where the arrival ions on the substrates were bombarding with equivalent ion energy of 75 eV. Hence the basic intention of the work was to understand the impact of HIPIMS on the microstructure of the TiAlCN/VCN coating by understanding its plasma characteristics. Further few more characterisations techniques have been used in order to reveal the overall performance of the coating in real world applications for which TiAlCN/VCN coating was developed. The results obtained from all characterisation experiments are supported by the discussions and conclusions presented in the following chapter of 5 and 6 respectively.

4.1 Plasma compositional analysis during TiAlCN/VCN deposition

The plasma compositional analysis was carried out to investigate the chemistry of ion flux, by calculating metal-to-gas ion ratio reaching the substrate during both surface pretreatment and coating deposition. Ionic composition of plasma was determined by energy resolved mass spectrometry. The ionic compositions during HIPIMS etching step and coating deposition of TiAlCN/VCN by UBM and HIPIMS was investigated near the substrate facing the 3 inch diameter targets of V, TiAl respectively. The results were recorded for conditions corresponding to V metal ion etching (using V target in HIPIMS mode in Ar atmosphere) and coating deposition of TiAlCN and VCN (using TiAl and V targets in HIPIMS and UBM mode operated in atmosphere of Ar, N_2, and C_2H_4).

4.1.1. Metal ion-to-gas ion ratio during HIPIMS etching

The plasma analysis is carried out in laboratory scale ultra high vacuum (UHV) chamber. During HIPIMS pre-treatment the peak pulse current to the substrates reachesj_s = 300 mA/cm^{-2} and average current wasj_s = 3 mA/cm^{-2}. Figure 4.1 shows a mass spectrum collected at the substrate position during the HIPIMS pre-treatment step. The majority of metal ions produced were V^{2+} with 27%, and ionization states of up to 5+ were detected. V ions had concentrations of V^{1+} (24%), V^{2+}(27%), V^{3+}(4%), V^{4+}(0.8%), and V^{5+}(0.2%) making up a combined relative percentage of 56%. Ar^{1+} (31%) and Ar^{2+} (13%) ions contributed together 44% of the total. Very clearly this has been shown below in a pie-chart 4.2. Figure 4.3 shows the energy distribution of single, double and triple charged ions. The average energy of all the ions was in the range of 1-2 eV.

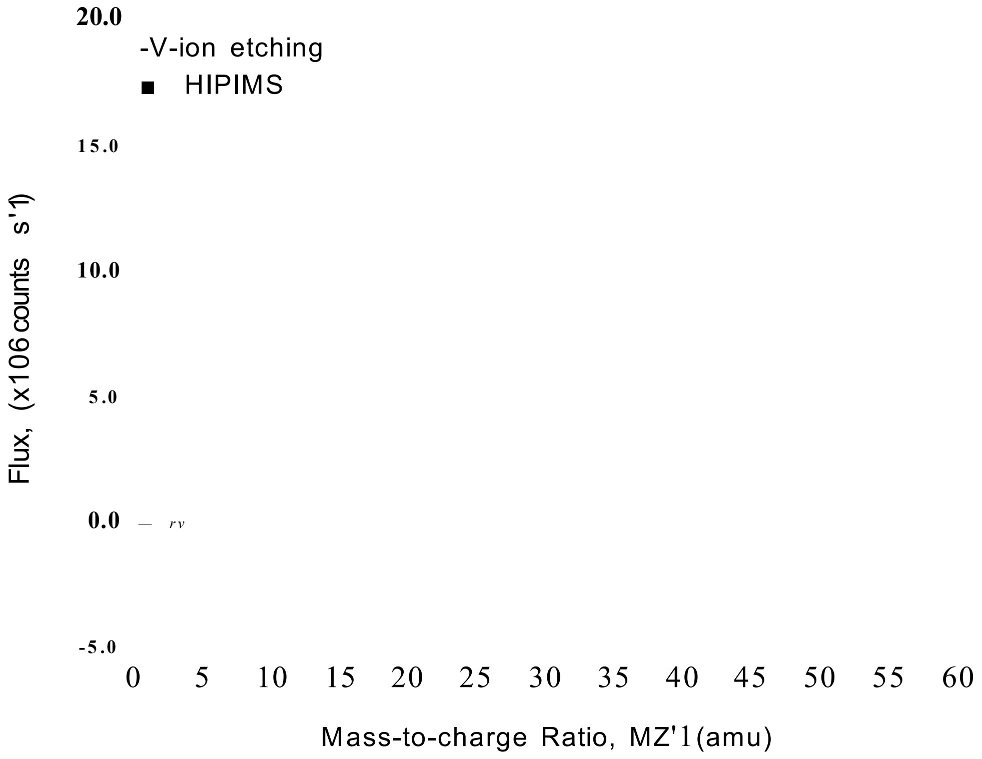

Figure 4.1 Mass spectrum of the substrate ion flux generated by a HIPIMS of V++ Ar+ discharge.

27%

0.8% 4%

Figure 4.2 V+ + Ar+ ion percentage calculated from time average mass spectrum collected at the substrate during HIPIMS etching step.

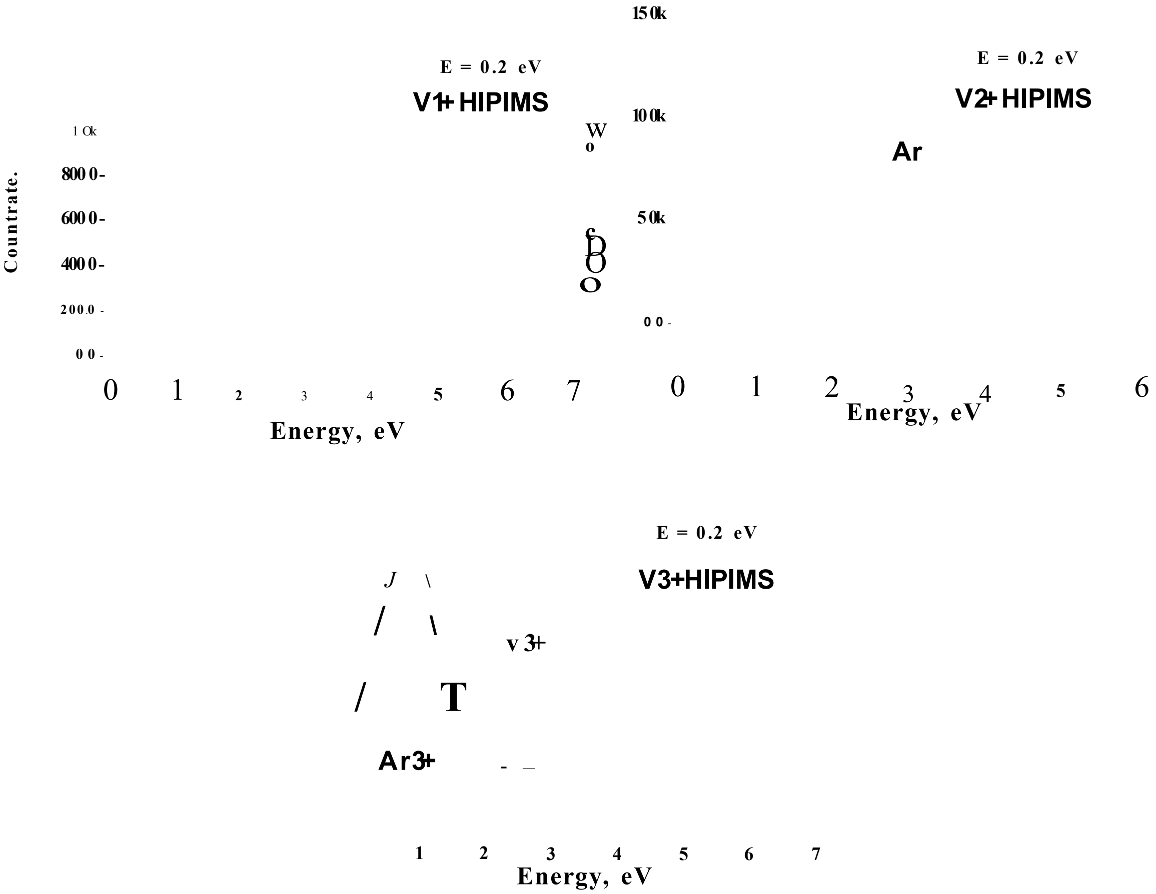

Figure 4.3 Energy spectra of the substrate ion flux generated by HIPIMS of V++Ar+ ion discharge.

4.1.2 Metal ion-to-gas ion ratio during deposition of TiAlCN and VCN by UBM

Figure 4.4 shows the time averaged mass spectrum collected at the substrate during the deposition of TiAlCN and VCN by HIPIMS and UBM techniques, respectively. During the deposition of TiAlCN in UBM mode, about 97% of the plasma was dominated by gas (Ar) and only -3% of metal ion content distributed among Al^{1+}= 2.8%, Ti^{1+}= 0.23%, and C^{1+}=0.13% was identified. Similarly during VCN deposition, the metal ion (V^{1+}) concentration was 0.56% with 0.18% of C^{1+} ion and 99.26% gas ions. This has been illustrated highlighted by the pie-chart Figure 4.5a and b.

4.1.3 Metal ion-to-gas ion ratio during deposition of TiAlCN and VCN by HIPIMS

During the coating the current was again $j_S = 3\,\mathrm{mA/cm^{-2}}$. During the deposition of TiAlCN in HIPIMS mode, the metal ion concentration was about 12% distributed among $\mathrm{Ti}^{1+} \approx 2\%$, $\mathrm{Al}^{1+} \approx 9\%$ and $\mathrm{C}^{1+} \approx 1\%$, and gas ion concentration was dominated with a value of 88%. For VCN, the metal ion (V^{1+}) concentration was 7.73% with 0.49% of C^{1+} ion and 91.78% gas ions. In Figure 4.6, pie chart explains the ionic content of the HIPIMS plasma, calculated from the time averaged mass spectrum (Figure 4.4) collected during HIPIMS deposition case.

During the deposition of TiAlCN/VCN coating by both HIPIMS and UBM, apart from metal ions and free carbon, the gas ions of the following species were identified in mass spectra: Argon, N_2, stable hydrocarbons (CH_4, C_2H_2, C_2H_4, C_2H_6, C_3H_8), radicals (CH, CH_2, CH_3, C_2H, C_2H_5, C_3H_2, C_3H_3, C_3H_6, C_3H_7), and nitril compounds (HCN, H_2CN, NH, and NH_3). This has been clearly shown in the mass spectrum of Figure 4.2.

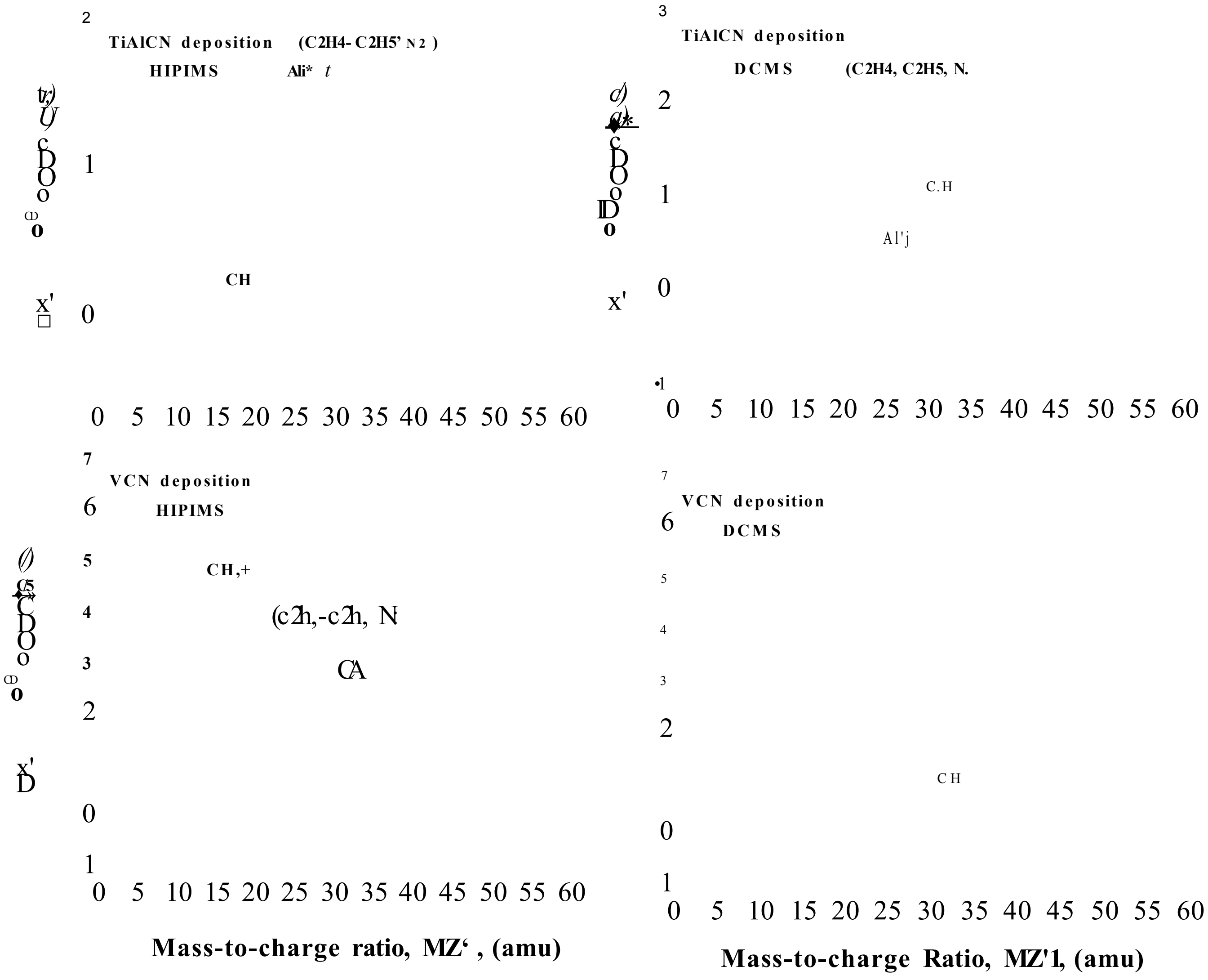

Figure 4.4 Mass spectrometry results for TiAlCN and VCN deposition by HIPIMS and UBMS technique respectively.

Figure 4.5 Time averaged mass spectrometry results for UBM deposited (a) TiAlCN (b) VCN coating.

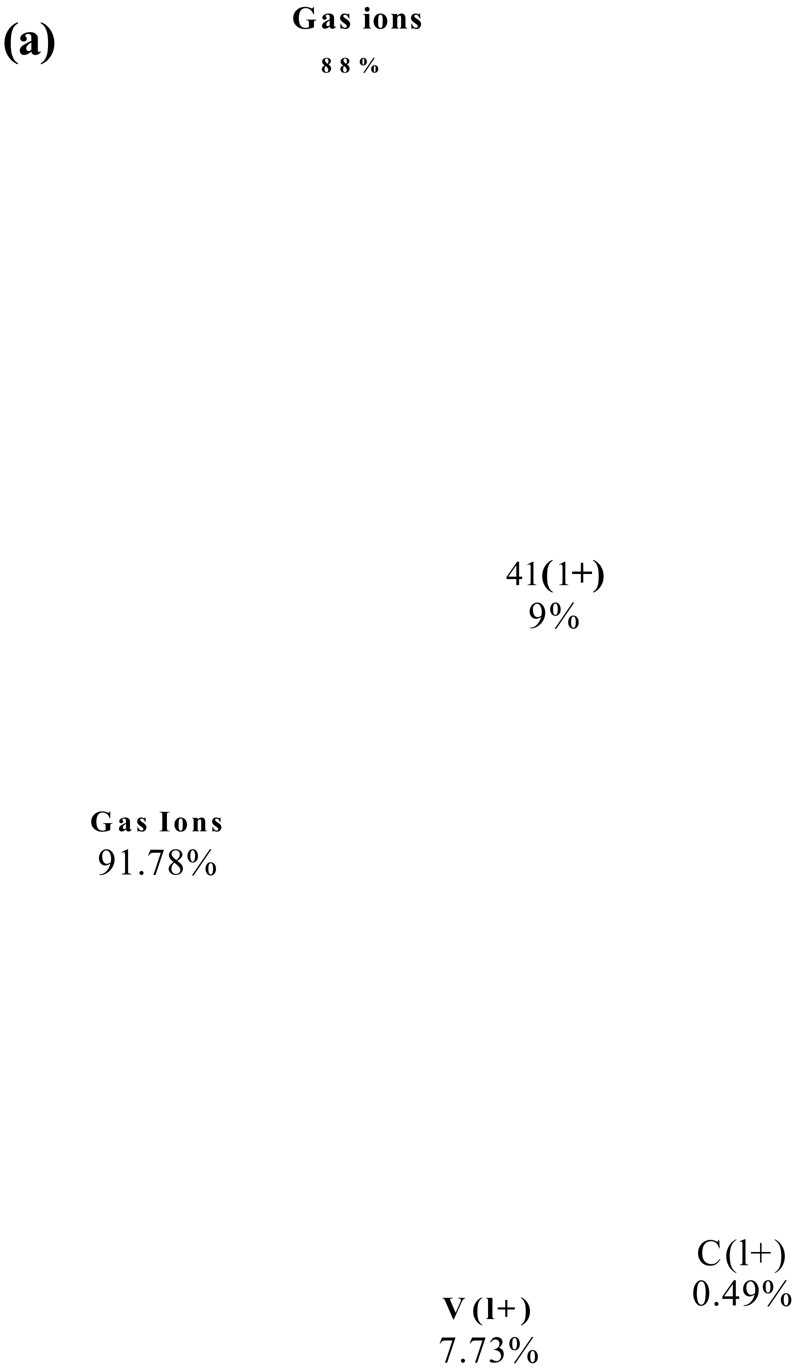

Figure 4.6 Pie chart explaining the ionic content of HIPIMS plasma during the deposition of (a) TiAlCN (b) VCN coating.

4.2 Mechanical and tribological properties

Table 4.1 summarises the mechanical and the tribological properties of nanoscale TiAlCN/VCN coatings deposited by three methods. The values measured for micro hardness ($HK_{0.025}$), adhesion (Lc), and surface roughness (Ra) were marginally differed. Whereas the remarkable difference can be seen in values of COF (μ) at room temperature and wear behaviour of the coating analysed for wear track generated at room temperature. The COF and wear coefficient results can be correlated which will be discussed in the discussion section. But it is very important to notice that the wear coefficient of UBM deposited coating has shown about two order of magnitude higher value than the coating deposited with HIPIMS-UBM and pure HIPIMS. Also the nano hardness value was observed to be lower for pure HIPIMS deposited coating than other two deposition techniques.

This clearly indicates the influence of high energy bombardment effect during the growth of TiAlCN/VCN coating when HIPIMS was utilized in combination with UBM and pure HIPIMS alone as a separate process. Table 4.2 summarises the tribological properties for TiAlCN/VCN coating at elevated temperatures of 200 °C, 450 °C and 650 °C.

Nanoscale TiAlCN/VCN Coating	Micro hardness, $HK_{0.025}$	Adhesion Lc (N)	Surface roughness, Ra (μm)	Nano-Hardness (GPa)	Coeff.of Friction (μ)	Sliding Wear coeff. ($m^3N^{-1}m^{-1}$)
UBM	2900	57	0.026	29	≈0.68	$4.2x10^{-15}$
HIPIMS-UBM	3000	57	0.023	25	≈0.45	$1.4x10^{-17}$
HIPIMS	2900	58	0.022	13	≈0.45	4.4×10^{-16}

Table 4.1. Summary of the mechanical and tribological properties of TiAlCN/VCN coating at room temperature.

In contrast, the elevated temperature tribological performance was marginally differing with respect the COF and wear coefficient values are concerned. High temperature pin-on-disc tests have shown (next section) that the COF of HIPIMS-deposited TiAlCN/VCN initially increases to $\mu = 0.8$ at 200 ^oC and then decreases to $\mu = 0.45$ at 650 ^oC. HIPIMS deposited TiAlCN/VCN show superior performance at elevated temperatures of 650 oC, (Kc = 1.0×10^{-13} $m^3N^{-1}m^{-1}$) over the UBM deposited (Kc = 5.8×10^{-13} $m^3N^{-1}m^{-1}$).

The reason behind individual coating performance at elevated temperature is believed to be the combined influence of tribo –oxidation (at the asperity contacts) and external oxidation which will be discussed in detail later in the discussion section.

Temperature (^oC)		**TiAlCN/VCN**		
		200	**450**	**650**
Coeff.of Friction (μ)	UBM	0.71	0.5	0.47
	H-U	0.7	0.5	0.45
	HIPIMS	0.8	0.5	0.4
Sliding Wear coeff. ($m^3N^{-1}m^{-1}$)	UBM	9.32×10^{-14}	1.1×10^{-13}	5.3×10^{-13}
	H-U	8.84×10^{-14}	9×10^{-14}	1.1×10^{-13}
	HIPIMS	1.96×10^{-14}	4.86×10^{-14}	1×10^{-13}

Table 4.2. Summary of the tribological properties of TiAlCN/VCN at elevated temperatures.

4.2.1 Adhesion scratch and Rockwell-C indentation test

The adhesion of TiAlCN/VCN coating deposited by all the three methods were measured using scratch adhesion and Rockwell-C indentation tests, which were evaluated by the critical load and categorized by the indentation grades (HF1-HF6) respectively. Figure 4.7 shows the optical images of the scratch (arrow indicates the direction of the scratch) and the Rockwell-C indent for TiAlCN/VCN coating deposited by all three methods. The coatings deposited for HIPIMS-UBM and HIPIMS have shown HF 1 and HF 4 grade for Rockwell-C indentation test respectively, whereas UBM deposited coating was appeared to be fallen under grade HF3 which are within acceptable standards of gradings. The critical load was increased from 5 N to 60 N for all coatings deposited by three methods. Irrespective of the deposition type, high but similar critical load values in scratch adhesion tests of Lc > 50 N were obtained for all the three cases of deposition. But significant difference in the images can be seen after 57 N load, where UBM deposited coating (fig. 4.7a) has shown some micro flaking and substrate under the coating was clearly exposed out. Where in later two cases (fig. 4.7b and 4.7c) coating was still adherent to the substrate even after exceeding the critical load limit to more than 60 N. The microhardness was in a range of $HK_{0.025}$ ~ 2900 - 3000, marginally different with higher values measured for the (HIPIMS-UBM) case. The surface roughness values were in the range of Ra = 0.022- 0.026, where slightly lower value for HIPIMS-UBM and HIPIMS deposited coating was measured than UBM deposited coating.

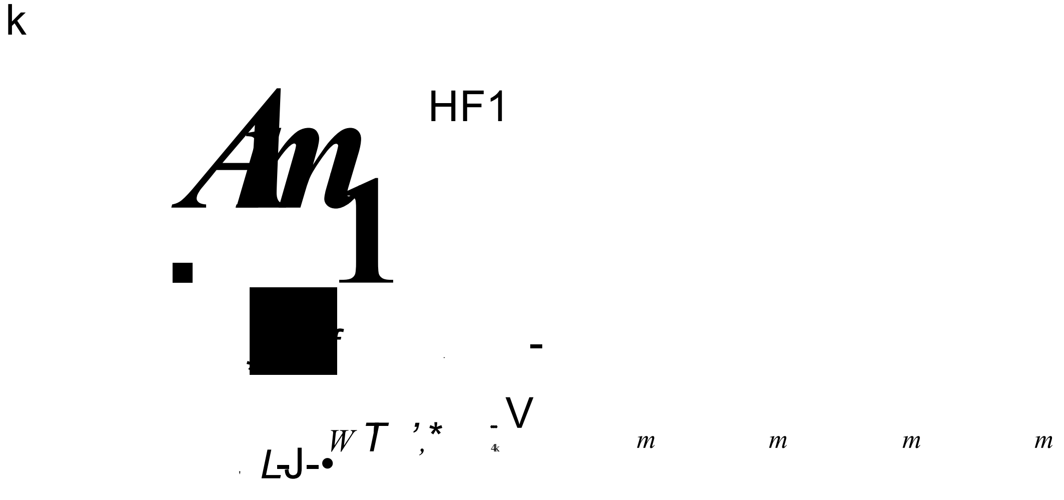

(a)

(C)

Figure 4.7 Optical images of Rockwell-C indentation and scratch adhesion test performed on TiAlCN/VCN coating deposited by (a) UBM (b) HIPIMS-UBM and (c) pure HIPIMS

4.2.2 Tribological test

Tribological tests were carried out to understand the friction and wear behaviour during the dry sliding conditions of the nanoscale TiAlCN/VCN coating against Al_2O_3 ball counterpart. The tests were conducted using pin-on-disc geometry tribometer capable to operate at both room and elevated temperatures as described in chapter 3. A comparative approach was taken by measuring the properties for TiAlCN/VCN coating deposited by three different methods.

(a) Friction behaviour of coating at room temperature

Room temperature friction behaviour of the coating is shown in Figure 4.8. The coating deposited by HIPIMS-UBM and pure HIPIMS technique shows lowest COF of $\mu \approx 0.45$, than COF of $\mu = 0.68$ has been measured for UBM deposited TiALCN/VCN coating. Instantaneous increase in the friction COF has been observed in all cases immediately after the run in period of sliding in the range of about 0 to 500 laps. Later the friction curve appeared to be stabilized which is called "steady state" zone. But the careful observation of "run in" stage of friction curve obtained for pure HIPIMS deposited coating (red colour), appeared to be very smooth than other friction curves obtained for UBM (black colour) and HIPIMS-UBM (purple colour). The room temperature friction curve for pure HIPIMS deposited coating is separately shown in Figure 4.9. The curve depicts clear slope of "run in" stage and beginning of the "steady state" of the dry sliding process. Through this curve one can clearly distinguish between two friction zones and possible contribution from that particular sliding zone of the coating against the counterpart (Al_2O_3 in this case). Immediately after the "run in" stage the friction curve changes its slope indicating the beginning of the first lower coefficient of friction zone where the mean value of μ=0.37. After that the friction gradually increases to reach a "steady state" where higher coefficient of friction values (μ=0.48) were recorded.

In an attempt to explain "depth profile" the friction behaviour of the HIPIMS deposited TiAlCN/VCN coatings a number of friction tests were carried out with stepwise increase of the sliding distance by changing the number of the sliding laps from 500 to 10000 with an increment of 1000 laps. In this attempt, the friction value of μ=0.37 was measured for initial 1000 laps and slightly higher COF of μ=0.48 was measured for larger sliding distances (or laps). Similarly after “depth profiling” by sliding, wear behaviour of the coating was also analysed which is discussed in the next section of this chapter.

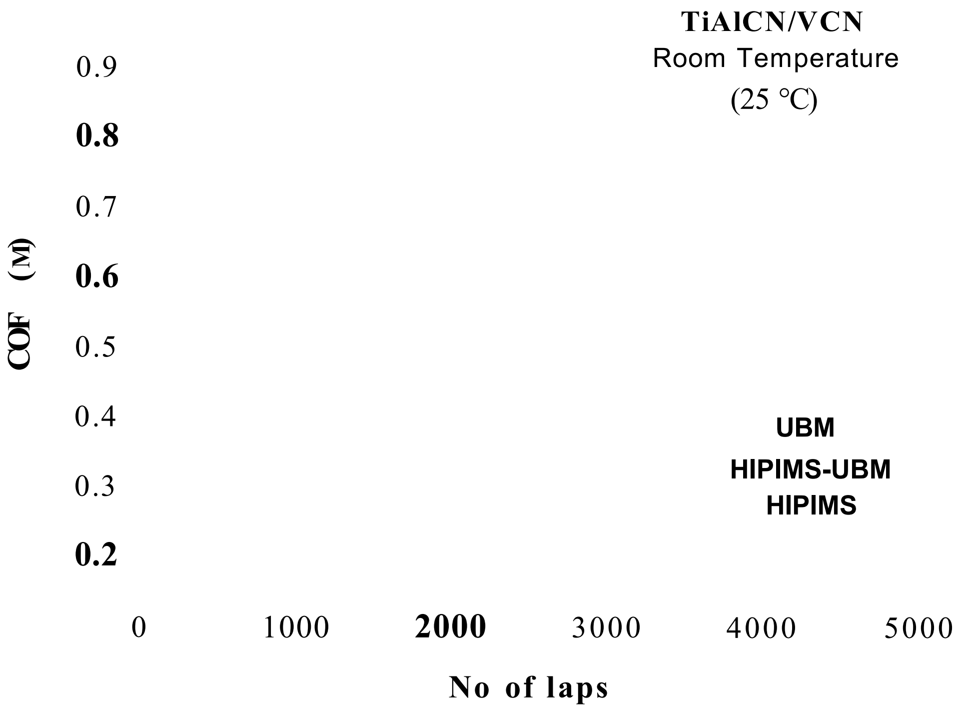

Figure 4.8 Room temperature friction curves against the number of laps for TiAlCN/VCN coating, deposited by UBM, HIPIMS-UBM, and HIPIMS.

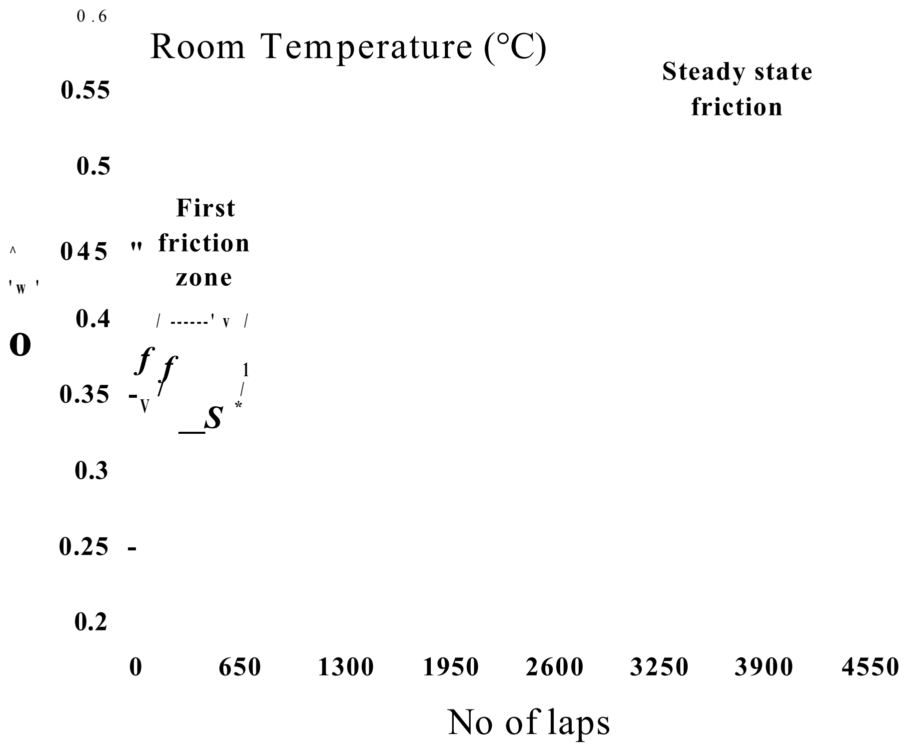

Figure 4.9 Coefficient of friction curves (p), versus number of laps for reactive HIPIMS deposited TiAlCN/VCN coating: a) - room temperature test.

(b) Friction behaviour at elevated temperature

Figure 4.10 shows the coefficient of friction (p) vs number of laps curve for TiAlCN/VCN coating during sliding and elevated temperatures of 200°C, 450°C, and 650°C at 20% humid atmospheric condition. The coatings deposited by all the three methods have shown almost similar trends and nearly equal COF friction values at above mentioned temperatures. Increase of the test temperature to 200°C resulted in increase of the coefficient of friction to p=0.8. Subsequently at 450°C and 650°C, a gradual decrease in the friction coefficient value to p=0.5 and p=0.45 was observed whereas the wear rate was negligibly increased which will be discussed next section.

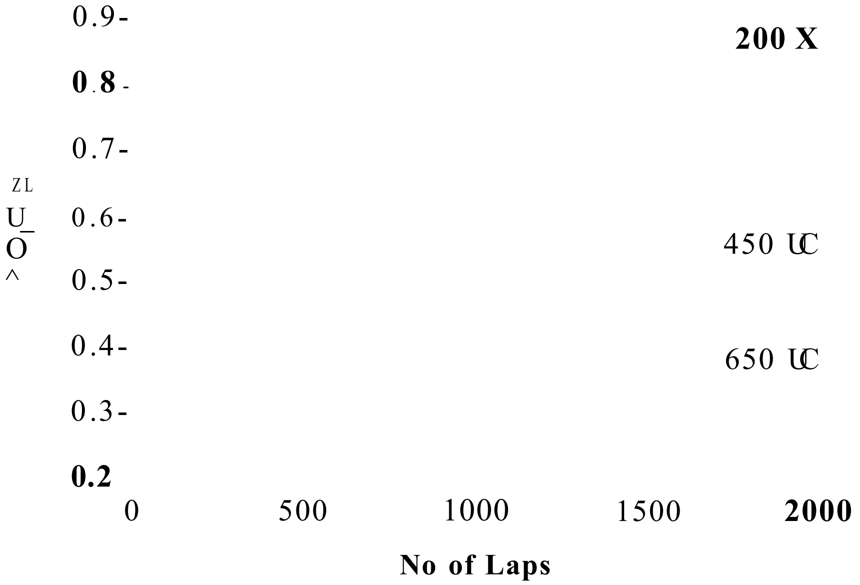

Figure 4.10 Coefficient of friction curves for TiAlCN/VCN coating during sliding for room and elevated temperatures of 200°C, 450°C, and 650°C.

(C) Sliding wear behaviour of the coating at room and elevated temperatures

The wear behaviour of the coating at room and elevated temperatures were evaluated by calculating their sliding wear coefficients using Archard’s equation as explained in chapter 3. The wear coefficients values measured for wear tracks generated on TiAlCN/VCN coated disc at room temperature are given in table 4.1. The respective wear track depths profile images are shown figure 4.11 below. The wear track depths were measured to be about ~ 2.3 pm, 0.7 pm and 1.8 pm respectively for UBM, HIPIMS-UBM and pure HIPIMS deposited TiAlCN/VCN coating. The approximate correlation between the COF and wear coefficient (Kc) can be clearly noticed as UBM deposited coating has shown higher COF with p = 0.68 with corresponding wear rate of Kc = 4.2x10'15m ^N 'W and higher depth of wear track. In the case of HIPIMS-UBM and pure HIPIMS deposited coating, wear track depth was comparatively less than UBM deposited coating with respective measured wear rate of Kc = 1.4x10 17 and 4.4 x 10'16 m 'W 1.

For UBM deposited TiAlCN/VCN coating, the increase of the dry sliding test temperature to 200°C resulted in the increase of wear coefficient to about 9.32x1 0"14 m3N’Im'1 from wear coefficient measured at room temperature. Subsequently at 450°C and 650°C, wear rate was negligibly increased to single order of 1.1x1O'13 -to- 5.3x10"13 rn^N'W 1 respectively.

In the case of HIPIMS-UBM deposited coating, wear rate coefficient was negligibly lower (8.84 x1O'14m V ’m'1) at 200 °C compared to UBM deposited coating. Further at 450 °C and 650 °C, though sliding wear was slightly higher (9 x1O'14m3N'*m' 1 and 1.1 x1O'14 m^N'W 1 respectively) when compared to UBM, value was lower by factor of 2 and 5 respectively. Finally, for pure HIPIMS deposited TiAlCN/VCN coating, the superior wear performance was observed (Table 4.1) over the UBM deposited ones tested at all temperatures.

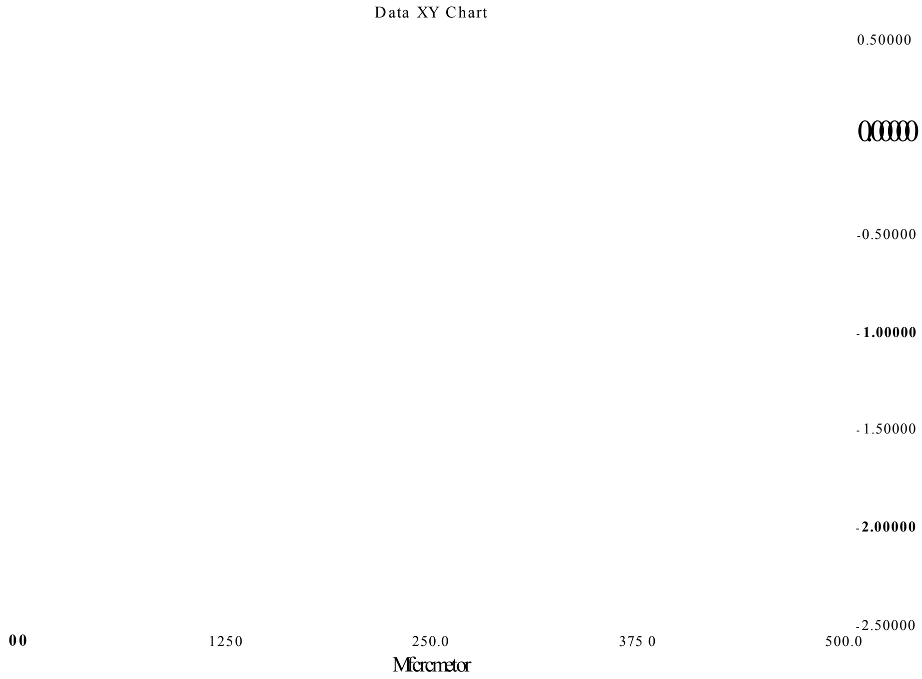

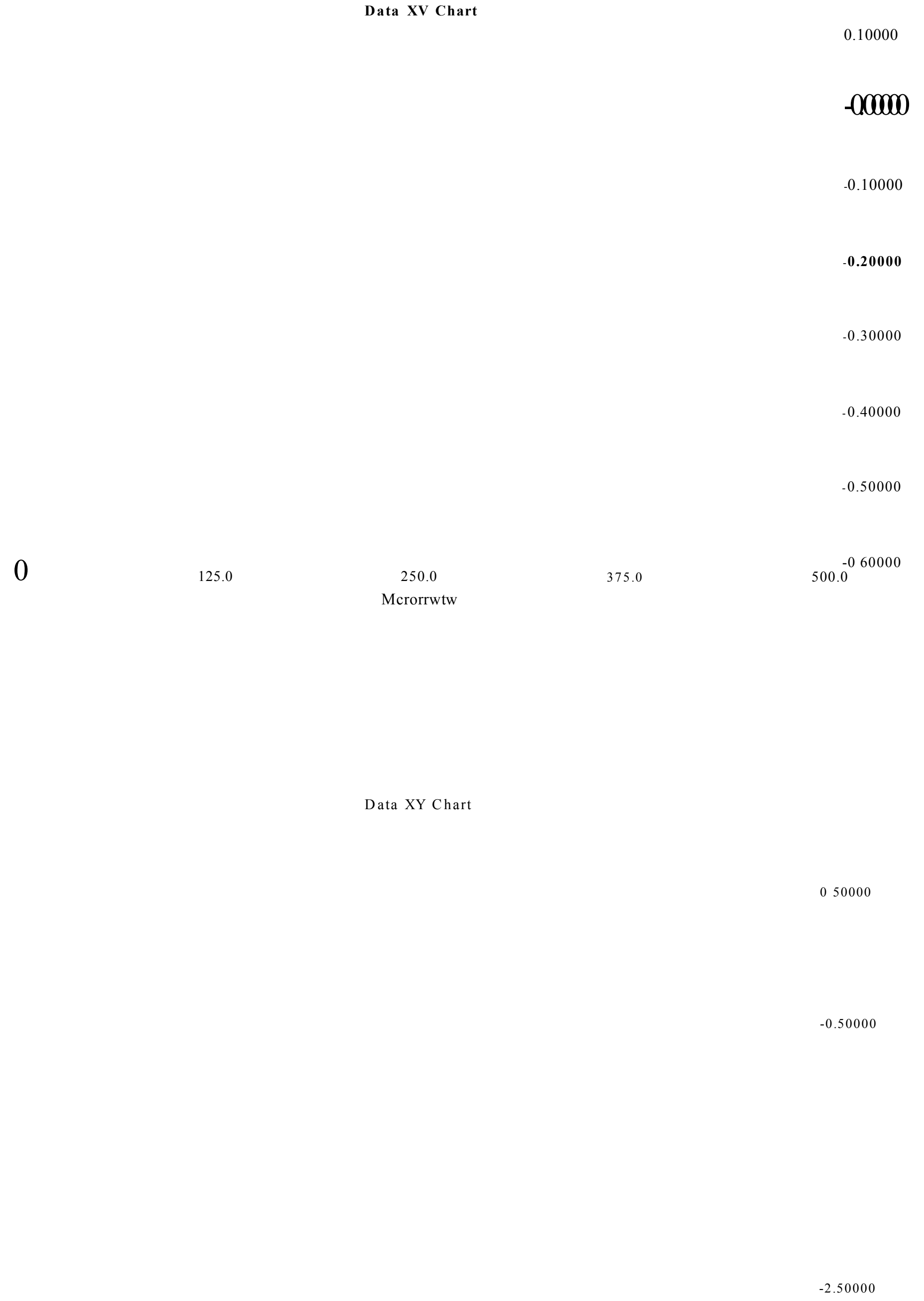

Figure 4.11 The wear track depth profile generated at room temperature for (a) UBM (b) HIPIMS-UBM and (c) pure HIPIMS deposited TiAlCN/VCN coating.

4.2.3 Nanohardness measurements

Nanohardness measurements were carried out to know the plastic response of TiAlCN/VCN coating from within 10% of its total thickness from top. Tests were conducted on all the coatings deposited by UBM, HIPIMS-UBM and pure HIPIMS technique. Plastic hardness values are given in table 4.1. Berkovich diamond indentor was released on the coated disc, by gradually increasing the normal load from 0 mN to maximum up to 20 mN. Figure 4.12 shows the maximum depth that indenter was released against the max normal load applied for TiAlCN/VCN coating deposited by all three techniques. The plastic hardness of HP = 13 GPa measured for coating deposited by pure HIPIMS technique was significantly lower compared to UBM and HIPIMS-UBM deposited coatings, i.e., 27 GPa and 30 GPa respectively. Moreover, the maximum indentation depth for pure HIPIMS deposited coating was more to about 350 nm under similar test conditions as explained above.

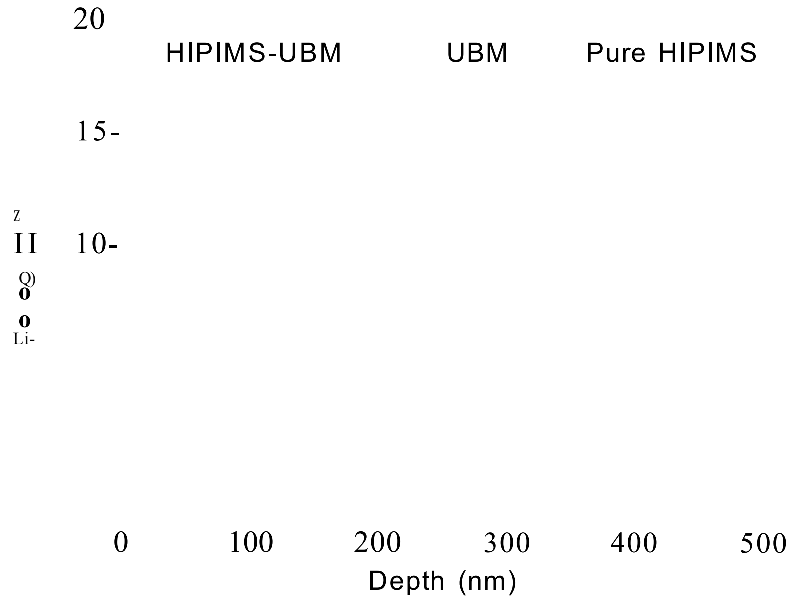

Figure 4.12 Nano-indentation curves showing normal force versus depth of indentation for TiAlCN/VCN coating deposited by UBM, HIPIMS-UBM and pure HIPIMS technique.

4.3 Structure and microstructure analysis

4.3.1 X-ray diffraction studies

4.3.1a Low angle XRD analysis

Low angle XRD spectrum was taken on TiAlCN/VCN coating deposited by all three techniques in order to confirm the multilayer structure. Figure 4.13 shows low angle XRD spectrum for coating deposited by UBM and HIPIMS-UBM, since it was difficult to detect the low angle reflections for pure HIPIMS deposited coating. Hence glancing angle XRD spectra was taken and structure of coating was analysed for coating deposited by pure HIPIMS technique, which will be discussed in coming paragraph 4.3.1c. Low angle XRD analysis unambiguously showed the nanoscale multilayered structure of the films by detecting the reflections at 20= 2.3° and 3.4° respectively for UBM and HIPIMS-UBM deposited coating. This pattern was used to calculate the bi-layer period (A) which was found to be 2.2 nm.

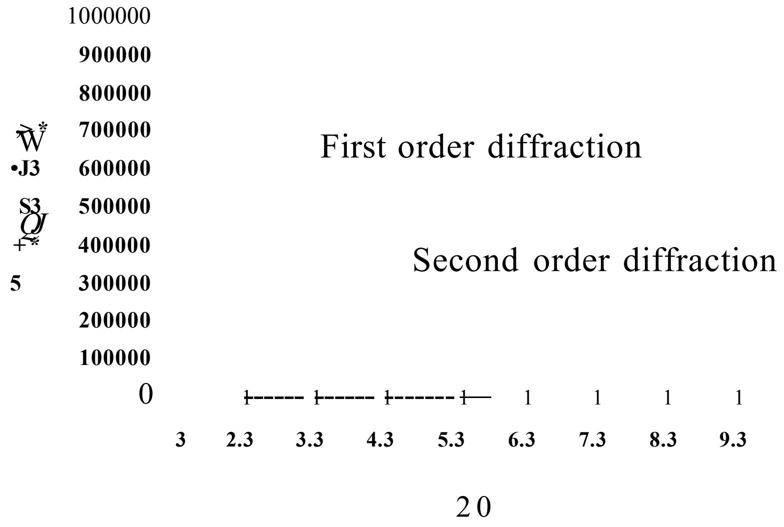

Figure 4.13 Low angle X-ray diffraction pattern reflecting the nanolayered structure of TiAlCN/VCN multilayer coating deposited by UBM and HIPIMS-UBM technique.

4.3.1b Brag’s Brentano XRD analysis

The average microstructure was determined using X-ray diffraction. The 0-20 XRD measurements using Philips X'pert MPD automated diffractometer and Cu Ka-radiation revealed the preferred orientation of TiAlCN/VCN coating. Figure 4.14 shows the 0-20 XRD measurements. The diffraction peaks have clearly exhibited single-phase NaCl FCC unit cell structure with a {111} and {220} preferred orientation. Also, planes oriented towards {200} direction overlapped with substrate peak was also observed.

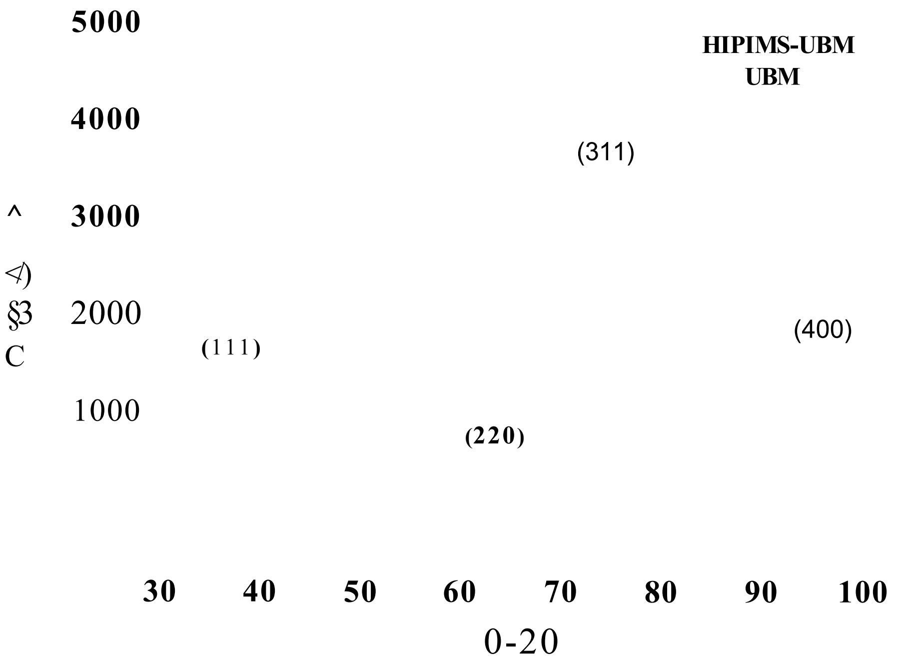

Figure 4.14 shows the 0-20 XRD diffraction pattern for TiAlCN/VCN multilayer structure.

4.3.1c Glancing angle XRD analysis

Glancing angle parallel beam geometry was used to determine the phase composition and structure of the coating as a function of the penetration depth using a Panalytical X'Pert automated diffractometer. In glancing angle geometry the penetration depth is defined as the distance, *xe* from the surface that the diffracting planes in the specimen contribute to the whole diffracted intensity by the ratio *Me* and can be calculated by the equation as explained in the chapter 3 section 3.5.1. The GA measurements were performed at incidence angles of 1°, 2°, 5° and 10°, respectively. The diffraction patterns are shown in Figure 4.15. The data for the calculations of TiAlCN/VCN is summarised in Table 4.3 and the results are presented in Table 4.4. The depths of penetration which were averaged between 20 values of 20-110° and assuming intensity attenuation *Me* were as follows: 0.360 pm, 0.720 pm, 1.798 pm and 3.583 pm at the incidence angles used (Table 4.4). The structure was found to be single phase *fee* structure (NaCl) and resolving individual reflections from the TiAlCN and VCN phases was not possible. Depending on the incidence angle the shape of the diffraction peaks changes from broader and lower intensity peaks at small angles, (1°, 2°) to sharper and higher intensity peaks as well as additional reflection from {311} and {222} plains at 5° and 10°. This is confirmed by the FWHM measurements where for the (111) reflection the values change from 2.77° at 1° to 1.55° at 10°.

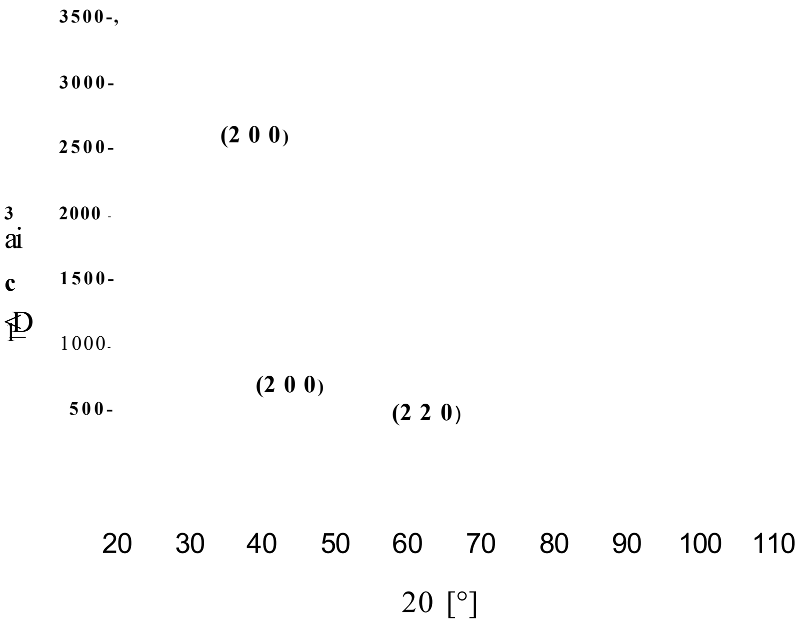

Figure 4.15 GAX-ray diffraction patterns taken at various incidence angles.

	TiAlCN/VCN	**Ti**	**Al**	**V**	**C_2**	**N_2**
Weight (amu)	178	48	27	51	24	28
Weight concentration, C_W (%)		26.97	15.17	28.65	13.48	15.73
μ/ρ at E = 8 keV		202	50	221.7	4.576	7.142
ρ (gcm^{-3})		4.51	2.7	5.96	3.51	1.17×10^{-3}
$C_W\ \mu/\rho$	127.3	54.47	7.58	63.52	0.62	1.12
$C_W\rho$	3.81	1.22	0.409	1.71	0.473	1.83×10^{-4}

Table 4.3 Physical parameters for individual elements and calculated values for TiAlCN/VCN used to evaluate x-ray absorption depth.

angle	**depth, x_e (μm):**
1	0.360
2	0.720
5	1.798
10	3.583

Table 4.4 X-ray absorption depth for TiAlCN/VCN as a function of angle of incidence

4.3.2 Raman Spectroscopy analysis

The Raman spectra were collected from the surface of as-deposited TiAlCN/VCN coatings deposited by UBM, HIPIMS-UBM and pure HIPIMS techqnique. The spectra were shown in figure 4.16. The spectra were collected in the range of 1000 cm^{-1} - 2000 cm^{-1}. In all three cases, the spectra have shown two important Raman features: broad bands around ~1380 cm^{-1} and ~1580 cm^{-1} which are designated to D (disorder) and G (graphitic) peaks respectively. The spectrum obtained was deconvoluted (fig 4.13) with a Lorentzian shape and ID/IG ratio was calculated to find out the sp_2/sp_3 contents of the film. The D peak position of 1379 cm^{-1} and G peak position of 1582 cm^{-1} have found to be down shifted to 1367 cm^{-1} and 1578 cm^{-1}, respectively, when measured for HIPIMS-UBM deposited coating. When compared to Raman spectra obtained for pure HIPIMS deposited coating, the G peak is slightly shifted to higher value of 1381 cm^{-1} and down shifted to 1575 cm^{-1}, respectively. The ID/IG value measured to about ~ 0.93 in case of UBM deposited coating, which is found to increase to about ~ 1.08 and ~ 1.64 respectively for HIPIMS-UBM and pure HIPIMS deposited coating.

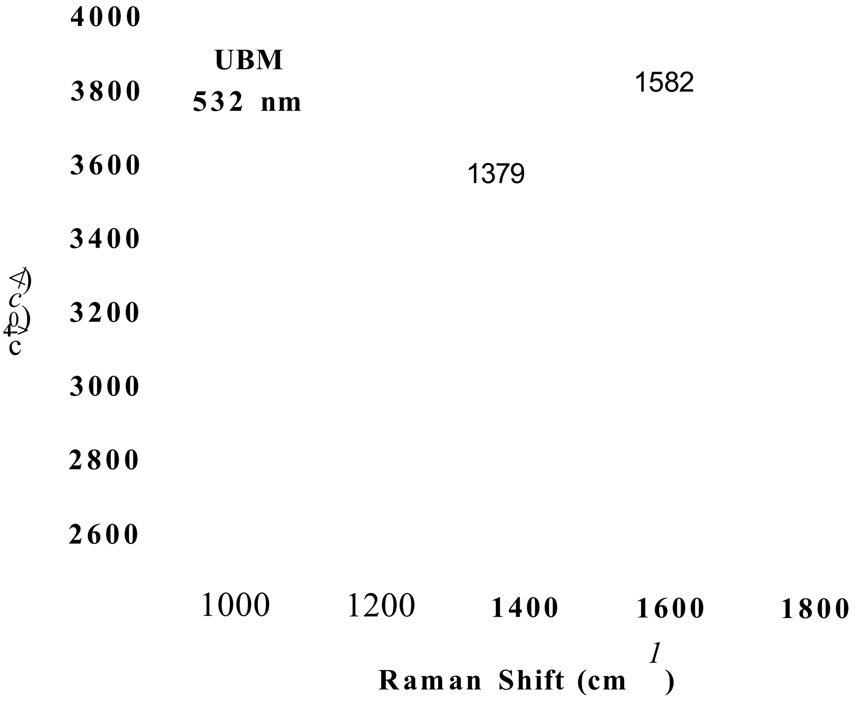

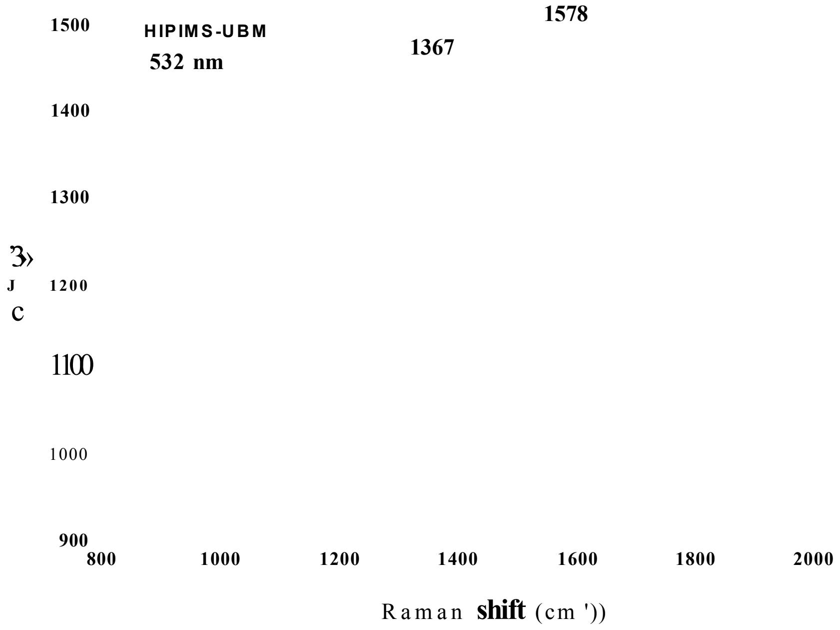

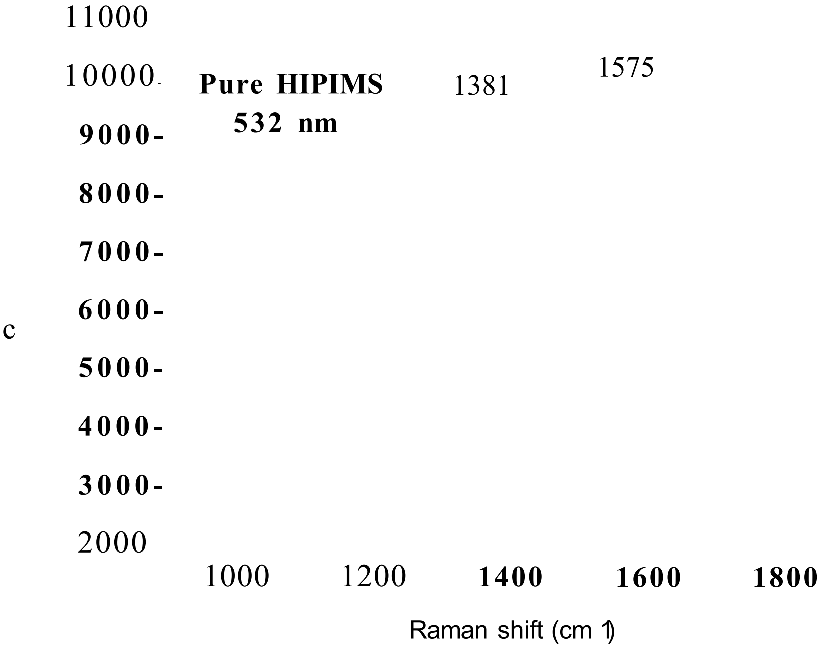

Figure 4.16 Raman spectra of as deposited TiAlCN/VCN coating by UBM, HIPIMS/UBM and pure HIPIMS technique showing the D and G bands.

4.4 Microstructural analysis

4.4.1 Scanning electron microscope analysis

The microstructure of TiAlCN/VCN films was studied by cross section SEM and TEM analyses. The coatings were deposited on Si wafers, which provide a better substrate for cross-section SEM samples and stainless steel coupons for the TEM studies. Figure 4.17 shows cross sectional SEM image of TiAlCN/VCN multilayer structure deposited by UBM and HIPIMS-UBM. Figure 4.17a image depicts open, broken-rock like coarse columnar structure. Most of the columns are terminated with horizontal terraces, which indicate relatively weak interface bonding between the individual layers of the nanolaminated material. In contrast a very dense almost glassy cross section is observed for the HIPIMS/ (HIPIMS-UBM) deposited coatings, Fig 4.17b. Further, clear contrast can be seen between the base layer and coating region without any horizontal terrace like fracture sites coating part which was observed in like UBM deposited coating 4.17a.

Similar cross-sectional studies have been carried out for TiAlCN/VCN coating deposited by pure HIPIMS technique. Figure 4.18(a) shows the fractured cross-sectional SEM micrograph of TiAlCN/VCN coating deposited on silicon wafer using pure HIPIMS technology. The micrograph reveals the columnar structure of the coating with three distinctive zones. The adjacent to the substrate first zone is the carbon free (TiAlN) base layer which shows highly dense small diameter (~60 nm) columns terminated with flat tops. This is followed by a narrow dark band (~250 nm) where no structural features can be observed under SEM, second zone. The third zone represents the bulk of the coating consisting larger diameter (~180 nm) columns. The columns are slightly wider on the top but no structural features associated with competitive growth mechanism can be clearly observed. Interestingly the columns have a peculiar granular (cauliflower like) structure which can be clearly seen on the micrograph taken at higher magnification, Figure 4.18(b). The major difference in the cross section structures between pure HIPIMS, UBM and HIPIMS-UBM deposited coating is the absence of the zone two (featureless dark band) for the coating produced by the UBM and HIPIMS-UBM process.

TiAICN/VCN coating

JHUfrfC

f

Base Layer regiorr ** **%**

Substrate

(a)

spot mode WD mag HV det 1 pm ■
' 3 0 SE 5 0 mm 69 363 x 5 00 kV TLD

coating

Base layer region

Substrate

m>3 spot HV moo# <J*t '.VO
50 000. 4Q 1?0Qny SE TLQ 5 9 mm

Figure 4.17 SEM cross-section of as-deposited TiAICN/VCN multilayer coating a) HIPIMS/UBM deposited b) HDPIMS/(HIPIMS-UBM) deposited.

TiAIN Base Layer

Substrate

spot model WD mag HV | det
3 0 SE 5.2 mm 67 252 x 5 00 kV TLD

Dense columns with
closely packed grain like structure

spot 1mode WD mag HV det
2.5 [SE '5.1 mm 208 868 x | 5.00 kV | TLD

------------ 500nm -------------
TiAICN/VCN Pure HIPIMS

Figure 4.18 SEM cross-sectional view of TiAICN/VCN nanoscale coating deposited by reactive pure HIPIMS deposition (a) lower magnification coating cross-section (b) higher magnification coating cross-section.

4.4.2 Transmission electron microscope analysis

Figures 4.19a and 4.19b depict low magnification bright-field images of TEM cross-sections of TiAICN/VCN multilayer coating deposited by HIPIMS/UBM and HIPIMS/(HIP1MS-UBM) techniques respectively. The structure of all important coating zones such as interface, base layer the bulk of the coating and the top surface of the coating has been clearly revealed. The coating -substrate interface appears very sharp and clean, no contamination or amorphous layers can be observed.

Significant structure differences however can be seen in the base layer as well as in the bulk of the coating depending on the deposition technique used. For the UBM deposited coatings (Fig 4.19a) a coarse columnar structure can be observed. The top of the columns in both base layer and coating are dome shaped which is typical for coatings grown in conditions of low energy ion bombardment. The structure is under-dense and many inter-columnar voids can be observed, indicated by arrows in the figure. The voids in some cases start right from the interface and continue through the base layer and bulk of the coating.

Coating

i-----------1
200 nm

Fig. 4.19 Cross-sectional TEM micrographs of a) HIPIMS/UBM, showing open columnar boundaries and b) HIPIMS/ (HIPIMS-UBM),

Further, cross-sectional TEM imaging has been revealed to understand the detailed fine structure of the HIPIMS deposited TiAICN/VCN coating which has shown significantly different morphological structure in SEM (in Fig. 4.18). Figure 4.20a is a low magnification BF image, which shows the structure of the main coating areas such as TiAIN base layer followed by uniform gray contrast narrow band, followed by area with columnar structure where the column boundaries are decorated with a white phase of a light atomic weight element. The location of the narrow grey contrast band adjacent to the base layer corresponds to the zone two of the SEM cross section, see Figure 4.18a. Higher magnifications revealed further details of the coatings architecture, Figure 4.20b. A nanoscale multilayer structure with bi-layer thickness of 5-8nm and total thickness of 30nm can be observed right above the TiAIN base layer. This is believed to correspond to zone two of the cross section SEM and the grey contrast band in the low magnification TEM image, Figure 4.20a. Careful observation reveals a white lateral phase segregated at the interfaces of the individual layers.

The structure which evolves further with coating growth is one of a typical nanocomposite consisting of dark contrast grains (most probably Me-CN where Me is Ti-Al-V) surrounded by carbon-based phase forming a white contrast tissue phase. The largest grains with diameter in the range of 5-10 nm are formed right after the band with nanoscale multilayer structure. Figure 4.21 is a High Resolution TEM micrograph showing the nanocrystalline grains and the surrounding tissue phase structure. The grain size reduces gradually with thickness at the expense of the white phase and no grains can be seen on the very top region of the coating.

(a)

Coating

Base Layer

Substrate **0.5 jim**

Figure 4.20 BF TEM cross-section of TiAlCN/VCN nanoscale coating deposited by reactive HIPIMS deposition (a) lower magnification coating cross-section (b) higher magnification coating cross-section.

Figure 4.21 HRTEM micrograph of the zone with nancomposite structure of TiAlCN/VCN.

4.4.3 Electron diffraction X-ray Analysis (SAED)

In order to further confirm the XTEM results such as X-ray amorphous and nanocomposite zone of the TiAlCN/VCN coating, point EDX analyses were carried out in different zones of the coating namely base layer and nanoscale multilayer, bulk of the coating and top of the coating. Figure 4.22 a, b, c. The analyses shi transformation in the structure with thickness of the coating takes p crystalline at the base to nanocrystalline in the bulk and finally randc grain nanocrystalline to almost X-ray amorphous structure on the top

O)

t '

5 1/nm

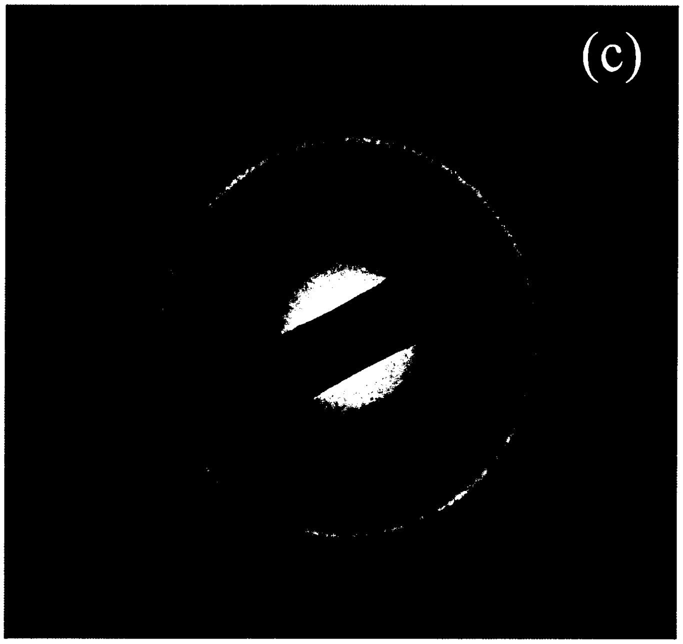

Figure 4.22 SAED patterns taken from various coating zones: a) TiAlN base layer/ nanoscale multilayer zone, b) nancomposite zone, c) top of the coating.

4.5 Oxidation analysis

The oxidation analysis of TiAlCN/VCN coating was carried out in order to understand the stability of the microstructure of as deposited coating and phase composition of oxidised surfaces of the coating. Oxidation tests were conducted on all as-coatings deposited by all three methods, after exposing the as-deposited coating surface to extreme thermal loads at both isothermal and non-isothermal conditions. That means, the analysis was carried out in two different conditions. Initially the isothermal oxidation test was carried out by Thermogravimetric (TG) analysis as explained in chapter 3, where the onset of oxidation capacity of the coating was determined and as-formed oxide phases were identified. In another analysis, the oxide debris formed inside the wear track generated by dry sliding friction operation at both room temperature and elevated temperature was studied. These particular studies were carried out by both XRD and Raman spectroscopic technique.

4.5.1 Thermo gravimetric analysis

Figure 4.23 plots TGA oxidation rate measurements for the TiAlCN/VCN coating on stainless steel substrates, deposited by UBM, HIPIMS-UBM and pure HIPIMS methods. In these measurements a linear temperature ramp at 1°C/ min from room temperature to 1000°C was used. The experiments reveal that the oxidation process develops in two stages. The coatings deposited by all the three methods have shown similar stages of oxidation process. After an initial slow mass gain, the first small step increase in the mass can be detected at around 550°C followed by a steep mass increase at 800°C, which represents the temperature the onset of rapid oxidation, at about 800°C. It is also interesting to note that the amount of oxygen diffusing into the coating at elevated temperatures, represented by a sample weight-gain, is greater for the UBM deposited coating (curve 1) as compared to both HIPIMS-UBM (curve 2) and pure HIPIMS (curve 3) deposited coating. This can be clearly seen in Figure below where the oxidation curve of the UBM deposited coating shows about 30% more weight gain compared to that of the HIPIMS-UBM deposited coating. Further, the weight gain due to the oxidation is lower by factor of two in the case of pure HIPIMS deposited coating when compared to UBM deposited TiAlCN/VCN coating. Furthermore, compared to the UBM and HIPIMS-UBM deposited coatings, no initial oxidation at 550 ^{o}C was observed for coating deposited by pure HIPIMS technique.

4.5.2 Phase composition and microstructure of the oxide scale on TiAlCN/VCN films deposited by mixed HIPIMS-UBM techniques

Glancing angle-XRD analyses were carried out to determine the phase composition of the oxides. Figure 4.24 shows GAXRD pattern of the as-deposited and oxidised surface of TiAlCN/VCN coating deposited by mixed (HIPIMS-UBM) taken at an incident angle of 2°. The coated samples were heat-treated isothermally in the furnace of the TGA system for 15 min at 560°C, 670°C, and 750°C respectively. The temperatures were chosen on the basis of the specific regions of the T-G curve in Figure 4.23.

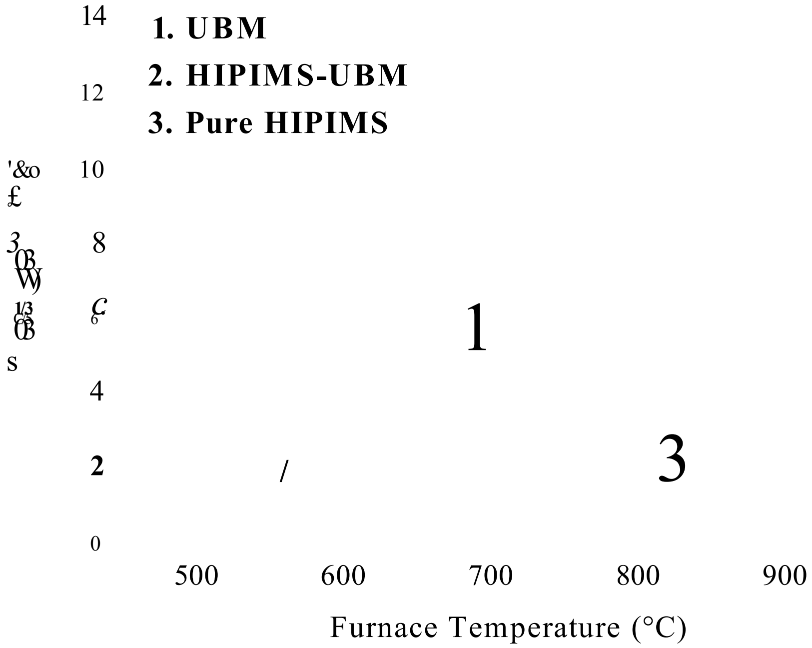

Figure 4.23 Thermo gravimetric oxidation rate measurements using linear ramp at 1 °C/min for UBM, HIPIMS-UBM and reactive HIPIMS deposited TiAICN/VCN coating.

The as-deposited coating has shown single phase Bl-NaCl structure, with strong (111), (200) and weak (220) peaks. The coating oxidised at 560°C, (immediately after the first step mass gain) show a mixture of different oxide phases of $TiC_{>2}$ (Rutile and Brookite), VCF V_2O_3, V_3O_7, V_2O_5 and $AIVO_4$. Due to peak overlap it is difficult to identify unambiguously the exact oxide phases present. The peaks from the as-deposited coating have not been detected, which may be due to the oxide thickness of the coating which cannot be penetrated by the X-rays at the selected small incident angle.

The oxidised surface of the coating after 200 °C have shown very thick layer, probably of crystalline $_{01}$-AI_2O_3, formed due to the initial reaction between the Al and oxygen molecules forming a protective layer against rapid oxidation. The figure 4.25 shows the SEM micrograph of oxidised surface of TiAICN/VCN coating after 200 °C. The EDX spectrum clearly shows the Al peak which clearly supports the fact of formation of Al-rich oxide phase at these early stages of oxidation process. This result is further confirmed through Raman analysis of wear track generated at 200 °C, which successfully identified the traces of α-Al_2O_3 phase formed due to tribo-oxidation.

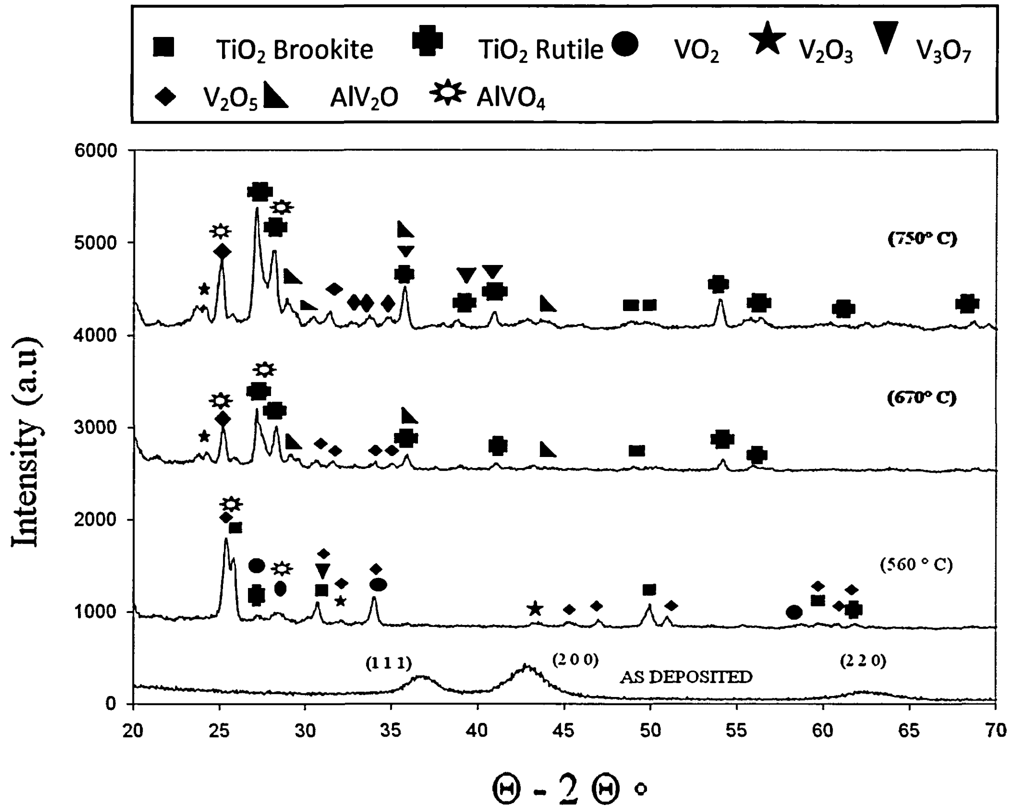

Figure 4.24 2° Glancing angle X-ray diffraction pattern of TiAlCN/VCN multilayer coating at as deposited condition and elevated temperature regions of 560°C, 670°C and 750°C.

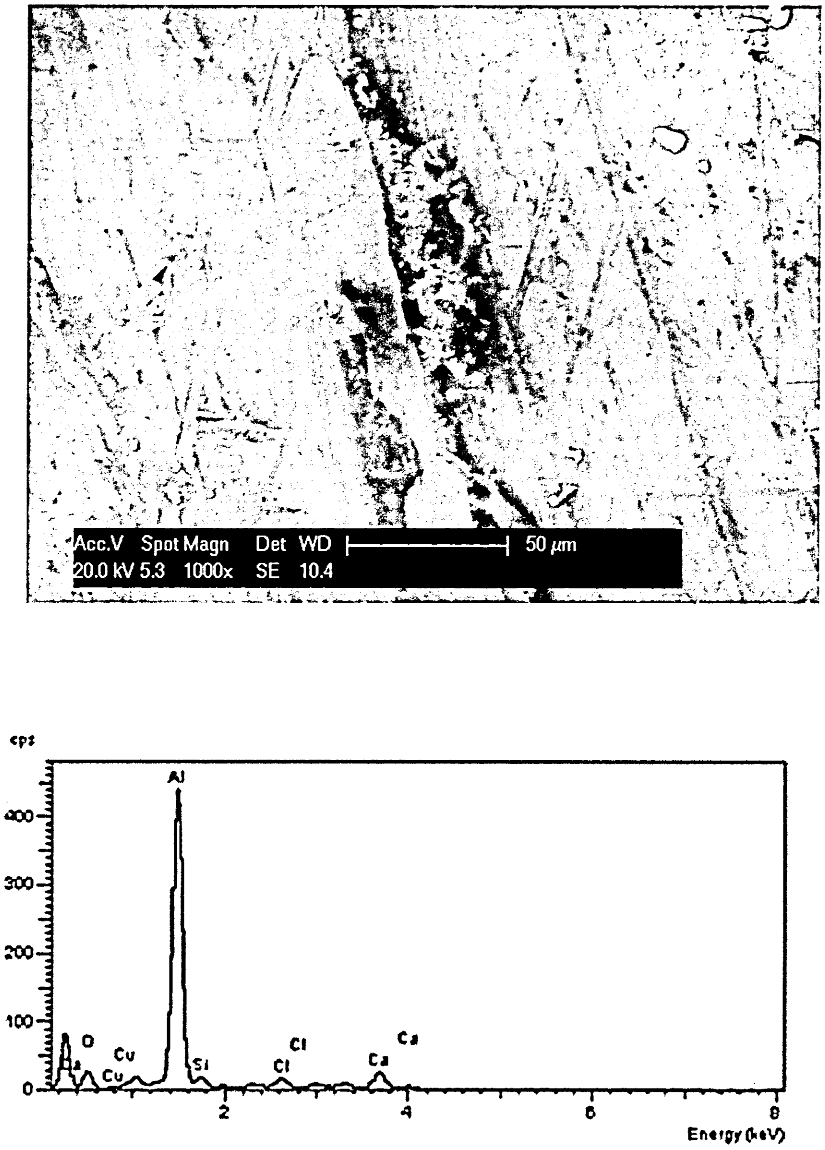

Figure 4.25 Oxidised surface morphology of TiAlCN/VCN coating below 450 °C, showing Al rich oxide phase (EDX graph).

Figure 4.26a shows the morphology of the oxide scale formed at 560°C. Two structural features can be identified, very small irregular shape oxide particles overgrown by plate-shape oxides. EDAX measurements showed that the plate-shape oxides were V- and Ti- deficient and richer in Al, which most probably indicates the $AlVO_4$ phase. Further increase of the temperature to 610°C leads to conversion of the small irregular shape oxides to oxides with fine needle-like structure, which grows around the plate-like oxides. The EDAX measurements [fig. 4.27] from the areas occupied by the needle-like oxides showed that they are richer in V. Some amount of AlV_2O phase was also detected. In summary, at 670°C the most dominant phases could be detected are V_2O_5, TiO_2 (Rutile) and $AlVO_4$ all of which classified as Magneli phases. Figure 4.26b shows the surface after 670°C, where uniform oxidation can be observed. The scale surface can be described as one with a cauliflower morphology produced by oxides, which contain more fractions of V-rich phases.

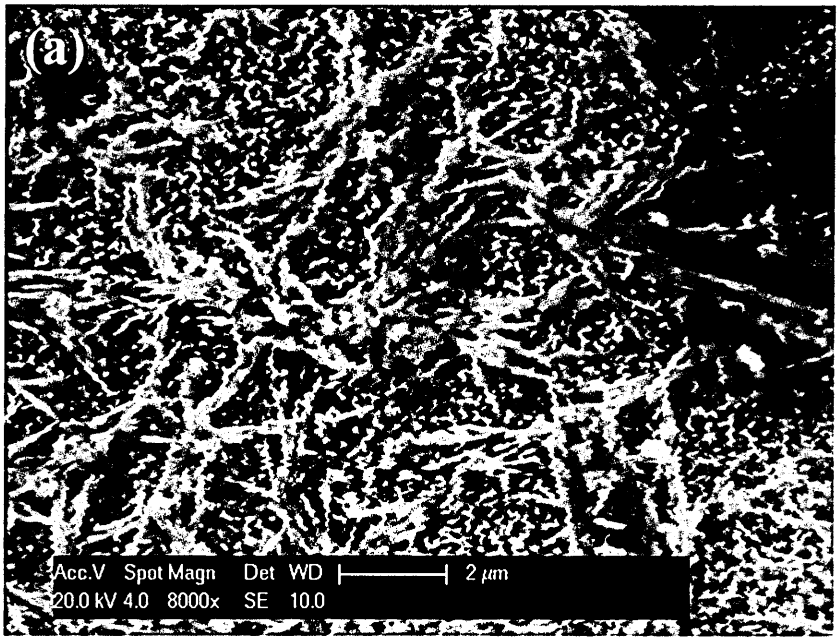

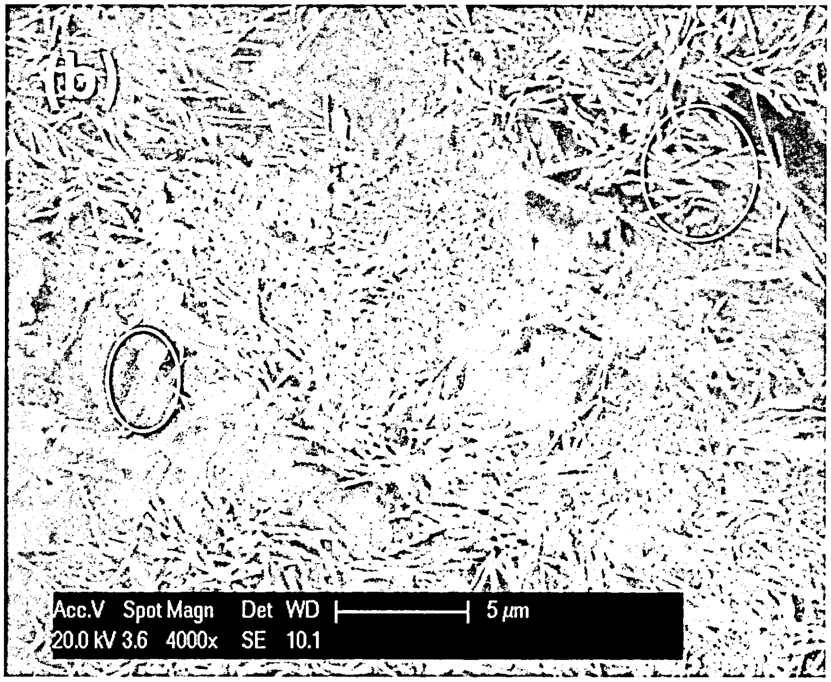

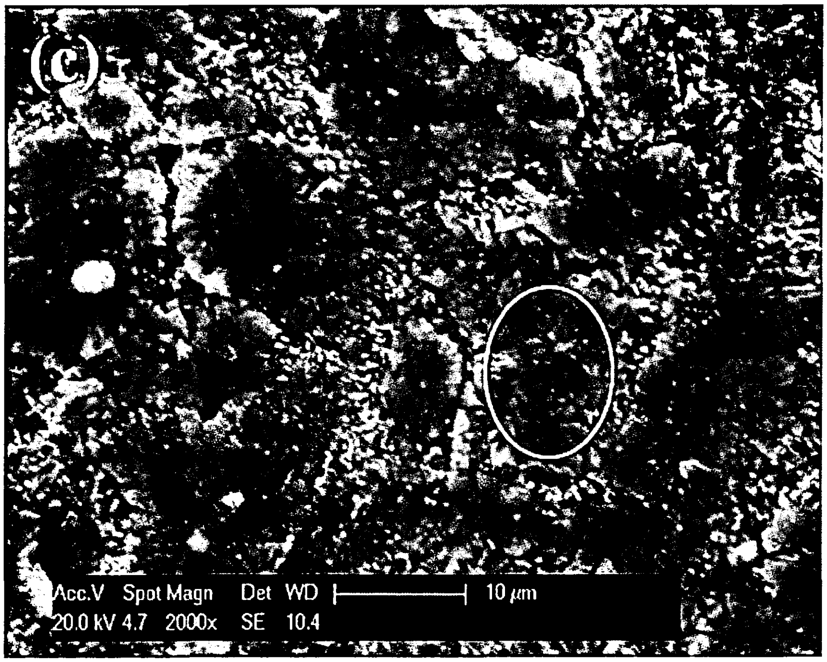

Figure 4.26 Oxide morphology of the TiAlCN/VCN coated surface after annealing at: a) 560°C, b) 610°C and c) 750°C.

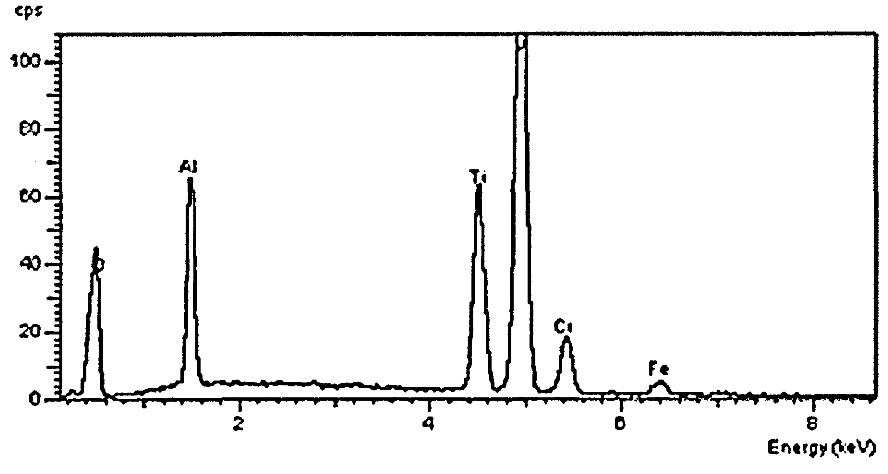

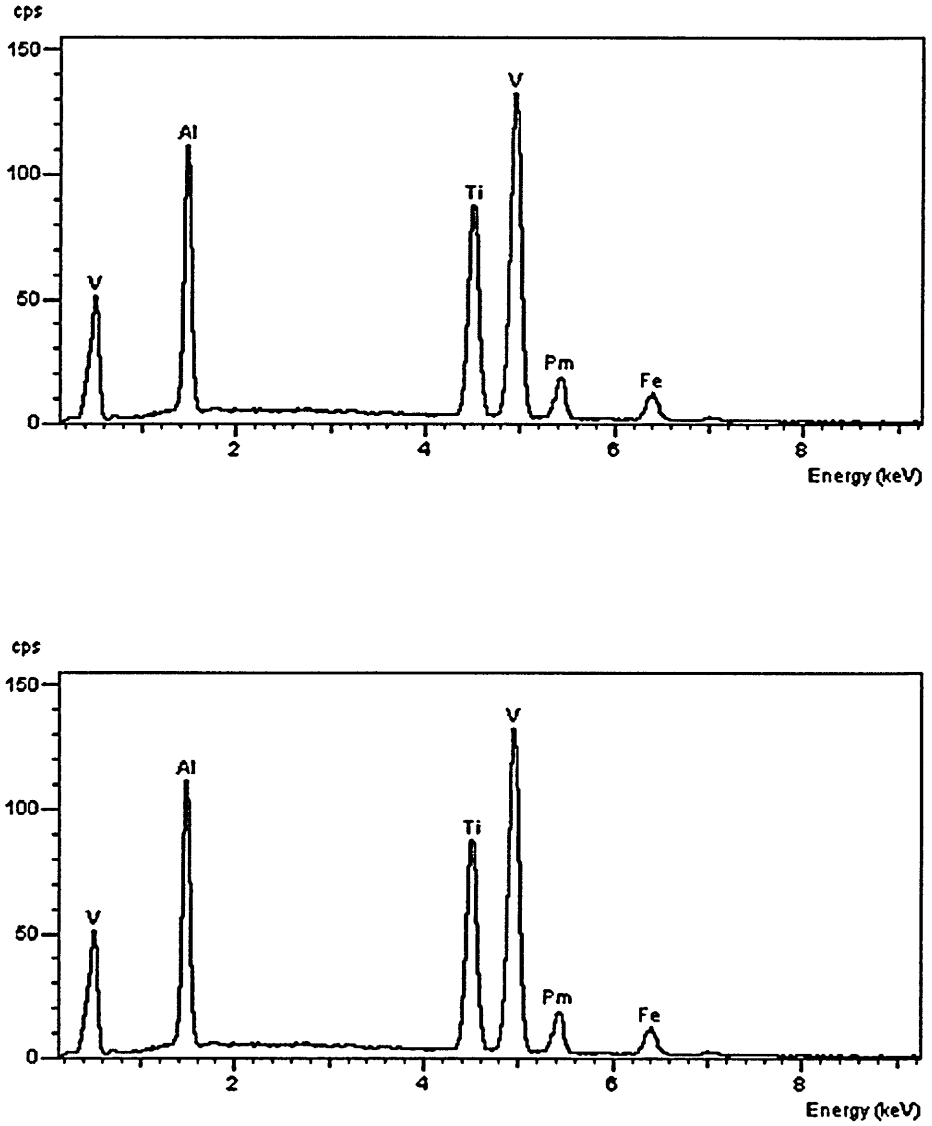

Figure 4.27 EDAX measurements showing the elemental peaks from the TiAlCN/VCN coating oxidised at (a) 560 °C and (b) 670 °C.

At 750°C, a temperature close but below the onset of rapid oxidation (800°C), a further increase of the intensity of the peaks detected at 670°C can be observed, which indicates simply a kinetic progression of the oxidation process. In comparison, in the case of UBM deposited coatings the potentially lubricious oxides of V_2O_5, $AlVO_4$ and TiO_2 well adherent to the substrate were present to temperatures up to 750°C. As no Cr, Ni or

Fe based oxides were detected. SEM observations showed oxide scale morphology similar to that formed at 670°C, Fig.4.26c.

4.5.3 Morphology of worn surface after sliding friction

To better understand the wear mechanism of the coating which takes place at different environmental conditions (temperature and humidity), the morphology of the wear tracks was studied by SEM. Figure 4.28 shows the SEM images of the wear tracks of HIPIMS-UBM deposited coating produced in dry sliding conditions at room and various elevated temperatures 200°C, 450°C and 650°C, which reveal further information about the wear mechanism. The wear tracks in all cases seem to be very smooth except for the one generated at 200°C.

SEM analysis showed that the wear track at room temperature is relatively narrow (≈157.9 μm) and very smooth with oxide debris (black in colour) accumulated along the track. Careful observation inside the wear track shows formation of shallow grooves parallel to the sliding direction. At 200°C, the wear scar appears to be rough with increased width of 338.43 μm. At 450°C, the wear track appears very smooth without any parallel grooves at the middle of the wear track. At this stage as indicated by the TG curve a larger amount of lubricious oxides is formed, which provide more effective solid lubrication resulting in smooth wear surface morphology. The smoothest wear track morphology is achieved at the highest test temperature of 650°C

mag Ispot I HV mode | det I WD
825x1 3.5 110.00 kV SE |ETDj5.1mm

mag spot HV mode det WD
342 * 4 0 7 00 kV SE ETD 4 1 mm

WD
3 9 mm

Figure 4.28 The SEM micrographs of wear track generated at (a) room temperature, (b) 200°C, (c) 450°C, (d) 650°C.

4.5.4 Raman analysis of worn surface

Figure 4.29 shows Raman spectra undertaken on the as-formed wear debris accumulated along the side of the wear track in the pin-on-disc test carried out at various temperatures, (ambient, 200, 450 and 650°C).

At ambient and 200 °C temperatures a series of broad Raman bands centred at 237, 652, 896, 1321 and 1579 cm^{-1} were clearly observed, Fig. 4.29. The spectra in the 200 cm^{-1} to 800 cm^{-1} band looks similar to the spectrum of TiAlN [202] except for the presence of V_2O_5 in the 600-800 cm^{-1} band [201]. The subsequent broad peak in between 800 and 1000 cm^{-1} can be assigned to the presence of highly crystalline α-Al_2O_3 [201] or attributed to $AlVO_4$ phase. There are two possible mechanisms for the formation of the $AlVO_4$ phase. The mixed oxide can be produced via tribo-oxidation mechanism or could form due to reaction between the V_2O_5 in the wear debris and the wear product from the alumina counterpart (Al_2O_3 ball) as reported in [203]. The highly diffused peaks corresponding to the disordered and graphitic carbon band were also detected in the 1200-1600 cm^{-1} band.

These observations lead to the conclusion that at low temperatures up to 200°C the wear product contains debris of the as-deposited coating as well as V based oxides formed due to high flash temperatures at the asperity contacts during sliding. This is in good agreement with the TG experiments where first effect of oxidation is observed at 550°C.

At 450°C the oxide formation is influenced not only by tribo-oxidation but also due to the external heating of the sample. The peaks of the spectra are with higher intensity and depict the presence of V_2O_5 phase in the 200-to-600 cm^{-1} band and TiO_2, V_2O_5, and $AlVO_4$ in the 600 to 1000 cm^{-1} band [204]. It is also important to notice that the amorphous carbon D and G bands in between 1321 cm^{-1} and 1579 cm^{-1} have shown more intensity.

At 650°C the peaks in the 200-700 cm^{-1} band appear with higher intensity showing the formation of a mixture of several oxides such as α -F_2O_3, V_2O_5, and TiO_2. This spectral range have also shown significant amount of V-containing Aluminium oxide phase, most probably $AlVO_4$ as identified by XRD analyses. The α-F_2O_3 is contributed by wear debris of the substrate material. More interestingly a graphitic peak was identified in between 1300-1400 cm^{-1} corresponding to the D band of disordered graphite.

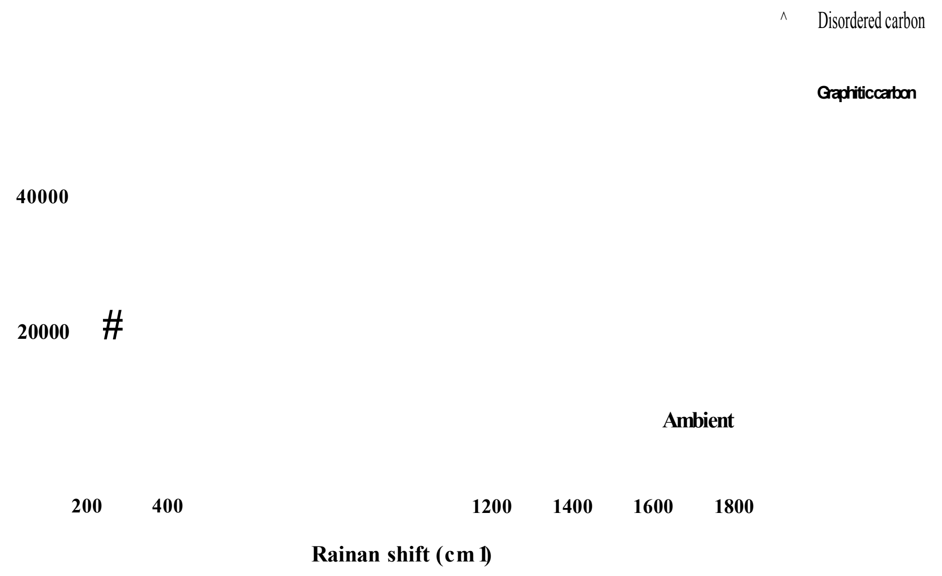

Figure 4.29 Raman spectra of the wear debris generated at ambient, 200°, 450° and 650°C in the wear track during pin-on-disk test.

4.6 Machining performance of TiAlCN/VCN coating deposited by combined HIPIMS-UBM technique

To study the wear behaviour of TiAlCN/VCN as well as coating work-piece material interaction a cutting experiment was conducted. Coated 25 mm diameter end mills were used to machine highly abrasive AlSi9Cu1 alloy in dry conditions. The tests were carried out on a high-speed milling centre, MAZAK FJV-25 using milling parameters which were specifically set to produce significant amount of built up material on the cutting edge and therefore guarantee complete material reaction between coating and work piece can be realised: spindle speed; 24000 rpm; cutting speed, V_c=1884 m. min^{-1}; cutting depth, A_p=4 mm; cutting width, Ae= 2 mm; feed rate, Vf= 0.165 mm per tooth (0.33 mm rev^{-1}). Optical image of the cutting edge with the built up

Al-alloy on the cutting edge is shown in Figure 10 (a) UBM deposited coated tool (b) HIPIMS-UBM deposited coated tool. This built up material was than mechanically removed from the tool and the contact surface was used for Raman analyses.

GNH 1 1480 passes
0.24mm Flank Wear

X

(a) **(b)**

Figure 4.30 Optical image of cutting edge with the built up Al-alloy on the cutting edge (a & b) UBM and HIPIMS-UBM deposited TiAICN/VCN.

In Figure 4.30 the TiAICN/VCN coated cutters by UBM and HIPIMS UBM technique have shown almost similar wear rate. However, longer lifetime for UBM deposited cutter can be seen when compared to HIPIMS-UBM deposited coating, which was attributed due to the much thicker coating deposited in the former case (~ 3.5 pm) when compared with the latter case (~ 2.5 pm). However, it is very important to notice that the HIPIMS-UBM deposited cutter exhibit more stability during the wear performance with slow increase in the flank wear rate with cutting length over 500 m (0.486 m in each cutting pass). This can be seen by sudden increase in the flank wear in the case of UBM deposited cutter. Also, the lower surface roughness value measured in the case of HIPIMS-UBM deposited cutter (0.023) when compared to UBM deposited cutter (0.026) prior to the machining process has lead to form reduced BUE formation after cutting operation. This can be clearly seen in Figure 4.30a. The surface finish after the machining operation for HIPIMS-UBM deposited cutter was better than UBM deposited cutter.

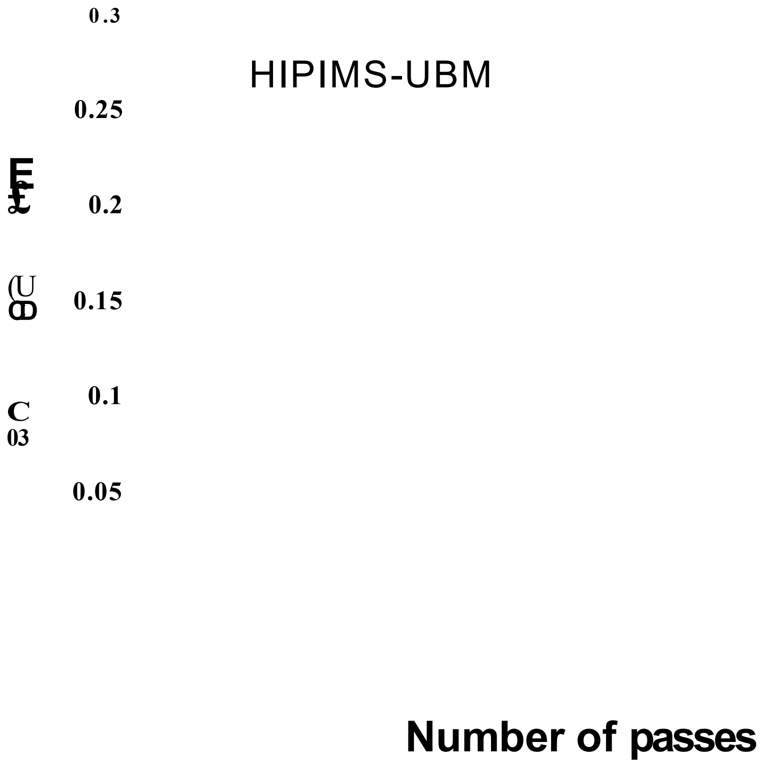

Figure 4.31 Flank wear of coated HSS tools plotted against cutting length in milling A17010 alloy.

4.6.1 Raman spectroscopy investigation of the worn tool-work piece material surface

(A) Analysis of tool cutter coated with TiAlCN/VCN by UBM and HIPIMS-UBM technique

Green (532nm excitation) and UV (325 nm excitation) Raman spectroscopy was employed to identify the coating phases and compounds formed on the cutting edge before and after the machining test as well as on the contact surface of the as-removed from the cutting edge built up material, Figure 4.32a and 4.32b. However, in the case of HIPIMS-UBM deposited tool edge the build-up edge is less pronounced when compared to UBM deposited tool edge (see Figure 4.23). Hence, in this case, it was possible only to collect the Raman spectra from the tool edge.

As deposited coating: Both Green and UV excitations of the as-deposited coating revealed the presence of TiAlCN and VCN as expected. However the more sensitive to carbon UV analysis showed, lower intensity peaks at 1568 cm^{-1} (G-band) and 1351cm^{-1}

(D-band) revealing the graphitic nature of the coating material which supports the GAXRD and XTEM analyses.

Coating surface after machining: Green laser Raman spectroscopy identified the presence of various oxides such as SiO_2, mixed (AlSi) O, V_2O_5 as well as the G and D bands of graphitic carbon. The graphitic G and D bands at 1372 cm^{-1} and 1605 cm^{-1} respectively were much more intensive in the UV 325nm spectra. In case of HIPIMS-UBM deposited case, Figure 4.33 shows the Raman spectra collected from the coated tool edge after immediately after the successive interval of operation. The high intensity graphitic peak of G and D peaks are clearly observed at 1375 cm^{-1} and 1607 cm^{-1} throughout the dry milling operation.

Contact surface: The compounds found on the contact surface of the built up SiAl-alloy were similar to those found on the tool surface after the machining test namely lubricious V_2O_5, abrasive SiCF and mixed (AlSi) O, as well as graphitic carbon.

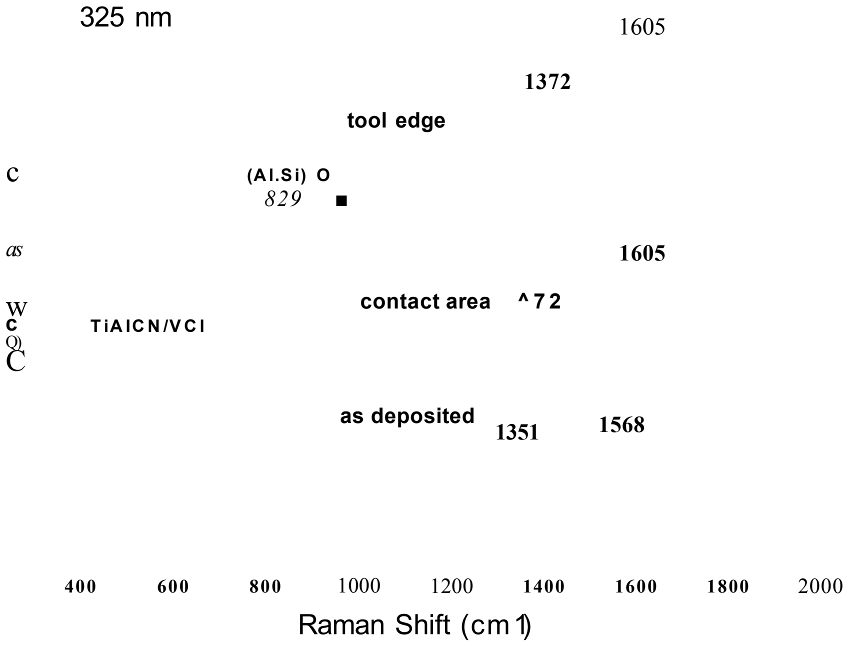

(a)

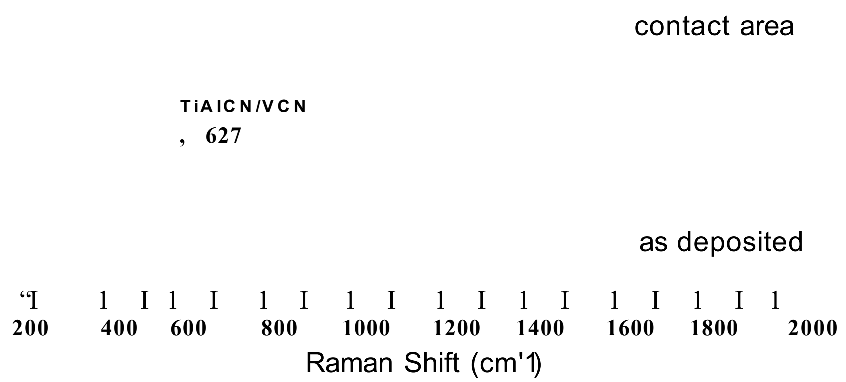

Figure 4.32 Raman spectra taken from various surfaces using: a) UV, 325 excitation and b) green laser 532 excitation.

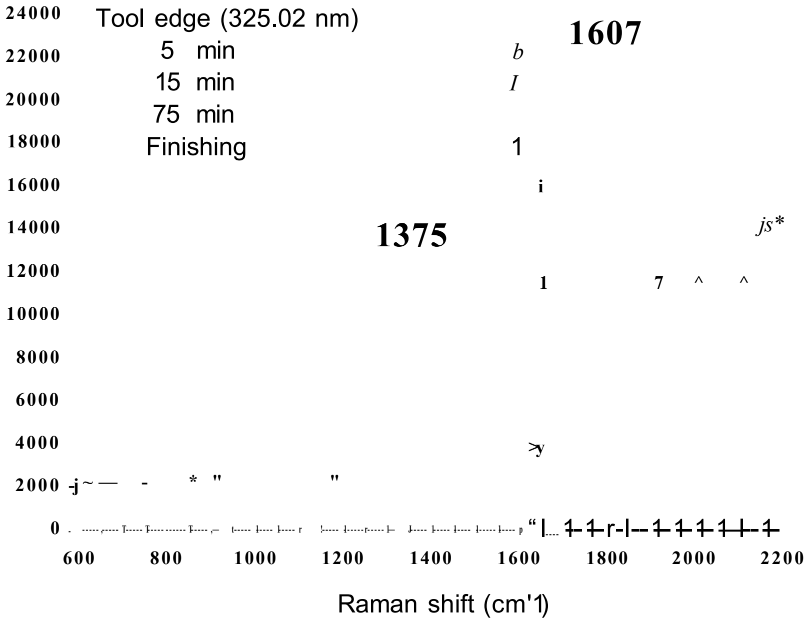

Figure 4.33 The Raman spectra collected from the machined tool edge after successive interval of operation.

CHAPTER 5

DISCUSSION

5.1 HIPIMS and UBM plasma-a comparison in terms of ionic composition

5.1.1 $V^+ + Ar^+$ ion etching by HIPIMS

Surface pretreatment by HIPIMS prior to the deposition of actual coating, is proven to be an effective method to enhance adhesion of the coating with substrate. Metal ion etching by physical sputtering is most commonly used to remove oxide and carbon contaminate from the substrate surface in order to avoid possible formation of nanocrystalline or amorphous structure at the coating-substrate interface. This is very important since nanocrystalline or amorphous structure create a very poor bonding with the condensing nuclei of the coating material. Hence, it is very essential to provide crystalline interface which create strong adhesive bond between subsequently deposited coatings. In this work, the substrates were pretreated by $V^+ + Ar^+$ ions, by HIPIMS. Time averaged ionic composition during this stage of the process has shown high metal-to-gas ion ratio as expected by HIPIMS. The results of energy resolved mass spectrometry was discussed in the chapter 4, in section 4.1.

The spectrum clearly showed (Figure 4.1 and 4.2) the HIPIMS plasma discharge dominated with higher content of metal ions (V^{1+}, V^{2+}, V^3) compared to gas ions (Ar^{1+}, Ar^{2+}) with a ratio of 1.25:1 respectively. In contrast, for UBM sputtering, earlier studies have reported about very lower proportion of metal ionisation as compared to gas ionisation during etching. For example UBM of Cr discharge has shown metal-to-gas ion ratio of 0.1 [205]. Careful analysis of the spectra has shown ionisation of V up to charge state of 5 (V^{4+}, V^{5+}). It is also interesting that metal-ion-to gas ion ratio for 2^+, 3^+, 4^+ and 5^+ are higher than 1^+. This may be due to the lower ionisation potential of multiply charged metal ions as compared to multiply charged gas ions (Ar^{1+}, Ar^{2+}). The energy distribution of single, double and triple charged ions were shown in figure 4.3. The average energy of all the ions was in the range of 1-2 eV.

Previously, Arc discharge of Ti has shown multiply charged ions with low gas ion percentage [206]. In the recent work, Ehiasarian et. al., have also shown similar results of high metal-to-gas ion ratio for Nb and Cr ions discharged during etching process by HIPIMS, prior to the deposition of CrN coating [205]. An analogy can also be seen in this case in terms of mass spectrometry result, where multiply charged ions were identified which effectively increased the metal ion ratio in the HIPIMS plasma when compared to the gas ion ration (see section 4.1). The high percentage of metal ionisation achieved during the Arc and HIPIMS etching have proved to create a strong bonding between the nitride coating and the substrate [205, 206]. However, the elimination of growth defects in the actual coating (often seen after Arc etching processes) [46], after HIPIMS pretreatment technique has increased the importance of this technique in metal ion etching process.

Two possible competitive mechanisms which occur at the substrate surface during metal ion etching process are sputtering of substrate atoms and diffusion of bombarding metal ions beneath the substrate surface [166]. These newly implanted atoms have clear tendency to form very strong bond with the substrate lattice as well as create fully dense crystalline surface which subsequently assist in coherent growth of coating [205]. For example HIPIMS of V pretreatment on stainless steel substrate with subsequent $Ti_{0.5}Al_{0.5}N_{0.5}$ base layer and HIPIMS of Cr pretreatement on the γ-TiAl substrate and subsequent CrAlN layer grown have shown clear crystallographic templating by cube-on-cube epitaxial growth with contaminant free coating-substrate interface [205]. High Energy ion bombardment is an efficient alternative method to temperature controlled thin film growth mechanism, which promotes effective diffusion of bombarding ions in to the growing film [207]. The implantation depth of bombarding atoms depends upon the energy it gains near the biased substrate sheath. For e.g implantation depth of singly ionised atoms at 600-1000 eV energies reported in previous literatures have implanted beneath the substrate surface to about 5-8 nm depth. This fact clearly suggests that the implantation depth is directly controlled by the energy of implanting ions. Hence, in this work also, the content of highly ionised states of V increases the depth of implantation of metals into the substrate since the energy that ions gain through biasing is multiplied by their charge state. Since, the energy of the bombarding ions are determined by the product of the substrate bias voltage (-1000 V in our case) and the charge state of the sputtered ion. Subsequently these highly charged metal ions energised near the substrate sheath and can have very high range of energy. This is believed to be leading to implantation of these high energy ions deeper (5-10 nm) into the substrate ensuring a thicker and stronger diffusion layer. This mechanism was referred to as the radiation enhanced diffusion [18] where the possible inclusion of inert gas ion is completely reduced and provides atomically clean surface for adatoms to create bond with substrate lattice.

Thus mass spectrometry results obtained here clearly suggest that the mechanism behind the TiAlCN/VCN coating-substrate bonding is analogous to previously explained nitride coating bonding with the substrates [205]. High content of multiply charged V^+ ions create clean interface prior to the growth of TiAlCN/VCN nanograins. This subsequently forms highly crystalline coating-substrate interfaces and increase the likelihood of atomic registry between coating and substrate lattices. This was confirmed by high adhesion value (> 50 N) obtained for TiAlCN/VCN coating against the substrate and the low magnification TEM cross section images of the coating (discussed in section 5.2). Also, the impact of high adhesion achieved has been advantageous in several aspects, such as increase of microhardness of the coating, better adhesive wear performance of TiAlCN/VCN coating both at room temperature and elevated temperature. This has been discussed in detail in the section 5.2.

5.1.2 Plasma composition during the deposition of TiAlCN/VCN coating

Table 5.1 shows the amount of Me^+, C^+ and Ar^++N^+ ions observed during the deposition of TiAlCN and VCN respectively. The plasma composition during coating deposition was studied by operating TiAl and V targets separately in HIPIMS and UBM (DC) modes, the influence of high energy bombardment during HIPIMS was clearly reflected in the microstructure of TiAlCN/VCN coating (will be discussed in section 5.2). Figure 4.4 shows the mass spectra collected near the substrate during the deposition of TiAlCN and VCN as separate process by both HIPIMS and UBM technique. The pie-chart (Figure 4.5a and b) drawn from the mass spectra for HIPIMS and UBM plasma has clearly shown major difference with metal-to-gas ion ratio when compared to UBM plasma. Achieving higher number of metal ions in the condensing plasma flux has been a major advantage as far as both energy delivery to the growing film and increase in the mobility of condensing atoms are concerned. Besides this high ion irradiation of ions are also results in stress free coatings which inhibits cracking or flaking problems.

	UBM Plasma		HIPIMS Plasma	
	TiAlCN	VCN	TiAlCN	VCN
Metal Ion (%)	2.8	7.5	11	7.5
C Ion (%)	0.1	0.1	1	0.5
Gas Ion (%)	97	99.2	88	91.7

Table 5.1 Ionic composition of plasma measured during the deposition of TiAlCN/VCN nanoscale coatings by UBM and HIPIMS technique.

During the deposition processes of both TiAlCN and VCN, the ratio of metal ions -to-gas ions during the sputtering of HIPIMS mode were 1:7 and 1:12 for TiAlCN and VCN discharge respectively. This value is greater than the ratio of metal ion-to-gas ion concentration produced in UBM discharge which is about 1:32 for TiAlCN and 1:177 for VCN. In the case of HIPIMS discharge, the estimated metal ionisation degree was about ~ 20 % (Al^{1+}=9%, Ti^{1+}=2%, V^{1+}= 7.5%), where as a factor of 2 lower metal ionisation ~ 10 % (Al^{1+}= 2.8%, Ti^{1+}= 0.23%, V^{1+}= 0.5%) was calculated for UBMS discharge. In addition, C^{1+} ion percentage detected was higher in the case of HIPIMS (1.5%) discharge than UBMS discharge (0.2%). Also, mass spectra of HIPIMS discharge has clearly identified the higher proportion of ionised stable hydrocarbons and nitril compounds than identified in case of UBMS discharge.

The results obtained about gaseous ion species in the discharge are consistent with published experimental results and chemical models performed on similar plasmas [208, 209, 210]. The higher metal ionisation of pulse sputtered flux achieved in HIPIMS discharge can be attributed to the high plasma density achieved (10^{12} cm^{-3}) due to high power density applied on the TiAl and V targets. Ehiasarian et. al., showed the influence of high power density on the composition of pulsed magnetron plasma of Cr and Ti discharge [211]. Author suggests that the high power dissipation on the target increases target voltage and target current, which increases in turn the plasma electron temperature in the plasma with high plasma density near the target. This argument further corroborate the mass spectrometry results obtained for HIPIMS discharge from TiAl and V target in mixed $Ar+N_2+CH_4$ plasma.

During the deposition step, high current densities applied in pulses are believed to stimulate several processes inside the active plasma, such as electron impact excitation of metastable N_2^*, excitation of atomic nitrogen, and the formation of free radicals [208], which are efficient to decompose methane (CH_4) into several gaseous ions of hydrocarbons, and nitrils [209, 210, 212]. The high frequency of electron impacts generating positive $C_xH_y^{1+}$ ions in the $Ar+N_2+CH_4$ plasma also produces stable free carbon ions of C^{1+} [212]. In HIPIMS the latter process is much more efficient as compared to UBM.

The higher metal and carbon ion fractions detected during the HIPIMS deposition of TiAlCN/VCN coating has very important impact on its growth. The Energy-resolved mass spectroscopy analyses of the plasma indicate that during the HIPIMS stage of deposition, the coating grow under conditions of higher energetic bombardment. High energy bombardment due to the metal ion dominated plasma flux is proven to transfer both energy and momentum to condensing adatoms, which increases adatom mobility on the substrate. This would unambiguously densify the microstructure with high mobility of dissociated reactive N^+ and $C_xH_y^{1+}$ ions in the film by reducing inter columnar porosity. Furthermore it can promote layer-by-layer growth and reduce the roughness of the coatings.

High amounts of free carbon produced in the HIPIMS plasma itself tend to enhance the incorporation of carbon in the actual film. In contrast C_xH_y molecules and radicals have lower sticking coefficients and/or may require additional energy to dissociate on the surface. Carbon incorporated in the film, segregates vertically to form layers between the individual layers of the coating [212, 213]. Thus, the segregation of carbon atoms between the individual layers of TiAlN and VN might also reduce the interfacial stress which is beneficial in terms of good adhesion and mechanical stability. Also, more number of carbon ion bombardment achieved in HIPIMS might also increase the sp^3 content inside the film, which has beneficial impact on the friction behaviour during the dry sliding conditions. Apart from its application oriented benefits, higher fraction of carbon ion detection in HIPIMS plasma also might lead to target poisoning effect, which could also show unique impact on the microstructure of the coating.

In summary, the novel HIPIMS technology offers better plasma conditions with higher ionisation and higher Me+ to Ar+ ratio for pre-treatment conditions: highly charged V metal ions - up to 4+ and metal ion -to- gas ion ratio >1 and for deposition conditions: factor 10 more carbon ions - fully stripped of hydrogen, factor 3 more Al ions and factor 10 more Ti ions when compared to UBM sputtering.

5.2 Mechanical and Tribological Properties of nanoscale TiAlCN/VCN coating

5.2.1 Mechanical properties determined for UBM and HIPIMS-UBM deposited coating

In this section, initially the mechanical and tribological properties are comparatively discussed for UBM and HIPIMS-UBM and in the following section the discussion is carried out for pure HIPIMS deposited case. The purpose of TiAlCN/VCN nanoscale coating is developed as a wear resistant coating for elevated temperature applications. Especially to protect the tools used for machining aerospace grade alloys such as Ti, Al and Ni based alloys. Hence the mechanical and tribological properties of nanoscale TiAlCN/VCN coating is not been discussed beyond the scope of its purpose.

Irrespective of deposition technique, high but similar critical load values in scratch adhesion tests of Lc = 57 N were measured for TiAlCN/VCN coating, as the surface pre-treatment was carried out by HIPIMS discharge using similar deposition parameters. The only possible mechanism by which formation of weak van-der-Walls bonding between the coating and substrate surface can be eliminated is achieving good adhesion at the substrate-coating interface. The high adhesion value measured for TiAlCN/VCN coating has demonstrated again the importance of metal ion (V^+) etching by HIPIMS. This adhesion value is higher than those for arc-pretreated TiAlCrYN (Lc ~ 50) and Ar^+ pretreated DLC (Lc ~ 30) grade coatings reported in previous literatures [12]. Thus the high adhesion value achieved is a prerequisite for any defect free coating growth. In the case of wear resistant coatings, adhesion plays a very important role in retaining the integrity of the coating with the substrate where the protection of substrate against adhesive and fatigue wear is essential. Especially for TiAlCN/VCN multilayer coating, good adhesion is essential in order to increase the tool life time at when used at elevated temperatures (400 °C – 800 °C).

The advantage of HIPIMS etching can also be realised in terms of the coating surface roughness (Ra). The lower surface roughness measured (Table 4.1) for TiAlCN/VCN coating has shown factor 3 lower values than previously reported for arc etched TiAlCrYN (~ 0.075) and carbon free TiAlN/VN (~ 0.06) coating [12]. This can be attributed to the droplet-free metal ion etching characteristic of HIPIMS utilized for surface pre-treatment. Further, more intense ion bombardment which produces higher re-sputtering of the coating as well as coating densification during growth could explain the lower surface roughness of the HIPIMS deposited coatings as compared to the UBM ones (Table 4.1). Both coatings however, show almost a factor of 3 lower surface roughnesses when compared to magnetron sputtered TiAlCN/VCN coatings where arc etching was used prior to the coating deposition step. This could be due to the denser microstructure produced by HIPIMS, where the concentration of metal ion sputtering was higher as compared to UBM, during the coating growth. As far as tool protective coatings are concerned, smooth surface finishing plays a major role which amounts to longer tool life time during machining. Microhardness value was marginally different with higher values measured for the (HIPIMS-UBM) case. The increase can be attributed to the higher coating density due to the higher level of ion bombardment as explained in plasma analysis (section 5.1). The higher the microhardness value of the coating, better it controls the abrasive resistance at cutting temperature. Although by adding the C to TiAlN/VN has reduced the microhardness value from 3200 to 2900, the value is sufficiently high enough and comparable to previously reported DLC (Cr/WC/a-CH) coating [12]. Previously reported plastic hardness (HP) values for carbon free multilayer coatings such as TiAlN/VN (~ 40), TiAlN/CrN (~ 55), TiAlN/ZrN (~ 55) were realised to be higher than TiAlCN/VCN multilayer coating. The higher plastic hardness values were corresponding to the higher residual stress measured for those coatings which were attributed to the intensive ion bombardment during the coating growth where Arcbond sputtering was the technology used for their deposition [177]. However, a factor of 2-to-4 lower HP values measured for TiAlCN/VCN coating is conclusively suggests the importance of light atomic weight carbon inside the coating and utilization of HIPIMS technology for its deposition. Lower plastic hardness values are important to achieve in wear resistant coatings used to machine sticky alloys (Ti, Al, Ni based alloys); as smooth plastic deformation between individual de-laminating atomic layers further helps to stabilize the wear behaviour of the coating against work piece.

Hence, the values measured for adhesion, microhardness, surface roughness, and plastic hardness for nanoscale TiAlCN/VCN coating, shows superior results when HIPIMS was used not only for etching, but also during the deposition. Hence without any surprise the HIPIMS technology outranks those traditional arc and UBM technologies used to deposit nitride multilayer coatings.

5.2.2. Room temperature friction and wear behaviour for UBM and HIPIMS-UBM deposition case

The mechanical and tribological properties of nanoscale TiAlCN/VCN coating at room temperature are summarised in Table 4.1 as a function of deposition technique.

The plastic hardness of the coating demonstrated that the addition of carbon to TiAlN/VN clearly distinguish the TiAlCN/VCN coating as "hard" coating rather classifying it to "Superhard" family. However, the coating deposited under pure HIPIMS technique with similar deposition conditions as that of UBM and HIPIMS-UBM has shown comparatively lower plastic hardness. In the case of pure HIPIMS deposited coating, the carbon percentage was higher as confirmed by the plasma analysis. Further, the TEM analysis have showed the transition of microstructure from nanocrystalline multilayer phase of TiAlCN and VCN to nanocomposite phase of Ti,Al,V(C-N)/a-C (figure 4.20), clearly demonstrate the reason for decrease in hardness value of the coating (~ 13 GPa), than observed for UBM and HIPIMS-UBM deposited case (~29 and 25 GPa respectively). Hence, the discussion in this section is limited to only for UBM and HIPIMS-UBM deposited coating.

The room temperature friction and wear coefficient value for TiAlCN/VCN coating deposited is given in Table 4.1 as a function of deposition technique used. The wear coefficient values are correlated to the values of friction coefficient measured against the Al_2O_3 counterpart. Low friction coefficient (COF) of μ=0.45 with wear coefficient of $1.4x10^{-17}$ $m^3N^{-1}m^{-1}$ was calculated for coating deposited by HIPIMS-UBM, which is two orders of magnitude lower than that for the UBM deposited $4.2x10^{-15}$ $m^3N^{-1}m^{-1}$ coatings with slightly higher COF of μ=0.68. This represents significant advantage of coatings deposited by (HIPIMS-UBM). Thus low friction and enhanced wear resistance measured in dry sliding wear conditions for HIPIMS-UBM deposited TiAlCN/VCN coating can be described in terms of its micro structure and chemical constituents. The extremely dense closed columnar multilayer structure observed for

TiAlCN/VCN coating produced by HIPIMS-UBM deposited technique significantly demonstrates its importance by enhanced friction and wear behaviour at room temperature. Further, the influence of chemical constituents, especially the synergy between V and C played a very important role in stabilizing the friction and wear performance of the coating. The importance of vanadium and carbon for low friction and wear resistant application was realised since two decades. For example monolithically grown Ti-Al-V-C-N [214], VTi (C,N) [215], (TiAlV) CNO + V_2O_5 top layer [216], AlCrV(CN) [217], etc. But the major problems with these coatings were concerned with rough surfaces which have lead to poor surface finishing problems due to arc deposition technology utilised for the respective deposition.

The concept of solid lubricants and its importance in dry milling applications, biomedical applications etc, is constantly increasing. The lubricious effects of solid lubricants also named as Magneli phase oxides such as Ti_nO_{2n-1}, V_nO_{2n-1}, V_nO_{3n-1} or V_nO_{3n-2} is explained by the presence of easy shearable crystallographic (CS) planes [234, 235]. XRD analyses reported previously for TiAlN/VN coatings showed the formation of a range of oxides such as TiO_2, V_2O_5 mixed with $AlVO_4$ all possessing lubricious properties due to their crystallographic structure [232, 233]. Also, the melting point of V_2O_5 is low (T_m = 685^0 C), and typically in the range as that of flash temperature ($T_f = 650^0 - 700$ °C) at the asperity contacts during sliding. This means that the dry sliding will takes place over the molten phase of tribo oxide phases. The mixed oxide can be produced via tribo-oxidation mechanism or could form due to reaction between the V_2O_5 in the wear debris and the wear product from the alumina counterpart (Al_2O_3 ball) as reported in [203]. This was confirmed by Raman spectra undertaken on the as-formed wear debris accumulated along the side of the wear track in the pin-on-disc test studies have identified the generation of highly lubricious phases such as (V_2O_5, TiO_2, $AlVO_4$) during sliding at room, thus providing additional tool for better understanding of tribological behaviour of TiAlCN/VCN coating deposited by HIPIMS-UBM technique. Hence, the lower COF of 0.45 for HIPIMS-UBM deposited coating can be due to the wear stabilizing behaviour of tribo-oxidised films containing all easily shearable planes. Additionally in the case of the TiAlCN/VCN multilayer coatings the presence of a carbon based phase between the individual layers of the nanolaminate further influences the wear behaviour by introducing layer by layer wear mechanism as reported previously. Raman spectra collected after room temperature sliding experiment from the wear debris formed at the wear track edges showed clearly the possibility of graphitization process where the possible contribution for friction reduction from graphitic layer structure is enhanced (Figure 4.29).

The plastic hardness of the coating also plays a major role in the wear resistance property of the coating. Carbon free multilayer nitride coatings For example, TiAlN/VN, TiAlYN/VN, TiAlN/CrN, have shown increasing wear coefficient as their plastic hardness value increased [237]. This conclusion can also be extended here, where TiAlCN/VCN has shown lower plastic hardness value (~ 30 GPa for UBM, (< 30 GPa for HIPIMS-UBM and pure HIPIMS deposited) than carbon free nitride multilayer coatings. As a consequence, decrease in the wear coefficient value is observed. Table 5.2 below compares the wear coefficient value with respect to plastic hardness value. Earlier reports on the effect of carbon incorporation into the TiN film clearly revealed the fact of decrease in its hardness value due to the increase in the content of carbon in the film [119]. This was attributed to the increase in a-C phase with the transition from nanocrystalline phase of nc-Ti(C, N) to nanocomposite of nc-Ti(C, $N_{x<1}$)/a-C film. However, it is very important to notice here that, for HIPIMS-UBM deposited case, there is no change is the microstructure of the coating has been observed due to the incorporation of carbon. Also, It was proposed that the amount of these oxides predominantly influence in the reduction of COF due to melting at flash temperature due to which formation of junction formation mechanism is very much suppressed by these molten oxide phases. Also, during sliding the tangential friction force exerted on the coating surface leads to plastic deformation. Due to this, the columnar structure is expected to break by producing micrometer size particles, which influence three body abrasive wear mechanism [236]. This mechanism might increase the friction and wear. However, enhanced adhesion of the coating with substrate, higher microhardness and denser microstructure has clearly increased the wear resistance of HIPIMS-UBM deposited coating against the abrasive wear. Further, the as formed solid lubricant oxides at the tribo contacts together with the influence of carbon have stabilized the friction behaviour of the coating. This can be realised by observing smooth wear track generated after the room temperature pin-on-disc experiment (Figure 4.8a). The SEM morphology of room temperature wear track was further helpful in understanding the wear behaviour of HIPIMS-UBM deposited TiAlCN/VCN coating. The formation of shallow grooves parallel to the sliding direction clearly indicated in Figure 4.28a. by high energy bombardment and synergy between above mentioned Magneli oxide phases which acts like dry solid lubricants and high amount of carbon phase between the individual layers of the nanolaminate further influences the wear and friction behaviour by introducing layer by layer wear mechanism as reported previously [213]. This can be associated to the layer by layer removal of the coating during the sliding action, as well as to the relatively high humidity 75% as described in the previously published wear studies of coatings utilising nanoscale multilayer structure [238, 239].

Multilayer nitride coating	H (GPa)	COF (μ)	Wear coefficient (m^3/Nm)	
TiAlYN/VN	78	0.65	4.5 x 10^{-16}	[Ref:237]
TiAlN/CrN	55	0.7	2.4 x 10^{-16}	[Ref:237]
TiAlN/VN	40	0.4	1.3 x 10^{-17}	[Ref:237]
TiAlCN/VCN	30	0.4	1.4 x 10^{-17}	

Table 5.2. Wear coefficient values of carbon free nitride multilayer coating with respect to their plastic hardness value; compared to carbon containing TiAlCN/VCN coating.

5.2.3 Room temperature friction and wear behaviour for pure HIPIMS deposited case

The discussion in the previous section being carried out on the tribological performance of TiAlCN/VCN coating which was deposited with HIPIMS-UBM technique because of its superior performance over UBM deposited coating. In this section the tribological behaviour of pure HIPIMS deposited TiAlCN/VCN coating is discussed, due to the unique microstructure observed in this particular deposition. Besides the influence of Magneli phase oxides and carbon, the room temperature friction and wear behaviour in this case was strongly correlated to the unique graded microstructure achieved in this case, as explained in the section 4.4.2 and 5.2.3. The microstructure is evolved in three stages. The figure 5.1 shows the low magnification cross sectional bright field TEM image of TiAlCN/VCN coating deposited by pure

HIPIMS technique. Adjacent to the base layer, usual multilayer structure with carbon atoms segregated at the interface can be observed. This toughest region was found to be about 10-15 nm thick and provide highest load bearing capacity to the coating. Subsequently, after this structure has evolved as nanocomposite structure with TiAlVCN grains surrounded by carbon tissue phase. Nanocomposite structures are known to improve wear resistant property of the coating. And the final top zone of the coating is where the microstructure appeared completely amorphous without grain boundaries. This amorphous phase of the coating has revealed the Me-C like structure which can be helpful in increasing the onset of oxidation.

Me-C amorphous structure

nc-TiAlVCN

Figure 5.1. Low magnification bright field TEM micrograph of pure HIPIMS deposited TiAlCN/VCN coating; showing graded microstructure of multilayer-nanocomposite-MeC.

Hence, the tribological behaviour for TiAlCN/VCN coating in this particular case was determined by the depth profiling the friction and wear behaviour of the HIPIMS deposited TiAlCN/VCN coatings a number of friction tests were carried out with stepwise increase of the sliding distance by changing the number of the sliding laps from 500 to 10000 with an increment of 1000 laps. Coefficient of friction values of μ=0.37 (Figure 4.9) as measured in the first friction zone at the top of the coating are typical for Me-DLC coatings which corresponds well to the Me-C phase and XRD amorphous structure of the coating in this area. Low friction in this stage is achieved due to the C, which acts as a solid lubricant. This COF value is in well agreement with previously reported values for Me-DLC type (C/Cr) structure deposited with magnetron sputtering technique [225]. Recently, researchers are trying to include crystalline phase into the DLC phase, which has promised to show better tribological properties in terms of low friction and wear resistance properties. In this direction C/W and C/Cr have emerged as better examples, which have demonstrated better tribological properties when tested under dry sliding conditions [240, 241]. Similar microstructure morphology can also be seen very clearly in our case, where Ti-Al-V-N grains are surrounded by carbon tissue phase, see figure 5.1.

Further, when the sliding distance/wear depth is increased the nanocomposite structure of the coating is reached which characterises with higher coefficient of friction compared to the C-rich top layers and enhanced wear resistance, which is expected when accounting for the higher hardness of the nancrystalline structures. In this region the friction and wear behaviour are determined by the interplay between two mechanisms the presence of C acting as solid lubricant and formation of highly lubricious V_2O_5 Magnèli phases. In this experiment it was found that the wear coefficient reduces by one order of magnitude with the wear depth, with initial value of $K_c = 3.8 \times 10^{-15}$ m^3/N/m after 500 laps to $K_c = 4.4 \times 10^{-16}$ m^3/N/m after 10000 laps. These nanocomposite structures are known for better wear resistance properties, since their structure inhibit crack propagation through the bulk of the coating and increases the fracture toughness [242]. When this nanocomposite structure combined with self lubricating and/or chemically inert materials are produced, then tribological performance of the coating can expected to meet the desired requirement of low friction and better wear performance. Considering this argument we have a nanocomposite structure where self lubricating and chemically inert materials such as V and C is present; which is sufficient enough to show superior tribological performance both at room temperature and elevated temperature (discussed in next section). In comparison, UBM deposited TiAlCN/VCN coatings tested under similar conditions show an order of magnitude higher wear coefficient of 4.1 x 10^{-15} m^3/N/m [20] thus demonstrating the beneficial effect of the HIPIMS process. Another, reason for the reduced friction coefficient (COF) for HIPIMS involved deposition technique is corresponding to the formation of denser and smooth surface with increased ID/IG ratio and therefore the amount of sp^2 bonded carbon inside the coating (Figure 4.16), as explained by the Raman spectra collected on as deposited coating. It is also very important to note the importance of HIPIMS technology in producing this special graded structure, constituting the toughest multilayer structure followed by nanocomposite and then on top, the Me-C amorphous structure, which is realized as a tribologicaly more advantageous for dry sliding and milling operations.

5.2.4 Friction and wear behaviour at elevated temperature

Figure 4.10 shows the coefficient of friction (μ) vs number of laps curve for TiAlCN/VCN coating during sliding for elevated temperatures of 200°C, 450°C, and 650°C. In table 4.2, the values of COF and wear coefficient is shown, which compares the tribological performance of TiAlCN/VCN coating as a function of deposition technology. No great changes in the friction behaviour of the coating have been observed as a function of deposition technique. It is believed that the friction is strongly influenced by the combined effect of tribo oxidation as well as surface oxidation process taking place at elevated temperature. The initial increase of the coefficient of friction at 200 °C (0.8) in all the three deposited case can be attributed to the removal of the condensed water vapour film from the sliding surface which has lubricious effect [232]. But this value was comparatively less to that of earlier reported COF value (~ 1.0) at 200 –to- 300 °C for TiAlN/VN [245]. According to this report, the formation of dehydrated tribofilm and high shear strength at the interfaces of multilayer was main cause for higher COF.

The SEM morphology of worn surface analysed after the dry sliding test further lead to understand the friction and behaviour of the coating at respective test temperature. The fundamental difference in the properties of the film was observed by the rough surface of the wear track at 200°C, when compared to the wear tracks generated at other test temperatures (Figure 4.28a, b, c, d). The wear scar at 200°C appears to be rough with increased width of 338.43 μm, which can be explained by the increase of the coefficient of friction due to the sudden loss of water vapour, which takes place at this temperature range, see Fig.4.28b. In the absence of humidity lubricious oxides are expected to form only at the asperity contacts therefore their amount is not sufficient enough to provide effective solid lubrication. Further more in these conditions a brittle failure of the coating material at the asperities is promoted where the generated wear debris establish three body abrasion wear mechanism, which defines the morphology of the wear track.

Further increase of the temperature however leads to intensive surface oxidation produced by the combined action of the high temperature exposure to air as well as the sliding wear. The smooth wear track with parallel grooves showed after sliding wear test at 450 °C indicates the solid lubrication mechanism that occurred during the sliding process at this stage. According to the TG curve (will be discussed later), a larger amount of lubricious oxides is formed, which provide further proof of more effective solid lubrication resulting in smooth wear surface morphology. The smoothest wear track morphology is achieved at the highest test temperature of 650°C as at this stage due to the synergy effect of the tribo and external heating oxidation the largest amount of the lubricious oxides is generated, which promotes the polishing effect during sliding. This situation is also reflected by the coefficient of friction curve on Fig. 4.10 where the coefficient of friction at 650°C is the lowest (0.4). This study shows that there is a clear link between the environmental conditions and the amount of the lubricious oxides generated during dry sliding and the friction and wear behaviour of the PVD coating.

However, very importantly, in case of pure HIPIMS deposited TiAlCN/VCN coating, Despite their low coefficient of friction the mechanical strength and therefore wear resistance of the oxide films is not very high which can be seen from the increase of the wear coefficient when compared to the room temperature wear conditions. Coating densification however reduces significantly the amount of the thermally grown oxides as revealed by the TG analyses, Figure 4.23 which explains the superior performance of the HIPIMS TiAlCN/VCN coatings, (Kc = 1.0 x 10^{-13} m^3/N/m) over the UBM deposited ones (Kc = 5.8 x 10^{-13} m^3/N/m) when tested at 650 °C. Additionally, the Raman spectra collected from the worn surface generated at elevated temperature showed the influence of carbon, which further stabilized the friction and wear behaviour of the coating at elevated temperature.

In summary, the Raman spectra observations lead to the conclusion that at low temperatures up to 200°C the wear product contains debris of the as deposited coating as well as V based oxides formed due to high flash temperatures at the asperity contacts during sliding. This is in good agreement with the TG experiments where first effect of oxidation is observed at 550°C. Despite Magneli phase oxides, it is also important to notice that the amorphous carbon D and G bands in between 1321 cm^{-1} and 1579 cm^{-1} have shown more intensity, which suggests graphitization process taking place during sliding at elevated temperatures of 450 °C and 650 °C. This suggests that the carbon phase has a clear contribution to the friction and wear behaviour of TiAlCN/VCN at elevated temperatures.

5.3 Microstructural analysis of TiAlCN/VCN coating – Impact of HIPIMS

5.3.1 X-ray diffraction and SEM cross sectional analysis of nanoscale TiAlCN/VCN deposited by UBM and HIPIMS-UBM technique

The crystalline structure of nanoscale TiAlCN/VCN coating was determined by Bragg-Brentano (θ/2θ) X-ray diffraction analysis. Low angle X-ray diffraction was carried out in order to confirm the multilayer structure and calculate bi-layer thickness of as deposited coating. Further, SEM cross sectional study of as deposited coating was carried out in order to understand the influence of high energy bombardment on coating microstructure.

The low angle X-ray diffraction spectra (Figure 4.13) confirmed the multilayer nature of the TiAlCN/VCN coating deposited by both UBM and HIPIMS-UBM technique. The bi-layer period (Δ), of alternate TiAlCN and VCN was calculated to be ~ 2.2 nm. The θ-2θ XRD measurements (Figure 4.14) have shown the single phase fcc NaCl structure, with preferred orientation of {111} and {220} for TiAlCN/VCN coating deposited by both UBM and HIPIMS-UBM technique. Many literatures in the past have demonstrated the influence of bias voltage applied during the coating deposition, ion bombardment and nature of atomic species on the texture of TiN-type coatings. For example, carbon free TiAlN/VN deposited at -75 V has shown preferred orientation along {110} direction with very strong {110} texture. Same coating when deposited between -85 V to -150 V [224], has shown {111} preferred orientation with preferred {111} texture. Similar effect of texture development has been observed for magnetron deposited TiAlN/CrN multilayer coating at similar conditions of bias voltage. The change is the texture from {110) to {111} in both the cases were attributed to the fact of high mobility of lighter elements (Ti, Al and V) caused due to increasing bias voltage from -75 V. Literature further reported that development of {110} texture in case of TiAlN/VN coating deposited at -75 V, is corresponding to the competitive columnar growth effect following the VN phase which develops along {110} direction when deposited at similar conditions [216, 217].

Recently XRD and pole figure analysis on the texture of nanoscale TiAlCN/VCN multilayer coating deposited by UBM technique at – 75 V has shown preferred orientation of {220} plane with mixed fibre structure (perpendicular to the substrate plane) and in plane azimuthal texture along {220} and {111} [12]. Besides, Ar^+, N_2^+ ion bombardment, the influence of milder bombardment of lighter elements such as CH^+ ion was attributed to the mixed fibre and in plane azimuthal texture development. Further, author suggested that the effect of deposition geometry with off normal angle incidence of bombarding ions (due to 3-fold rotation of substrate) on the condensing surface was also contributed to the formation this mixed texture in case of TiAlCN/VCN coating.

In this particular work of nanoscale TiAlCN/VCN coating deposition, the deposition parameters such as bias voltage (-75 V) and gas pressure (x 10^{-3} mbar) were similar to that of previously carried deposition experiments by same research group [12]. Hence, the texture development of nanoscale TiAlCN/VCN coating deposited by UBM, HIPIMS-UBM technique is also believed to develop as mixed texture with preferred orientation along {220}, {111} as confirmed by $\theta/2\theta$ XRD measurements shown in figure 4.14. Also, the competitive growth of individual component layer with coherent interfaces is not affected for UBM deposited case. However, in the second case of the TiAlCN/VCN deposition when HIPIMS is involved along UBM (HIPIMS-UBM), the intensity of (220) is less pronounced and appeared broad than that of observed in pure UBM deposited TiAlCN/VCN coating. This suggests that the during the competitive growth of individual component layer, the influence of VN phase (which influence {220} texture) is slightly hindered due to the excessive high energy bombardment of C^+ and $C_xH_y^+$ ions by due to HIPIMS. Excessive stable hydrocarbon ion bombardment was confirmed by the HIPIMS plasma analysis explained in section 5.1. As a result of high energy bombardment, the ad-atom mobility of light elements (Ti, Al, V, $C_xH_y^+$) also expected to increase. Hence the broad peak along {220} in HIPIMS-UBM deposited case can be attributed to the high proportion of free carbon atoms with its increased mobility on the condensing film are believed to occupy more nitrogen position of fcc-VN forming VCN phase.

5.3.2 Raman Spectroscopy

The vibrational spectra of the as deposited TiAlCN/VCN coating was collected by 325 nm wavelength UV laser, which helped to understand the chemical state of the carbon. UV laser has the ability to excite both π and σ states of electron clouds [224, 221], hence helped to probe both sp^2 and sp^3 carbon phase fraction present inside TiAlCN/VCN coating deposited by all the three cases. The spectrum deconvoluted with a Lorentzian shape is shown Figure 4.16. The evidence for the D and G band was clearly observed in all the three cases of deposited coating, which confirms the both amorphous and nanocrystalline state of carbon (a-C) in TiAlCN/VCN coating. This is further confirmed through ID/IG ratio (sp^2/sp^3) calculated in all the three cases which is corresponding to the zone between nanocrystalline graphite and amorphous carbon according to "amorphization trajectory" model explained in [222]. Generally, the ratio of ID/IG ratio, full width half maximum (FWHM) and dispersion of G peak are three important parameters used to explain the bonding between the carbon and their structural disorder inside the film [223]. The FWHM of G peak is always corresponding to structural disorder, whereas dispersion of G peak is sensitive for topological disorder [223]. The structural disorder arises if distortion occurs between the bond angle or bond length between carbon atoms and size or shape distribution of sp^2 clusters give raise to topological disorder [223].

In our case, the G peak position at 1582 cm^{-1} observed for UBM deposited coating gradually dispersed to lower wave number of 1578 cm^{-1} and 1575 cm^{-1} for HIPMS-UBM and HIPIMS deposited TiAlCN/VCN coating. This can be associated with increased sp^2 clustering phase of carbon with minimal disorder in their bonding. Also, the D band position for HIPIMS deposited coating was found to be shifted to higher wave number (1381 cm^{-1}) than those measured for UBM (1379 cm^{-1}) and HIPIMS-UBM (1367 cm^{-1}) deposited case. The shifting of D band to higher wave number side was associated with the increase of compressive stress inside the coating, especially when high energy bombardment conditions are involved during the deposition of thin films [243]. Tool protective coatings especially, should posses small amount of residual compressive stress, as they would help to delay the micro-crack initiation and propagation into the tool substrate [244]. Further, the ID/IG ration was increasing with respect to the deposition process. Pure HIPIMS deposited TiAlCN/VCN coating has revealed the ID/IG ration to about 1.64, which clearly suggests the significant increase in the sp^3 content inside the film. This fact leads to realise the possibility of forming DLC bonding inside the coating. The sp^3 bonding can occur only if the deposition involves high energy carbon ion bombardment during the growth. This has been clearly proved in our pure, where high amounts of free carbon produced in the HIPIMS plasma itself tend to enhance the incorporation of carbon in the actual film. As result of which, the reduction of COF (~ 0.3) when sliding against the top Xray amorphous zone of the coating was clearly observed.

5.3.3 SEM cross sectional analysis of nanoscale TiAlCN/VCN deposited by pure UBM and HIPIMS-UBM technique

The influence of high energy bombardment of HIPIMS utilised during the deposition of TiAlCN/VCN has also been observed on the microstructure of the as deposited coating. Figure 5.1 shows the SEM cross sections which clearly demonstrate the structural evolution of nanoscale TiAlCN/VCN coating as a function of deposition technology. In all the three cases, columnar type of coating growth can be seen with significant microstructural difference for UBM deposited coating to that of HIPIMS involved processes (HIPIMS-UBM and pure HIPIMS). Since, all the deposition processes carried out with same deposition conditions, For example bias voltage was -75 V, pressure of gas mixture ($Ar+N_2+CH_4$) of about ~ 4.1×10^{-3} mbar, target power on all the target was 8 kW, with three fold rotation given to substrates in all the three processes. Hence, the significant structural difference can be attributed to the chemistry of the reactively sputtered gas, especially the highly ionised state of reactive plasma achieved when HIPIMS was involved during the deposition, thus confirming the findings of energy resolved mass spectrometry.

In case of UBM deposited coating, the broken rock like, coarse columnar structure with horizontal terminated terrace like structure of UBM deposited TiAlCN/VCN coating (Figure 4.17a) indicate the weak interface bonding between the individual layers of the nanolaminated material. It can be speculated that this is due to the segregation of carbon at the interfaces between the individual nano-layers, which forms a lateral phase and therefore reduces the shear strength of these interfaces [213]. In contrast a very dense almost glassy cross section is observed for the HIPIMS-UBM deposited coatings, Fig 4.17b. It has been reported for CrN coatings deposited by HIPIMS [224] that the high ad-atom mobility of the condensing particles generated in the HIPIMS discharge leads to the growth of large diameter columns effectively reducing crack propagation in fracture sites in the material such as column boundaries. The absence of lateral fracture terraces demonstrates further the overall integrity of the TiAlCN/VCN coatings deposited by a process where HIPIMS is involved.

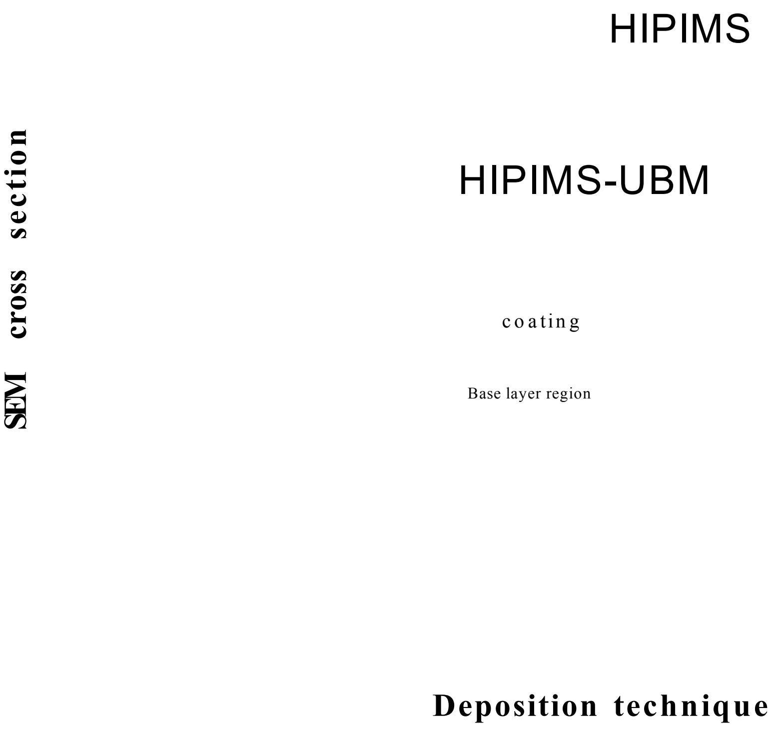

Figure 5.2 The Microstructural difference shown by SEM for nanoscale TiAlCN/VCN coating, as a function of deposition technique.

The paramount influence of high energy bombardment was observed in SEM cross-section of nanoscale TiAlCN/VCN coating when deposited by reactive pure HIPIMS process. It is very important to recall the fact that, during pure HIPIMS deposition, only two targets of TiAl and V were operated (as explained in Experimental part) with constant power applied on both. The careful observation of fractured cross-section SEM micrograph of TiAlCN/VCN coating deposited in this case reveals the columnar structure of the coating with three distinct zones (Figure 4.18a). The adjacent to the substrate carbon free dense TiAIN base layer (~ 60 nm wide first zone) with flat top columns, subsequently a narrow dark band like feature (~ 250 nm thick second zone). The columns are slightly wider on the top but no structural features associated with competitive growth mechanism can be clearly observed in third zone. Further, the intra-columnar structure (Figure 4.18b) is believed to be due to the effect of carbon and enhanced ion bombardment in the case of pure HIPIMS deposition on the coating growth mechanism. When compared this structural evolution to that of pure UBM and HIPIMS-UBM deposited TiAlCN/VCN coating, the major difference is the absence of the zone two (featureless dark band) for the coating produced by the later two processes. Further deep investigation of microstructure was elucidated by GAXRD and TEM cross sectional analysis of TiAlCN/VCN coating, which revealed the unique impact of HIPIMS during the deposition of this coating.

5.3.4 Glancing angle X-ray diffraction analysis of reactive pure HIPIMS deposited TiAlCN/VCN coating

Glancing angle parallel beam geometry was used to determine the phase composition and structure of the coating as a function of the penetration depth in to the film. The depths of penetration which were averaged between 2θ values of 20-110° and assuming intensity attenuation$1/e$ is shown in table 5.2 as a function of Glancing angle of incidence. The coating deposited in this case also shown single phase *fcc* structure and resolving individual reflections from the TiAlCN and VCN phases was not possible. The less intense peaks with broad shape (at GA of 1°, 2°; Figure 4.12) changes to sharper with higher intensity, as the X-ray diffracts from the films when measured at higher GA angles (5°, 10°). This observation further confirmed by the FWHM (table 5.2) calculation which helped to understand the three zones structure seen in SEM cross section. The GAXRD results suggests that the structure of the coating gradually changes with thickness from larger grain crystalline at the base to random orientation smaller grain nanocrystalline to almost X-ray amorphous structure on the top. In fact the 1° GA pattern is very similar to the previously discussed by the authors [225] patterns taken from Cr-C coatings where the carbon content exceeds 80% with respect to bias voltage, which sheds further light on the nature of the top 0.360 μm of the film.

Angle of Incidence o	Depth of penetration (µm)	FWHM (1 1 1)
1	0.36	2.77
2	0.72	2.13
5	1.78	1.67
10	3.58	1.55

Table 5.2 Illustrates the diffraction of X-ray with respect to the film with respect depth and FWHM calculated for (111) peak as a function of glancing angle of incidence.

5.3.5 Microstructural evolution of nanostructured TiAlCN/VCN coating – TEM study

A. Reactive pure UBM and mixed HIPIMS-UBM deposited case

More detailed fine structure of nanoscale TiAlCN/VCN coating deposited in all the three cases were analysed by Transmission Electron Microscopy. In this section the difference between the microstructure of TiAlCN/VCN coating is clearly revealed as a function of deposition technique. Many advantages of HIPIMS have been revealed in the past literatures by many authors by utilizing it during the deposition process. For example in case of metallization Mozgrin et al [226] showed the importance of HIPIMS as technique which can produce higher deposition rate. Kouznetsove et al demonstrated HIPIMS as highly ionised source for filling trenches with high aspect ratio for Cu flux [227]. Alami et al. showed that HIPIMS deposited Ta film on complex geometry substrates can grow with a direction normal to substrate surface [228]. On the other side of application, HIPIMS was successfully used to deposit single nitride film. Systematic study by Ehiasarian et al demonstrated the importance of HIPIMS over UBM deposition where HIPIMS deposited CrN film showed dense microstructure with flat top columns. Thus HIPIMS technique is evolved as successful deposition technique for metal layer deposition to single nitride to oxide and nano layer deposition. After the scaling up of this technique at industrial applications by Ehiasarian et al [229], nano layer CrN/NbN coating was successfully deposited by mixed HIPIMS-UBM, where the influence of HIPIMS was clearly revealed by showing its efficiency in producing highly ionised state of metal atoms and denser microstructure without any inter columnar voids [228].

Figure 5.2 shows the TEM cross-section showing the microstructure of nanoscale TiAlCN/VCN coating as a function of deposition technique. The microstructure of TiAlCN/VCN multilayer coating deposited by reactive pure UBM and HIPIMS-UBM techniques have clearly revealed the all important coating zones such as interface, base layer the bulk of the coating and the top surface of the coating (See Figure 4.19a and 4.19b respectively in Chapter 4). The coating -substrate interface appears very sharp and clean, no contamination or amorphous layers can be observed, which indicates effective surface sputtering during the HIPIMS etching step used prior to the deposition. The physical and metallurgical processes taking place during HIPIMS surface pre-treatment are explained in details in [205]. The clean and sharp interface, which is a fingerprint of HIPIMS etching is produced by effective removal of surface oxide or other contamination layers by bombardment with accelerated to 1000 eV and higher metal ions generated by the HIPIMS discharge. A shallow (5nm-10nm) metal ion implantation also takes place during surface bombardment without deteriorating the crystallinity of the substrate material, which promotes local epitaxial growth of the subsequently deposited coating resulting in high adhesion of the coating. The adhesion value of the coating is listed in Table 4.1.

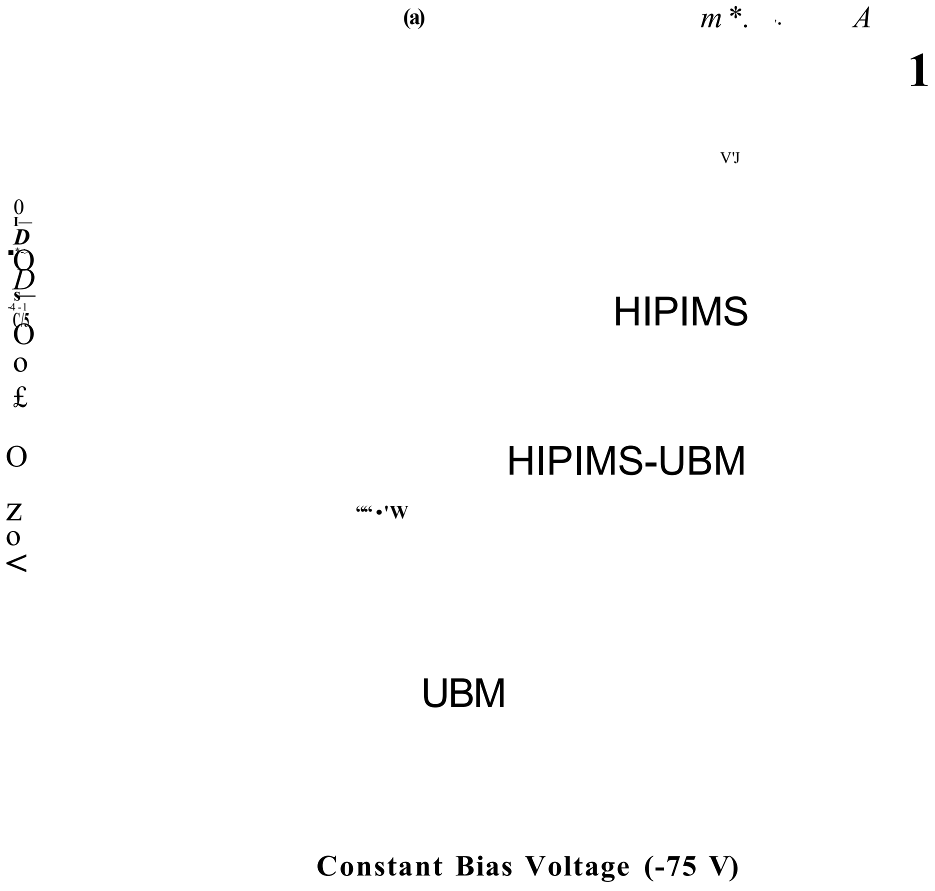

Figure 5.3 TEM cross sectional image of nanoscale TiAlCN/VCN coating as a function of coating deposition.

Significant structural differences were explained in section 4.4.2. The under dense structure with many intercolumnar voids segregated with carbon was resulted for milder ion bombardment case of UBM deposition. The void like intercolumnar structure in some cases start right from the interface and continue through the base layer and bulk of the coating thus providing direct access for the working environment to attack the substrate (see the intercolumnar region pointed by a broken arrow, figure 4.19a). These type of columnar structure might be susceptible to show deformation and fracture under heavy loading conditions. Hence it is very important to close this open columnar week structures, which can be possible only by increasing the kinetic energy transferred to the condensing atoms during the coating growth.

In contrast, when HIPIMS involved, the microstructure was very dense which is attributed to the high energy of the arrival particles resulting in high ad-atom mobility on the substrate surface, increases the nucleation density and significantly reduces the atomic shadowing effect during the coating growth Figure 4.19b. Atomically clean coating-substrate interface appears any contamination or amorphous zone to the effective bombardment of the surface by high energy V^+ metal ions generated in the HIPIMS discharge, resulting in intensive sputter-cleaning of the surface and low energy ion implantation as described in details in [205]. It is expected that the void- free structure of HIPIMS-UBM coatings could provide better protection against wet or high temperature corrosion and show enhanced mechanical properties such as hardness and wear resistance. Also, careful observation of the coating microstructure reveals a dense, free of inter-columnar voids coating, which is a pre requisite for better protection against rapid oxidation at high temperatures and enhanced mechanical and tribological properties at elevated temperature. The figure 5.3 shows the higher magnification image of Base layer (TiAlN) – coating (TiAlCN/VCN) interface and highly dense part of the coating which clearly reveals the multilayer structure.

Thus, when HIPIMS is involved during the coating growth, the significant advantage has been seen in two aspects. First, the average kinetic energy transferred to the film during the coating growth is increased. This can be justified by the high fraction of metal ions sputtering observed through energy resolved mass spectrometry. Hence, higher fraction of metal ions bombardment during the HIPIMS-UBM deposition has significantly increased the adatom mobility on the substrate surface and as a result denser microstructure was achieved. The column boundaries are closed which has reduced vertical segregation of carbon atoms. Thus highly dense microstructure achieved in this case, has shown its tribological advantage in terms of enhanced wear resistance when compared to UBM deposited coating. The carbon interface between the individual layer is believed to reduce the bonding strength and helps to delaminate individual layer laterally along sliding direction. Further, benefit of closed columnar dense microstructure was observed in terms of oxidation resistance of the coating, which will be discussed in the coming section.

Figure 5.4 High magnification image of TiAlCN/VCN coating deposited by HIPIMS-UBM technique showing highly dense microstructure.

B. Reactive pure HIPIMS deposited case

The major microstructural change has been observed for TiAlCN/VCN coating, when deposited by reactive pure HIPIMS technique. The high energy bombardment by higher fraction of metal ions (Ti^+, Al^+ and V^+) and carbon ions (C^+, $C_xH_y^+$) have influenced the grain growth of TiAlCN and VCN, in a unique way. Figure 5.1 shows the variation in the microstructure of TiAlCN/VCN coating grown under the influence of milder ion bombardment (UBM), high energy bombardment (HIPIMS-UBM) and pure HIPIMS technique at constant bias voltage of -75 V.

The low magnification BF image of pure HIPIMS deposited coating shows the microstructure which is distinct itself from other two cases of UBM and HIPIMS-UBM. The TEM micrographs of HIPIMS deposited coating further revealed the fine structure of the base layer (TiAlN), and bulk of the TiAlCN/VCN coating. The coating clearly demonstrated the “graded microstructure” of TiAlCN and VCN grains. The coating showed 5-8 nm thick multilayer structure adjacent to TiAlN base layer. This region reveals a white lateral phase segregated at the interfaces of the individual layers. This structure is typical for TiAlCN/VCN coatings deposited by sputtering and its growth mechanism was described previously in [213]. The structure which evolves further with coating growth is one of a typical nanocomposite consisting of dark contrast grains (most probably Me-CN where Me is Ti-Al-V) surrounded by carbon-based phase forming a white contrast tissue phase (figure 4.21). The grain size reduces gradually with thickness at the expense of the white phase and no grains can be seen on the very top region of the coating (figure 4.21).

The Point EDX analyses were carried out in different zones of the coating namely base layer and nanoscale multilayer, bulk of the coating and top of the coating, has further confirmed the gradual transformation in the structure with thickness of the coating takes place changing from crystalline at the base to nanocrystalline in the bulk and finally random orientation small grain nanocrystalline to almost X-ray amorphous structure on the top. The GAXRD measurements (Figure 4.15) taken on pure HIPIMS deposited TiAlCN/VCN coating at various angles have further confirmed the graded structure of the coating.

Usually, the nanocomposite or graded microstructure was possible to achieve only through hybrid processes involving two or more sequential deposition steps. But in this particular case of "pure HIPIMS", we could achieve graded like microstructure for TiAlCN/VCN coating in single deposition run. This unique structure and obviously compositional evolution obtained in one deposition process is believed to be due to the target poisoning effect which takes place in reactive (carbon-nitrogen containing atmosphere) HIPIMS. A clear evidence about the reactivity of the HIPIMS plasma sustained in a mixed CH_4+N_2+Ar atmosphere was gathered by the energy resolved mass spectrometry, see paragraph 4.1 and 5.1. The large amount and variety of reactive gas ions as well as free carbon ions (C^+) influences strongly both the target poisoning effect (reduction of the metal content in the film with time) as well as the C incorporation in the film. AES depth profile (not shown here) revealed that the C content in the film gradually increased with the film thickness from 25 at % at the TiAlN base layer-TiAlCN/VCN coating interface to 70% at the very top of the coating. Thus, increased condensation of free carbon atoms on the grain boundaries of growing film can hinder the (Ti-Al-V)-CN grain growth by forming extra nucleation sites for a-C and C_xN_y grain growth surrounding Me-CN phase. Similar results of structural transitions from solid solution Ti (N, C) to nanocomposite of nc-Ti(N,C)/a-(C,CN_x) was reported for pulsed DC magnetron sputtered Ti-C-N coating[230]. In this case, the graphite target was used to incorporate C in the TiN matrix. Graphite targets usually require higher discharge powers in order to incorporate more C inside the Me-N phase, which is not advisable since the process of C incorporation from graphite have often reported to produced dislocations/defects inside the coating [230, 231]. As a contrary, in our case, since high energy ionic species of methane ($C_xH_y^+$) is obtained by high frequency electron impact with CH_4 molecule, the possibility of C atom implantation inside the growing film is more precise. This fact avoids the possible formation of porous structure or defects inside the deposited film, thus leading to denser microstructure, as seen in Figure 4.20.

5.4 Oxidation behaviour

Elevated temperature (up to ~750 °C) oxidation behaviour of TiAlCN/VCN multilayer coating deposited by all the three technique was analysed by two different approaches. First one is by iso-thermal oxidation analysis using thermogravimetric (TG) analyser (room temperature to 1000 °C), and second one is by tribo-oxidation during dry sliding process performed at three set of temperatures from room temperature (RT) to 650 °C. Only difference between above mentioned approach is that, in the former case, coating surface is influenced by only surface oxidation process, where as in the later case, both surface oxidation and tribo-oxidation processes were played an important role in determining the oxidation behaviour of the coating at elevated temperature. Subsequently the characterisation of oxidised surface was carried out by TG, XRD, Raman and SEM analysis only on HIPIMS/UBM deposited coating, since the chemical composition is same in all the three deposited case. The influence of as formed oxide phases identified by above mentioned analysis is then correlated to friction and wear behaviour of the coating.

In case of isothermal oxidation, the substrate (stainless steel) was deposited on all the sides, oxide contribution from the substrate was prohibited. But, during dry sliding conditions, the oxides from the substrate (High speed steel) were also identified. In case of polycrystalline thin films the oxidation process is assumed to be governed by the diffusion of oxygen molecules within the coherent layers; in our case it is within alternate layers of TiAlCN and VCN. Hence, the oxidation behaviour of the nanoscale

TiAlCN/VCN multilayer coating has clearly shown its dependency on coating microstructure, which is strongly influenced by the deposition technique utilised to deposit the coating.

The T-G curves for the coatings deposited by all the three processes of UBM, HIPIMS-UBM and pure HIPIMS have shown similar trends (see figure 4.23). The oxidation process in all the three cases developed in two stages except for pure HIPIMS deposited TiAlCN/VCN coating. GAXRD pattern of the as deposited and oxidised surface of TiAlCN/VCN coating deposited by mixed HIPIMS-UBM taken at an incident angle of $\omega = 2°$. The coated samples were heat-treated isothermally in the furnace of the TGA system for 15 min at 200 °C, 560°C, 670°C, and 750°C respectively. The temperatures were chosen on the basis of the specific regions of the T-G curve (Figure 4.23). As discussed in the results section 4.5.2, important oxide phases of Al_2O_3, TiO_2 (Brookite), TiO_2 (Rutile), VO_2, V_2O_3, V_3O_7, V_2O_5, AlV_2O, $AlVO_4$ have been identified from the oxidised surface of TiAlCN/VCN coating. Despite Al_2O_3, all other oxide phases are found to be stable after thermal and tribo-oxidation process. These oxide phases are classified as Magneli phase oxides based on the earlier literature reports illustrating their special crystal structure with low inter atomic layer shear strength. Numerous literatures are available explaining the contribution of Magneli phase oxides in stabilizing friction and wear performance of the coating under dry sliding conditions. For example oxygen deficient crystal structures for Ti-based oxides with rutile form of TiO_{2-x} have known to change their shear strength when tangential force is applied through sliding wear conditions [246, 247]. Similarly, Vanadium is known to form Magneli phase with oxygen. General stoichiometric formula for these vanadium based Magneli oxides can be given as [248]:

$$V_nO_{2n-1} = V_2O_3 + (n-2)\ VO2 \text{ where } 3 \leq n \leq 9.$$

These oxide crystal structures based on Ti and V are known to accommodate velocity between the two sliding counterparts leading to reduced friction force between the tribo couples. Further the Raman spectra (see Figure 4.29) collected from the wear track have also shown signature of similar oxide phases with additional oxides of Fe_2O_3 and Cr_2O_3 which are contributed from the substrates during the tribo-oxidation mechanism.

TiAlN is probably one of the oldest PVD coatings dedicated to high temperature applications. Alloying TiN with Al was a successful approach due to formation of a double layer oxide scale (TiO_2/Al_2O_3) where the dense top Al_2O_3 layer provides a barrier for the diffusion of oxygen from the environment thus enhancing the oxidation resistance of the coating [249]. Reported values for the temperature of the onset of rapid oxidation of TiAlN are in the range of 850°C [250]. Unlike Al, addition of V and C to the coating constitution is expected to deteriorate the oxidation resistance; therefore the application of TiAlCN/VCN is restricted to the medium temperature range of up to 800°C.

The oxidised surface of the coating after 200 °C have shown very thick layer, probably of crystalline α-Al_2O_3, formed due to the initial reaction between the Al and oxygen molecules forming a protective layer against rapid oxidation. The figure shows the SEM micrograph of oxidised surface of TiAlCN/VCN coating after 200 °C. The EDX spectrum clearly shows the Al peak which clearly supports the fact of formation of Al-rich oxide phase at these early stages of oxidation process. This result is further confirmed through Raman analysis of wear track generated at 200 °C, which successfully identified the traces of α-Al_2O_3 phase formed due to tribo-oxidation.

The possible reaction at this stage can be written as,

$$4Al + 3O_2 \rightarrow 2Al_2O_3$$

At this particular stage, since Al_2O_3 acts like potential barrier for oxygen molecule to penetrate further into the grain boundaries of the coating, the oxidation of coating element is not been observed. At this stage, the tribo-oxidation process is observed to be less pronounced in forming lubricious oxides. This fact was confirmed through the Raman spectra collected from the wear debris which showed minimal signature for lubricious Magneli phase oxides (see Fig. 4.29). This is due to the less humid condition countered on the coated rotating disc at this particular temperature, where sufficient lubrication by Magneli phase oxide against alumina ball is significantly less than that observed at higher temperatures. Hence combined effect of surface oxidation and tribo-oxidation is not much favoured in producing lubricious oxides are believed to be the important reason for sudden increase of the coefficient of friction value (0.8) when sliding test performed against alumina (Al_2O_3) ceramic ball at 200 °C (see figure 4.10). It is also important to notice that in all the three deposited case, wear rate of the TiAlCN/VCN coating at 200 °C, where the wear rate was higher by one-to-two order of magnitude when compared to the wear rate calculated for the same coating at room temperature (see table 4.1). This was attributed due to the brittle failure of the coating material at the asperity contacts and causes three body wear mechanism at this particular stage.

Subsequently after 200 °C, gradual increase in the mass gain was observed in case of UBM and HIPIMS-UBM deposited coating at 550°C. This is believed to be due to oxidation of V which is then followed by a steep mass increase at 800°C representing the temperature for the onset of rapid oxidation of the entire coating. However, the onset of rapid oxidation for the UBM and HIPIMS-UBM deposited coatings is higher by 162°C than that reported earlier for the carbon-free arc- bond-sputtered TiAlN/VN (≈638 °C) coatings where the etching step is carried out by arc discharge [232]. This significant increase of the oxidation resistance of the HIPIMS etched coatings (A and B) can be attributed to the elimination of the droplet phase in HIPIMS and therefore the growth defects which are a common feature for the arc etched and UBM deposited coatings [251]. It is also interesting to note that the amount of oxygen diffusing into the coating at elevated temperature, represented by the sample weight-gain, is greater for the UBM deposited coating compared to HIPIMS-UBM deposited coating. This can be clearly seen in Figure 4.23 where the oxidation curve of the UBM deposited coating shows about 30% more weight gain compared to that of the (HIPIMS-UBM) deposited coating. This can be attributed to the more porous microstructure of the UBM deposited coating compared to that of the (HIPIMS-UBM) deposited one. These observations clearly demonstrate the effect of the more energetic ion bombardment achieved during the HIPIMS deposition process on the microstructure of the coating, which in turn improved the oxidation resistance of the coating at elevated temperatures.

Significant difference can be seen in the case of reactive HIPIMS deposited TiAlCN/VCN coating. The onset of rapid oxidation was shifted to higher temperatures of about ≈ 810 °C as compared to the UBM and HIPIMS+UBM cases. Furthermore, compared to the UBM deposited coatings, no initial oxidation at 550 °C was observed. The weight gain due to oxidation is lower by factor of two when compared to UBM deposited TiAlCN/VCN coating which again demonstrates the effect of the coating densification due to utilisation of HIPIMS. Further, the top X-ray amorphous zone of the coating expected to delay the diffusion of oxygen molecules as zone is of free from grain boundaries to provide diffusion path.

The coating oxidised at 560 °C, (immediately after the first step mass gain) show a mixture of different oxide phases of TiO_2 (Rutile and Brookite), VO_2, V_2O_3, V_3O_7, V_2O_5 and $AlVO_4$. These observations of V-based Magneli phase oxides are consistent with the previously reported literature by Lugscherider et.al. [252], where stable polycrystalline mixtures of V_2O_5 and VO_2 are observed up to a temperature of 605 °C in vanadium oxide coating deposited by MSIP-PVD process. N. Fetch et.al. [203] has also reported the formation of various type oxygen reduced state of V-based oxides formed after oxidising VN coating at 600 °C. Recently, Zhou et.al. [232], studied the oxidation property of carbon free TiAlN/VN coating deposited by UBMS technique, has also shown the formation of V_2O_5 dominated phase in the oxidised surface of TiAlN/VN coating at 600 °C. The morphology of the oxide scale formed at 560°C, is showed in result section (see Figure 4.26). The oxide particles with plate like shape were V- and Ti- deficient and richer in Al, which most probably indicates the $AlVO_4$ phase. This was confirmed through EDAX measurement as shown in Figure 4.27. Further increase of the temperature to 610 °C, only V rich oxides with needle like morphology (see Figure 4.26) have been identified which is also confirmed through EDAX measurement as shown in Figure 77b.

These findings are further supported by GAXRD pattern taken at 670 °C (figure 4.24), which has clearly showed the mixed phase of oxides dominated with rutile and $AlVO_4$ with increased peak intensity in the region between $2\theta = 26°- 27°$. At the same time, a decrease in the intensity of the peak at $2\theta = 25°$was observed, which can be explained by the transformation of Brookite phase to Rutile phase which takes place at >500 °C [253]. At the same time, a decrease in the intensity of the peak at $2\theta = 25°$was observed, which can be explained by the transformation of Brookite phase to Rutile phase which takes place at >500°C [253]. Some amount of AlV_2O phase was also detected. The formation of $AlVO_4$ and AlV_2O are reasoned with bulk reaction of Al_2O_3 and V_2O_5 [233]. The Raman spectra collected from the wear track generated at 450 °C, has shown high intensity peaks for V_2O_5, which is combined effect of oxide formation by tribo-oxidation (flash temperature > 600 °C and external heating of the sample. It is very important to notice here, that the V_2O_5 has the tendency to go to molten phase at this stage i.e. at flash temperatures achieved at the asperity contacts during sliding, implies friction reduction (0.5 measured in our case at 450 °C), due to sliding over molten phase. The smooth surface morphology of the wear track at this stage discussed in section 4.5.3 is clear evidence of this fact.

At 750°C, a temperature close but below the onset of rapid oxidation (800°C) a further increase of the intensity of the peaks detected at 670 °C can be observed, which indicates simply a kinetic progression of the oxidation process. It is important to mention however that in previous studies of the oxidation behaviour of UBM deposited TiAlN/VN [244], oxides such as V_2O_5, $AlVO_4$, TiO_2 were only detected at temperatures below 635°C. Above this temperature rapid oxidation and oxide scale spallation was reported. In comparison, in the case of (HIPIMS-UBM) deposited coatings the potentially lubricious oxides of V_2O_5, $AlVO_4$ and TiO_2 well adherent to the substrate were present to temperatures up to 750°C. As no Cr, Ni or Fe based oxides were detected, it can be assumed that the stainless steel substrate was reliably protected by the PVD coating up to the test temperature. The Raman spectra from wear track generated at 650 °C has shown (see Figure 4.29) higher intensity showing formation of a mixture of several oxides such as α -F_2O_3, V_2O_5, and TiO_2. This spectral range have also shown significant amount of V-containing Aluminium oxide phase, most probably $AlVO_4$ as identified by XRD analyses. The α-F_2O_3 is contributed by wear debris of the substrate material. SEM observations showed oxide scale morphology similar to that formed at 670°C, Fig.4.26c. At this stage as indicated by the TG curve a larger amount of lubricious oxides is formed, which provide more effective solid lubrication resulting in smooth wear surface morphology. The smoothest wear track morphology is achieved at the highest test temperature of 650°C as at this stage due to the synergy effect of the tribo and external heating oxidation the largest amount of the lubricious oxides is generated, which promotes the polishing effect during sliding. This situation is also reflected by the coefficient of friction curve on figure 4.10 here the coefficient of friction at 650°C is the lowest. This study shows that there is a clear link between the environmental conditions and the amount of the lubricious oxides generated during dry sliding and the friction and wear behaviour of the PVD coating.

5.5 Wear mechanism and cutting performance of TiAlCN/VCN coated cutter in machining Al-alloy

During the dry sliding conditions, formation of thick tribofilm adhered to the worn surface was considered as a major setback for the tool life time [254]. The thickness of this tribofilm was measured to be around 5-10 nm. These strongly bonded tribofilms pluck several 10s of nanometre thick coating material from the tool edge there by leading to faster wear rate [213]. This tribofilm formation was reduced by producing coating which is chemically inert to the work piece used during the machining process. One of the major challenges in the aerospace industry are machining of sticky alloys (Ti, Al, Ni). The TiAlCN/VCN multilayer coating has emerged as an alternative [213], to the carbon free TiAlN/VN coating which has shown faster wear rate during the machining [255] of those sticky alloys. The intention behind the carbon inclusion between the individual layers of TiAlN/VN was to reduce the metallurgical reaction with work piece materials (sticky alloys) such as Ti, Al and Ni based alloys during machining process [213]. The segregation of carbon between the interface of TiAlN and VN is shown in Figure 5.4. Further, this carbon layer has reduced the shear strength between the multilayers, which has been a key requirement for the smooth wear mechanism dry sliding conditions. This mechanism was termed as "layer by layer" wear mechanism [213]. The recent report has revealed the fact that during dry machining of aerospace grade Al-based alloy, TiAlCN/VCN coated tools have shown a factor four longer life time than compared to DLC and TiAlN/VN coating [213]. In one more experiment, the TiAlCN/VCN coated drill has produced 130 holes on the MMC in contrast to 2 holes produced by uncoated drills [213]. Here, the coating was deposited by UBM technology. The enhanced tribological performance of TiAlCN/VCN coating in this report was attributed to the layer by layer wear mechanism.

Wear mechanism during the dry sliding conditions are often controlled by the oxides formed between the tribo-couples which further determine the performance of the coated tools. The successful protective tool requires good adhesion, high wear resistance at cutting temperatures, chemical stability and inertness relative to the work piece. Besides this preliminary requirement structurally, the coatings should be denser with fine grain, crystalline microstructure, smooth surface morphology and controlled compressive residual stress are also important. Hence the effort in this thesis was to meet all the above requirement to protect the tools utilised in for machining sticky alloys used in aerospace industries.

Two flute 25 mm diameter, 2.5 radius high speed machining end mills from S290 HSS materials is coated with TiAlCN/VCN coating by HIPIMS-UBM technique. The purpose of conducting this test was to correlate the oxidative wear mechanism of TiAlCN/VCN coating determined at laboratory conditions with that of practical application of dry high speed milling test. At laboratory scale, the pin-on-disc dry sliding tests were carried out and as formed oxide debris were analysed with Raman spectroscopy. Similarly, after dry milling test, the tool edge was characterised from Raman spectroscopy in order to understand the chemical integrity with the coating stability.

The Raman spectroscopy and XRD has clearly revealed the formation of the lubricious Magnèli phase oxides suchas as V_2O_5 [20], TiO_2, $TiAlVO_4$, etc, both after isothermal and tribo oxidation mechanism. Similar oxide phases have also been identified on the tool edge after performing metal cutting operations. These facts clearly confirm the beneficial effect of the V in the reduction of friction. Apparently the effect of carbon has also been observed very clearly in stabilizing the friction and wear both in pin-on-disc and during milling test. The higher intensity D and G bands observed in both Green and UV laser spectra demonstrate that during machining graphitic carbon is formed on the coating surface which acts as a solid lubricant. This has been shown in both the case of deposition i.e., UBM and HIPIMS-UBM (Figure 4.32 and 4.33). Hence, there is not much difference in terms of chemical integrity of the TiAlCN/VCN coating has been seen with respect to the technology being utilised to deposit the coating.

Careful observation of the flank wear curve (Figure 4.31) vs number of laps suggests that the HIPIMS-UBM deposited cutter exhibit more stability during the wear performance with slow increase in the flank wear rate with cutting length over 500 m (0.486 m in each cutting pass). This can be seen by sudden increase in the flank wear in case of UBM deposited cutter. Also, the lower surface roughness value measured in case of HIPIMS-UBM deposited cutter (0.023) when compared to UBM deposited cutter (0.026) prior to the machining process has lead to form reduced BUE formation after cutting operation. This can be clearly seen in Figure 4.30a. The surface finish after the machining operation for HIPIMS-UBM deposited cutter was better than UBM deposited cutter.

The Raman spectroscopy measurements collected from the UBM deposited tool cutter has shown the evidence of graphitisation process that is believed to develop due to the combined mechanical and thermal load exerted on the tool surface during cutting. The high hardness SiO_2 and mixed (AlSi) O constitute the built up material which is "cold welded" to the tool surface. The periodic removal of this material which carries away some portions of the coating represents one of the wear mechanisms taking place on the cutting edge another being the micro abrasion. Moreover, the Raman identification of lubricious oxides both at SiAl alloys BUE contact surface and tool edge (Figure 4.30 a and b) demonstrates that the material removal by cutting is accompanied by intensive material transfer between the surfaces of the tool and work piece material in the sliding contact. While this is a common situation in any cutting process this study shows that a proper coating material selection in the coating design stage could dramatically influence the tribology in the contact area by providing compounds with lubricious properties in dry sliding conditions.

In summary, after comparing the milling test by tools coated with UBM and HIPIMS-UBM deposited coating, it is very difficult to draw a conclusion as which technique is better. This is because, the wear performance in both the cases is appeared to be stabilizing due to lubricating oxides forming between the tribocouples. However, the slight impact of structural difference observed in TEM micrograph for coating deposited with two techniques (UBM and HIPIMS-UBM) has shown marginal variation in the flank wear during the milling test. This has been explained in the above paragraph.

Chapter 6

Conclusions

This research work was aiming to decrease the gap existed between understanding the HIPIMS technology and its impact on microstructure and functional properties of nanoscale TiAlCN/VCN coating, which was previously developed in our group by conventional UBM technology. A systematic investigation of high metal ion bombardment observed during HIPIMS technique and its impact on the microstructure, mechanical, oxidation and tribological properties of nanoscale TiAlCN/VCN coatings has lead to an important contribution to the understanding of the growth processes taking place in TiAlCN/VCN system especially when HIPIMS was utilized. The importance of HIPIMS technology has been realised in each and every aspect of the results obtained in this research work. But, a very important and unique finding has been in terms of microstructural evolution of TiAlCN/VCN coating from multilayer to graded like microstructure, which was achieved for TiAlCN/VCN coating when deposition was carried out with pure reactive HIPIMS process. This has further increased the important of HIPIMS and opened a new door for advanced research and development in the field of thin film, where functionally graded nanostructures and their importance in real world nano device application are increasing. Since, HIPIMS technology is plasma based PVD technique, the advantage of HIPIMS technique was realized in dissociation of hydro carbon molecules in to high energy carbon ions during the deposition of TiAlCN/VCN. Hence, it will not be a surprise if HIPIMS replaces PIII and PACVD technology, which were predominantly used in industries to deposit carbon based coatings such as DLC, Me-C etc.

Following conclusions are made for TiAlCN/VCN coating deposited by UBM and HIPIMS-UBM techniques

- Nanoscale TiAlCN/VCN coating was successfully deposited in industrial PVD coating machine (Hauzer HTC-1000-4) by reactive UBM, HIPMS-UBM and pure HIPIMS techniques on various substrates including complex geometry milling tools.
- Mass spectrometry analysis of the HIPIMS of V plasma during the surface pre-treatment process revealed the presence of higher content of V^+ metal ions as

compared to Ar^+ gas ions with a ratio of 1.25:1, respectively. The majority of metal ions were V^{2+} with 27% and ionization states of up to 5^+ were detected.

- Mass spectroscopy compared the plasma composition during TiAlCN coating deposition process using HIPIMS or UBM discharges. It was found that the metal ion content in the HIPIMS discharge was about 12% with Al^{1+}=9%, Ti^{1+}=2%, C^{1+}=1%, whereas in UBM mode only 3% of metal ions with Al^{1+}= 2.8%, Ti^{1+}= 0.23%, and C^{1+}=0.13% were detected which is significantly lower than in the HIPIMS. Likewise, during the deposition of VCN, the metal ion concentration was found to be 7.73% in case of HIPIMS and significantly lower at 0.56% in case of DC discharge.

- The ion flux in the coating step for both HIPIMS and UBM processes was dominated by gas. Ions of the following species were identified in the mass spectra: Argon, N_2, stable hydrocarbons (CH_4, C_2H_2, C_2H_4, C_2H_6, C_3H_8), radicals (CH, CH_2, CH_3, C_2H, C_2H_5, C_3H_2, C_3H_3, C_3H_6, C_3H_7), and nitril compounds (HCN, H_2CN, NH, and NH_3).

- Cross-sectional SEM imaging revealed clear differences in the structure of HIPIMS-UBM and UBM deposited TiAlCN/VCN coatings. UBM coatings show open, broken-rock like coarse columnar structure where mejority of columnar structures are terminated with horizontal terraces, which indicates relatively weak interface bonding between the individual layers of the nanolaminated material. In contrast a very dense almost glassy cross section is observed for the HIPIMS-UBM deposited coatings.

- XTEM analyses further confirmed the under-dense structure of UBM coatings showing a course structure with many inter-columnar voids. When HIPIMS is involved in the deposition step, extremely dense and smooth coatings were deposited, which was attributed to the high energy of the arrival particles resulting in high ad-atom mobility.

- Thermo gravimetric analysis showed that TiAlCN/VCN coatings have relatively high onset of rapid oxidation temperature in the range of 800°C. However, HIPIMS-UBM coatings showed by 30% less oxidation weight gain as compared to pure UBM coatings.GA-XRD analyses demonstrated that not only the thickness but also the phase composition of the oxide scale varies with the exposure temperature. It was found that for HIPIMS-UBM deposited coatings the potentially lubricious oxides of V_2O_5, $AlVO_4$ and TiO_2 well adherent to the substrate were present to temperatures up to 750°C.

- Low coefficient of friction of μ=0.65 was measured for TiAlCN/VCN coatings for both deposition techniques, HIPIMS-UBM and UBM. However, the wear coefficient of the coating deposited by HIPIMS-UBM showed two orders of magnitude lower value ($1.4x10^{-17}$ $m^3N^{-1}m^{-1}$) than that for the UBM deposited coatings ($4.2x10^{-15}$ $m^3N^{-1}m^{-1}$), which represents significant advantage. This enhanced performance in dry sliding wear conditions can be attributed the extremely dense structure of the HIPIMS coatings.

- The Pin-On-disc measurements revealed a significant reduction in the friction coefficient from 0.67 ambient temperatures to about ≈0.5 at 450 °C and ≈0.4 at 650 °C. This can be attributed to the as-formed highly lubricious magnelie phase structured oxides such as V_2O_5, VO_2, TiO_2, and $AlVO_4$ during the sliding process. Also, the presence of a carbon based phase between the individual layers of the nanolaminate further influences the wear behaviour by layer by layer wear mechanism. This can be seen by measured low wear rate of $Kc=1.4x10^{-17}$ $m^3N^{-1}m^{-1}$, during the sliding process.

- The Raman spectroscopy studies have identified the generation of highly lubricious phases (V_2O_5, VO_2, TiO_2, and $AlVO_4$) during sliding at room and elevated temperature thus providing additional tool for better understanding the high temperature tribological behaviour of TiAlCN/VCN.

Following conclusions are made for TiAlCN/VCN coating deposited by pure HIPIMS process

- The novel HIPIMS technology offers better plasma conditions with higher ionisation and higher Me+ to Ar+ ratio: For pre-treatment conditions: highly charged V metal ions - up to 4^+ and metal ion -to- gas ion ratio >1

  For deposition conditions: factor 10 more carbon ions - fully stripped of hydrogen, factor 3 more Al ions and factor 10 more Ti ions when compared to UBM sputtering.

- The analysis showed that a gradual transformation in the structure with thickness of the coating takes place evolving from crystalline nanoscale multilayer of TiAlCN/VCN at the base to nanocomposite structure comprising nanocrystalline TiAlVCN surrounded by C-based tissue phase in the bulk and finally to Xray amorphous structure of Me-C on the top. This is a unique coating architecture where the toughest multilayer zone is at the bottom leading to enhanced load bearing capacity, followed by a nanocomposite zone which provides for high wear resistance finally followed by a dense X-ray amorphous top layer (having no grain boundaries) which enhances the oxidation resistance.

- "Depth profiling" the friction and wear behaviour at room temperature of the HIPIMS deposited TiAlCN/VCN coatings revealed that immediately after the "running" stage, a low friction coefficient zone exists where the mean value of COF is $\mu = 0.37$. After that the friction gradually increases to reach a "steady state" zone where higher coefficient of friction values of $\mu = 0.48$ were recorded. In comparison, UBM deposited TiAlCN/VCN coatings tested under similar conditions show an order of magnitude higher wear coefficient of 4.1×10^{-15} $m^3N^{-1}m^{-1}$.

- TG analyses revealed that the onset of rapid oxidation for reactive HIPIMS deposited TiAlCN/VCN coatings was shifted to higher temperatures as compared to the UBM and HIPIMS+UBM cases to about 800 °C. The weight gain due to oxidation was factor of five lower than UBM deposited coating.

- High temperature pin-on-disc tests revealed that the COF of HIPIMS-deposited TiAlCN/VCN initially increases to $\mu = 0.8$ at 200 °C and then decreases to $\mu = 0.45$ at 650 °C. HIPIMS deposited TiAlCN/VCN show superior performance at elevated temperatures of 650 °C, ($Kc = 1.0 \times 10^{-13}$ $m^3N^{-1}m^{-1}$) over the UBM deposited ($Kc = 5.8 \times 10^{-13}$ $m^3N^{-1}m^{-1}$).

  Raman spectroscopy analysis on the cutting edge of TiAlCN/VCN coated end mills and the contact surface of the built up material produced during machining of Al-Si alloy revealed that the cutting process produces lubricious phases: V_2O_5 Magnèli phases via tribooxidation and graphitic carbon via high temperature exposure. At the same time highly abrasive phases of SiO_2 and mixed (AlSi)O are formed as well which are the main source of wear of the cutting edge.

Further research

The following points will highlight the possible research work which can be carried out in near future as pertaining to the present research work projected in thesis:

TiAlCN/VCN coatings are successfully deposited by different techniques, such as reactive UBM, HIPIMS-UBM and pure HIPIMS process. Since all the deposition techniques carried out under similar bias voltage (-75 V), the comparative microstructural investigation can be studied by producing the coating at different ion bombardment conditions (different bias voltages) by above mentioned techniques.

The TGA analysis performed on the coating has shown successively lower oxide mass gain for each of the three types of IPVD techniques used in this work. A systematic study on type of oxide formation, their structure can be carried out at elevated temperature inorder to correlate its importance for wear performance at respective temperatures. For this, cross sectional SEM, TEM and Raman and XRD analysis would be necessary.

The importance of wear engineering oxides both at room and elevated temperature tribological applications can be investigated by crossectional TEM analysis of wear tracks generated by pin-on-disc measurement at specific test temperatures. This would lead to understand the role of tool wear mechanism in real world applications of high speed machining against the work piece. Here, it is important to carry out the crosssectional TEM analysis and Raman spectroscopy of worn coated tool edge. This helps to compare the laboratory scale experimental results with real time problem faced during the application.

In case of reactive pure HIPIMS deposited TiAlCN/VCN case, the microstructure with functionally graded zones (multilayer-nanocomposite-Xray amorphous) were observed. Moving further, the deposition parameters such as CH_4 gas flow or change in the partial pressure of CH_4 can be altered at various bias voltages, so that the carbon incorporation and its effect on the microstructure of TiAlCN/VCN can be studied. Simultaneously, the systematic plasma monitoring during the reactive HIPIMS deposition process can be carried out, where "target poisoning" effect triggering the onset for transition in microstructural zones can be understood in detail. This could lead to optimise the reactive HIPIMS process in producing graded like microstructure.

After optimising the reactive pure HIPIMS process, the mechanical and tribological properties of individual zones can be studied in detail separately after achieving individual zones of the functionally graded microstructure. This amounts to detailed understanding of the importance of reactive pure HIPIMS deposited nanostructured TiAlCN/VCN coating for advanced tribological applications.

The important finding revealed in this research work by utilising reactive HIPIMS for nanostructured TiAlCN/VCN coating further motivates to use this technology in the development of other coatings involving carbon, especially, C/Cr, Me-DLC etc.

References

[1] P. Eh. Hovsepian, Q. Luo, G. Robinson, M. Pittman, M. Howarth, D.Dowerwald,"TiAlN/VN superlattice structured PVD coatings: A new alternative in machining of aluminium alloys for aerospace and automotive components", Surf. Coat.Technol, Vol. 201, 265-72, 2006.

[2] O. Knotek, F. Löffler, G. Krämer. "Cutting performance of multicomponent and multilayer coatings on cemented carbides and cermets for interrupted cut machining", Int. J. Refractory Metals Hard Mater, Vol 14, No l/3, 195-202, 1996.

[3] H. Hollek, "Material selection for hard coatings", J.Vac.Sci.Technol. Vol A(4) 6, 2661, 0734-2101, 1986.

[4] D. T. Quinto "PVD Coating Applications for Cutting Tools", in plasma surface engineering research and its practical applications, edited by R. WEI.

[5] D. McIntyre, J.E. Greene, G. Hakansson, J.-E. Sundgren, W.-D. Münz, "Oxidation of metastable single-phase polycrystalline Ti0.5Al0.5N films: Kinetics and mechanisms", J.Appl.Phys. Vol. 67, 1542, 1990.

[6] M.Lahres, P. Müller-Humel and O. Doerfel, Applicability of Different Hard Coatings in Dry Milling Aluminium Alloys, Surf. Coat.Technol, Vol. 91(1-2), 116-121, 1997.

[7] Y.T.Pei, Galvan, D. & De Hosson, J.T.M., "nc-TiC/a-C nanocomposite coatings for low friction and wear resistance", Materials Science Forum, Vol. 475, 3655-3660, 2005.

[8] S. Veprek, M. G. J. Veprek-Heijman, P. Karvankova, J. Prochazka, "Different approaches to superhard coatings and nanocomposites", Thin Solid Films, Vol. 476, 1-29, 2005.

[9] O.Knotek, A.Barimany, B.Bosserhoff and F.Loffler, "Structure and properties of magnetron-sputtered Ti-V-N coatings", Thin Solid Films, Vol. 193-194, 557-564, 1990.

[10] K. Noguchi, N. Kitagawa, H. Ohara, H. animoto, 1st French & German Conf. on High Speed Machining, University of Metz, 407-413, 1997.

[11] C.P. Constable, J. Yarwood, P. Eh. Hovsepian, L.A. Donohue, D.B. Lewis, W.-D. Münz, "Structural determination of wear debris generated from sliding wear tests on ceramic coatings using Raman microscopy", J. Vac. Sci. Technol, Vol. A(18) 40, 1681, 2000.

[12] P.Eh.Hovsepian, A.Ph.Ehiasarian, A.Deeming, C.Schimpf, "Novel TiAlCN/VCN nanoscale multilayer PVD coatings deposited by the combined high-power impulse magnetron sputtering/unbalanced magnetron sputtering (HIPIMS/UBM) technology", Vacuum, Vol. 82, 1312–1317, 2008.

[13] P. Eh. Hovsepian, A.P. Ehiasarian, U. Rataysaki, “CrAlYCN/CrCN nanoscale multilayer PVD coatings deposited by the combined High Power Impulse Magnetron Sputtering/Unbalanced Magnetron Sputtering (HIPIMS/UBM) technology”, Surface and Coatings Technology, Vol. 203, 1237-1243, 2009.

[14] G. Kamath, A. P. Ehiasarian, P.Eh. Hovsepian, “Tribological and oxidation behaviour of TiAlCN/VCN nanoscale multilayer coating deposited by the combined HIPIMS/(HIPIMS-UBM) technique”, Surf. Coating and Technol, Vol. 205, 8-9, 2823-2829, 2011.

[15] T. Reeswinkel, D. Music, J.M. Schneider, "Ab initio calculations of the structure and mechanical properties of vanadium oxides", J. Phys. Condens. Matter, Vol. 21 145404, 2009.

[16] P Eh. Hovsepian, A P Ehiassarian, Y. P. Purandare, R.Braun, IM Ross, "Effect of high ion irradiation on the structure properties and high temperature tribology of nanoscale CrAlYN/CrN multilayer coating deposited by HIPIMS-HIPIMS technique", Plasma Processes and Polymers, Vol. 6, Issue S1, S118 – S123, 2009.

[17] A.P.Ehiasarian, R.New, W.-D.Münz, Hultman, U.Helmersson, V.Kouznetsov, "Influence of high power densities on the composition of pulsed magnetron plasmas", Vacuum, Vol. 65, 147, 2002.

[18] A.P. Ehiasasrian, J.G. Wen, I. Petrov, "Interface microstructure engineering by high power impulse magnetron sputtering for the enhancement of adhesion," Journal of Appl. Physics, Vol. 101, 054301, 2007.

[19] Y.P.Purandare, A.P.Ehiasarian, P.Eh.Hovsepian,"Deposition of Nanoscale Multilayer CrN/NbN Physical Vapour Deposition Coatings by High Power Impul Magnetron Sputtering", J. Vac. Sci. Technol, Vol. A 26 (2), 288-296, 2008.

[20] G.Kamath, A.Ph.Ehiasarian, P.Eh.Hovsepian," Properties of TiAlCN/VCN Nanoscale Multilayer Coatings Deposited by Mixed High Power Impulse Magnetron Sputtering and Unbalanced Magnetron Sputtering (HIPIMS-UBM) Processes-Impact of HIPIMS during coating", IEEE Transaction on Plasma Science, Vol. 38, (11), 3062-3070, 2010.

[21] B. Chapman, chapter 3, “Plasmas”, taken from “Glow discharge processes, sputtering and etching”.

[22] R. F. Bunshah, chapter 2, “Plasmas in deposition processes”, taken from “Handbook of deposition technologies for films and coatings”, Second Edition. 1994, Noyes Publications.

[23] R. F. Baddour and R. S. Timmins, “The Applications of Plasmas to chemical Processing”, MIT Press, Mass. (1967).

[24] A. Anders, “Fundamentals of pulsed plasmas for materials processing”, Surface and Coatings Technology, Vol. 183, 301–311, (2004).

[25] D. Bohm, Minimum ionic kinetic energy for a stable sheath, in: A. Guthrie, R.K. Wakerling (Eds.), The Characteristics of Electrical Discharges in Magnetic Fields, McGraw-Hill, New York, 77–86, 1949.

[26] S. G. Walton, "An overview of plasma processes", Chapter 13, in 50 years of Vacuum coating and technology, SVC, 2010.

[27] B.Navinsek, "Sputtering—Surface changes induced by ion bombardment", Progress in Surf. Sci. Vol. 7, 49, 1976.

[28] A. I. Alan. "A dictionary of physics", Ed. (2003), Oxford university press.

[29] G. Brauer, B. Szyszka, M. Vergohl, R. Bandorf, Magnetron Sputtering – Milestones of 30 Years, Vacuum, Vol. 84, 1354-1359, 2010.

[30] J. A. Thornton, "J. Vac. Sci. Technol., "Magnetron sputtering: basic physics and application to cylindrical magnetrons", Vol. 15, 171, 1978.

[31] J.A. Thornton and A.S. Penfold, J.L. Vossen, W. Kern, Editors , Thin Film Processes, Academic Press, New York, Vol. 75, 113, 1978.

[32] F. F. Chen, "Introduction to Plasma Physics", 1974.

[33] J. A. Thornton, "Metal Finishing", Vol. 74, 46, 1976.

[34] S Swann, "Magnetron Sputtering", Phys. Technol, 19, 1988.

[35] T. Iseki, "Flat erosion magnetron sputtering with a moving unbalanced magnet", Vacuum, Vol. 80, 662, 2006.

[36] W. Bosscher, H. Lievens, "Advances in magnetron sputter sources", Thin Solid Films, Vol. 351, 15, 1999.

[37] L. P. Sabalev, US. Patent 179, 1974.

[38] A. M. Dorodnov, Soviet Phys. Tech. Phys. Vol. 23, 1058, 1978.

[39] R. L. Boxman, D. M. Sanders, P. J. Martin, "Handbook of Vacuum Arc Science and Technology", Noyes Publications 1995.

[40] A. Anders, "Physics of arching and implications to sputtering", Thin solid Films, Vol. 502, 22-28, 2006.

[41] G. A. Mesyats, "Cathode Phenomena in a Vacuum Discharge: the Breakdown, the Spark, and the Arc", Nauka, 2000.

[42] B. Juttner, "Cathode spots of electric arcs", J. Phys., D, Appl. Phys. Vol. 34, R103, 2001.

[43] E. Hantzsche, Beitr. Plasmaphys, Vol. 23, 77, 1983.

[44] I. G. Brown, A. Anders, S. Anders, M. R. Dickinson, R. A. MacGill, E. M. Oks, "Recent advances in vacuum arc ion source", Surf. Coat. Technol. Vol. 84, 1-3, 550, 1996.

[45] W. D. Munz, D. B. Lewis, S. Creasey, T. Hurkmans, T. Trinh, W. Vonijzendorn, " Defects in TiN and TiAlN coatings grown by combined Cathodic arc/unbalanced magnetron technology", Vacuum, Vol. 46, 323-330, 1995.

[46] W. D. Munz, I. J. Smith, D. B. Lewis, S. Creasey, "Droplet formation on steel substrates during Cathodic steered arc metal ion plating", Vacuum, Vol. **48** (5), 473-481, 1997.

[47] H. W. Wang, M. M. Stack, S. B. Lyon, P. Hovsepian and W. D. Munz, "The corrosion behaviour of macroparticle defects in arc bond-sputtered CrN/NbN superlattice coatigs", Surf. Coat. Technol**.** Vol. 126 (2-3), 279-287, 2000.

[48] B. Window, F. Sharples, N. Savvides, "Magnetically confined sputter source for high ion flux", J. Vac. Sci Technol, Vol. 3 (6), 2368-72, 2009 .

[49] A. P. Ehiasarian, "Development of PVD Coating Processes Informed by Plasma Diagnostics-Ph.D thesis", 2002.

[50] T. E. Sheridan, M. J. Goeckner, J. Goree, "Observation of two temperature electrons in magnetron plasma", J.Vac.Sci.Technol., Vol. A **9** (3), 1623, 1991.

[51] S. Kadlec, J. Musil, W. D. Munz, G. Hakanson, J. E. Sundgren, "Reactive deposition of tin films using unbalanced magnetron sputtering", Surf. Coat. Technology, Vol. 40, 487, 1989.

[52] S. Kadlec, J. Musil, United States Patent, Vol. 5, 234, 560.

[53] D. G. Teer, United States Patent, 5, 556, 519.

[54] W. D. Munz, D. Schulze, F. J. M. Hauzer, A new method for hard coatings: ABS (arc bond sputtering) Surf. Coat. Technol, Vol. 50 (2), 169, 1992.

[55] A. Anders, "Discharge physics of high power impulse magnetron sputtering", Surf. Coat. Technol, DOI: 10.1016/j.surfcoat.2011.03.081.

[56] V. Kouznetsov, K. Macak, J. M. Schneider, U. Helmersson, and I. Petrov, Surface and Coatings Technology, Vol. 122, 290, 1999.

[57] P. J. Kelly, R. D. Arnell, "Magnetron sputtering: a review of recent developments and applications Vacuum", Vol. 56, 159, 2000.

[58] D. V. Mozgrin, I. K. Fetisov, G. V. Khodachenko, "High-current low-pressure quasi-stationary discharge in a magnetic field: experimental research", Plasma Phys. Rep. Vol. 21, 400, 1995.

[59] S. P. Bugaev, N. N. Koval, N. S. Sochugov, A. N. Zakharov, Proceedings of the XVIIth International Symposium on Discharges and Electrical Insulation in Vacuum, 1074, 1996.

[60] K. Macak, V. Kouznetsov, J. Schneider, U. Helmersson, I. Petrov, “Ionized sputter deposition using an extremely high plasma density pulsed magnetron discharge”, J. Vac.Sci. Technol. A, Vac. Surf. Films, Vol. 18, 1533, 2000.

[61] A. P. Ehiasarian, R. New, W. D. Munz, L. Hultman, U. Helmersson, V.Kouznetsov, “Influence of high power densities on the composition of pulsed magnetron plasmas Vacuum”, Vol. 65, 147, 2002.

[62] J. T. Gudmundsson, J. Alami, U. Helmersson, “Evolution of the electron energy distribution and plasma parameters in a pulsed magnetron discharge”, Appl. Phys. Lett. Vol. 78, 3427, 2001.

[63] J. Bohlmark, J. T. Gudmundsson, J. Alami, M. Lattemann, U. Helmersson, “Spatial electron density distribution in a high-power pulsed magnetron discharge”, IEEE Trans. Plasma Sci. Vol. 33, 346, 2005.

[64] J. Bohlmark, J. Alami, C. Christou, A. P. Ehiasarian, U. Helmersson, “Ionization of sputtered metals in high power pulsed magnetron sputtering”, J. Vac. Sci. Technol, A, Vac. Surf. Films. Vol. 23, 18, 2005.

[65] J. Alami, P. Persson, D. Music, J. T. Gudmundsson, U. Helmersson, “Ion-Assisted physical vapor deposition for enhanced film properties on nonflat surfaces”, J. Vac. Sci Technol. Vol. A (23), 278, 2005.

[66] B. M. Dekoven, P. R. Ward, R. E. Weiss, D. J. Christie, R. A. Scholl, W. D. Sproul Proceedings of the 46th annual technical conference of the Society of Vacuum coaters, Albuquerque: SVC; 158, 2003.

[67] A. P. Ehiasarian, P. Hovsepian, L. Hultman, U. Helmersson, I. Petrov., “High power pulsed magnetron sputtered CrNx films”, Surf Coat Technol. Vol. 163, 267–272, 2003.

[68] A. P. Ehiasarian, P. Hovsepian, L. Hultman, U. Helmersson, "Comparison of microstructure and mechanical properties of chromium nitride-based coatings deposited by high power impulse magnetron sputtering and by the combined steered cathodic arc/unbalanced magnetron technique", Thin Solid Films, Vol. 457, 270, 2004.

[69] U. Helmersson, M. Lattemann, J. Bohlmark, A. P. Ehiasarian, J. T. Gudmundsson, “Ionized physical vapor deposition (IPVD): A review of technology and applications”, Thin Solid Films, Vol. 513, 1–24, 2006.

[70] J. T. Gudmundsson, J. Alami, U. Helmersson, "Spatial and temporal behavior of the plasma parameters in a pulsed magnetron discharge", Surf. Coat. Technol. Vol. 161, 249, 2002.

[71] D. V. Mozgrin, I. K. Fetisov, G. V. Khodachenko, Plasma Phys. Rep. Vol. 21, 400, 1995.

[72] S. P. Bugaev, N. S. Sochugov, Surf. Coat. Technol. Vol. 131, 474, 2000.

[73] I. K. Fetisov, A. A. Filippov, G. V. Khodachenko, D. V. Mozgrin, A. A. Pisarev, Vacuum, Vol. 53, 133, 1999.

[74] R. Chistyakov, World Patent No. WO 2004/095497 A2, 2004.

[75] V. Kouznetzov, Swedish Patent No. SE 525231 C2, 2005.

[76] A. P. Ehiasarian, R. Bugyi, "Industrial Size High Power Impulse Magnetron Sputtering", Proceedings of the Society of Vacuum Coaters, 486, 2004.

[77] D.J. Christie, F. Tomasel,W.D. Sproul, D.C. Carter, J. Vac. Sci. Technol., A, Vac. Surf. Films Vol. 22, 1415, 2004.

[78] W.D. Sproul, D.J. Christie, D.C. Carter, F. Tomasel, T. Linz, Surf. Eng. Vol. 20, 174, 2004.

[79] P. Vasina, M. Mesko, M. Ganciu, J. Bretagne, C. Boisse-Laporte, L. De Poucques, M. Touzeau, Europhys. Lett. Vol. 72, 390, 2005.

[80] A. P. Ehiasarian, "Industrial Size High Power Impulse Magnetron Sputtering", 47th Annual Technical Conference Proceedings, USA.

[81] R. W. Behrisch, "Sputtering by particle bombardment", Springer publications, 1981.

[82] M. A. Van Huis, A. Van Veen, F. Labohm, A. V. Fedorov, H. Schut, B. J. Kooi, J. T. M. De Hosson, Vol. 216, 149, 2004.

[83] G. Hakansson, L. Hultman, J. Sundgren, J. E. Greene, W. Munz, Surf Coat Technol, Vol. 48 (1), 51, 1991.

[84] P. Hovsepian, Archives of Metallurgy, Vol. 33 (4), 577, 1988.

[85] A. P. Ehiasarian, J. G. Wen, I. Petrov, "Interface microstructure engineering by high power impulse magnetron sputtering for the enhancement of adhesion", J. Appl. Phys. Vol. 101, 054301, 2007.

[86] W. R. Grove, Phil. Mag., Vol. 5, 203, 1853.

[87] B. A. Movchan and A. V. Demchishin, Fiz. Met. Metalloved. Vol. 28, 83, 1969.

[88] I. Petrov, P. B. Barna, L. Hultman, J. E. Greene, "Microstructural evolution during film growth", J. Vac. Sci. Technol. Vol. A(5), 21, 2003.

[89] J. A. Thorton, "Influence of apparatus geometry and deposition conditions on the structure and topography of thick sputtered coatings", J. Vac. Sci. Technol, Vol. 11, 666, 1974.

[90] G. H. Gilmer, H. Huang, T. Diaz de la Rubia, J. Dalla Torre, and F. Baumann, Thin Solid Films Vol. 365, 189, 2000.

[91] C. V. Thompson, "Grain growth in thin films", Annu. Rev. Mater. Sci. Vol. 20, 245, 1990.

[92] R. Messier, "Toward quantification of thin film morphology", J. Vac. Sci. Technol. Vol. A 4, 490, 1986.

[93] J. Musil, "Hard and Superhard nanocomposite coatings", Surf. Coat. Technol, Vol. 125, 322-330, 2000.

[94] I. Petrov, A. Myers, J. E. Greene, J. R. Abelson, "Mass and energy resolved detection of ions and neutral sputtered species incident at the substrate during reactive magnetron sputtering of Ti in mixed Ar+N_2 mixtures", J. Vac. Sci. Technol. Vol. A 12 (5), 2846, 1994.

[95] D. M. Mattox, "Particle bombardment efects on thin-film deposition: A review", J. Vac. Sci. Technol. Vol. A 7 (3), 1105-1114, 1989.

[96] K. H. Muller, "Ion beam induced epitaxial vapour-phase growth: A molecular dynamics study", Phys. Rev. B Vol. 35 (15), 7906-7913, 1987.

[97] L. Hultman, W.-D. Munz, J. Musil, S. Kadlec, I. Petrov, J. E. Greene, "Low-energy (~ 100 eV) ion irradiation during growth of TiN deposited by reactive magnetron sputtering: Effects of ion flux on film microstructure", J. Vac. Sci. Technol. Vol. A 9(3), 434, 1991.

[98] I. Petrov, L. Hultman, U. Helmersson, J. E. Sundgren, J. E. Greene, "Microstructure modification of TiN by ion bombardment during reactive sputter deposition", Thin Solid Films Vol. 169, 299-314, 1989.

[99] P.J. Kelly, R. D. Arnell, "Development of a novel structure zone model relating to the Closed-field unbalanced magnetron sputtering system", J. Vac. Sci. Technol. Vol. A 16(5), 2858, 1998.

[100] Ajayan, P. M., Schadler, L.S., and Braun, P.V. Nanocomposite Science and Technology, (2003), Wiley- VCH-Verlag GmbH, Weinheim, Germany.

[101] Nalwa, H.S. Handbook of Organic-Inorganic Hybrid Materials and Nanocomposites, Vol. 1–2, Stevenson Ranch, CA, USA, 2003, American Scientific Publishers.

[102] S. A. Barnett, A. Madan, I. Kim, and K. Martin, "Stability of nanometer-thick layers in hard coatings", MRS Bull, Vol. 28, 169-172, 2003.

[103] W. D. Munz, "Large scale manufacturing of nanoscale multilayered hard coatings deposited by Cathodic arc/unbalanced magnetron sputtering", MRS Bull. Vol. 28, 173-179, 2003.

[104] J. Patscheider, "Nanocomposite hard coatings for wear protection, MRS Bull,

Vol. 28, 180-183, 2003.

[105] G.M. Demyashev, A.L. Taube, E. Siores, "Superhard Nanocomposite coatings", in "Handbook of Organic-Inorganic Hybrid Materials and Nanocomposites, Volume 1: Hybrid Materials" ed. H. S Nalwa, 2003, American Scientific Publishers, p. 1.

[106] Lee, K.Y. and L.A. Goettler, "Structure-property relationships in polymer blend nanocomposites", Polym. Eng. Sci., Vol. 44, 1103–1111, 2004.

[107] Vollath, D. and D. V. Szabo, "Synthesis and properties of nanocomposites", Adv. Eng. Mater., Vol. 6,117–127, 2004.

[108] L. Hultman, "Synthesis, Structure, and Properties of Superhard Superlattice Coatings", in Nanostructured coatings, edited by A. Cavaleiro, and Th.M.De. Hosson.

[109] P. Eh. Hovsepian, and W. D. Muz, "Recent progress in large-scale production of nanoscale multilayer/superlattice hard coatings", Vacuum, Vol. 69, 27-36, 2003.

[110] J. Musil, P. Baroch and P. Zeman, "Hard nanocomposite coatings. Present status and trends", Chapter 1, from Plasma Surface Engineering Research and its Practical Applicationgs, 2008.

[111] H. Polakova, J. Musil, J. Vlcek, J. Allaart, and C. Mitterer, "Structure-hardness relations in sputtered Ti–Al–V–N films", Thin Solid Films, Vol. 444, 189, 2003.

[112] J. Musil, H. Polakova, J. Suna, J. Vlcek, "Effect of ion bombardment on properties of hard reactively sputtered Ti(Fe)Nx films", Surf. Coat. Technol. Vol. 177, 289, 2004.

[113] J. Musil, D. Herman, J. Sicha, R. Cerstvy, "Role of energy in low-temperature high-rate formation of hydrophilic TiO_2 thin films using pulsed magnetron sputtering", J. Vac. Sci. Technol. A, Vol. 25(4), 666, 2004.

[114] J. Musil, "Nanocomposite coatings with enhanced hardness", Acta Metallurgica Sinica (English letters), Vol. 18(3), 433, 2002.

[115] J. Musil, "Physical and mechanical properties of hard nano-composite films prepared by reactive magnetron sputtering", in Nanostructured Hard coatings, eds. J.T.M. De Hosson, A. Cavaleiro, Springer Science+Business Media, LCC, New York, 407.

[116] J. Suna, J. Musil, and V. Ondok, "Enhanced hardness in sputtered Zr–Ni–N films", Surf. Coat. Technol. Vol. 200, 6293, 2006.

[117] U. Wahlstrom, L. Hultman, J.E. Sundgren, F. Abidi, I. Petrov, and J.E. Greene, "Crystal growth and microstructure of polycrystalline $Ti_{1-x}Al_xN$ alloy films deposited by ultra-high-vacuum dual-target magnetron sputtering", Vol. 235, 1-2, 62-70,1993.

[118] A. Pelisson, M. P. Wojtan, H.J. Hug, J. Patscheider, "Microstructure and mechanical properties of Al–Si–N transparent hard coatings deposited by magnetron sputtering", Surf. Coat. Technol, Vol. 202, 884-889, 2007.

[119] Y.H. Lu, Y.G. Shen, "Effect of carbon content on thermal stability of Ti–C*x*–N*y* thin films", J. Mater. Res. Vol. 23, 671-678, 2008.

[120] S. Zhang, D. Sun, Y. Fu, and H. Du, "Recent advances of superhard nanocomposite coatings: a review," Surf. Coat. Technol, Vol. 167, 113–119, 2003.

[121] P. Holubar, M. Jilek, and M. Sima, "Present and possible future applications of Superhard nanocomposite coatings", Surf. Coat. Technol., Vol. 133–134, 145–151, 2000.

[122] A. Erdemir, "Review of engineered tribological interfaces for improved boundarylubrication",Tribol. Int, Vol. 38, 249–256, 2005.

[123] P. Eh. Hovsepian, D.B. Lewis, C. Constable, Q. Luo, Y. N. Kok, and W. D. Munz, "Combined steered Cathodic arc/unbalanced magnetron grown C/Cr nanoscale multilayer coatings for tribolocial applications". Surf. Coat. Technol. Vol. 174, 762-769, 2003.

[124] P. Eh. Hovsepian, W. D. Munz, B. Schlomer, G. Gregory, and I.J. Smith, "PVD CrN/NbN super lattice coatings to protect components used in the textile industry", in Proceedings of 44th, Annual Conference of Soc. Of Vacuum Coaters SVC, Philadephia, USA, pp. 72-77, 2001.

[125] W.D. Münz, "Super lattice-structured hard coatings", in Trends and Applications of Thin Films, pp. 12–16, 2000.

[126] C. Mitterer, and P.H. Mayrhofer, Some materials science aspects of PVD hard coatings, Adv.Solid State Phys., Vol. 41, 263–274, 2001.

[127] R. Hauert, J. Patscheider, L. Knoblauch, and M. Diserens, "New coatings by nanostructuring", Adv. Mater, Vol. 11, 175–177, 1999.

[128] P.Eh. Hovsepian, D.B. Lewis, Q. Luo, W.D. Munz, P.H. Mayrhofer, C. Mitterer, Z. Zhuo, and W.M. Rainforth, "TiAlN based nanoscale multilayer PVD coatings designed to adapt their tribological properties at elevated temperatures", in Invited paper presented at ICMCTF 2004, San Diego, CA, 2004, Thin Solid Films, Vol. 485, 160-168, 2005.

[129] A.A. VoevodinJ.P. O'Neill, and J.S. Zabinski, "Nanocomposite tribological coatings for aerospace applications", Surf. Coat. Technol., Vol. 119, 36–45, 1999.

[130] D. M. Gruen, "Nanocrystalline diamond films", Annu. Rev. Mater. Sci., Vol. 29, 211-259, 1999.

[131] L. Holland and S.M. Ojha, "Deposition of hard and insulating carbonaceous films on an r.f. target in a butane plasma", Thin Solid Films, Vol. 38, L17, 2001.

[132] E.G. Spencer, P.H. Schmidt, D.C. Joy and F.J. Sansalore, "Ion beam deposited polycrystalline diamond films", Appl. Phys. Letters, Vol. 29, 118, 1976.

[133] Erdemir, A. and Donnet, C. in Tribology of Diamond, Diamond like Carbon and Related Films,Modern Tribology Handbook, Bhushan, B., Ed., CRC Press, Boca Raton, FL, pp. 871–899, 2000.

[134] J. Ullmann, K. Baba, H. Martin, G.K. Wolf, "Effect of deposition conditions on the growth and behaviour of thin carbon films prepared by ion-assisted evaporation", Surf. Coat. Technol. Vol. 74-75, 746-753, 1995.

[135] R.G. Lacerda, P. Hammer, F.L. Freire, F. Alvarez, F. C. Marques, "On the structure of argon assisted amorphous carbon films", Dia. Relat. Mater. Vol. 9 (3-6), 796-800, (2000).

[136] S. Yang, D.G. Teer, "Investigation of sputtered carbon and carbon/chromium multi-layered coating", Surf. Coat. Technol. Vol. 131, 412-416, 2000.

[137] S.K. Field, M. Jarratt, D.G. Teer, "Tribological properties of graphite-like and diamond-like carbon coatings", Tribology International, Vol. 37, 949-956, 2004.

[138] S. Yang, X. Li, N.M. Renevier, D.G. Teer, "Tribological properties and wear mechanism of sputtered C/Cr coating", Surf. Coat. Technol. Vol. 142-144, 85-93, 2001.

[139] J. Robertson, "Diamond like carbon", Pure Appl. Chem. Vol. 66, 1789, 1994.

[140] A.C. Ferrari and J. Robertson, "Interpretation of Raman spectra of disordered and amorphous carbon", J. Appl. Phys, Vol. 61, 14095, 2005.

[141] R.H.Savage, "Graphite lubrication", J.Appl.Phys, Vol. 19, 1, 1948.

[142] W Jacob, W Moller, "On the structure of thin hydrocarbon films", App Phys Lett Vol. 63, 1771, 1993.

[143] V.M. Tiainen, "Amorphous carbon as bio-mechanical coating-mechanical properties and biological applications", Dia. Relat. Mater. Vol. 10, 153, 2001.

[144] B. T. Kelly, "Physics of graphite", Applied Science publishers, London; N.J. Englewood, 1991.

[145] A.A. Voevodin, M.A. Capano, S.J.P. Laube, M.S. Donley, J.S. Zabinski, "Design of a Ti/TiC/DLC functionally gradient coating based on studies of structural transitions in Ti-C films", Thin Solid Films, Vol. 298, 107-115, 1997.

[146] A.A. Voevoidn, J.P.O'Neill, S.V. Prasad, J.S. Zabinski, "Nanocrystalline WC and WC/a-C composite coatings produced from intersected plasma fluxes at low deposition temperature", J.Vac. Sci. Technol. Vol. A 17, 986-992, 1999.

[147] G. Kamath, P.Eh.Hovsepian, A.P.Ehiasarian, “Microstructural, oxidation and tribological properties of TiAlCN/VCN nanoscale coating deposited by reactive HIPIMS”, in Annual 57th SVC conference, 2011, Chicago, USA.

[148] Said Jahanmir, Hooshang Heshmat, and Crystal Heshmat, “Evaluation of DLC Coatings for High-Temperature Foil Bearing Applications, J. Tribol., Vol. 131, 011301, 2009.

[149] S. Yang, D. Camino, A.H.S. Jones, D.G. Teer, “Deposition and tribological behaviour of sputtered carbon hard coatings”, Surf. Coat. Technol. Vol. 124,110-116, 2000.

[150] A. Bloyce, “Carbon PVD coatings wear it well”, Materials World, P. 13. 2000.

[151] Ch. Donnet, A. Erdemir, “Tribology of Diamond-Like Carbon Films-Fundamental and Applications”, 2000, Springer line publications.

[152] A.R. Krauss, O. Auciello, D.M. Gruen, A. Jayatissa, A. Sumant, J. Tucek, D.C. Mancini, N. Moldovan, A. Erdemir, Ersoy, D., Gardos, M.N., Busmann, H.G. E.M. Meyer, and Ding, M.Q. Ultrananocrystalline diamond thin films for MEMS and moving mechanical assembly devices, Diamond Relat. Mater, Vol. 10, 1952–1961, 2001.

[153] P.Eh.Hovsepian, A.P.Ehiasarian, A. Deeming, C. Schimpf, “Novel TiAlCN/VCN nanoscale multilayer PVD coatings deposited by the combined high-power impulse magnetron sputtering/unbalanced magnetron sputtering (HIPIMS/UBM) technology”, Vacuum, Vol. 82, 1312–1317, 2008.

[154] S. Veprek, “Superhard nanocomposites: design concept, properties, present and future industrial applications”, Eur. Phys. J. App. Phys., Vol. 28, 313–317, 2004.

[155] C. Donnet, and A. Erdemir, "Historical developments and new trends in tribological and solid lubricant coatings", Surf. Coat. Technol., Vol. 180–181, (2004),76–84.

[156] E. Bergmann, G. I. van der Kolk, B. Buil, and T. Hurkmans, “The next generation of deposition equipment for wear protection coatings”, Surf. Coat. Technol., Vol. 114, 101–107, 1999.

[157] K.L. Choy, “Chemical vapour deposition of coatings”, Prog. Mater. Sci., Vol. 48, 57–170, 2003.

[158] S. Safaie, L. F. Pochet, and C. Howard, “CVD coatings: From cutting tools to aerospace applications and their future potential”, Surf. Coat. Technol., Vol. 94–95, 70–77, 1997.

[159] J. M. Schneider, S. L. Rohde, W. D. Sproul, and A. Matthews, “Recent developments in plasma assisted physical vapour deposition”, J. Phys. Appl. Phys., Vol. 33, 173–186, 2000.

[160] J.H. Jeon, S.R. Choi, and W.S. Chung, "Synthesis and characterization of quaternary Ti-Si-C-N coatings prepared by a hybrid deposition technique", Surf.Coat.Tech, Vol. 188–189, 415–419, 2004.

[161] J.P. Celis, D. Drees, M.Z. Huq, P.Q. Wu, and M. De Bonte, Hybrid processes — a versatile technique to match process requirements and coating needs, Surf. Coat. Technol., Vol. 113, 165–181, 1999.

[162] P.Eh. Hovsepian, D.B. Lewis, C. Constable, Q. Luo, Y.N. Kok, and W.D. Münz, "Combined steered cathodic arc/unbalanced magnetron grown C/Cr nanoscale multilayer coatings for tribological applications, Surf. Coat. Technol., Vol. 174, 762–769, 2003.

[163] C. Strondl, N.M.Carvalho, J.T.M. De Hosson, and Van der Kolk, G.J. Investigation on the formation of tungsten carbide in tungsten-containing diamond like carbon coatings, Surf. Coat.Technol., Vol. 162, 288–293, 2003.

[164] A.J.Perry, and D.G. Teer, Surface technology for temperature-sensitive materials, Surf. Coat.Technol., Vol. 97, 244–249, 1997.

[165] A.P. Ehiasarian, W.D. Münz, L. Hultman, U. Helmersson, and I. Petrov, High-power pulsed magnetron-sputtered CrNx films, Surf. Coat. Technol, Vol. 163, 267–272, 2003.

[166] A.P. Ehiasarian, A. Anders, I. Petrov, "Combined filtered Cathodic arc pretreatment- magnetron sputter deposition of highly adherent CrN film", J. Vac. Sci. Technol, Vol. A 25(3), 543-547, 2007.

[167] A. P. Ehiasarian, J.G. Wen, I. Petrov, "Interface microstructure engineering by high power impulse magnetron sputtering for enhancement of adhesion", J. Appl. Phy, Vol. 101, 154301, 2007.

[168] A. P. Ehiasarian, R. Tietema, P. Hovsepian, D. Doerwald, R. Bugyi, A.Klimczak, Pat appl. US2010/0025230A, Apr. 10.2007.

[169] A. P. Ehiasarain, "Fundamentals and applications of HIPIMS", in plasma surface engineering research and its practical applications, edited by R. Wei. year

[170] A.A. Voevodin, M.S. Donley, J.S. Zabinski, "Pulsed laser deposition of diamond like carbon wear protective coatings: a review", Surf. Coat. Technol. Vol. 92 (1-2), 42-49, 1997.

[171] D.T. Quinto, "Technology perspective on CVD- and PVD-coated metal-cutting tools", Int. J. Refract. Metals Hard Mater, Vol. 14, 7–20, 1996.

[172] W.D. Munz, D. Schulze, F.J.M. Hauzer, "A new method for hard coatings: ABS^{TM}(arc bond sputtering), Surf. Coat. Technol. Vol. 50, 169-178, 1992.

[173] A. Anders, "Ion charge state distributions of vacuum arc plasmas: The origin of species, Phys. Rev. E, Vol. 55, 969-981, 1997.

[174] C. Schonjahan, L.A. Donohue, D.B. Lewis, W.D. Munz, R.D. Twesten, I. Petrov" Enhanced adhesion through local epitaxy of transition-metal nitride coatings on ferritic steel promoted by metal ion etching in a comibined cathodic arc/unbalanced magnetron deposition system, J. Vac. Sci. Technol., Vol. A18(4), 1718-1723, 2000.

[175] W.D. Munz, D. B. Lewis, P.Eh. Hovsepian, C. Schonjahn, A.P. Ehiasarian, and I. Smith, "Industrial scale manufactured superlattice hard PVD coatings", Surf. Eng. Vol. 17(1), 15-27, 2001.

[176] I. Petrov, P. Losbichler, D. Bergstrom, J. E. Greene, W.D.Munze, T. Hurkmans, and T. Trinh, "Ion assisted growth of Ti1-xAlxN/Ti1-yNbN multilayers by combined cathodic-arc/magnetron sputter deposition, "Thin Solid Films, Vol. 302, 179-192, 1997.

[177] P. Eh. Hovsepian and W.D. Munz, "synthesis, structure of nanoscale multilayer/superlattice PVD coatings" chapter 14 in "Nanostructured Coatings", edited by A. Cavaleiro, M. De. Hosson. 2006, Springer.

[178] W.D.Munz, I.J. Smith, D.B. Lewis, and S. Creasey, " Droplet formation on steel substrates during cathodic steered arc metal ion etching", Vacuum, Vol. 48, 473-481, 1997.

[179] Eh. Hovsepian et.al, Vacuum, Vol. 82, 1312-1317, 2008.

[180] P.Eh.Hovsepian, A.P.Ehiasarian, A. Deeming, C. Schimpf, "Plasma processes and polymers Vol. 4, S897, 2007.

[181] A. P. Ehiasarian, P. Eh. Hovsepian,, "PVD Coated Substrate" UK Patent: GB2425780B, 05.09.2007, EP 1874981, 14.01.2009

[182] "Mechanical Testing and Evaluation," Volume 5, ASM Handbook, 2000.

[183] T. Forster, "Coating technologies and measurement methods", in Evolution, Business and technology from SKF, SKF Industrial Division, Steyr, Austria, 2008.

[184] I. M. Hutchings, "Friction", chapter 2 from "Tribology, friction and wear of engineering materials", Fifth edition. 1992, BH publishers.

[185] Nano-indentation, Manual from CSM instruments.

[186] B. Bhushan, V. N. Koinkar, "Nanoindentation hardness measurements using atomic force microscopy", Appl. Phys. Lett. Vol. 64, 1653–1655, 1994.

[187] D. A. Skoog, F. J. Holler, and T. A. Nieman, Principles of Instrumental Analysis (Harcourt Brace College Publishers, 1992.

[188] B. Henning and J. Holger, "Surface and Thin Film Analysis:". 2002, Wiley-VCH publishers.

[189] Hiden analytical, *PSM003 User's manual.* (http://www.hidenanalytical.com/?gclid=CL7vpa7B2a0CFVGKfAodwwn8oA)

[190] B.D.Cullity & S.R.Stock, "Elements of X-ray diffraction", 3 Edition, 2001, Wesley publishers.

[191] M. Birkolz, "Principles of X-ray diffraction", in Thin films analysis by X-ray Diffraction, 2006, Wiley VCH.

[192] V. Holy, U. Pietsch, T. Baumbach, "High Resolution X-ray Scattering from Thin Films and Multilayers", Springer Tracts in Modern Physics. 2006, Springer

[193] C.N. Banwell and E. McCash, Infrared and Raman spectroscopy, in "Fundamental of spectroscopy", 5th edition. 1994, McGraw Hill Publishers.

[194] Raman spectroscopy manual from HORRIBA JOBINVYONG. (http://www.horiba.com/scientific/products/raman-spectroscopy/)

[195] "Thermo gravimetric Analysis" by SETARAM instrumentation. (http://www.labwrench.com/?equipment.view/equipmentNo/12429/Setaram-Instrumentation/SETSYS-Evolution-TGA/)

[196] L. Reimer, Scanning electron microscopy: physics of image formation and microanalysis. Springer, p. 527, 1998.

[197] NOVA FEI SEM200 Manual. (http://www.fei.com/products/scanning-electron-microscopes/nova-nanosem-50.aspx)

[198] D.B.Williams, C. B.Carter, "Transmission Electron Microscopy". 1996, Pienum Publishers.

[199] Electron microscopy of nanostructured coatings, in "in Nanostructured coatings",edited by A. Cavaleiro, and Th.M.De. Hosson. 2006, Springer.

[200] Introduction to TEM, HVEM, JEOL, Ultra high vacuum TEM manual. (http://www.fei.com/products/transmission-electron-microscopes/titan.aspx)

[201] Harish C, Barshilia, K.S.Rajam, "A Raman-scattering study on the interface structure of nanolayered TiAlN/TiN and TiN/NbN multilayer thin films grown by reactive DC magnetron sputtering, J. Appl. Phy, Vol. 98, 2005.

[202] C.P.ConstableJ. Yarwood, P.Eh.Hovsepian, L.A.Donohue, D.B.Lewis, W.-D.Münz, "Structural determination of wear debris generated from sliding wear tests on ceramic coatings using Raman microscopy", J. Vac. Sci. Technol, Vol.

A 18(4), p. 1681, 2000.

[203] N.Fateh, G.A.Fontalvo, G.Gassner, C.Mitterer, "Influence of high-temperature oxide formation on the tribological behaviour of TiN and VN coatings", Wear, 262, 1152-1158, 2007.

[204] K. Kutschej, P. H. Mayrhofer, M. Kathrein, P. Polcik, C. Mitterer, "Influence of oxide phase formation on the tribological behaviour of Ti-Al-V-N coatings", Surf.Coat.and Tech, Vol. 200, 1731-1737, 2005.

[205] A.P.Ehiasarian, J.G.Wen, I.Petrov, “Interface microstructure engineering by high power impulse magnetron sputtering for the enhancement of adhesion”, J. Appl. Phys. Vol. 101, 054301, 2007.

[206] P.Eh.Hovsepian, Archives of matullurgy, Vol. 33, (4), (1988), 577.

[207] W. Carr, M. Seidl, G.S. Tompa, A. Souzis, “Composite thin film production by ion bombardment”, J.Vac. Sci. Technol A., Vol. 5, 1250, 1987.

[208] C. D. Pintassilgo, J. Loureiro, G.Cernogora and M. Touzeau, “Methane decomposition and active nitrogen in a N_2-CH_4 glow discharge at low pressures”, Plasma Sources Sci.Technol, Vol. 8, 463-478, 1999.

[209] C.D.Pintassilgo, J.Loureiro, “Production of hydrocarbons and nitriles using a N_2–CH_4 afterglow plasma for simulation of Titan's atmosphere”, Planetary and Space Science, Vol. 57, 1621-1630, 2009.

[210] J.C.Legrand, A.M.Diamy, R.Hrach, V.Hrachova, “Mechanisms of methane decomposition in nitrogen afterglow plasma”, Vacuum, Vol. 52, 27-32, 1999.

[211] A.P.Ehiasarian, R.New, W.-D.Münz, Hultman, U.Helmersson, V.Kouznetsov, "Influence of high power densities on the composition of pulsed magnetron plasmas", Vacuum, Vol. 65, 147, 2002,.

[212] J.C.Legrand, A.M.Diamy, R.Hrach, V.Hrachova, “Kinetics of reactions in CH_4/N_2 afterglow plasma”, Vacuum, Vol. 48, 671-675, 1997.

[213] P. Eh. Hovsepian, A.P. Ehiasarian, I.Petrov, “TiAlCN/VCN nanolayer coatings suitable for machining of Al and Ti alloys deposited by combined high power impulse magnetron sputtering/unbalanced magnetron sputtering”,Surface Engineering 2009.

[214] Knotek IO, Atzor M, Prengel H-G. Surf Coat Technol, Vol. 36. 265, 1988.

[215] Yusuke T. Kobe Steel 1990; JP4221057.

[216] D.B. Lewis, Q. Luo, P.Eh. Hovsepian, W.-D. Munz, "Interrelationship between atomic species, bias voltage, texture and microstructure of nano-scale multilayers", Surf. Coat. Technol, Vol. 184, 225–23, 2004.

[217] G. Farges, E. Beuprez, M.C. Staine-Catherine, "Preparation and characterization of V- N films deposited by reactive triode magnetron sputtering", Surf. Coat.Technol. Vol. 54–55, 115, 1992.

[218] Hisanori O, et al. Sumitomo Electric Industries 1996. JP 32406797.

[219] K. Yamamoto, et al. Kobe Steel 2003; US2003/0148145 A1.

[220] W. R. Gilkes, H. S. Sands, D. N. Batchelder, J. Robertson, and W. I. Milne, "Direct observation of sp3 bonding in tetrahedral amorphous carbon using ultraviolet Raman spectroscopy", Appl. Phys. Lett. Vol. 70, 1980, 1997.

[221] V. I. Merkulov, J. S. Lannin, C. H. Munro, S. A. Asher, V. S.Veerasamy, and W.I.Milne, "uv Studies of Tetrahedral Bonding in Diamond like Amorphou Carbon", Phys. Rev. Lett. Vol.78, 4869, 1997.

[222] A.C.Ferrari, J.Robertson, "Interpretation of Raman spectra of disordered and amorphous carbon", Physical Review B, Vol. 61, 20, 1993.

[223] C.Casiraghi, A.C.Ferrari, J.Robertson, "Raman spectroscopy of hydrogenate amorphous carbons", Phy.Rev.B, Vol. 72, 0845401, 2005.

[224] A.P.Ehiasarian, W.-D.Münz, L.Hultman, U.Helmersson, I. Petrov, "High power pulsed magnetron sputtered CrN_x films", Surf. Coat. Technol, Vol. 163-164, pp. 267-272, 2003.

[225] Y.N. Kok, P. Eh. Hovsepian, Q. Luo, D.B. Lewis, J. G. Wen, I. Petrov, Thin Solid Films, Vol. 475, 219-226, 2005.

[226] D.V. Mozgrin, I.K.Fetisov, G.V.Khodachenko, Plasma Physics Reports, Vol. 21 (5), 400, 1995.

[227] V. Kouznetsov, K. Macak, M. Schneider, U. Helmersson, I. Petrov, Surface and Coatings Technology, Vol. 122 (2-3), 290, 1999.

[228] J. Alami, P.O.A. Persson, D. Music, J.T. Gudmundsson, J. Bohlmark, U. Helmersson, "Journal of Vacuum Science and Technology A:" Vacuum, Surfaces and Films, Vol. 23(2), 278, (2005).

[229] A.P. Ehiasarian and R. Bugyi, Proc. 47th Annual Technical Conference of Society of Vacuum Coaters, 437, (2004).

[230] Y.H. Lu, Y.G.Shen, “Nanostructure transition: From solid solution Ti (N, C) to Nanocomposite nc-Ti (N, C)/a-(C, CNx)”, Applied Physics Letters, Vol. 90, 2219, 2007.

[231] W. Ensinger, “Ion bombardment effects during deposition of nitride and metal films”, Surface Coating & Technology, Vol. 99, 1-13, 1998.

[232] Z. Zhou, W.M Rainforth, D.B Lewis, S Creasy, J.J Forsyth, Clegg E, A.P Ehiasarian, P.Eh Hovespian, W-.D Munz, "Oxidation behaviour of nanoscale TiAlN/VN multilayer coatings", Surface and Coatings Technology, Vol. 177, 198-203, 2004.

[233] D.B.Lewis, S. J. Creasey, Z. Zhuo, J.J. Forsyth, A.P. Ehiasarian P.Eh. Hovsepian, Q. Luo, W. M. Rainforth, W.-D. Münz , “The effect of (Ti+Al):V ratio on the structure and oxidation behaviour of TiAlN/VN nano-scale multilayer coatings”, Surf. Coat. Technol, Vol. 177-178, p. 252-259, 2004.

[234] M.N.Gardos, Magneli phases of anion-deficient rutile as lubricious oxides. Part I. Tribological behavior of single-crystal and polycrystalline rutile (Ti_nO_{2n-1}), Tribology letters, Vol. 8, 65-78, 2000.

[235] M.Woydt, A.Skopp, I.Dorfel, K.Witke, "Wear engineering oxides/anti-wear oxides", Wear, Vol. 218, 84–95, 1988.

[236] Q. Luo, W.M. Rainforth, W.D. Munz, “TEM observation of wear mechanisms of TiAlCrN and TiAlN/CrN coatings grown by combined steered-arc/unbalanced magnetron deposition”, Wear, Vol. 74, 225-229, 1999.

[237] P.Eh.Hovsepian, D.B.Lewis, W.D.Munz, “Recent progress in large scale manufacturing of multilayer/superlattice hard coatings”, Surf. Coat. Technol., Vol. 133, 166-175, 2000.

[238] A.P.Ehiasarian, A.Anders, I.Petrov, "Combined filtered cathodic arc etching pretreatment-magnetron sputter deposition of highly adherent CrN films", J.Vac.Sci.Technol. Vol. A 25, 543, 2007.

[239] W.D.Munz, D.B.Lewis, P.Eh.Hovsepian, C.Schonjahn, A.Ehiasarian, I.J.Smith, "Industrial scale manufactured superlattice hard PVD coatings", Surf Engineering, Vol. 17, 15, 2001.

[240] Hovsepian, P.E., Lewis, D.B., Constable, C., Luo, Q., Kok, Y.N., and Münz, W.D. (2003) Combined steered cathodic arc/unbalanced magnetron grown C/Cr nanoscale multilayer coatings for tribological applications, Surf. Coat. Technol., Vol. 174, 762 - 769, 2008.

[241] P.Eh. Hovsepian, Y.N. Kok, A.P. Ehiasarian, A. Erdemir, J.G. Wen, and I. Petrov, Structure and tribological behaviour of nanoscale multilayer C/Cr coatings deposited by the combined steered cathodic arc/unbalanced magnetron sputtering technique, Thin Solid Films, Vol. 7 - 13, 447 - 448, 2004.

[242] Czyzniewski, A. (2003) Deposition and some properties of nanocrystalline WC and nanocomposite WC/a-C:H coatings, Thin Solid Films, Vol. 433, 180 - 185, 2003.

[243] C.A. Taylor, M.F.Wayne and W.K.S. Chiu, "Residual stress measurements in thin carbon films deposited spectroscopy and nanoindentation", Thin Solid Films , Vol. 429, 190, 2003.

[244] D.T.Quinto, "PVD coating applications for cutting tools", chapter 4 from plasma surface engineering research and its practical applications. 2008.

[245] Z. Zhou, W.M Rainforth, Q.Luo, P.Eh.Hovsepian, J.J.Ojeda, M.E.Romero-Gonzalez, "Wear and friction of TiAlN/VN coatings against Al2O3, in air at room temperature and elevated temperature", Acta Materilia, Vol. 58, (2010), 2912-2925.

[246] M.N. Gardos, "The Effect of Anion Vacancies on the Tribological Properties of Rutile (TiO_{2-x})", Tribol. Trans. Vol. 31, 427, 1988.

[247] M.N. Gardos, H.-S. Hong and W.O. Winer, "The Effect of Anion Vacancies on the Tribological Properties of Rutile (TiO2-x), Part II: Experimental Evidence Tribol. Trans. Vol. 33, 209, 1990.

[248] U. Schwingenschlogl and V. Eyert, "The vanadium Magneli phases V_nO_{2n-1}" Ann. Phys. (Leipzig) Vol. 13, No 9, 475-510, 2004,

[249] D.McIntyre, J.E.Greenne, G. Håkansson, J.-E.Sundgren, W.-D.Münz, "Oxidation of metastable single-phase polycrystalline Ti0.5Al0.5N films: Kinetics and mechanisms", J. Appl. Phys, Vol. 67,1542-1553, 1990.

[250] W.-D Münz, "Titanium aluminium nitride films – a new alternative to TiN coatings", J. Vac. Sci. Technol, Vol. A4 (6), 2717-2725, 1986.

[251] I.Petrov, P.Losbichler, D.Bergstrom, J.E.Greene, W.-D.Münz, T.Hurkmans, and T.Trinh, "Ion-assisted growth of $Ti_{1-x}Al_xN/Ti_{1-y}Nb_yN$ multilayers by combined cathodic-arc/magnetron-sputter deposition", Thin Solid Films, Vol. 302, 179. 1997.

[252] E. Lugscheider, O. Knotek, K. Bobzin, S. Barwulf, "Tribological properties, phase generation and high temperature phase stability of tungsten- and vanadium-oxides deposited by reactive MSIP-PVD process for innovative lubrication applications Surf. Coat.Technol, Vol. 362, 133-134, 2000.

[253] Ji-Guang Li' and T. Ishiga, “Brookite-rutile phase transformation of TiO_2 studied with monodispersed particles”, Acta Materialia, Volume 52, Issue 17, 5143.

[254] O. O. Ajayi and K. C. Ludema: Wear, Vol. 140, 191, 1990.

[255] Q. Luo, C. Schimpf, A. P. Ehiasarian and P. E. Hovsepian, " Structure and Wear Mechanisms of Nano-Structured TiAlCN/VCN Multilayer coatings, Plasma Process. Polym, Vol. 4, S916, 2007.

[256] P.H.Mayhofer, P.Eh.Hovsepian, C.Mitterer, W.D.Munz, “Calorimetric evidence for frictional self-adaptation of TiAlN/VN superlattice coatings”, Surf.Coat.Technol. Vol. 177-178, 341-347, 2004.